Data Processing and Investigations for the GRACE Follow-On Laser Ranging Interferometer

Master Thesis

by

Malte Matthias Misfeldt

June 2019

Max Planck Institute for Gravitational Physics
(Albert Einstein Institute)
Gottfried Wilhelm Leibniz Universität Hannover
Germany

1st Examiner:	Apl. Prof. Dr. Gerhard Heinzel
2nd Examiner:	Prof. Dr. Karsten Danzmann
Supervisor:	Dr. Vitali Müller

Kurzzusammenfassung

Diese Arbeit, deren Titel zu deutsch *Datenverarbeitung und Untersuchungen für das GRACE-Follow On Laser Ranging Interferometer* lautet, präsentiert erste ausführliche Ergebnisse des *Laser Ranging Interferometers* (LRI, zu deutsch etwa *Laser Distanz Interferometer*), welches Teil der *Gravity Recovery And Climate Experiment - Follow On* (GRACE-Follow On) Mission ist. Das LRI ist ein neuartiges Messinstrument, das in einer amerikanisch-deutschen Kollaboration entwickelt wurde, welche das Albert-Einstein Institut (AEI) in Hannover einschließt. Das LRI hat erfolgreich die Eignung von Laser Interferometrie zur Abstandsmessung zwischen zwei räumlich getrennten Satelliten demonstriert und wird die satellitengestützte Gravimetrie auf ein neues Sensitivitätslevel heben.

Der Autor dieser Arbeit hat zu diesem Projekt beigetragen, indem er ein umfassendes Programmiergerüst zur Verarbeitung der LRI Telemetrie entwickelt und verschiedenste Arten von LRI Daten untersucht hat. Daher umfasst der Titel der Arbeit beide Aspekte, die Datenverarbeitung und Untersuchungen an den Daten.

Im Rahmen dieser Arbeit wird eine Einführung in Laser Interferometrie gegeben und in die verschiedenen Nutzlasten der GRACE-Follow On Satelliten eingeführt. Außerdem wird der Aufbau des LRI diskutiert, um die tiefgreifenden Zusammenhänge zu verstehen, wenn es ins Detail der Untersuchungen geht. Die verschiedenen Arten von Telemetriedaten und ihre Verarbeitungsstufen werden vorgestellt, was einen Einblick in die Vielzahl der Datensätze gibt, die von den Satelliten heruntergeladen werden.

Die Untersuchungen umfassen mehrere große Themenfelder. Diese reichen von verschiedenen Modellen zur Abschätzung der absoluten Laser Frequenz, die als Umrechnungsfaktor zwischen den rohen Phasenmessungen und dem entsprechenden Abstand der Satelliten dient, und beinhalten eine umfangreiche Erforschung des Signal-zu-Rausch Verhältnisses, welches Informationen über die Qualität des gemessenen Signals bietet. Darüber hinaus werden die Eigenschaften der Laserstrahlen im Fernfeld betrachtet, wobei speziell auf die Intensität und Phasenfront eingegangen wird. Diese Untersuchungen haben zu einem Vorschlag für ein neues Scan Muster geführt, das kürzlich auf den Satelliten ausgeführt wurde. Zu guter Letzt wurde eine umfangreiche Beurteilung des LRI Spektrums durchgeführt. Dieses offenbart Zusammenhänge zwischen dem Navigationssystem der Satelliten (engl. *attitude and orbit control system, AOCS*), insbesondere der Sternenkameras zur Lagebestimmung und Aktivierungen der Schubdüsen zur Lagesteuerung, und der Distanzmessung des LRI.

Zusammenfassend handelt diese Arbeit von verschiedenen Aspekten der LRI Charakterisierung und Datenauswertung. Da die generelle Qualität und Sensitivität der Messdaten die Ansprüche und Erwartungen für die derzeitige Gravimetrie-Mission übertreffen, sind die meisten der behandelten Themen eher von akademischer Natur, z.B. um das Verständnis des LRI Teams über das Messinstrument zu vertiefen und für die Entwicklung von zukünftigen Satellitenmissionen im Themenfeld der Geodesie oder des weltraumbasierten Gravitationswellenoberservatoriums LISA.

Schlagworte: Laser Interferometrie, GRACE-Follow On, Laser Ranging Interferometer

Abstract

This thesis presents first in-depth results of the *Laser Ranging Interferometer* (LRI) onboard the *Gravity Recovery And Climate Experiment - Follow On* (GRACE-Follow On) mission. The LRI is a novel instrument, which was developed in a U.S.-German collaboration including the Albert-Einstein Institute (AEI) in Hanover. It successfully demonstrated the feasibility of ranging measurements by means of laser interferometry between two distant spacecraft and will push space-borne gravimetry missions to the next sensitivity level.

The author of this thesis contributed to this project by programming a comprehensive framework for ground-processing of LRI telemetry and analyzing various kinds of instrument data streams. Therefore, the title of this thesis covers both topics, data processing and investigations within the data.

Within this thesis, an introduction to laser interferometry is given and the various payloads of the GRACE-Follow On satellites are presented. Furthermore, the design of the LRI itself is discussed, in order to understand the profound causal relations when getting into the details of investigations. The various kinds of telemetry data and their processing levels are presented, giving an insight about the variety of data sets, that are downlinked from the satellites.

The investigations cover various major topics. These reach from different models to assess the absolute laser frequency, which sets the scale to convert the raw phase measurements into corresponding inter-satellite displacements, and comprise a detailed investigation of the carrier to noise ratio, which provides information about the signal quality. Furthermore, the laser's beam properties in the far-field are investigated by means of the intensity and the phasefront. These investigations even lead to a proposal for a new scan pattern, which has actually been performed. Last but not least, a comprehensive assessment of the LRI spectrum was performed, which reveals correlation between the satellite's attitude and orbit control system (AOCS), i.e. the star cameras for attitude determination and thruster activations for attitude control, and the ranging signal, measured by the LRI.

In summary, this thesis is concerned with several aspects of the LRI characterization and data analysis. Since the overall data quality and sensitivity of the LRI exceeds the needs and expectations for the current gravimetric mission, many of the discussed effects are rather of academic interest, e.g. to deepen the instrument understanding of the LRI team and for the development of future missions in the field of geodesy or the space-based gravitational wave detection (LISA mission).

Keywords: Laser Interferometry, GRACE Follow-On, Laser Ranging Interferometer

Table of Contents

List of Acronyms

A

ACC Accelerometer
ADC Analog-to-Digital Converter
AEI Albert Einstein Institute
AGC Automated Gain Control
AOCS Attitude and Orbit Control System
AS Amplitude Spectrum
ASD Amplitude Spectral Density

C

CHU Camera Head Unit
CNR Carrier to Noise Ratio
CoC Center of Curvature
CoM Center of Mass
CS Cycle Slip
CSR Center for Space Research at the University of Texas

D

DFT Discrete Fourier Transform
DLR Deutsche Luft und Raumfahrtgesellschaft
DOWR Dual One Way Range
DPLL Digital Phase-Locked Loop
DWS Differential Wavefront Sensing

E

EOM Electro-Optical Modulator
ESA European Space Agency

F

FFT Fast Fourier Transform
FPGA Field Programmable Gate Array
FSM Fast Steering Mirror
FSR Free Spectral Range
FWHM Full Width at Half Maximum

G

GAGB General Astigmatic Gaussian Beam
GB Gaussian Beam
GFZ Geoforschungszentrum Potsdam
GPS Global Positioning System
GRACE Gravity Recovery And Climate Experiment
GRACE-FO GRACE Follow-On
GRAIL Gravity Recovery And Interior Laboratory
GSOC German Space Operations Center

H

HK Housekeeping

I

IL In-loop
IMU Inertial Measurement Unit
IOC In-Orbit Commissioning
IPU Instrument Processing Unit

J

JHU/APL Applied Physics Laboratory of the John Hopkins University
JPL Jet Propulsion Laboratory

K

KBR K-Band Ranging

L

LEO Low-Earth Orbit
LISA Laser Interferometer Space Antenna
LO Local Oscillator
LOF LRI optical frame
LoS Line of Sight
LRI Laser Ranging Interferometer
LRP Laser Ranging Processor
LSB Least Significant Bit
LSQ Least Squares
LUT Look-Up Table

M

MATLAB MATrix LABoratory, software package by Mathworks, Inc

MWI Microwave Instrument

N

NASA National Aeronautics and Space Administration
NCO Numerically Controlled Oscillator
NEN Near Earth Network
NPRO Non-Planar Ring Oscillator

O

OBA Optical Bench Assembly
OBC Onboard Computer
OBE Optical Bench Electronics
OBS Optical Bench Subsystem
OCXO Oven-Controlled Quartz Oscillator
OOL Out-of-loop

P

PA Phase Accumulator
PD Photodiode
PDH Pound-Drever-Hall
PIR Phase Increment Register
PJ Phase Jump
PL Phaselocker
PM Phasemeter
PSD Power Spectral Density
PSLL Peak Sidelobe Level
PSS Position Sensing System
PUS Packet Utilization Standard
PZT Piezoelectric Transducer

Q

QPD Quadrant Photodiode
QPR Quadrant Photoreceiver

R

RDC Raw Data Center
rms Root mean square
RX Received

S

S/C Spacecraft
SAGB Simple Astigmatic Gaussian Beam
SCA Star Camera Assembly
SDS Science Data System
SGB Stigmatic Gaussian Beam
SLDR Sidelobe Drop Rate
SRF Science Reference Frame
SST Satellite-Satellite Tracking

T

TMA Triple Mirror Assembly
TRP Thermal Reference Point
TTL Tilt-To-Length coupling
TWR Two-Way Range
TX Transmitted
TXF TX Beam Frame

U

ULE Ultra-Low Expansion
USO Ultra-Stable Oscillator

Y

YAML YAML Ain't Markup Language

List of Figures

List of Tables

1. Introduction

The twin-satellite mission Gravity Recovery And Climate Experiment (GRACE) (2002-2017), a joint US-German project, refined the understanding of Earth's gravity field and it's variations (Tapley et al., 2003; Tapley et al., 2004), e.g. due to the hydrological cycle (Schmidt et al., 2008; Wahr et al., 2004) or ice mass variations (Chen et al., 2006) among many others. The gravity field is derived from inter-satellite distance measurements (Wahr et al., 1998; Tapley et al., 2004). These ranging measurements have been performed by a dual channel Microwave Instrument (MWI) in GRACE. Due to the broad application of the valuable data stream, a continuation mission, called GRACE Follow-On (GRACE-FO), was planned since 2009 and launched in mid 2018 (GFZ-Potsdam, 2018). While a similar MWI is also used in GRACE-FO, there is an additional instrument, the Laser Ranging Interferometer (LRI). This instrument is the very first laser interferometer to measure an inter-satellite distance ever flown (Abich et al., 2019).

Since the commissioning of the LRI in June 2018, it measures the inter-spacecraft (S/C) range with a previously unknown precision. The ranging data, measured by the LRI is in a very good condition. The noise density in absence of the gravity signal is well below the requirement of $80\,\mathrm{nm}/\sqrt{\mathrm{Hz}}$ (Abich et al., 2019), compared to the MWI noise, which is in the order of 1 to $2\,\mu\mathrm{m}/\sqrt{\mathrm{Hz}}$ (Müller, 2017, sec. 1.4.2). Therefore, the LRI is expected to improve the accuracy of the gravity field by about 13-23% at a spatial resolution of 240 km (Flechtner et al., 2015).

Moreover, the LRI acts as a technology demonstrator, which successfully proved the feasibility of inter-satellite laser interferometers for future geodesy missions. In a next generation gravity mission, a laser interferometer might replace the MWI as the primary science instrument (Flechtner et al., 2015). Furthermore, the development and successful commissioning of the LRI is a milestone in the development of the Laser Interferometer Space Antenna (LISA), which is a space-based gravitational wave detector, currently being developed (Danzmann, 2003; Shaddock, 2008).

In order to assess the instrument behavior and to learn for the development of similar instruments for future gravity missions or for LISA, the LRI has to be characterized in all it's details. For example, the phase measurements of the LRI, which contain the desired ranging information, show several unforeseen jumps. However, these jumps can be modeled and removed with ease and will not affect the gravity field recovery. Other effects like the so called scalloping loss, which will be covered within this thesis could be explained to some extent, but some open questions remain.

The author of this thesis joined the LRI team at the Albert Einstein Institute (AEI) in Hanover one month before the launch of the GRACE-FO satellites. From this date onward, he supported the LRI operations and contributed to the project with his work on data analysis. His thesis time approximately coincides with the first year of LRI operations. Most of the time, the author developed a comprehensive software framework to preprocess, monitor, analyze and visualize the LRI and GRACE-FO telemetry. This framework is extensively used by the LRI team in Hanover and basically established an alternative LRI data processing pipeline next to the nominal Science Data System (SDS) processing. In this thesis, data analysis results obtained with the framework are presented. These comprise investigations regarding the instrument noise level, assessments of the accuracy of pre-flight models, e.g. concerning the laser's frequency as well as the determination of the laser beam's properties in the far-field and the quality of the phase measurements by means of the Carrier to Noise Ratio (CNR). Even if this thesis covers various topics, most of them are very advanced and relate to details. These are expected to have little significance for the GRACE-FO mission, but are of interest for the LRI team

to deepen their understand of the instrument and for future laser interferometers.

This thesis gives an overview about the architecture of the LRI and provides a comprehensive insight into the current status of the LRI data investigation. It presents assessments about the condition and performance of the instrument and it's data quality. Furthermore, new models and algorithms regarding the data analysis are developed and pre-flight models and measurements are tested and verified. In chapter 2, an introduction to the basic principles of laser interferometry are presented. Chapter 3 discusses the payloads and instruments onboard the GRACE-FO satellites, while the design and architecture of the LRI and it's subsystems are covered in chapter 4. The different stages of data processing are explained in chapter 5, before the widespread investigations on the LRI data streams and it's performance are explained in chapter 6.

2. Basics of Laser Interferometry

Interference, the coherent superposition of waves, can be observed for many types of waves, like acoustic ones, water waves, matter waves and also electromagnetic waves like light. When two waves interfere, there can be destructive interference, meaning the local annihilation of light, or the counterpart, constructive interference.

Interferometry with light waves was shown for the first time by Michelson and Morley, who measured the relative length changes (or in fact, almost no relative length changes) over a distance of eleven meters with a stunning precision in 1887 (Michelson et al., 1887). The principle of interferometry is to superimpose two light beams on a photo plate (or nowadays on a photodiode) and to retrieve the phase difference of the electric fields of the two beams. This difference gives information about the different pathlengths of the two beam paths. It should be noticed, that interferometers in general measure distance changes, not absolute distances, due to an initial phase ambiguity. This is the reason for the so-called "biased" range measurements in GRACE Follow-On (GRACE-FO) Laser Ranging Interferometer (LRI) and K-Band Ranging (KBR).

The lasers used for the GRACE-FO LRI and also for the Laser Interferometer Space Antenna (LISA) have a near infrared wavelength of $\lambda = 1064\,\text{nm}$. For such a displacement measurement, the longitudinal pathlength changes, $\Delta\rho$, can be written as

$$\Delta\rho = \frac{c}{2\pi\nu}\cdot\Delta\phi = \frac{\lambda}{2\pi}\cdot\Delta\phi\,, \tag{2.1}$$

where the optical phase changes, $\Delta\phi$, is measured by means of interferometry. Here, ν is the frequency of the electromagnetic wave, λ the corresponding wavelength and c is the speed of light in vacuum.

In the following sections, the formalism of Gaussian beams will be introduced (section 2.1), how phase retrieval of heterodyne interferometers is realized and thus, the recovery of the longitudinal pathlength signal (section 2.2). Furthermore, some techniques that are used within the LRI such as Differential Wavefront Sensing (DWS) (section 2.3), laser frequency stabilization (section 2.4), the phase locking mechanism (section 2.5) and spectral analysis techniques (section 2.6) are explained.

2.1. Gaussian Beam Propagation

In order to understand the phase measurement within an interferometer, it is necessary to understand the properties of the light, that propagates through it. For the purpose of this thesis, it is sufficient to model the laser beams as Gaussian Beams (GBs) in the fundamental TEM_{00} mode, where TEM stands for transversal electromagnetic. As the light between the two spacecraft (S/C) propagates over several hundreds of kilometers, the beam evolves in it's width, radius of curvature and more. The derivation of Gaussian beams as solutions of the Helmholtz equation can be found in many textbooks (Saleh et al., 2007; Reider, 2016) and theses (e.g. Kochkina (2013)).

The complex-valued electric field of a fundamental GB can be written as

$$\vec{E}(\vec{r},t) = E(\vec{r})\cdot\vec{P}(\vec{r},t)\cdot\exp(\mathrm{i}\omega t)\,, \tag{2.2}$$

whereas the actual electric field is given by the real part of this complex expression. Here, $\omega = 2\pi f$ is the angular beam frequency and $E(\vec{r})$ the complex-valued amplitude of the electric field at a given

point in space. The polarization $\vec{P}(\vec{r},t)$ is of minor importance for this thesis and will be neglected as of now.

The nomenclature within the following sections is such that w.l.o.g. the beam propagation axis is parallel to the x-direction.

2.1.1. Stigmatic Gaussian Beam

The simplest realization of a GB is a so called Stigmatic Gaussian Beam (SGB), which features radial symmetry. With the paraxial approximation, the complex field amplitude, $E(\vec{r})$, can be written as a function of only the coordinate in direction of the propagation, x, and the radial offset, $r = \sqrt{y^2+z^2}$, of this axis. One can now express the electric field amplitude as

$$E(x,r) = E_0(x) \cdot \exp\left[-\mathrm{i}(kx - \eta(x)) - \mathrm{i}k\frac{r^2}{2R(x)} - \frac{r^2}{w^2(x)}\right]. \tag{2.3}$$

The third term in the exponential function in eq. (2.3) can be interpreted as a phase term, which approximately represents a sphere with curvature $1/R(x)$, while the fourth term is the Gaussian amplitude profile of width w (Reider, 2016). The geometrical meanings of the quantities in eq. (2.3) are shown in fig. 2.1 and explained now.

First of all, the wavenumber is defined as $k = 2\pi/\lambda$ for the wavelength λ. Here,

$$x_R = \frac{\pi w_0^2}{\lambda} \tag{2.4}$$

denotes the Rayleigh range. It gives the offset in direction of propagation, at which the beams phasefront shows the maximum curvature. The curvature of the phasefront is zero at the waist position, x_0, i.e. it is a planar phasefront. Most of the parameters of a GB can be derived using the Rayleigh range x_R.

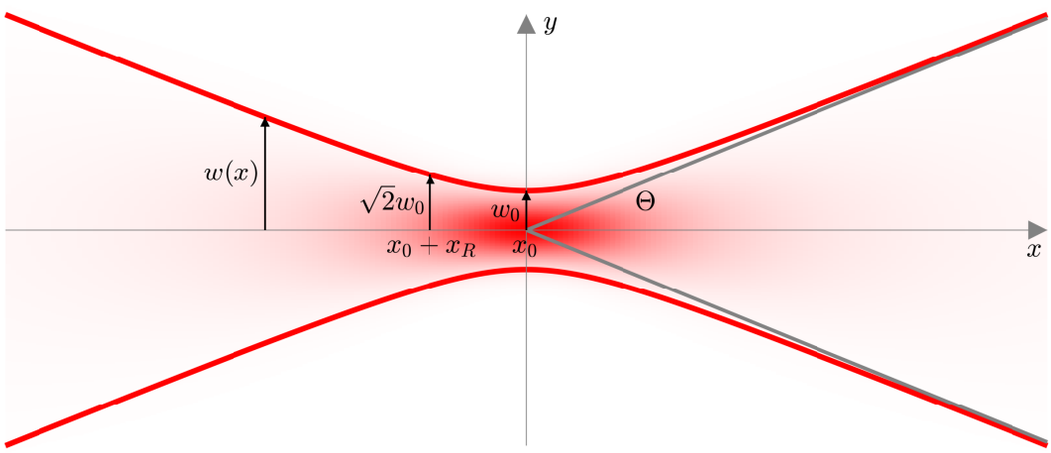

Figure 2.1.: Beam parameters for a stigmatic Gaussian beam. The red background coloring indicates the intensity of the beam at that position. Due to radial symmetry, only one of the lateral directions y and z is shown. x_0: waist position, w.l.o.g $x_0 = 0$; $w_0 = w(x_0)$: beam radius at waist; x_R: Rayleigh range; $w(x)$: waist size as function of the propagation; Θ: Half-angle, that defines the asymptotic beam divergence in far-field (gray lines).

The so called Gouy phase,

$$\eta(x) = \arctan\left(\frac{x - x_0}{x_R}\right), \tag{2.5}$$

defines a phase change of π, whenever the beam propagates through the waist, which is located at $x = x_0$. The waist denotes the focus point of the beam. In the far-field, the Gouy phase converges to $\pm\pi/2$.

The radius, in which $(1 - 1/e^2) \approx 86\,\%$ of the optical beam power is transported, is defined as

$$w(x) = w_0\sqrt{1 + \left(\frac{x - x_0}{x_R}\right)}, \tag{2.6}$$

which is minimal at the waist position, $w_0 = w(x_0)$. At x_R, the beam radius is $w(x_R) = \sqrt{2}w_0$. The waist radius w_0 also gives the divergence angle, that defines the asymptotic beam divergence in far-field,

$$\Theta = \frac{\lambda}{w_0\pi}. \tag{2.7}$$

Given the beam radius at the waist, $w_0 = 2.5\,\mathrm{mm}$, and the wavelength, $\lambda = 1064\,\mathrm{nm}$, for the GRACE-FO LRI, one derives a divergence angle of approximately $135\,\mu\mathrm{rad}$, which, in a distance of $220\,\mathrm{km}$, expands to a circle of $30\,\mathrm{m}$ radius.

In the far-field, the phasefront of a laser beam in TEM_{00} mode approaches a spherical shape. The radius of curvature of these equiphase spheres is given by

$$R(x) = (x - x_0)\cdot\left[1 + \left(\frac{x_R}{x - x_0}\right)^2\right] \tag{2.8}$$

$$= x - x_0 + \frac{x_R^2}{x - x_0}. \tag{2.9}$$

The optical intensity I_{op} can be written as

$$I_{\mathrm{op}}(x, r) = |E(x, r)|^2 = E_0^2(x)\exp\left[-\frac{2r^2}{w^2(x)}\right], \tag{2.10}$$

yielding the optical power P as integral over the transverse plane (Kochkina, 2013), which may be the surface of a large Photodiode (PD),

$$P = \int_0^\infty 2\pi r \cdot I_{\mathrm{op}}(x, r)\,\mathrm{d}r \tag{2.11}$$

$$= \frac{\pi}{2}E_0^2(x)\,w^2(x). \tag{2.12}$$

This allows the computation of the normalization constant

$$E_0(x) = \frac{1}{w(x)}\sqrt{\frac{2P}{\pi}}, \tag{2.13}$$

if the optical power P is given. With this choice of E_0, the unit of the intensity $I_{\mathrm{op}}(x, r)$ is $\mathrm{W/m^2}$.

2.1.2. Astigmatic Gaussian Beam

A generalization of the stigmatic GB is the Simple Astigmatic Gaussian Beam (SAGB), where the waist position differs for the two transverse directions. The beam spot is no longer a circle but an ellipse. These SAGB will be used in later sections as model for laser beams. The complex amplitude of such a SAGB is not a function of $r = \sqrt{y^2 + z^2}$ as before, but instead of the two coordinates y and z. For the purpose of a short notation, $\mathfrak{r} = (y, z)^\intercal$ is introduced. It should be noted, that these two lateral axes are not fixed to an outer reference frame but are the principal semi-axes of the beam spot ellipse. Equation (2.3) then reads

$$E(x, \mathfrak{r}) = E_0(x) \cdot \exp\left[-\mathrm{i}(k(x - x_0) - \eta(x)) - \sum_{i=1}^{2}\left(\mathrm{i}k\frac{\mathfrak{r}_i^2}{2R_i(x)} + \frac{\mathfrak{r}_i^2}{w_i^2(x)}\right)\right] . \tag{2.14}$$

The other quantities like waist positions $x_{0,i}$, beam radii $w_i(x)$, radii of curvature $R_i(x)$ and Rayleigh range $x_{R,i}$ are defined according to the above expressions but now result in two independent sets of parameters for the two orthogonal directions $\mathfrak{r}_i$, $i = \{1, 2\}$. The Gouy phase for a SAGB needs to be redefined as the average over the Gouy phase for the SGB in the two independent directions,

$$\eta(x) = \frac{1}{2}\sum_{i=1}^{2} \arctan\left(\frac{x - x_{0,i}}{x_{R,i}}\right) . \tag{2.15}$$

The intensity distribution of a SAGB reads

$$I(x, \mathfrak{r}) = E_0^2(x) \cdot \exp\left[-\sum_{i=1}^{2}\left(\frac{\mathfrak{r}_i^2}{w_i^2(x)}\right)\right] . \tag{2.16}$$

One further step of generalization would yield General Astigmatic Gaussian Beam (GAGB), where the the elliptical beam spot rotates while the beam propagates (Kochkina, 2013). It will not be discussed further, because simple astigmatism is sufficient to describe the beams for the purpose of this thesis.

2.1.3. Phase of a Gaussian Beam

From eq. (2.14), one can write the phase, ϕ, of a SAGB as the imaginary part of the argument of the exponential function:

$$\phi(x, \mathfrak{r}) = -k(x - x_0) + \eta(x) - \sum_{i=1}^{2} \frac{k\mathfrak{r}_i^2}{2R_i(x)} . \tag{2.17}$$

The phase of an electromagnetic wave is not measurable directly, only the electric field, i.e. the real part of eq. (2.14), can be measured where the phase is hidden in the argument of the cosine, that arises from the real part of the complex field amplitude (cf. eq. (2.13)) using Euler's formula for the exponential function. As the cosine is even and periodic, it leads to a sign ambiguity, which is physically irrelevant, and a phase wrapping into the interval $[0, 2\pi)$. For interferometric measurements, the absolute range needs to be determined with other methods, while the phase wrapping during continuous measurements can be obtained by an unwrapping algorithm that detects and corrects the unphysical jumps that are occurring.

Within this thesis, it is only dealt with free beam propagation between two S/C and thus, no introduction to beam transformations by means of reflection or refraction is given.

2.2. Heterodyne Phase Readout

The heterodyne photocurrent, $I(t)$, is the signal that is generated with the PD by sensing two interfering beams. Heterodyne means, that the two superimposing beams do not have the same frequency, resulting in a time-variable interference pattern even without length variations. The photocurrent, $I(t)$, can be related to the corresponding optical power, $P(t)$, on the PD area by scaling with the responsivity, R_{PD}, of the PD,

$$P(t) = I(t)/R_{\mathrm{PD}} \,. \tag{2.18}$$

The responsivity, R_{PD}, has numerical values around 0.7 A/W for commonly used InGaAs diodes at a wavelength of 1064 nm.

Many interferometers nowadays do not utilize a single PD but a Quadrant Photodiode (QPD), which has four independent segments. Within this thesis, these quadrants are referred as A, B, C and D where A and B are the upper two segments and A and C are on the left side. The heterodyne photocurrent and power are defined for each single channel as well as the sum over all channels, which is comparable to a single segment PD. For simplicity, the following formulas are given for a single channel PD but can easily be extended to multiple channels by applying an index that specifies the segment.

The optical power, $P(t)$, has a sinusoidal shape with a non-zero mean. This can be split into a constant (DC) and a time variable (AC) part, of which only the latter contains the desired phase, or ranging, information. In Mahrdt, 2014, sec. 2.1, the full derivation of the optical power on a PD is given. For clarity, the derivation is not repeated in this thesis, but will be recovered shortly. Mahrdt defines

$$P(t) = \bar{P} + \tilde{P}(t) \tag{2.19}$$

$$= \underbrace{P_{\mathrm{LO}} + P_{\mathrm{RX}}}_{\mathrm{DC}} + \underbrace{2\sqrt{\eta_{\mathrm{het}} P_{\mathrm{LO}} P_{\mathrm{RX}}}\cos\left(\phi(t)\right)}_{\mathrm{AC}} \tag{2.20}$$

with $\bar{P} = P_{\mathrm{LO}} + P_{\mathrm{RX}}$ being the DC part and $\tilde{P}$ the AC part of the total beam power at the PD. Here, P_{LO} denotes the fraction of the Local Oscillator (LO) power that is routed to the PD and P_{RX} is the received (RX) beam power. The heterodyne efficiency η_{het} and the phase ϕ, where the latter is the desired observable, are defined via the normalized overlap integral (Mahrdt, 2014). The heterodyne efficiency is the coherent detection signal-to-noise ratio giving information about the interference quality. The instantaneous phase

$$\phi(t) = \phi_{\mathrm{LO}}(t) - \phi_{\mathrm{RX}}(t) \tag{2.21}$$

is given as the phase difference of the LO phase, ϕ_{LO}, and the RX phase, ϕ_{RX}. For further interpretation, it can be rewritten as

$$\phi(t) = \left\langle \frac{\mathrm{d}}{\mathrm{d}t}\phi(t) \right\rangle_{\tau} \cdot t + \Phi(t) = 2\pi f_{\mathrm{b}}(t) \cdot t + \Phi(t) \,, \tag{2.22}$$

where $\langle\cdot\rangle_{\tau}$ denotes an averaging over a specific time interval τ. Here, τ can be chosen in two ways, that are both very useful in the scope of this thesis. First, for an interferometric signal with a fixed beatnote frequency f_{b}, one could think of a large averaging interval compared to the orbital period of a satellite, e.g. 90 min for GRACE-FO, $\tau \ggg T_{\mathrm{Orbit}}$. The first summand in eq. (2.22) then is a phase ramp, whose slope corresponds to the constant beatnote frequency f_{b}. The term $\Phi(t)$ then refers to deviations from the constant phase ramp, e.g. caused by phase or frequency noise.

For the second interpretation, a smaller averaging interval of e.g. $\tau \approx 1\,\mathrm{s}$ is used, which effectively splits the phase in two frequency regimes. One of which is regarded as the slowly varying beatnote frequency, $f_{\mathrm{b}}(t)$, while the other term represents higher frequency variations. This is useful whenever

the heterodyne frequency is varying largely and periodic, but the deviations from the periodicity are of greater interest.

The longitudinal pathlength signal, the desired quantity in space-borne missions utilizing laser interferometry like GRACE-FO and LISA, is obtained by interpreting changes of the instantaneous phase, $\Delta\phi(t)$, as differential length changes, $\Delta\rho$, in the beam paths. The range variation, $\Delta\rho$, is computed as the mean phase change over all four QPD segments and the scale factor from phase to range differences is given by the wavelength λ. For measurements utilizing a QPD, eq. (2.1) now reads

$$\Delta\rho = \frac{\lambda}{2\pi}\frac{\Delta\phi_A + \Delta\phi_B + \Delta\phi_C + \Delta\phi_D}{4} \,. \tag{2.23}$$

To obtain the phase from the measured photocurrent $I(t)$ on the PD, the widest spread technique used is IQ-Demodulation, see section 2.5 below.

2.3. Differential Wavefront Sensing (DWS)

Differential Wavefront Sensing (DWS) is a technique introduced by Morrison et al. (1994) to measure angular tilts between two beams that interfere on a multi section photodiode. If the two incoming beams, that superimpose on the QPD, are tilted against each other, there are differences in the phase measurements for the individual QPD segments. One can derive the so called DWS signals for horizontal and vertical angular offsets of the beams with respect to each other, cf. eqs. (2.24) and (2.25).

$$\mathrm{DWS_v} = \frac{\phi_A + \phi_B - \phi_C - \phi_D}{2} \tag{2.24}$$

$$\mathrm{DWS_h} = \frac{\phi_A - \phi_B + \phi_C - \phi_D}{2} \tag{2.25}$$

These quantities are in units of radian referring to phase measurements, but can approximately be converted to angles α and β with a linear relation (Sheard et al., 2012):

$$\begin{pmatrix}\alpha\\ \beta\end{pmatrix} \approx \sqrt{2}\frac{16r}{3\lambda}\begin{pmatrix}\mathrm{DWS_v}\\ \mathrm{DWS_h}\end{pmatrix} \,. \tag{2.26}$$

Here, r denotes the beam radius, λ the wavelength. For exemplary parameters of $r = 4\,\mathrm{mm}$ and $\lambda = 1064\,\mathrm{nm}$, the coupling factor between wavefront tilts, (α, β), and DWS signals, ($\mathrm{DWS_v}$, $\mathrm{DWS_h}$), is in the order of 30 000 rad/rad. If the DWS signals are all zero, the two beams interfering on the photodiode are parallel. Noise sources like laser frequency noise (see section 4.2.1) are common on all QPD segments and therefore cancel out (Sheard et al., 2012). Further details on the exact conversion from phase radian to angles is given in section 4.4.

2.4. Pound-Drever-Hall Technique (PDH)

Arising from eq. (2.23), all effects that lead to phase changes, including laser frequency noise, can not be distinguished from physical length changes in the interferometer arms by only observing the phase. If the frequency and thus the wavelength of the oscillation is not stabilized, the ranging signal is not precisely determined. Stabilization is achieved, using the Pound-Drever-Hall (PDH) technique. It is wide spread and often used to effectively lock a lasers frequency to a cavity resonance. It is now

described in general, while the details of the cavity and laser that are used within the LRI are discussed in section 4.2.

A conceptual scheme of the PDH technique is shown in fig. 2.2. The stabilization is done by adjusting the frequency of a laser f_0 such that it matches one of the resonances of an optical reference cavity of length L. This might be a Fabry-Pérot cavity. For the laser with frequency f_0 being in resonance, it must be fulfilled, that

$$f_0 = n \cdot f_{\text{Cav}} = n \cdot \frac{c}{2L}\,, \tag{2.27}$$

where the cavity frequency f_{Cav} is the lowest frequency, that can form a standing wave within the cavity. It also denotes the Free Spectral Range (FSR), which is the frequency difference between two subsequent resonant frequencies. Typically, these cavities are built of Ultra-Low Expansion (ULE) materials and are actively temperature stabilized to keep the geometric properties stable.

If the laser is in resonance, no light is reflected by the cavity, but forms a standing wave within the cavity. If the laser is out of resonance, a part of the incoming light, or all of it, is reflected and can be detected with the PD on the reflection port, marked with Refl.-PD in fig. 2.2.

For a closed-loop setup, monochromatic light is not sufficient yet, because an active stabilization is not feasible if the reflected power vanishes in resonance. Thus, the closed-loop would loose lock. Therefore, an Electro-Optical Modulator (EOM) is used to imprint sidebands on the laser beam by phase modulation. For small modulation depths, the beam has in principal two sidebands, being at $f_0 \pm f_{\text{mod}}$. If the carrier frequency, f_0, is in resonance with the cavity, a part of the electromagnetic wave, oscillating at $f_0 \pm f_{\text{mod}}$ still is not and therefore is reflected and can be detected as the reflected

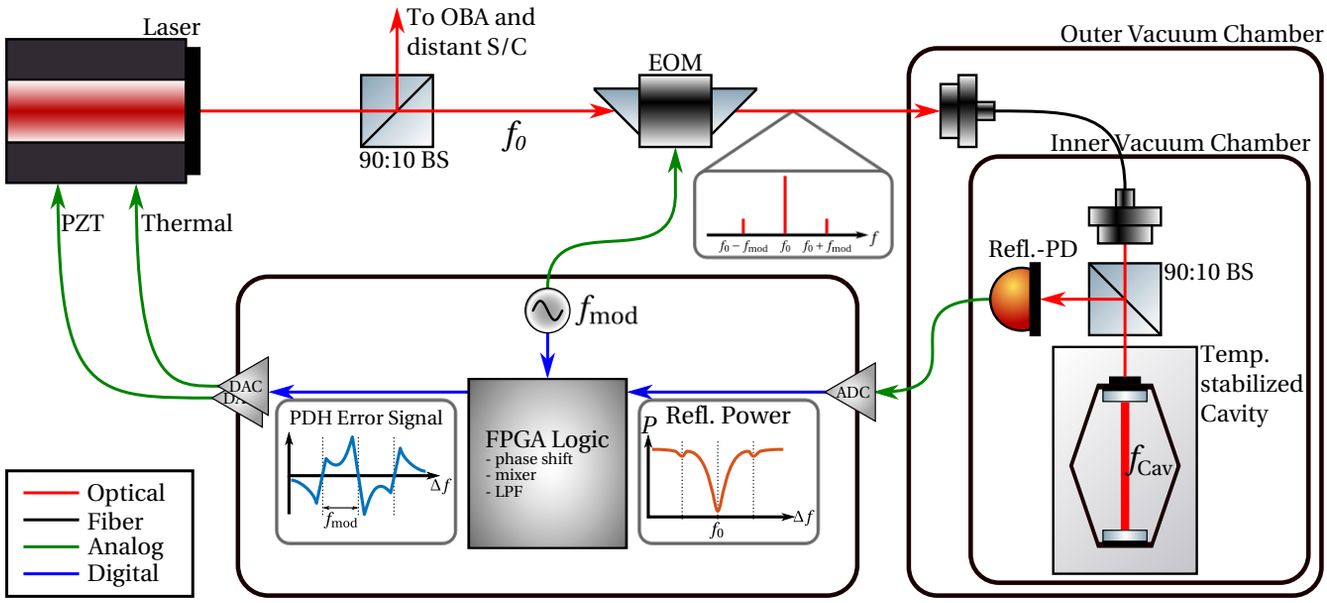

Figure 2.2.: Scheme of the PDH technique. The laser beam is phase modulated via an EOM with a modulation frequency f_{mod}, before it is sent into the cavity, which itself is temperature stabilized to keep the geometric properties fixed. A fraction of the reflected light from the cavity is sensed by a PD. Within the Field Programmable Gate Array (FPGA) circuit, the signal gets demodulated, again using f_{mod}, and low-pass filtered to obtain the phase, which is used as an error signal. The slope at the resonance frequency is almost linearly dependent on the frequency difference between the laser and the cavity resonance. This error signal is then used as actuator signal for the thermal and PZT actuators. Image created using the Component Library.

power. The signal obtained is shown in fig. 2.2 as the orange trace. It shows a sharp drop at every resonance of the cavity.

The beam, showing oscillations at the carrier frequency as well as the sidebands, is sent through the cavity. The cavity is obviously not in resonance for all three different frequencies simultaneously. On the PD, the three parts of the beam interfere, showing a beat pattern at the modulation frequency, f_{mod}. The reflection signal is mixed with the modulation frequency, e.g. within a FPGA circuit. A phase shifter is used to match the phases of the reflection signal and the modulation signal, that might be out of phase due to the different signal paths. The outcome of such a mixing for two arbitrary frequencies ω and ω' can be written as

$$\sin(\omega t)\sin(\omega' t) = \frac{1}{2}\left[\cos\big((\omega-\omega')t\big) - \cos\big((\omega+\omega')t\big)\right] . \tag{2.28}$$

Note, that if $\omega = \omega' = f_{\mathrm{mod}}$, the first term on the right hand side is constant and can easily be retrieved using a low-pass filter. This DC amplitude gives the error signal, shown in fig. 2.2 as the blue trace. Close to the resonance, the error signal is linear dependent on the frequency deviation (Black, 2001), which makes it perfectly suitable for control loops, which feeds back the error signal to the laser using a thermal actuator or a Piezoelectric Transducer (PZT). These modify the laser frequency.

If the resonance of the cavity is initially unknown, one might apply a ramp to the thermal actuator to sweep over at least one free spectral range of the cavity and use the temperature of one of the resonance frequencies as a nominal setpoint to the thermal actuator. Afterwards, the PDH scheme can lock to the resonance and hold the frequency.

2.5. Digital Phase-Locked Loop (DPLL)

A Digital Phase-Locked Loop (DPLL) is a commonly used technique to retrieve the phase of an oscillating electronic signal. It makes use of the so-called IQ-Demodulation. A conceptual scheme of a DPLL is shown in fig. 2.3. The AC part of the interferometric signal, which can, according to eq. (2.20), be written as

$$y = a_0 \cos(\phi) , \tag{2.29}$$

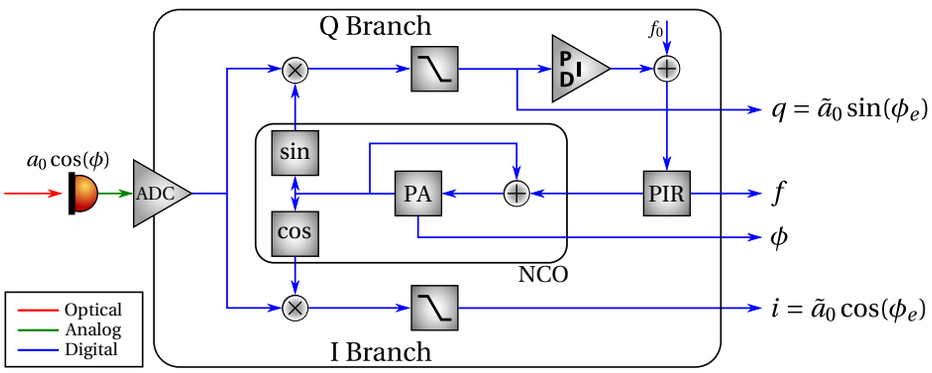

Figure 2.3.: Schematics of a single-channel Digital Phase-Locked Loop (DPLL). The signal is demodulated using the reference frequency, which is stored in the Phase Increment Register (PIR) of the Numerically Controlled Oscillator (NCO). To match this reference, the quadrature q value, i.e. ϕ_e, is used as the error signal for the feedback control loop. The actual phase value is stored in the Phase Accumulator (PA), which contains the integrated PIR values. The output is i, q, f and ϕ. Image created using the Component Library.

is sensed by the PD and digitized by an Analog-to-Digital Converter (ADC). This signal is then demodulated into an in-phase (i) and a quadrature (q) component, by multiplying with a sine and cosine with a reference frequency. In general, an incoming signal oscillating with the phase ϕ mixed with a sine or cosine with the phase ϕ' read

$$\text{I Branch}: \qquad \cos(\phi)\cos(\phi') = \frac{1}{2}\left[\cos(\phi+\phi') + \cos(\phi-\phi')\right] \tag{2.30}$$

$$\text{Q Branch}: \qquad \cos(\phi)\sin(\phi') = \frac{1}{2}\left[\sin(\phi+\phi') + \sin(\phi-\phi')\right] . \tag{2.31}$$

Both branches are low-pass filtered, to remove the high frequencies, i.e. the first term on the right hand side of eqs. (2.30) and (2.31), arising from the mixing. The reference frequency for demodulation is matched using the q-value, $q = \tilde{a}_0 \sin(\phi_e)$, which is used as the error signal of the feedback control loop. In the small angle approximation, $\sin(\phi_e) \approx \phi_e$, the q-value is linearly dependent on the phase error $\phi_e = \phi - \phi'$, which represents the phase mismatch between the reference frequency and the measured signal, y, coming from the ADC. On the other hand, the i-value is

$$i = \tilde{a}_0 \cos(\phi_e) \approx \tilde{a}_0 , \tag{2.32}$$

if the loop is working properly and $\phi_e \approx 0$. Thus, the i-value is a digital representative for the amplitude of the incoming sinusoidal AC signal. The tilde is used to indicate a root mean square (rms) estimate, due to the low-pass filtering.

If the DPLL is running properly, the error signal ϕ_e is zeroed continuously and therefore, the i-value is a direct, digital measure for the amplitude of the heterodyne amplitude. In a more general case, one can use the norm

$$\tilde{a}_0 = \sqrt{i^2 + q^2} . \tag{2.33}$$

Due to the increasing phase values, the Phase Accumulator (PA) will overflow at some point, since it has a finite bit depth, e.g. 64 bit in the LRI. Therefore, a phase wrapping correction is applied. This correction intentionally introduces phase-reducing steps with a fixed size, e.g. 2^{63} counts, before the PA would overflow. During down-sampling in the Laser Ranging Processor (LRP) afterwards, the filter response of this well-known step is corrected (Müller, 2017).

2.6. Discrete Fourier Transform

Frequency estimation for measured signals is a topic of high importance for a wide range of applications dealing with electronic setups and signal processing. Thus, the basics of the Discrete Fourier Transform (DFT) are introduced within this section. It will match the implementations used by MATLAB, the author's programming language of choice. Like most of the modern software for signal processing, it relies on the well-established and mature `fftw` library (Mathworks, 2018, fft Documentation).

An important part of computing spectra is the choice of window functions. This is necessary, because the DFT algorithm implies a periodic signal, which is obviously not given in general. If a step between the last and first sample of a given signal is present, it spreads power over all the spectrum, known as spectral leakage (Beucher, 2019, chap. 4.5). It can be avoided by ensuring an integer number of periods falling into the sampling interval, but this is only feasible for one fixed frequency, that needs to be known prior to the actual DFT computation (Breitenbach, 1999). By using an appropriate window function, i.e. by softly suppressing the edges of the signal in time domain, this leakage effect

can be reduced. Different window functions have differing outcomes regarding the decreasing rate of spectral leakage into adjacent frequency bins, the amplitude accuracy and the width of the peak in frequency domain (Heinzel et al., 2002).

2.6.1. Window Functions

Window functions can be characterized well by using a small set of characteristic parameters. These include the suppression level of the highest adjacent peak, called Peak Sidelobe Level (PSLL), the Sidelobe Drop Rate (SLDR), which is the rate at which leakage into other bins decreases, given by the exponent n of f^{-n}, and the maximum amplitude error as the deviation from 0 dB as the frequency sweeps through one bin. This quantity is also called scalloping loss and will be handled for LRI data in section 6.4. The window functions, which are used the most within this thesis, are briefly introduced by means of the set of characterizing parameters (see table 2.1). The four windows are also shown in fig. 2.4. In the upper left panel, the windows are shown in time domain. Especially notable is the rectangular window, which does not suppress the edges. The lower left image shows the windows in frequency domain. Visible are the width of the main lobe, the PSLL (denoted by the colored, dashed lines) as well as the SLDR, which is linear for all windows but Nuttal4a. In the lower right panel, again the frequency domain is shown but only the center region. From this plot, the scalloping loss is visible.

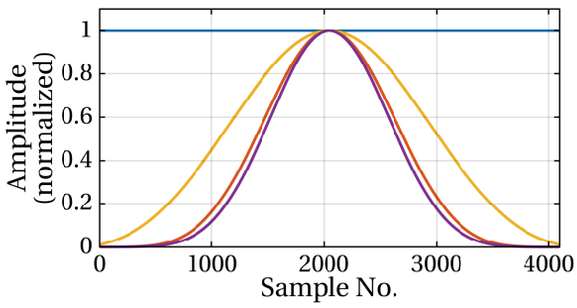

(a) Window functions in time domain.

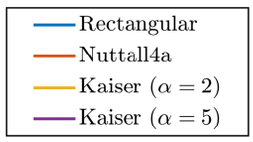

(b) Legend.

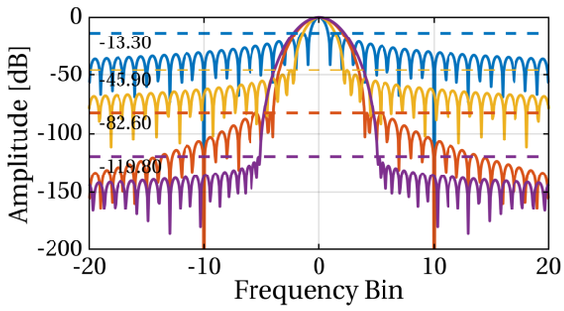

(c) Window functions in frequency domain. Here, the differences in the Peak Sidelobe Level (PSLL) and Sidelobe Drop Rate (SLDR), especially for the Nuttall4a window, are visible. For these windows, it is true that the lower the PSLL, the wider is the main lobe.

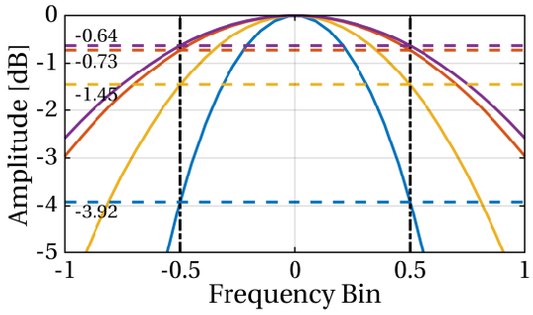

(d) Window functions in frequency domain, cropped to the center bin. Here, the scalloping loss is shown for each of the windows, which is the amplitude suppression at ±0.5 bins.

Figure 2.4.: Properties of different window functions for spectral estimation and filtering in both, time and frequency domain. All windows are created for 4096 samples in time domain.

Rectangular

If no explicit window function is applied, this is called a rectangular window. It does not apply any specific suppression, just as if an interval from a longer time series was cutted out. It does not aim to correct any disadvantages caused by the periodic continuation of the DFT. Fourier transforms using this window have shorter computation times, compared to others. The scalloping loss reaches up to $-3.9224\,\mathrm{dB}$ and a SLDR of $n = 1$ is present.

Nuttall4a

This window is suited for data with a high dynamic range, where some Fourier frequencies exhibit much larger amplitudes than others, i.e. several orders of magnitude. It's SLDR has a high value of $n = 5$, which is easily visible in the lower left panel of fig. 2.4, though it is the only window shown, that has a SLDR other than $n = 1$. The first sidelobe has an amplitude of $-82.6\,\mathrm{dB}$. The scalloping loss is relatively low at $-0.7321\,\mathrm{dB}$, giving a good amplitude accuracy. Thus, this window is a good choice to compute spectra of ranging signals from LRI data, where variations of several hundred meters for orbital frequencies as well as some picometers at high frequencies can occur.

Kaiser

The Kaiser window has the advantage of an additional parameter α, that can be used to tune the PSLL. By increasing α, the width of the main peak increases and therefore the scalloping loss decreases. Kaiser windows are suitable for applications comparable to those, Nuttall4a is used for, but can be optimized by tuning the α-parameter. Two different realizations, using $\alpha = 2$ and $\alpha = 5$ are shown in fig. 2.4 and table 2.1.

2.6.2. Scalloping Loss for Rectangular Window

Scalloping loss is a feature of every Fast Fourier Transform (FFT) computation and describes the effect, that the peak height of a sinusoidal oscillation, computed from the complex FFT outcomes, is dependent on the frequency position within the discrete frequency bins. Only if the measured frequency is located perfectly at the center of a bin, the amplitude is estimated correctly. A deviation from the frequency bin center leads to a decrease of the amplitude. This effect is the same for every frequency bin.

Within the LRI, an FFT of the interferometric AC signal is computed every $N = 4096$ samples at $f_{\mathrm{USO}} \approx 39\,\mathrm{MHz}$, which yields a bin width of

$$f_{\mathrm{bin}} = \frac{f_{\mathrm{USO}}}{N} \approx 9.5\,\mathrm{kHz}\,. \tag{2.34}$$

		Rectangular	**Nuttall4a**	**Kaiser** ($\alpha = 2$)	**Kaiser** ($\alpha = 5$)
Scalloping loss	[dB]	-3.9224	-0.7321	-1.4527	-0.6403
PSLL	[dB]	-13.3	-82.6	-45.9	-119.8
SLDR n in f^{-n}		1	5	1	1

Table 2.1.: Characterizing parameters of four exemplary window functions, Rectangular, Nuttall4a, Kaiser2 and Kaiser5. PSLL: peak sidelobe level, SLDR: sidelobe drop rate.

Hence, every frequency that fulfills

$$f = f_{\text{bin}}\left(n + \frac{1}{2}\right)\,,\; n \in \mathbb{N}\,, \tag{2.35}$$

which are the center frequencies of each bin, is represented correctly, while others show some loss.

Since the instantaneous frequency $f(t)$ of the interferometric signal within the LRI can be derived from phase readings, giving approximately 10 MHz plus Doppler shifts (cf. section 4.1), it is possible to estimate the magnitude of the loss and correct it.

The frequency $f(t)$ normalized to the bin width reads

$$\tilde{f}(t) = \frac{f(t)}{f_{\text{bin}}} \tag{2.36}$$

and the corresponding wrapped position within a each bin

$$\Delta\tilde{f}(t) = \tilde{f}(t) - \text{round}(\tilde{f}(t))\,. \tag{2.37}$$

This quantity is bound by $-0.5 \leq \Delta\tilde{f} \leq 0.5$ and can be used to calculate the scalloping loss for a given window function. Within the LRP, no explicit window function is used, thus it can be regarded as a rectangular window. After Heinzel et al. (2002), one derives the scalloping loss for a rectangular window as

$$L(\Delta\tilde{f}) = \frac{\sqrt{2 - 2\cos\left(2\pi\Delta\tilde{f}\right)}}{\left|2\pi\Delta\tilde{f}\right|} \tag{2.38}$$

The scalloping loss can easily be converted into dB as

$$L_{\text{dB}} = 20\log_{10}(L)\,, \tag{2.39}$$

which yields

$$-3.9224\,\text{dB} \leq L_{\text{dB}} \leq 0 \tag{2.40}$$

for

$$-0.5 \leq \Delta\tilde{f} \leq 0.5\,. \tag{2.41}$$

Thus, the expected maximal loss at the edge of each frequency bin is -3.9224 dB for the rectangular window, which is shown in fig. 2.4d.

3. GRACE Follow-On Satellites

This chapter briefly introduces the idea and concepts of the Gravity Recovery And Climate Experiment (GRACE) and GRACE-FO mission. It shows the satellites architecture and scientific instruments. An overview of some of the components within each spacecraft (S/C) is shown in fig. 3.1. Some of the scientific instruments onboard the S/C will be introduced in section 3.2. Afterwards, the different types of onboard time frames are explained in section 3.3. The subsystems belonging to the LRI, marked in blue in fig. 3.1, are discussed later in chapter 4.

3.1. Mission Concept

The GRACE mission, a joint mission of National Aeronautics and Space Administration (NASA) and Geoforschungszentrum Potsdam (GFZ), was designed to monitor the time-varying gravity field by low-low satellite-satellite tracking. The so called ranging signal, i.e. the inter-S/C distance, indicates the Earths mass distribution. By deriving this distribution regularly, e.g. on a monthly basis, one is able to track redistribution of mass, e.g. due to hydrological or oceanographical reasons (Wahr et al., 1998). Even if GRACE did not reach its baseline sensitivity (Goswami et al., 2018), it measured the static geoid with an estimated error of 2 cm and a spatial resolution of up to 400 km in over an interval of about 100 days in 2002 (Tapley et al., 2003; Tapley et al., 2004).

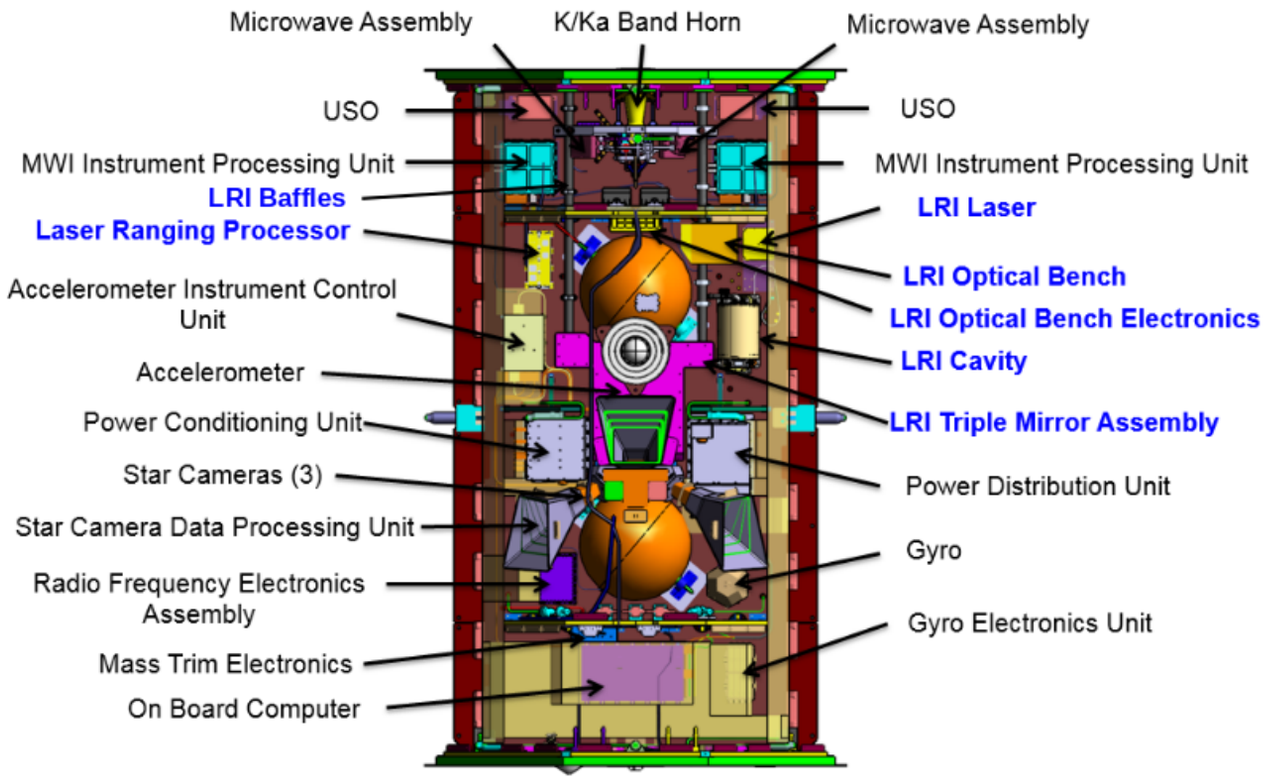

Figure 3.1.: Sketch of the GRACE-FO satellite's interior showing the locations of some parts within the GRACE-FO satellites. Blue marked components are part of the LRI. Image credit: Dubovitsky et al. (2018)

The GRACE mission was launched in 2002 with a designed lifetime of five years. When it was turned off in 2017, many research fields concerned with Earth sciences gained a profit of the gathered data, e.g. researches on glaciers (Luthcke et al., 2008), sea-level variations (Feng et al., 2015), ground water storage (Wang et al., 2015) and more. To continue this extremely valuable data stream, the GRACE Follow-On (GRACE-FO or GFO) mission has been set up, basically as a rebuild of the original GRACE satellites in order to have comparable data and to reduce construction effort and costs (Sheard et al., 2012). The two S/C are basically equal, and differ only in the clock rate of the Ultra-Stable Oscillator (USO) and the frequency of the S-band unit used for Up- and Downlink (Wen et al., 2019). They have been successfully launched by SpaceX on 2018-05-22 (SpaceX, 2018). The mission operation is performed by the German Space Operations Center (GSOC) of Deutsche Luft und Raumfahrtgesellschaft (DLR).

The metrology principle of the GRACE and GRACE-FO mission is to measure the distance changes between the two S/C, that are "chasing each other" on circular, nearly polar orbits with an inclination of 89° at an initial altitude of about 500 km and with a separation of 220 ± 50 km (NASA, 2017). The motion of the two satellites, which are denoted as GF-1 and GF-2 within this thesis, sometimes also GF-C and GF-D, is determined by gravitational and non-gravitational forces and can be determined with High-Low Satellite-Satellite Tracking (SST) via GPS in combination with Low-Low SST via the Microwave Instrument (MWI) and the Laser Ranging Interferometer (LRI). When the satellites fly over a massive region (e.g. the Himalayas), one can observe an accordion-like effect in the range, because the leading satellite gets attracted by the higher mass first, which will increase the inter-satellite distance. Shortly afterwards, the second satellite gets accelerated too, which shortens the inter-satellite distance again. After flying over the massive region, the satellites get slowed down one after the other which yields to a decreasing and then again increasing distance. Within the range data, these oscillations can be seen qualitatively with an amplitude of some ten micrometers, which can be made visible in a so called Himalaya plot, shown in fig. 3.2. The magnitude of the oscillation is dependent on the high-pass filter, that is used to assess the tiny variations over the orbital motion of several hundred meters.

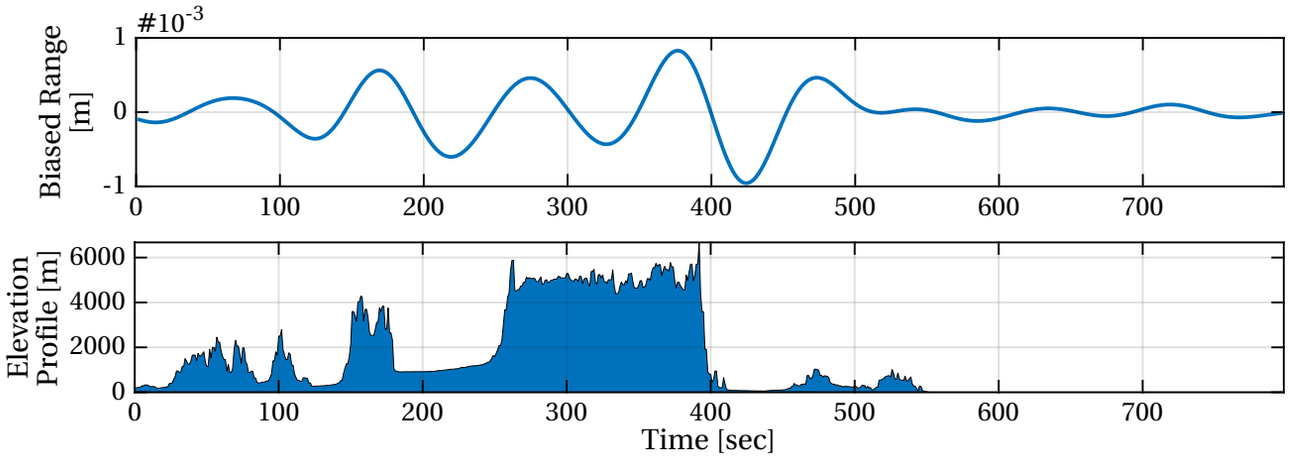

Figure 3.2.: A so called Himalaya plot: changes in the inter-spacecraft distance while flying over the Himalayas. The range variations are shown in the upper panel, while the lower one shows the topography beneath the satellites. The oscillatory effect, caused by changing mass distribution, is clearly visible. However, it's magnitude highly depends on the filtering. A 3D version of such a Himalaya plot is shown as the cover image of this thesis.

3.2. Onboard Instruments

3.2.1. Accelerometer

For a precise measurement of non-gravitational accelerations, the usage of a Accelerometer (ACC) is necessary. The ACC is built by ONERA (France) and is an improved version of the SuperSTAR ACC used for GRACE (Christophe et al., 2015; Kornfeld et al., 2019). It is located at the Center of Mass (CoM) of the S/C and measures linear and angular accelerations in all three degrees of freedom. The ACC is intended to measure non-gravitational accelerations such as air drag, accelerations induced by attitude and orbit control thruster usage, solar radiation pressure and more. However, if the CoM and the ACC reference point do not coincide, the coupling of angular in linear accelerations does not vanish. Therefore, the CoM can be adjusted using small trim masses onboard the S/C to compensate for CoM shifts, e.g. caused by fuel usage by the thrusters. The ACC data is used in post-processing to separate gravitational and non-gravitational effects and to remove non-gravitational impacts from the range measurement. The impact of linear accelerations to the LRI ranging is investigated in section 6.6.2.

3.2.2. Inertial Measurement Unit

The Inertial Measurement Unit (IMU) is an instrument to precisely measure angular accelerations. It is implemented using four ring laser gyroscopes, being arranged in a tetrahedron shape (Wen et al., 2019). The measurement principle makes use of the Sagnac effect (Lefèvre, 1997). The Euler angles for the local S/C attitude (Roll, Pitch and Yaw) can be derived approximately. IMU and ACC can measure precise variations at high frequencies, but no absolute attitude angles.

3.2.3. Star Camera Assembly

The Star Camera Assembly (SCA) also provides attitude angles. However, other than the IMU, the SCA angles are measured w.r.t. an absolute reference frame and are more stable in terms of long term drifts, whereas the high frequency noise on the other hand is much higher. The principle is to autonomously detect the star constellation that is visible within the camera images. Star catalogs are available on board and a comparison to the camera images gives information about the S/C attitude. Three Camera Head Unit (CHU) belong to the SCA, two pointing to the lateral sides of the S/C and one upwards, cf. fig. 3.1. The latter one is new in GRACE-FO compared to GRACE. It has been included because sometimes two CHUs can get blinded by the Sun or the Moon, resulting in less precise attitude angles. Investigations have shown that the CHU blindings can influence the gravity field recovery (Goswami et al., 2018). The SCA was built at the DTU (Denmark).

3.2.4. Attitude and Orbit Control System

The Attitude and Orbit Control System (AOCS) is to manipulate the current spacecrafts attitude. It uses the attitude sensors, SCA and IMU among others, as well as the geographical position provided by GPS (see below) as input data streams (Astrium GmbH, 2013).

The actuators are six cold-redundant magneto-torque rods and 14 cold gas thrusters. There are two magneto-torque rods and four Attitude Control Thrusters (ACT) per angular degree of freedom. While the magneto-torque rods are used continuously with varying currents to achieve more or less torque, the thrusters are activated when the rods are insufficient, e.g. due to parallel alignment of the magnetic field lines (Herman et al., 2004). The thrusters are split in two branches, whereas each two

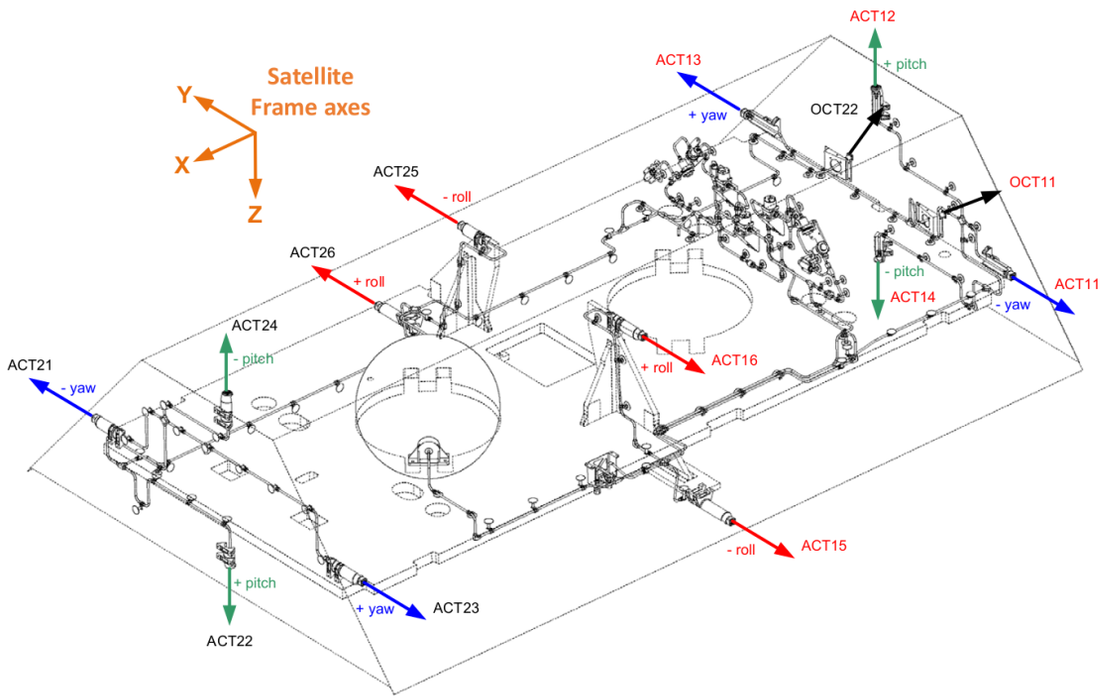

Figure 3.3.: Locations of the thrusters on the satellite body. They are labeled ACT for Attitude Control Thruster and OCT for Orbit Control Thruster with the first number specifying the branch, the second number the thruster itself. Image from Wen et al., 2019.

related thrusters are on opposite sides of the S/C w.r.t. the CoM. The locations of these are shown in fig. 3.3. The AOCS activates the two related thrusters in the both branches simultaneously in order to rotate the S/C around the CoM. Two additional thrusters are attached on the rear of each S/C for orbital control (OCT). The ACT have a force of 10 mN, while the OCT have a force of 50 mN.

The AOCS features several pointing modes. One of which is the normal fine pointing (NOM-FP) mode, used during scientific measurements. In this mode, the S/C pointing is not in the flight direction, but towards the other S/C within a range of a ±300 µrad (ESA eoPortal).

3.2.5. Microwave Instrument (MWI)

Continuing the legacy of GRACE, the Microwave Instrument (MWI) is again the primary scientific instrument for providing range information (Kornfeld et al., 2019). For the inter-satellite ranging, two microwave frequencies per S/C of about 24.5 and 32.7 GHz, known as K- and Ka-band, are used. The range is measured for both of these bands by means of interferometry. By combining the two data streams, one can derive a so-called ionosphere-free ranging solution, which corrects delays due to refraction in the atmospheric layer of a Low-Earth Orbit (LEO), the ionosphere. This is possible by using two frequencies, because the ionosphere is dispersive, i.e. it delays the two signals by a different amount of time of which the ratio is precisely known. The K-Band Ranging (KBR) instrument is measuring the one-way phase at both, K- and Ka- frequencies and on both S/C simultaneously. Thus, the measurement is called Dual One Way Range (DOWR) and calculated as

$$\rho_{\mathcal{K}} = c\,\frac{\phi_{\mathcal{K}}^{(1)} + \phi_{\mathcal{K}}^{(2)}}{f_{\mathcal{K}}^{(1)} + f_{\mathcal{K}}^{(2)}}\,, \tag{3.1}$$

where $\rho_{\mathcal{K}}$ is the biased range of $\mathcal{K} = \{\mathrm{K}, \mathrm{Ka}\}$ band phase measurements, $\phi_{\mathcal{K}}^{(1/2)}$ are the phase measurement and $f_{\mathcal{K}}^{(1/2)}$ denotes the K- or Ka-band frequency on each S/C, GF-1 and GF-2. It is notable, that this ranging signal is obtained on each S/C.

The microwave frequencies are derived from the onboard clock, the USO (see below). The ionosphere-free correction is then calculated as a linear combination

$$\rho_{\text{ion.}} = C_{\mathrm{Ka}}\rho_{\mathrm{Ka}} - C_{\mathrm{K}}\rho_{\mathrm{K}} \tag{3.2}$$

using the coefficients $C_{\mathcal{K}}$, which are computed as

$$C_{\mathrm{Ka}} = \frac{\bar{f}_{\mathrm{Ka}}^2}{\bar{f}_{\mathrm{Ka}}^2 - \bar{f}_{\mathrm{K}}^2} = \frac{16}{7} \quad \text{and} \quad C_{\mathrm{K}} = \frac{\bar{f}_{\mathrm{K}}^2}{\bar{f}_{\mathrm{Ka}}^2 - \bar{f}_{\mathrm{K}}^2} = \frac{9}{7} \tag{3.3}$$

via the effective frequency (Kim, 2000)

$$\bar{f}_{\mathcal{K}} = \sqrt{f_{\mathcal{K}}^{(1)}\, f_{\mathcal{K}}^{(2)}}\,. \tag{3.4}$$

Apart from removing the ionospheric delay, it also has to be taken into account, that the KBR antenna phase centers are not located at the CoM, but have a offset of approximately 1.4 m in x-direction of the Science Reference Frame (SRF) (Wen et al., 2019).

The instrument noise of the MWI, i.e. the Amplitude Spectral Density (ASD) of the KBR ranging noise, can be modeled as (Kim, 2000; Darbeheshti et al., 2017)

$$\delta\rho_{\mathrm{KBR}} = \sqrt{1 + \left(\frac{0.0018\,\mathrm{Hz}}{f}\right)^4}\ \mu\mathrm{m}/\sqrt{\mathrm{Hz}} \tag{3.5}$$

with

$$10^{-5}\,\mathrm{Hz} \leq f \leq 10^{-1}\,\mathrm{Hz} \tag{3.6}$$

This model will be used later, to compare the LRI and KBR accuracy.

Global Positioning System Receiver Assembly

The Global Positioning System (GPS) Receiver Assembly is used for precise orbit determination of the satellites. The GPS antenna is located on the top of the S/C, depicted as the gray concentric circles beneath the Triple Mirror Assembly (TMA) in fig. 3.1. The GPS navigation solutions, i.e. the position, velocity and time (PVT) solution, provide an absolute positioning of the S/C with a precision of up to a few cm (NASA, 2017). The GPS time information contained in the PVT product is also used as an absolute timing reference for the onboard clock.

Instrument Processing Unit (IPU)

The Instrument Processing Unit (IPU) of the MWI is the main processing unit for the GPS and the KBR instruments. On each S/C are two units, of which one is redundant. They are shown in light blue in the top part of fig. 3.1. The IPU evaluates GPS observations and provides the local position and velocity to the AOCS in form of a navigation solution. The IPU distributes the timing information from the navigation solutions to the Onboard Computer (OBC) and the LRI. Note section 3.3 on the different time frames onboard each S/C. The development of the IPU is based on heritage from GRACE and GRAIL (Kornfeld et al., 2019).

Ultra Stable Oscillator

The onboard clock rate is given by the Ultra-Stable Oscillator (USO). It is an highly stabilized Oven-Controlled Quartz Oscillator (OCXO), which serves as a local time reference. It is an accurate time reference on short time scales but shows a drift w.r.t. absolute time references, like the GPS time. The base frequencies of the OCXO on the two S/C are slightly different, i.e. (Wen et al., 2019)

$$f_{\text{OCXO,GF-1}} = 4.832\,000\,\text{MHz} \tag{3.7}$$
$$f_{\text{OCXO,GF-2}} = 4.832\,099\,\text{MHz}\,. \tag{3.8}$$

These are upscaled by a factor of eight via electrical frequency multiplication to the USO frequencies of

$$f_{\text{USO, GF-1}} = 38.656\,000\,\text{MHz} \tag{3.9}$$
$$\text{and} \qquad f_{\text{USO, GF-2}} = 38.656\,792\,\text{MHz}\,. \tag{3.10}$$

They are then used as timing reference for the KBR, LRI and GPS. The K- and Ka-band frequencies are derived from these fundamental frequencies, again via electrical frequency multiplication. According to eq. (3.1), the frequencies of the K- and Ka-band are the scale factor to convert phase measurements to ranging data. Thus, the USO frequency fulfills the task as length reference, just like the cavity for laser frequency stabilization does (cf. section 2.4).

The USOs are manufactured by the JHU/APL as an improved version of the GRACE and GRAIL USOs (ESA eoPortal; Weaver et al., 2010).

3.3. Time Frames

The payloads on the GRACE-FO satellites use different time frames. The main frames are introduced here, but the interested reader is referred to Girerd et al. (2014), Dubovitsky (2016a) and Wen et al. (2019).

In general, the onboard GPS reference epoch is January 6, 1980, which also holds for Level 0 data. The epoch used in Level 1A and 1B data products is January 01, 2000 at noon. The absolute difference between these two reference epochs is 630 763 200 s. The different data processing levels are introduced in chapter 5.

3.3.1. IPU Receiver Time

The IPU receiver time is generated using the clock rate from the USO and is synchronized with absolute GPS time. This synchronization is done at every reboot of the IPU. In the meantime, the IPU receiver time is drifting w.r.t. GPS time as the USO drifts. This offset or drift is reported in the Level 1B data release in nanosecond resolution as CLK1B product. The IPU, GPS and KBR time tags are sampled within 50 picoseconds to IPU receiver time (Wen et al., 2019). Each S/C has its own realization of IPU receiver time.

3.3.2. OBC Time

The Onboard Computer (OBC) does not use the USO as reference but has its own quartz oscillator built-in, which serves as an independent time reference. If the IPU is available, the OBC clock is

synchronized by one electric pulse per second to the IPU. If no pulses from the IPU are available, the quartz oscillator can not achieve the same stability as the USO but is suitable to fill smaller gaps without synchronization.

If the synchronization is working properly, the OBC is able to control the internal quartz oscillator, such that the OBC time does not drift to far from the IPU receiver time. To do so, it can insert or hide individual pulses from the IPU, to achieve a drift correction. This ensures a smooth OBC time without jumps, that is always synchronized to the IPU receiver time. The maximum allowed difference is ±500 ms (Girerd et al., 2014).

This timing difference between OBC and IPU receiver time is then reported within the data releases in the TIM1B data product. Instruments, that are not the IPU, KBR and GPS, are time-tagged with respect to OBC time within a maximum delay of 100 picoseconds (Wen et al., 2019).

3.3.3. LRI Time

The LRI times frame relies on the accuracy of the USO for sampling. However, a reference time tag is sent by the OBC to the LRP at every reboot. This procedure introduces a small offset between OBC time and LRI time, which is not larger than 1.5 s and remains constant until the next reboot of the LRP (Girerd et al., 2014). To derive an absolute timing without this offset, there are telecommands that request a so-called datation report, that tells about the offset between LRI and IPU receiver time. It should be requested at least after every reboot of the LRP or the IPU. Hence, the complete correction from LRI to GPS time corrects for the constant offset as well as the IPU correction, namely the CLK1B product. It is available in the LLK1B package, which combines the two corrections mentioned above, providing the numerical values for the offset of the LRI time w.r.t. GPS time in seconds.

3.4. Coordinate Systems

In the context of GRACE-FO, several coordinate reference frames are commonly used. In essence, each instrument has it's own frame. Therefore, the frames used the most within this thesis, are briefly introduced in the following. The LRI frame in introduced in Dubovitsky et al. (2018), while the other coordinate systems are explained in Wen et al. (2019).

3.4.1. Science Reference Frame

The Science Reference Frame (SRF), sometimes also Spacecraft Frame (SF), is fixed to the satellite body. It's origin is the center of the ACC proof mass, which itself is approximately co-located to the satellite's CoM. The x-axis points from the origin towards the K-band antenna and defines the roll axis, which approximates the Line of Sight (LoS). The z- or yaw-axis points radially downwards (nadir pointing) while the y- or pitch-axis forms a right-handed base with the other two axes. All data products as of Level-1B are transformed into this frame to share a common base.

3.4.2. Accelerometer Frame

The Accelerometer Frame (AF) shares the origin and axes with the SRF but has a different naming convention:

$$(x, y, z)^{\intercal}_{\mathrm{AF}} = (y, z, x)^{\intercal}_{\mathrm{SRF}} \,. \tag{3.11}$$

The ACC is rotated, such that the least sensitive axis of the instrument measures the least critical axis for gravity field recovery, i.e. y_{SRF} (Kornfeld et al., 2019).

3.4.3. LRI Optical Frame

The LRI optical frame (LOF) arises from the SRF by a 180 ° rotation around the pitch-axis and additionally a small rotation by an angle δ around the roll-axis. The inversion of the x-axis direction is done such that it points in direction of the outgoing beam, i.e. alongside the LoS. The small deviation, δ, arises from imperfect integration of the Optical Bench Assembly (OBA) into the satellite body (Dubovitsky et al., 2018). However, this integration error was measured prior to the launch and will be corrected internally. The three reference frames, SRF, AF and LOF are depicted in fig. 3.4

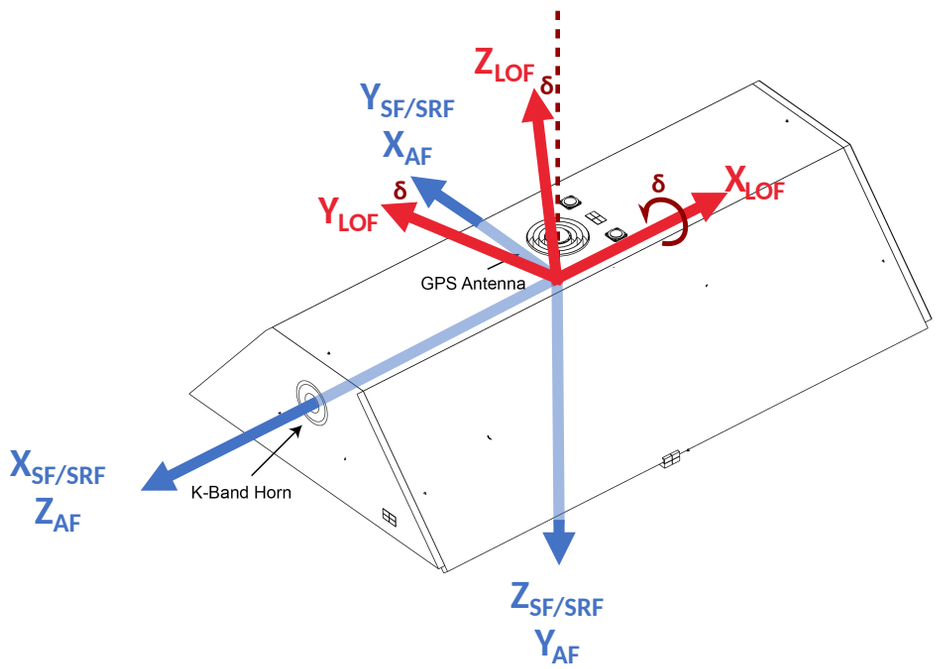

Figure 3.4.: SRF, AF and LOF definitions within the satellite body. Image after Wen et al. (2019).

4. Design and Commissioning of the Laser Ranging Interferometer

This chapter introduces the working principle of the LRI in section 4.1, followed by the description of individual components sections 4.2 to 4.6. Finally, an overview of the mission timeline and commissioning process of the LRI is given in section 4.7.

4.1. LRI Design

4.1.1. Design and Working Principle

The architecture of the LRI has first been published in Sheard et al. (2012). A simplified design of the setup is shown in fig. 4.1. Naming conventions, for frequencies and optical paths, that will be used in this section, are given in fig. 4.2.

Because the GRACE-FO satellites are basically a rebuilt of the original GRACE satellites, the LRI had to be implemented into an already crowded setup. Due to the cold-gas tank (not shown in fig. 4.1) and the KBR antennas, that are on the connecting line between the two accelerometer reference points, it was not possible to build an on-axis interferometer. "On-axis" relates to the LoS, the connecting axis between the two CoM. This led to the "racetrack configuration", an off-axis system.

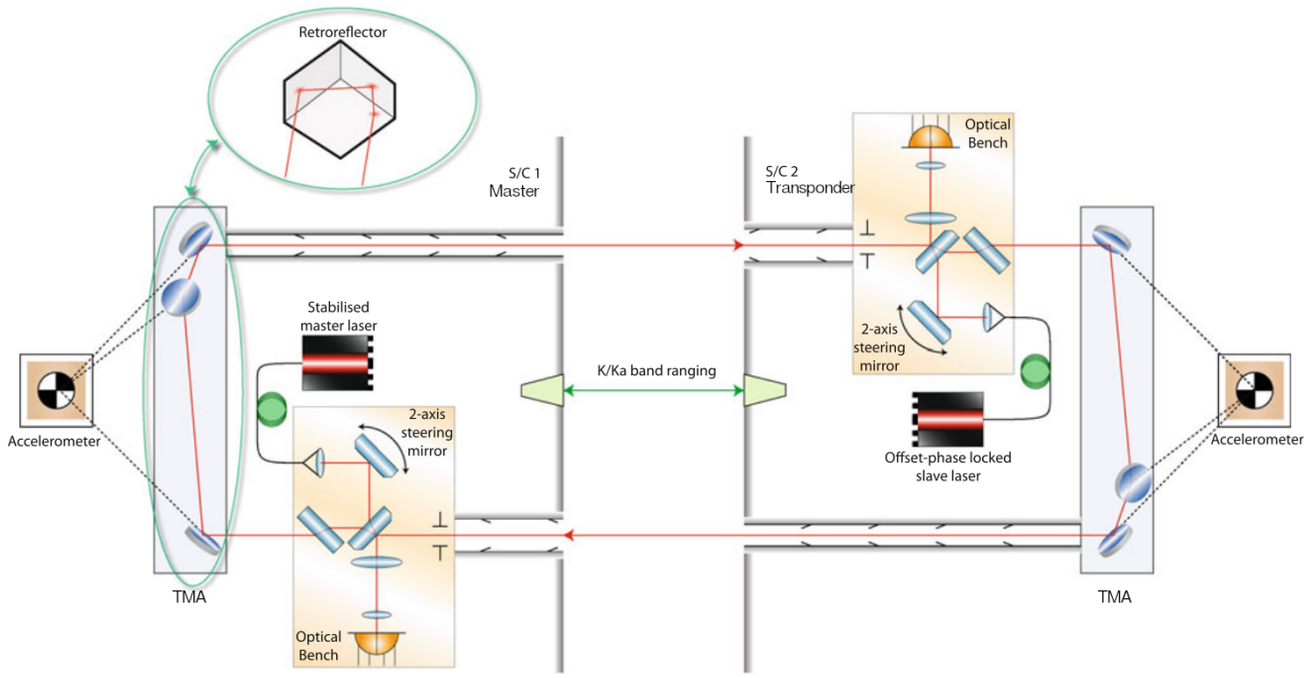

Figure 4.1.: Simplified optical layout for the LRI. Note the microwave ranging system (labeled K/Ka band ranging) is occupying the connecting line between the two accelerometer. The master S/C is depicted on the left side, transponder on the right. Redundant QPDs are left out. Image after Sheard et al. (2012, ©Springer).

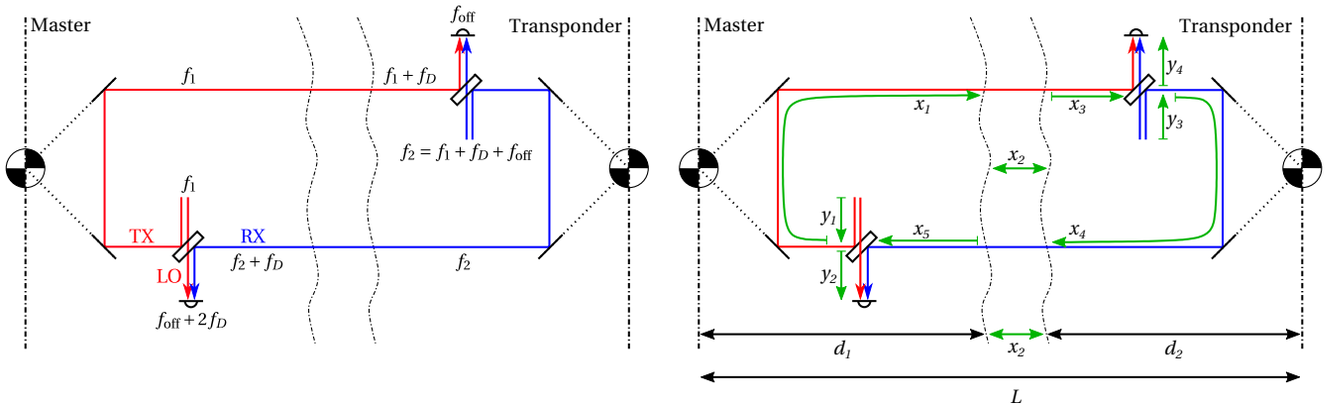

Figure 4.2.: Nominal lengths and frequencies in the LRI. **Left:** Frequencies inside the LRI. Lower frequencies are depicted in red, higher ones in blue. The offset frequency f_{off} is 10 MHz for the GRACE-FO LRI. **Right:** Lengths within the LRI. The total measured length $L = d_1 + x_2 + d_2$ is exactly one half of the roundtrip length $x_1 + x_2 + x_3 + x_4 + x_2 + x_5$. Refer to Sheard et al. (2012); Abich et al. (2019) for more information.

On the master side, a GB (cf. section 2.1) with the frequency

$$f_1 = f_0 + \delta f_1 \tag{4.1}$$

is emitted by a laser, which is stabilized to a frequency reference, f_0, using an optical cavity (cf. section 4.2) and a PDH scheme (cf. section 2.4). Laser frequency noise is denoted as δf_1. The beam pointing is controlled using DWS (cf. section 2.3) as sensor and a 2-axis steering mirror, also called Fast Steering Mirror (FSM) (cf. section 4.4) as actuator.

The beam reaches the beamsplitter, which separates the Local Oscillator (LO) beam and the transmitted (TX) beam. The LO beam propagates the path y_2 and is sensed on the Quadrant Photodiode (QPD) (cf. section 4.5), while the TX beam gets routed through the Triple Mirror Assembly (TMA) (cf. section 4.3) to the other S/C, following the optical paths x_1 and x_2. The length of x_2 is varying with time. This variation is to be measured. A Doppler shift, i.e. (Halliday et al., 2010, section 17.9)

$$f_D(t) = f_1 \cdot \left(\sqrt{\frac{1 - \frac{v_{12}(t)}{c}}{1 + \frac{v_{12}(t)}{c}}} - 1 \right), \tag{4.2}$$

that is caused by the relative velocity of the two S/C, $v_{12}(t)$, slightly changes the frequency of the received (RX) beam that is detected on the transponder. Note, that with this notation, f_D is not the *shifted* frequency, but the *shift* of the frequency. Hence, if the relative velocity $v_{12} < 0$, i.e. the range is decreasing, the absolute Doppler shift f_D is positive and vice versa. Approximately, it holds that

$$f_D \approx -\frac{v_{12}}{\lambda}, \tag{4.3}$$

which, for the parameters of the LRI setup, approximately yields -1 MHz of Doppler shift per 1 m/s relative velocity.

The beam reaches the transponder S/C with this shifted frequency $f_1 + f_D$. However, the power of the received light is in the order of a few picowatts (Sheard et al., 2012), which is sufficient for interferometric measurements on the transponder side, but not enough to be reflected back to the

master S/C (Müller, 2017). Therefore, the transponder S/C also carries a laser, whose frequency, f_2, is adjusted using a frequency-offset DPLL, such that it reproduces the incoming frequency but adds up a constant offset, f_{off}. It reads

$$f_2(t) = f_1 + f_D(t) + f_{\text{off}} + \delta f_1 + \delta f_{\text{off}} \,. \tag{4.4}$$

Hence, the beatnote frequency on the transponder's QPD reads $f_2 - (f_1 + f_D) = f_{\text{off}} + \delta f_{\text{off}}$. The frequency-offset DPLL again introduces noise, δf_{off}, but preserves the phase of the incoming beam. All in all, the beam is amplified in power and frequency shifted on the transponder side. Afterwards, the beam is again routed through the TMA and sent back to the master S/C, adding up a second Doppler shift. It is assumed, that during the flight time of a photon, the relative velocity, v_{12}, stays constant and thus, the Doppler shift, f_D, does not change during one roundtrip and has approximately the same magnitude for the two frequencies f_1 and f_2. Finally, the LO beam and the RX beam superimpose on the recombination beamsplitter on the master side. This interferometric signal is then sensed on the master's QPD. It's beatnote frequency reads

$$f_{\text{b}} = f_1 - (f_2(t) + f_D(t)) = f_{\text{off}} + 2 f_D(t) \; + \delta f_1 + \delta f_{\text{off}} + \delta f_{y_1} \,. \tag{4.5}$$

A third noise source is added, which accounts for length changes on the optical bench, i.e. in the path y_1 from the laser to the beamsplitter. The changes in the total geometrical pathlength L are contained in the Doppler shifts. It should be noted, that the formulae introduced above do not attribute for the photon travel time between the two S/C and the related variability of the relative velocity v_{12} during this time.

The main scientific measurement, i.e. the phase retrieval, takes place on the master S/C, where the transponder's main task is to amplify the beam power. This measurement scheme is called Two-Way Range (TWR), in contradiction to the Dual One Way Range (DOWR) scheme of the MWI (cf. section 3.2.5).

4.1.2. Ranging Measurement

Since frequency and phase are connected via the time integral, i.e.

$$\phi(t) = 2\pi \int_{t_0}^{t} f\left(t'\right) \mathrm{d}t' + \text{const.} \,, \tag{4.6}$$

the beatnote frequency, eq. (4.5), can be rewritten in terms of a phase, that is measured by a phasemeter (Ware et al., 2006). The measurement of the phase on the master's QPD, i.e. the averaged phase over all four segments, is the main observable of the LRI. After Sheard et al. (2012), the phase reads

$$\begin{aligned}
\phi_M(t) \approx \;& 2\pi f_{\text{off}} \cdot t && \text{noise free frequency offset of transponder laser} \\
& + 2k\rho(t) && \text{desired quantity, fluctuations in inter-S/C range } \rho(t) \\
& + \left[\delta\phi_{f_1}(t) - \delta\phi_{f_1}(t-\tau)\right] && \text{noise of master laser's frequency } f_1 \\
& - \left[\delta\phi_{y_1}(t) - \delta\phi_{y_1}(t-\tau)\right] && \text{geometrical pathlength noise of } y_1 \\
& + \delta\phi_{\text{off}}(t) && \text{noise of the frequency-offset DPLL} \\
& + \text{const.} && \text{initial phase ambiguity}
\end{aligned} \tag{4.7}$$

with the wavenumber $k = 2\pi/\lambda$. The first and second term directly correspond to f_{off} and $2f_D$ in eq. (4.5), while the third to fifth term arise from the different frequency noise sources, which can be

converted to phases using eq. (4.6). Here, τ denotes the roundtrip travel time of a photon, which is approximately 1.6 µs (Sheard et al., 2012).

The phase on the transponder S/C reads

$$\phi_T(t) = 2\pi \left(f_{\text{off}} + \delta f_{\text{off}}(t)\right) \cdot t + \text{const.} \,. \tag{4.8}$$

The corresponding longitudinal pathlength signal, or ranging phase, ϕ_{LRI}, is the difference of master's and transponder's phase measurements, i.e.

$$\phi_{\text{LRI}}(t) = \phi_M(t) - \phi_T(t) \,, \tag{4.9}$$

which can be converted to units of meter and to a one-way instead of a roundtrip range. It reads

$$\begin{aligned} \rho_{\text{LRI}}(t) &= \frac{1}{2k}\left(\phi_{\text{LRI}}(t)\right) + \text{const.} && (4.10)\\ &\approx \rho(t) + \frac{1}{2k}\left[\delta\phi_{f_1}(t) - \delta\phi_{f_1}(t-\tau)\right] \\ &\quad + \frac{1}{2k}\left[\delta\phi_{y_1}(t) - \delta\phi_{y_1}(t-\tau)\right] \\ &\quad + \text{const.} \,. && (4.11) \end{aligned}$$

Assuming that the transponder's frequency offset lock is perfectly held, one could also simply remove a ramp with constant slope from the master's phase, without using the transponder phase at all. This quantity, $\rho_{\text{LRI}}(t)$, is a measurement of the desired ranging information, $\rho(t)$, biased via the constant and with added noise terms. The pathlength noise of y_1 is negligible, while the laser's frequency noise is one of the largest contributors to the overall LRI noise (Sheard et al., 2012). It will be further introduced in section 4.2.

4.2. Laser and Cavity

4.2.1. Laser Properties

The lasers of the LRI provide the light for the interferometer. They are solid-state lasers, utilizing a Nd:YAG (Neodymium doped Yttrium Aluminum Garnet) laser crystal with a Non-Planar Ring Oscillator (NPRO) structure. The continuously emitted electromagnetic waves have a wavelength of 1064 nm and an optical power of about 25 mW. The lasers were built by Tesat-Spacecom GmbH (Dubovitsky et al., 2018).

Most of the optical power is routed via the TMA to the distant S/C, while a small fraction, approximately 10 %, is sent to the optical reference cavity for frequency stabilization using PDH technique (cf. section 2.4 and Folkner et al. (2010)). The frequency stability is a key point for the ranging measurement, since fluctuations directly introduce an error, cf. eq. (4.11).

For visualization, an ASD of LRI ranging measurement is shown in fig. 4.3 (blue trace) alongside the very same spectral density, scaled with 1 ppm (part per million). The details of the ASD of LRI ranging measurements in general will be discussed in section 6.6. For now, it should be noted that the scaled trace (orange) represents the error in the ranging for a wavelength uncertainty of roughly 1 pm. The corresponding error of the absolute laser frequency is 281 MHz. For frequencies below 3 mHz, the ranging error corresponding to 1 ppm frequency error surpasses the noise requirement for the LRI (cyan trace). For comparison, an estimate of the KBR noise is added (green trace), based

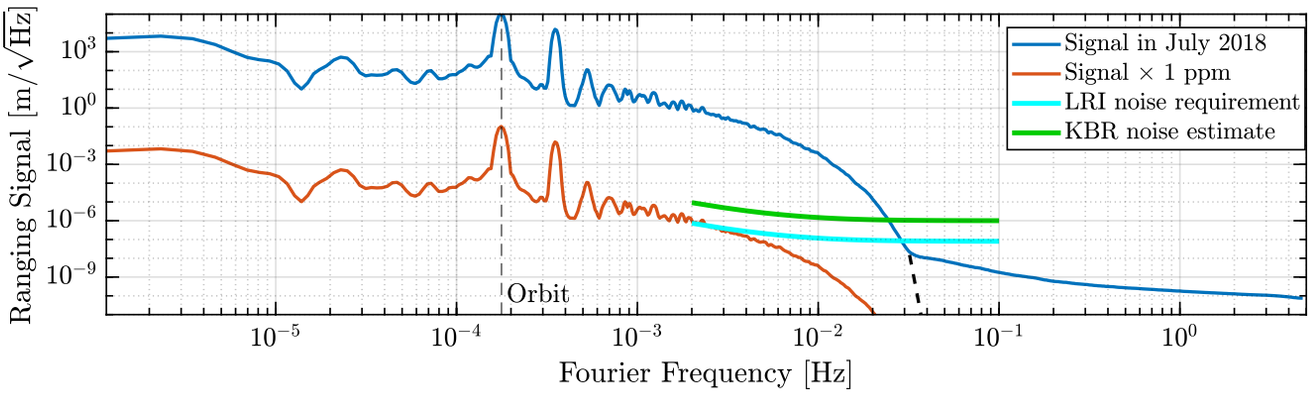

Figure 4.3.: ASD of the ranging signal for ten subsequent days of measurement in July 2018, shown with the 1 ppm error. It reaches the noise requirement already in the main measurement band of the gravity signal and overwhelms it for the orbital frequency and higher harmonics.

on Darbeheshti et al. (2017). Therefore, the laser's frequency has to be stabilized using an optical Fabry-Pérot reference cavity (see below) and PDH technique (cf. section 2.4). The tuning of the laser frequency, which is necessary for the PDH lock and also for the offset-frequency DPLL, is done using two actuators: a thermal actuator and a Piezoelectric Transducer (PZT). Both affect the crystalline structure and therefore the optical properties of the NPRO. The thermal actuation is slower but has larger ranges, while the PZT acts faster. Note, that the PDH frequency stabilization is only used on the S/C being in master role, while the transponder S/C uses an offset-frequency DPLL. However, both S/C carry an identical setup, including the cavity, providing redundancy. Also the laser diode, that is pumping the NPRO is redundant on each S/C (Dubovitsky et al., 2018).

The requirement for the laser frequency noise of the LRI lasers is an ASD of

$$\widetilde{\delta\nu} = 30\,\mathrm{Hz}/\sqrt{\mathrm{Hz}} \tag{4.12}$$

between 10 mHz and 100 mHz, which is the frequency range of the major gravity signal (Folkner et al., 2010). It is chosen such that the LRI is not limiting the gravity field recovery at all. Below this range, the accelerometer noise is expected to have larger contributions, higher frequencies are limited by the phase sampling rate of the downlinked ranging phase (Thompson et al., 2011). Laser frequency noise couples linearly with the inter-S/C distance into the ranging measurements. The relation is given by (Sheard et al., 2012)

$$\widetilde{\delta x} = \frac{\rho}{\nu}\widetilde{\delta\nu}\,, \tag{4.13}$$

which is at a level of about $30\,\mathrm{nm}/\sqrt{\mathrm{Hz}}$ for the worst case distance of $\rho = 270\,\mathrm{km}$ and a laser frequency of $\nu = c/1064\cdot 10^{-9}\,\mathrm{m} \approx 281\,\mathrm{THz}$.

The telemetry of the lasers is reported in the housekeeping packet (cf. section 5.2.3), containing the in-loop (IL) and out-of-loop (OOL) status of the PZT and thermal control loops, that drive the laser frequency. The data rate is 1/12 Hz.

4.2.2. Calibration of the Absolute Laser Frequency

By now and within the near future, it is not possible to electronically measure oscillations as fast as electromagnetic waves within the visible spectrum. Therefore, some tricks are needed to determine an absolute value for the frequency of light, e.g. by using interferometry. Onboard of the S/C, these

additional devices can not be used and therefore, a calibrated model of the absolute frequency of the two flight lasers is needed.

As stated before, the lasers are tunable using the thermal and PZT controllers. However, the absolute laser frequency additionally is dependent on the surrounding temperature variations, that are not covered by the actuators. Therefore, the influence of both actuators and outer temperature changes on the laser frequency should be well known to derive a reliable frequency model.

The outer temperature of the laser unit is measured at the so called Thermal Reference Point (TRP), which is a sensor, mounted inside of the laser housing, but not directly at the NPRO. Thus, outer temperature variations, measured at the TRP, need some amount of time, $\Delta t = 520\,\mathrm{s}$, to propagate to the NPRO. The TRP temperature is reported in the OFFRED data packets (cf. section 5.2.5).

Both flight units have undergone a calibration procedure, to determine the coupling factors of the two actuators and the external temperature (Müller et al., 2017a). For the calibration, the flight unit laser was offset-frequency locked to another commercial reference laser. During the testing, the reference laser's frequency was monitored using a wavemeter. The wavemeter, i.e. the better one out of two, was capable to measure the absolute frequency of light with an accuracy of 60 MHz and was calibrated beforehand (Müller et al., 2017b). The reference laser's frequency was then tuned to different setpoints and the frequency of the flight laser, still being locked to the reference laser, was deduced as the measured reference laser's frequency plus 10 MHz offset frequency. The telemetry packets of the flight laser were recorded during this test.

Afterwards, a model for the optical frequency of the flight lasers could be derived using the measured optical frequency plus the offset frequency and the telemetry data. The linear model reads (Müller et al., 2017a)

$$\nu_{\mathrm{abs}}(t) = \begin{pmatrix} c_{\mathrm{PZT,IL}} \\ c_{\mathrm{PZT,OOL}} \\ c_{\mathrm{Therm,IL}} \\ c_{\mathrm{Therm,OOL}} \\ c_{\mathrm{TRP}} \end{pmatrix} \cdot \begin{pmatrix} \mathrm{PZT_{IL}}(t) \\ \mathrm{PZT_{OOL}}(t) \\ \mathrm{Therm_{IL}}(t) \\ \mathrm{Therm_{OOL}}(t) \\ \mathrm{TRP}(t-\Delta t) - 26^{\circ}\mathrm{C} \end{pmatrix} + \nu_0 + \Delta\nu_{\mathrm{air}}\,. \tag{4.14}$$

It should be noted, that except the TRP, the telemetry values used here are reported as unsigned 32-bit integer, but within this model they are converted to signed and normalized to the interval $[-0.5, 0.5]$ (Müller et al., 2017a). Thus, they have no unit and the corresponding coefficients have the unit of MHz. The TRP is reported in units of degree Celsius and normalized to a reference temperature of 26 °C, giving a coefficient in the unit of MHz/K. The constant parameter, $\Delta\nu_{\mathrm{air}}$, is given by the manufacturer of the laser units.

The coefficients and offsets are fitted for both laser flight units using the above model and the absolute frequency obtained with the wavemeter, using a Least Squares (LSQ) method. The results of this calibration are shown in table 4.1. The estimate for the TRP is not well determined, because the temperature at the TRP during the calibration procedure was connected to the room temperature and therefore could not be modulated. Hence, the coupling of the TRP temperature and the laser frequency could not be measured well. Since the value of c_{TRP} for GF-2 is far from the expected value of roughly −8 MHz/K, the model was refined, i.e. $c_{\mathrm{TRP}} = -8.337\,\mathrm{MHz/K}$ and $\nu_0 = 281\,614\,657\,\mathrm{MHz}$ are used. With these values for GF-2, the absolute frequency estimation using flight data is in better agreement with the estimated frequency of GF-1. A comprehensive investigation of the frequency, derived by using this model, is done in section 6.1.

Factor	$c_{\mathrm{PZT,IL}}$	$c_{\mathrm{PZT,OOL}}$	$c_{\mathrm{Therm,IL}}$	$c_{\mathrm{Therm,OOL}}$	c_{TRP}	$\Delta\nu_{\mathrm{air}}$	ν_0
Unit	MHz	MHz	GHz	GHz	MHz/K	MHz	MHZ
GF-1	10	90	1.038	8.9921	-8.454	40	281614712
GF-2	10	90	1.093	8.8540	-24.337*	30	281614721*

Table 4.1.: Coupling factors to derive absolute laser frequencies. Note the star for c_{TRP} and ν_0 for GF-2, see the text for an explanation.

4.2.3. Cavity

The cavity is built by Ball Aerospace in collaboration with the JPL. It has a length of 77.5 mm and is made of ULE glass to provide geometric stability (Thompson et al., 2011). The FSR is in the order of 2 GHz. To ensure temperature stability, it is built into a two-staged vacuum shielding to prevent thermal induced length changes of the cavity, which is temperature stabilized within 0.1 °C (Thompson et al., 2011). The light is coupled in using fiber optics, as depicted in fig. 2.2 (section 2.4).

To initially put the laser in resonance with the cavity, in order to prepare for the PDH locking, a diagnostic scan of type 1 is taken. An example of this scan, measured by GF-1, is shown in fig. 4.4. For this scan, the laser frequency is tuned by applying a linear ramp to the thermal actuator (lower left panel), while the PZT is not used. The reflected DC power and the PDH error signal are recorded in parallel at a rate of 10 kHz (upper left panel). The reflected DC power shows minima whenever the laser frequency matches the cavity resonance. During this scan, two resonances were covered, which are shown in detail in the center and right panels. The PDH error signal (upper panels) shows the expected pattern (cf. fig. 2.2), as well as the reflected DC power (lower panels). After post-processing

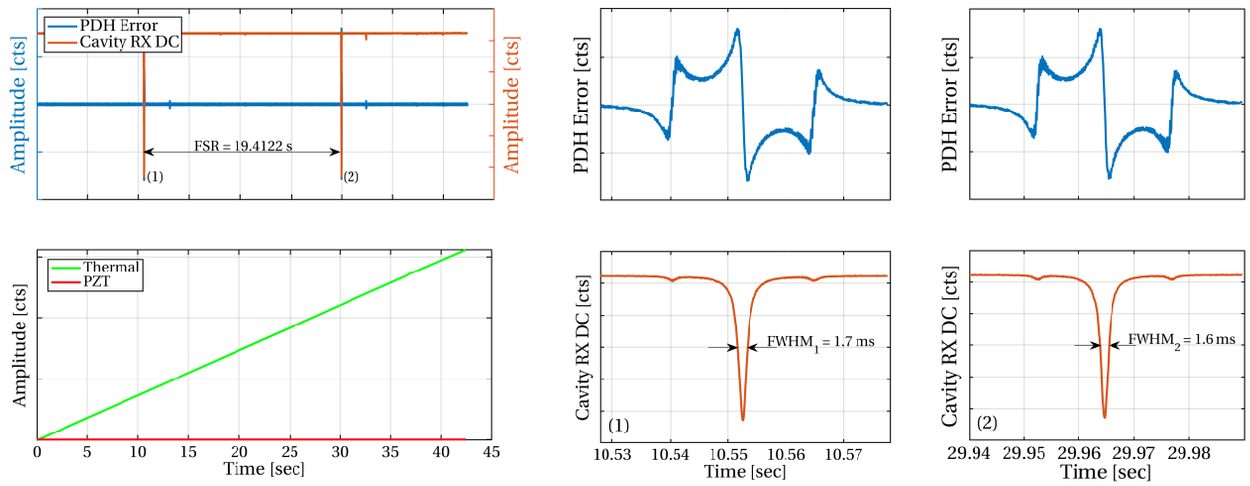

Figure 4.4.: Results of diagnostic scan type 1, a cavity scan on GF-1, based on file `GF1_NYA_20180611T201748_cavityScan_2.bin`. **Upper left:** PDH Error and reflected cavity power signals for the full scan duration. The resonances marked with (1) and (2) are shown on the right hand side. **Lower left:** Thermal ramp over the scan duration. PZT setpoint is constant zero. **Center:** PDH Error and reflected cavity power for the first resonance after roughly 10.5 s. **Right:** PDH Error and reflected cavity power for the second resonance after roughly 30 s. FSR: Free spectral range; FWHM: Full width at half maximum.

and evaluation of the minima, the thermal actuator is set to the temperature corresponding to one of the resonances and the PDH loop is started to keep the laser frequency close to this resonance.

From this scan, the finesse $\mathcal{F}$ of the cavity can be determined. The finesse is the ratio between the FSR and the Full Width at Half Maximum (FWHM) and is a quality indicator of a cavity. Here, for the two resonances, an estimated finesse of

$$\mathcal{F}_{\text{GF-1}} = \frac{1}{2}\sum_{i=1}^{2}\frac{\text{FSR}}{\text{FWHM}_i} \approx 11\,776 \pm 357 \tag{4.15}$$

is obtained, while the finesse on the other S/C is obtained in the same way as

$$\mathcal{F}_{\text{GF-2}} \approx 12\,091 \pm 378\,. \tag{4.16}$$

The errors have been estimated using Gaussian error propagation with a standard deviation $\sigma_{\text{FSR}} = \sigma_{\text{FWHM}} = 0.1\,\text{ms}$, which account for the finite sampling rate of this scan. These results are in good agreement to the finesse requirement of 10 000 (Thompson et al., 2011) and the measurements by Ball Aerospace using the cavity flight models, which gave $\mathcal{F}_{\text{GF-1}} = 11\,880 \pm 210$ and $\mathcal{F}_{\text{GF-2}} = 11\,811 \pm 139$ (priv. comm. V. Müller, AEI, 2019).

It should be noted, that the accuracy of these estimates, eqs. (4.15) and (4.16), is limited by the time resolution of this scan. Furthermore, it relies on the assumption that the lasers frequency changes linearly with the temperature. Hence, a qualitative conclusion can be drawn.

4.3. Triple Mirror Assembly (TMA)

4.3.1. TMA Properties

It is recalled, that the LoS between the two S/C is occupied by the MWI and the cold-gas tanks. Therefore, the beam needs to be routed around these parts, which is the task of the TMA. It introduces a lateral shift of the incoming and outgoing beam by 600 mm (Schütze et al., 2014b) and reverses the beam propagation direction. In principal, the TMA forms a cornercube. Because the variations of the beam path through this cornercube is highly restricted, only small sections of the three mirror planes are needed. Hence, the TMA is a called a virtual cornercube, whose vertex point, i.e. the intersection point of the three mirror planes, is outside the TMA itself.

The TMA has three important properties, that are preserved under rotation of either the TMA, or the incoming beam, around the vertex point of the TMA (Sheard et al., 2012). They are depicted in fig. 4.5.

1. The pathlength through the TMA, $\vec{r}_1+\vec{r}_2+\vec{r}_3 = \vec{r}_1'+\vec{r}_2'+\vec{r}_3'$, is exactly twice the distance, d, from the beam starting point and a plane which is normal to the impinging beam direction and crosses the TMA vertex.
2. The lateral offset, 2ℓ, is constant under rotations of the TMA and is symmetric w.r.t. an axis, that is parallel to the incoming beam and crosses the TMA vertex.
3. The outgoing beam is anti-parallel to the incoming beam, i.e.

$$\frac{\vec{r}_1}{|\vec{r}_1|} = -\frac{\vec{r}_3}{|\vec{r}_3|} \quad \text{and} \quad \frac{\vec{r}_1'}{|\vec{r}_1'|} = -\frac{\vec{r}_3'}{|\vec{r}_3'|}\,. \tag{4.17}$$

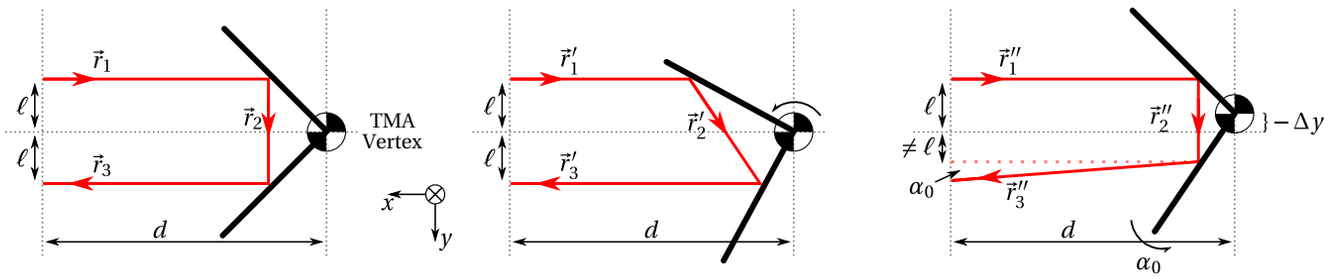

Figure 4.5.: Working principle of the TMA in 2D. **Left and center:** The total pathlength $2d$ through the TMA as well as the lateral offset 2ℓ are independent from rotations of the TMA around it's vertex. The outgoing beam is anti-parallel w.r.t. the incoming beam. **Right:** One mirror is misaligned by α_0 and the TMA vertex is shifted by $-\Delta y$. The misalignment causes a non-preserved total roundtrip length as well as a non-parallelism of the incoming and outgoing beams. The vertex shift changes the lateral offset ℓ.

If the TMA vertex point is co-located to the CoM of the S/C, which is the actual rotational pivot point, these properties hold for attitude variations of the whole S/C. However, these properties do not hold if the mirror surfaces are not perpendicular, or misaligned, see the right panel of fig. 4.5. The angular mismatch is attributed as the TMA co-alignment error.

4.3.2. Tilt-to-Length Coupling (TTL)

The requirements for the TMA in terms of the vertex position is ±100 µm around the S/C CoM in the pitch and yaw axes (Schütze et al., 2014b). However, in general the rotational pivot point of the S/C does not coincidence with the TMA vertex point and the properties listed above do not hold anymore. For a vertex point offset Δx in along-track, Δy in cross-track and Δz in radial direction, rotations around the CoM couple into the roundtrip pathlength of the TMA. This phenomenon is called Tilt-To-Length coupling (TTL) and is given by (Sheard et al., 2012)

$$\delta d = \left(\Delta x \theta_y - \Delta z\right)\delta\theta_y + \left(\Delta x \theta_z + \Delta y\right)\delta\theta_z \,. \tag{4.18}$$

Here, $\theta_{y,z}$ are static angular misalignment errors of the TMA w.r.t. the SRF and $\delta\theta_{y,z}$ are infinitesimal rotations in Pitch and Yaw. The static misalignment errors are in the order of mrad (Schütze, 2015), which sufficiently suppresses the along-track offset of the TMA vertex, Δx. Moreover, TTL does not depend on Roll rotations to first order. The error noise budget for the TMA is 21 nm/$\sqrt{\text{Hz}}$ (Ward et al., 2014), which makes TTL the second largest contributor to the LRI noise, after laser frequency noise (cf. section 4.2.1). For the full LRI setup, i.e. by considering both S/C and neglecting the suppressed along-track offset, Δx, the ranging error caused by TTL reads (Wegener et al., 2018)

$$\delta\rho_{\text{TTL}} = \sum_{i=\{y,z\}} \left(\zeta_{i,\text{GF-1}} \cdot \delta\theta_{i,\text{GF-1}} + \zeta_{i,\text{GF-2}} \cdot \delta\theta_{i,\text{GF-2}}\right) \,. \tag{4.19}$$

The prior misalignment offsets are expressed here as coupling factors, ζ_i, with the unit of µm/rad. They can be estimated by e.g. correlating the local S/C attitude angles, θ_i, with the ranging signal, ρ. This is actually done for short periods, during a so-called CoM calibration maneuver, in which the two S/C consecutively wiggle in all rotational degrees of freedom within short periods using the magneto-torque rods (Wang, 2003), which will cause ranging variations, if the coupling factors, ζ_i, are non-zero. The requirement for the two coupling factors is (ESA eoPortal)

$$\zeta_{y,z} < 200\,\mu\text{m/rad} \,. \tag{4.20}$$

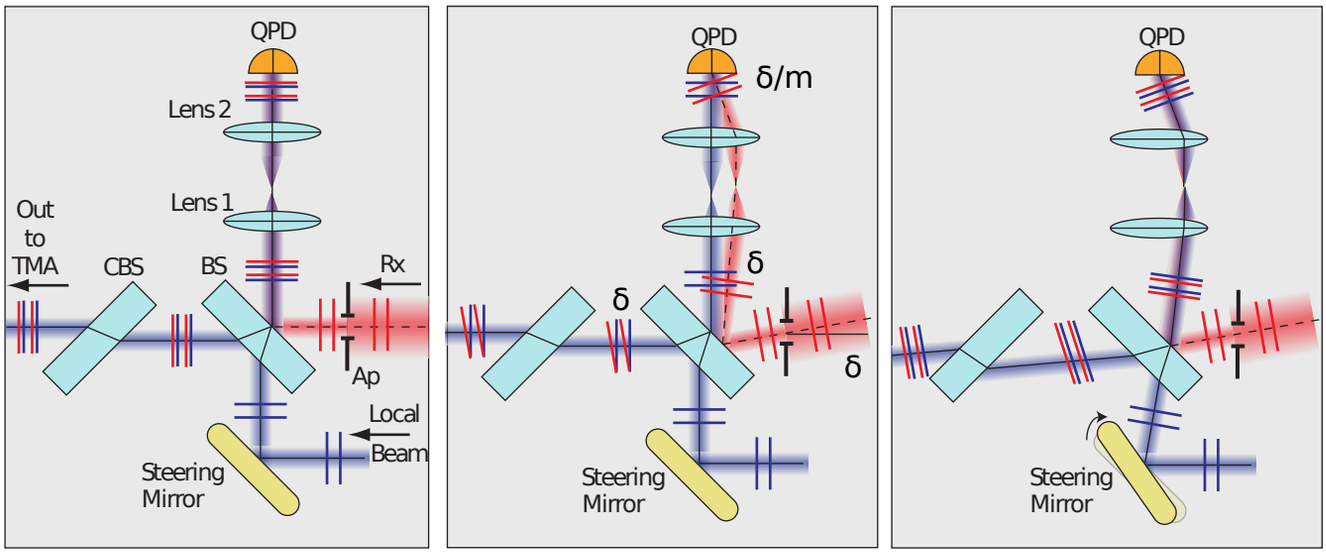

Figure 4.6.: DWS-FSM control loop working principle. **Left:** The incoming RX beam (red) and the local oscillator beam (blue) are aligned. Thus, the DWS signal is zero and the outgoing TX beam towards the TMA is parallel to the incoming RX beam. The combination of Beamsplitter (BS) and Compensation Beamsplitter (CBS) have a negligible influence on the beam alignment here. **Center:** The RX beam has a tilt of δ w.r.t the local beam, leading to an angle, δ/m with $m = 1/8$, on the QPD, magnified by the telescope (Lens 1 and Lens 2). The outgoing and incoming beam are not parallel. The tilt is measured by DWS. **Right:** The DWS control loop rotates the steering mirror in order to zero the DWS signal. This results in co-alignment of the local and the RX beam. Image and caption courtesy of V. Müller (Müller, 2017).

Apart from the vertex offsets, there are other sources of ranging errors. The beam walk on the last TMA mirror can, for a FSM walk of some hundred µrad, be given a numerical value in the order of mm, which is not negligible. The mirrors surfaces of the TMA are in general not perfectly planar and therefore change the properties of the wavefront. Furthermore, they might be not perfectly clean. Therefore, the mirror planarity and cleanliness do have impact on the beam's phasefront. The phasefront in the far-field will be investigated in section 6.5.2.

Misalignment of the three mirrors itself, and the corresponding distinction between the vertex point and the point of minimal TTL coupling (Schütze et al., 2014b; Müller, 2017), is not discussed within this thesis, however the numerical value for the TMA co-alignment error will be deduced later on.

4.4. Fast Steering Mirror (FSM)

The LRI setup requires a precise laser beam pointing w.r.t. the LoS. While the attitude accuracy of the AOCS is at ±300 µrad (ESA eoPortal), the LRI requirement is at 10 µrad (Schütze et al., 2014a) due to the finite divergence angle of the beam. Therefore, an active beam steering using the Fast Steering Mirror (FSM) is required. Steerable mirrors are widely spread for laser communication in space (Langenbach et al., 2005). The FSM can move in pitch and yaw direction with a magnitude up to several mrad to compensate for local S/C attitude jitter. The FSM was built by Airbus Defence and Space (Schütze et al., 2014a). The principle of the DWS-FSM feedback control loop, introduced now and depicted in fig. 4.6, holds for both S/C, regardless of their role as master or transponder.

The RX beam can always considered to be in direction of the LoS, as it is coming from the re-

mote S/C. It has an almost flat phasefront, perpendicular to the LoS. Therefore, to ensure the anti-parallelism of the TX beam utilizing the TMA properties, the local beam needs to be parallel to the RX beam before exiting the OBA (see below).

The DWS-FSM control loop continuously monitors the DWS signals, DWS_h and DWS_v, (cf. section 2.3) in two axes, horizontal and vertical. If the LO beam is not parallel to the RX beam, i.e. if the local S/C is tilted against the LoS by an angle δ, the DWS signals are non-zero (see center panel of fig. 4.6). This angle is magnified by the telescope on the optical bench, Lens 1 and Lens 2, by a factor of eight. Consequently, the FSM is actuated, which tilts the local beam, to again zero the DWS signals (right panel).

Another important reason for the FSM is the unknown misalignment of the LoS in the LOF w.r.t. the LoS in the SRF. They differ due to imperfect alignment of the OBA within the satellite body. The static angular offsets in horizontal and vertical direction, $DWS_{h,0}$ and $DWS_{v,0}$, can be compensated using the FSM. The process of estimating the horizontal and vertical offset angles is called initial acquisition, sometimes also initial LoS-calibration (Mahrdt, 2014). It is performed during the Dual-S/C checkout and is described in section 4.7.2. After applying these static angular offsets as the nominal setpoint for the FSM position, the LOF and SRF differ by a rotation around the LoS and a sign in z-direction (cf. section 3.4).

The FSM position is monitored using the Position Sensing System (PSS) with a resolution of 4 µrad. Another control loop, besides the DWS-FSM loop, uses the PSS and DWS readings as input to finely steer the FSM to the desired position. If the movement of the FSM is fast, the PSS readings are delayed a little w.r.t. the actual FSM position, because of the finite evaluation speed of the PSS readings. This delay is visible during initial acquisition, but can easily be corrected. During the normal science mode, the FSM movements are much slower. Nonetheless, the high FSM speed is needed to ensure a feasible acquisition scan time (cf. section 4.7.2).

Throughout this thesis, DWS_v and DWS_h denote the DWS signals by means of the phase difference of the two interfering beams. The DWS angles are denoted as α and β, cf. section 2.3. Those DWS signals can be converted to angles with a linear relation (cf. eq. (2.26)). Even if eq. (2.26) holds approximately, the DWS signals have been calibrated prior to the launch. The exact tilt of two interfering beams was actively controlled and the DWS signals evaluated. Afterwards, a linear relation of the conversion factors was derived. The measurements are given in table 4.2. The slope derived from a polynomial fit of first order on these measured data points gives the linear conversion factor from the DWS signals to DWS angles. Note, that the measured DWS signals need to be multiplied with 2π for conversion to radian.

S/C	**Angle**	**Commanded beam tip/tilt** [µrad]						
		0	16	33	50	66	83*	100
		Measured DWS signal [cycles]						
GF-1	Pitch (α)	0	0.07897	0.1634	0.2473	0.3268	0.4107	0.4952
GF-1	Yaw (β)	0	0.07732	0.1596	0.2424	0.3197	0.4020	0.4842
GF-2	Pitch (α)	0	0.08062	0.1656	0.2512	0.3318	0.4173	0.5029
GF-2	Yaw (β)	0	0.07732	0.1596	0.2424	0.3198	0.4020	0.4842

Table 4.2.: Measurements for DWS angle calibration. **Annotations:** *) This commanded wavefront tip/tilt was 83 µrad for pitch, 82 µrad for yaw.

However, one important convention needs to be considered. Due to the frequency ordering within the LRI, i.e. that the transponder laser has a higher frequency than the master, a sign needs to be taken into account. Therefore, whichever S/C is in transponder mode, has a negative coupling factor. The values in table 4.2 are given for the role as master. The angles can therefore be expressed in the following form.

$$\begin{pmatrix} \alpha_{\text{GF-1}} \\ \beta_{\text{GF-1}} \\ \alpha_{\text{GF-2}} \\ \beta_{\text{GF-2}} \end{pmatrix} = (-1)^R \cdot \begin{pmatrix} 31\,112.70\,\text{rad/rad} \cdot \text{DWS}_{\text{v,GF-1}} \\ 30\,562.49\,\text{rad/rad} \cdot \text{DWS}_{\text{h,GF-1}} \\ 31\,594.28\,\text{rad/rad} \cdot \text{DWS}_{\text{v,GF-2}} \\ 30\,563.73\,\text{rad/rad} \cdot \text{DWS}_{\text{h,GF-2}} \end{pmatrix} \tag{4.21}$$

Here, R denotes the role as a boolean operator and is $R = 0$, if the S/C is in master role and $R = 1$ for transponder role.

4.5. Optical Bench Subsystem (OBS)

The Optical Bench Subsystem (OBS) consists of two parts, the Optical Bench Assembly (OBA) and the Optical Bench Electronics (OBE). The OBA has two optical input ports, namely the fiber coupling adapter, that accepts the laser's light and the aperture, in which the RX beam is pointing. Furthermore, it has one optical output port, from which the light is going to the TMA. The OBE is responsible for the electronics, i.e. QPD measurements and FSM steering and therefore has the DWS signals as input for FSM steering and the QPD currents as outputs. The OBS is controlled by the LRP and the telemetry is routed through the LRP to the OBC.

One of the main tasks of the OBS is the imaging of the measurement signal, i.e. converting the optical superposition of the LO and RX beams on the QPD to an electrical signal. The QPD together with their pre-amplifiers are denoted as Quadrant Photoreceiver (QPR) subsystem. The measured currents of the four channels contain the phase information, which is retrieved within the LRP (see below). In fact, on each optical bench, there are two redundant QPDs. The OBE directly computes a sum over each corresponding segment of the two. This is called a channel. The distinction between segment and channel is not of greater importance for this thesis, the summation is always assumed to be the outcome of one single QPD. Afterwards, the signal is split into an AC and a DC part, of which the AC part contains the ranging information, while the DC part mainly contains the power of the LO, cf. eq. (2.20). Both signals are sent to the LRP to be processed further.

The frequencies for the LRI setup are arranged such that the beatnote frequency, f_{b} (cf. eq. (4.5)), on the master's PD varies between 4…16 MHz, which is also the bandwidth of the QPDs. Therefor, the offset frequency, $f_{\text{off}} = 10\,\text{MHz}$, for the transponder's frequency-offset DPLL is chosen such that it is larger than the maximal Doppler shift to avoid ranging ambiguities due to a zero crossing of the beatnote frequency (Schütze, 2015). This maximal Doppler shift (cf. eq. (4.2)) is equivalent to frequency variations of ±4.7 MHz, caused by the relative velocity between the two S/C of up to ±2.35 m/s on each photon path in the TWR (Mahrdt, 2014).

The other main task of the OBS is the steering of the beam. Either to align the TX beam w.r.t. the RX beam or to sweep the TX beam over a specific spatial region to make the acquisition process possible. For alignment, the LRP derives the DWS signals and those signals are send back to the FSM, which is then realigns the LO beam. This DWS-FSM control loop is further discussed below.

Minor tasks of the OBS comprise the QPD redundancy and the signal leveling, that is needed to convert the signal amplitudes from the LRP to the OBS conformal ranges. Furthermore, each QPD

channel get amplified individually by variable gains, using the Automated Gain Control (AGC). Therefore, the LRP i- and q-values need to be divided by these amplification factors, to derive the actual signal strength. The gains are changed only sparsely and in following sections, the i- and q-values are considered to have the gain correaction already applied.

4.6. Laser Ranging Processor (LRP)

The computing unit for the LRI is the Laser Ranging Processor (LRP). It has been developed and built by NASA/JPL (Bachman et al., 2017). The functionalities of the LRP include the phase measurement, the control of the laser, e.g. locking the frequency either to the cavity or via the frequency-offset DPLL, the DWS evaluation and FSM steering. A block diagram of the LRP and its interaction with the other parts of the LRI is shown in fig. 4.7. A closer look at the phase and angle tracking is shown in fig. 4.8.

Starting from the QPD on the OBA, where the heterodyne signal of the interfering RX and TX beams on the four segments is sensed, the signals pass an ADC converter within the LRP and reach the Phasemeter (PM), which is tracking the phase using a DPLL (see. section 2.5). From the phase measurements of the single channels, the DWS combinations are derived after a first decimation stage. The $\mathrm{DWS_h}$ and $\mathrm{DWS_v}$ signals, sampled at 10 kHz, correspond to the angular mismatch between the two interfering beams (cf. section 2.3). They are compared to the DWS setpoints, i.e. $\mathrm{DWS_{h,0}}$ and $\mathrm{DWS_{v,0}}$ to derive the error signals, which are then used for the DWS-FSM control loop. If the two DWS signals are zero, the two interfering beams are perfectly co-aligned on the QPD.

Another DPLL is running to derive the frequency of the sum channel, which is called the Phase-locker (PL) channel. This signal is, on transponder side, used to steer the laser frequency to the desired setpoint using the frequency-offset DPLL, see fig. 4.8. On master side, the PL channel remains unused, due to the PDH frequency lock. The difference is indicated by the switch in fig. 4.7.

One more important functionality of the LRP is the provision of data that can be used to calculate the Carrier to Noise Ratio (CNR), which is an indicator for the interferometric contrast, or, in other words, for the signal strength of the heterodyne phase detection. For this, an FFT algorithm is running continuously on the sum phase channel and stores the amplitude of the highest peak in the spectrum, called `fftSNR`. For noise estimation, the rms over the FFT amplitudes in the frequency bands between 8...9 MHz and 11...12 MHz, called `noise8_9` and `noise11_12`, respectively, are derived. They are downsampled by picking the last computed value at a rate of 0.1 Hz. Afterwards, they are reported as telemetry. The CNR is further investigated in section 6.3. The FFT is also used during link acquisition to determine, if the RX beam interfered with the local laser on the QPD. A description of the link acquisition process during the LRI commissioning is given in section 4.7.2.

4.7. Mission Timeline and Current Status

4.7.1. Launch and Early Operations Phase (LEOP)

The GRACE-FO satellites have been launched by SpaceX from the Vandenberg Airforce Base in California on 22$^{\mathrm{nd}}$ of May 2018 at 19:47 UTC (SpaceX, 2018). The payloads on board of the Falcon 9 rocket were five communication satellites by Iridium alongside the two GRACE-FO satellites. The GRACE-FO twin satellites were deployed about eleven and a half minutes after launch from the second stage of the Falcon 9 simultaneously, while the Iridium satellites have been deployed later. The orbit injection of the GRACE-FO satellites was in the required range of 490 ± 10 km and the inclination angle of

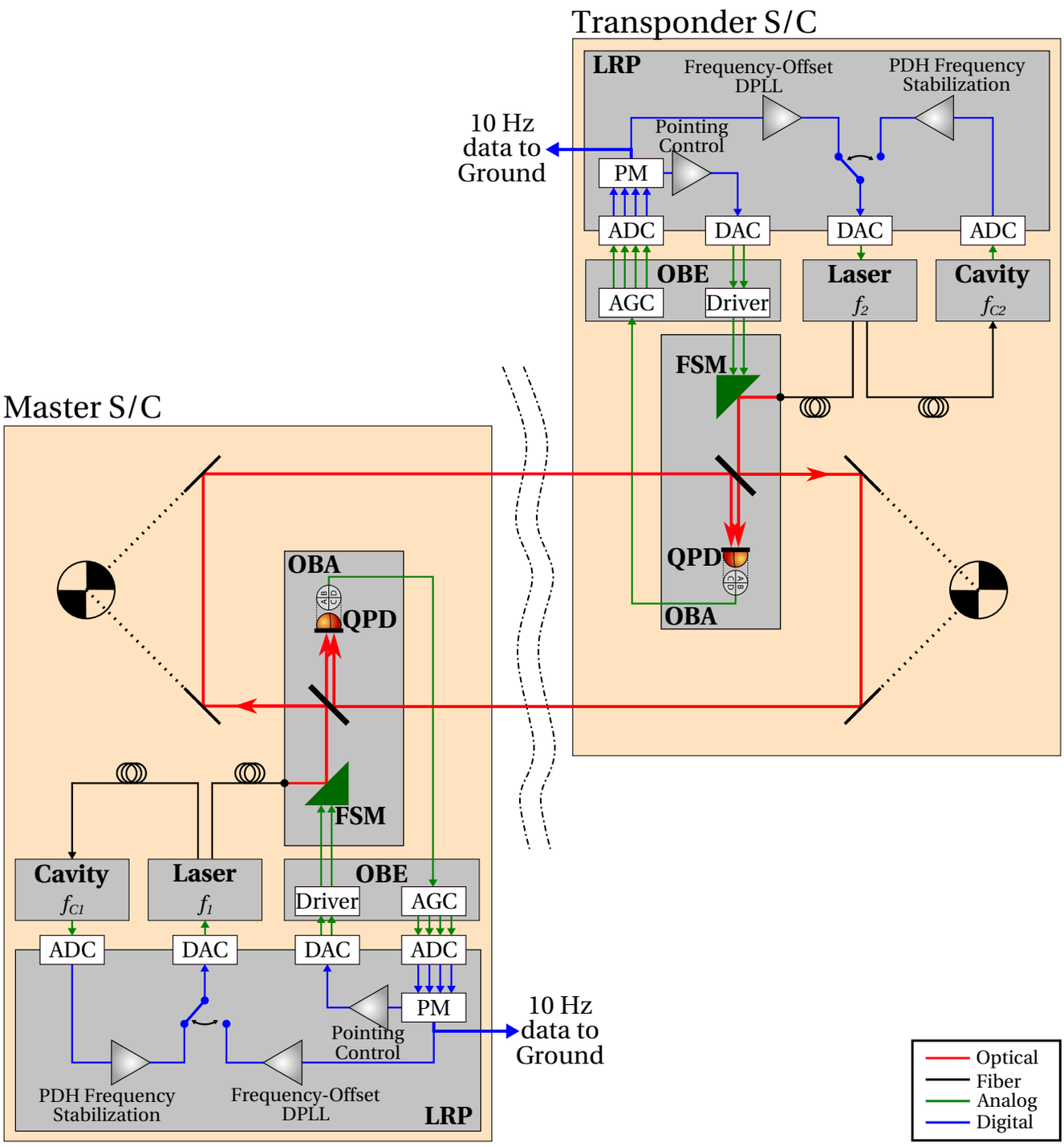

Figure 4.7.: Block diagram of the LRI components. The laser frequency is controlled either via PDH frequency stabilization or frequency-offset DPLL, depending on the S/C role. The interferometric signal, sensed by the QPD on the OBA is processed within the LRP. The redundant QPD on the OBA is neglected here. Image recreated from Bachman et al., 2017, Fig. 1 with minor changes, using the Component Library.

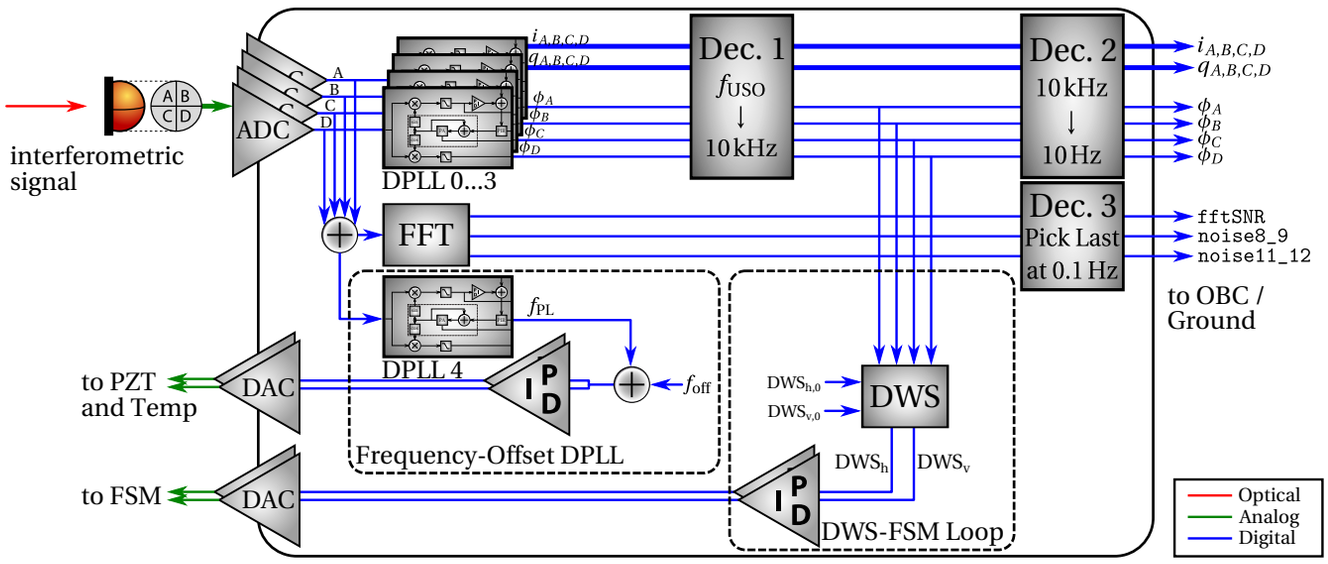

Figure 4.8.: Simplified block diagram of the frequency-offset DPLL and DWS-FSM control loop within the LRP for the transponder S/C. For the master, the frequency-offset DPLL is replaced by locking to the reference cavity using PDH technique (cf. section 2.4), which is not depicted here. The phase of the interferometric signal, sensed by the four QPD segments, is derived using DPLLs and decimated to 10 kHz. The DWS_h and DWS_v linear combinations are calculated and used as feedback for the DWS-FSM control loop. The second decimation filter produces the 10 Hz downlink signals of all quantities coming from the DPLL, which are then send to the OBC for ground station downlink. From an FFT instance, the amplitude of the highest peak, `fftSNR`, alongside noise estimates, `noise8_9` and `noise11_12`, are computed and downsampled for downlink. This downsampling simply picks the last calculated value at a rate of 0.1 Hz. A fifth DPLL derives the frequency, f_{PL}, of the sum channel, the so-called Phaselocker (PL) channel. The offset frequency, $f_{off} = 10\,\text{MHz}$, is added up and the resulting frequency is used as actuator signal for the PZT and thermal controllers to regulate the laser frequency. Image created using the Component Library.

89° has been met almost perfectly (GFZ-Potsdam, 2018). The DLR ground stations, used for satellite communication, established a connection to both satellites during their first orbit.

The early operations phase mainly consisted of attitude and orbit maneuvers, to get the satellites in a distance of 200 km, rotate one of them 180° around its z-axis and some instrument checkout procedures not connected to the LRI. After three days of increasing range and a little below the nominal distance of 220 km, the leading spacecraft, GF-1, slowed down to have the same velocity as GF-2, which is the trailing one. The wiggles in the range and the inter-satellite velocity in fig. 4.9 originate from orbital deviations. The range varies by several hundred meters during one orbit.

On 26th of May, the Launch and Early Operations phase was declared as completed. Until then, both satellites reached a stable orbit with a drift rate of 0.4 km/d and the USO (Ultra Stable Oscillator), GPS and the Microwave Assembly (MWA) were turned on (GFZ-Potsdam, 2018).

4.7.2. In-Orbit Commissioning Phase (IOC)

All other instruments, including the LRI are powered on during the In-Orbit Commissioning (IOC) phase. The commissioning of the LRI is described in the following sections.

Single-S/C Checkout

The LRI subsystems were powered on and checked out on 11th of June on GF-1 and one day later on GF-2. The team at the GSOC started with the so-called single-S/C checkout to ensure that all parts of the LRI are working nominally. The procedure comprises various diagnostic scans. Within the recorded data on both S/C, all units were found to be functioning. Thus, the acquisition procedure could be started.

Dual-S/C Checkout

In order to create a stable laser link between the two S/C, the beam pointing and laser frequencies must fulfill stringent conditions, cf. section 4.4.

On both S/C, the beam pointing in pitch and yaw direction of the outgoing beam is considered to be unknown, due to the imperfect alignment of the optical bench within the S/C body as well as alignment errors of the optical components and shifts during the rocket launch (Koch et al., 2018). Therefore, the outgoing beam of the LRI for a zero FSM position is in general not pointing in direction of the LoS, i.e. the LOF and SRF are misaligned. These offsets between the nominal optical bench axis and the LoS need to be smaller than 3 mrad (Ales et al., 2014). The four angular offsets, two per S/C, need to be estimated simultaneously. A remote beam's misalignment w.r.t. the LoS decreases the received power (cf. eq. (2.10)), while a local beam misalignment w.r.t. the received beam decreases the interferometric contrast (Mahrdt, 2014).

According to the bandwidth of the photoreceiver, which is limited between 4 and 16 MHz, the absolute laser frequencies, ν, of the two lasers must match up to $|\Delta\nu| \leq 15\,\text{MHz}$ to ensure that the interferometric signal can be sensed by the electronics (Mahrdt, 2014).

The so called initial acquisition scan is used to solve this problem of simultaneously estimating these five degrees of freedom, i.e. the pointing angles and the frequency difference $\Delta\nu$. It consists of two nested loops on the transponder S/C and a third loop on the master, cf. table 4.3. The outermost loop is a frequency ramp, that scans the transponder's laser frequency by changing the temperature of the NPRO. The temperature is changed at a rate such that the beatnote frequency sweeps over the QPR bandwidth once per master loop duration, i.e. once per 2×2D angular scans. The uncertainty of

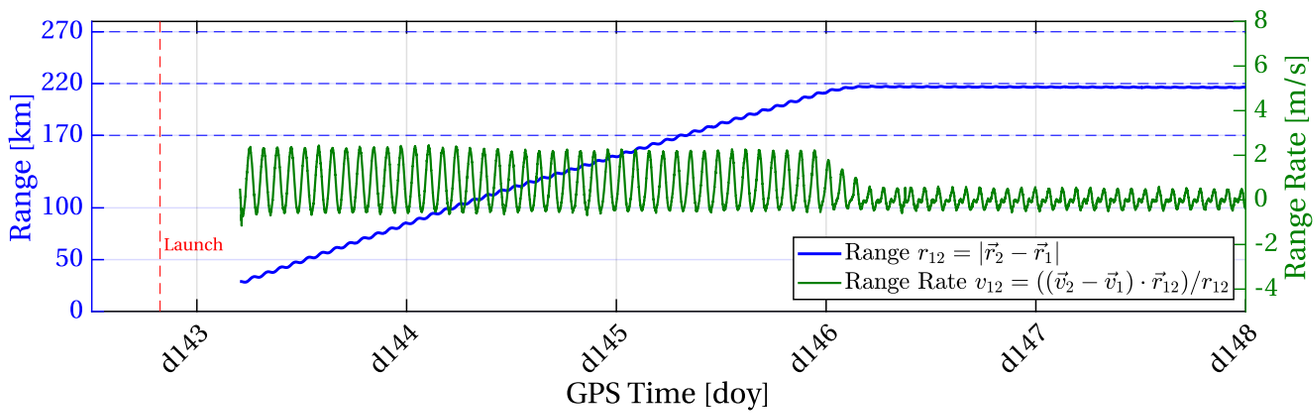

Figure 4.9.: GPS derived range (blue) and range rate (green) during LEOP, based on the GNV1A data product (see section 5.3). The positions, $\vec{r}_{1,2}$, denote the two S/C, while the relative velocity, or range rate, is the velocity difference projected on the LoS. The nominal range of $220 \pm 50\,\text{km}$ is depicted as the dashed blue lines.

	Frequency Scan	Slow Spatial Scan	Fast Spatial Scan
S/C	Transponder	Master	Transponder
Pattern	Linear Ramp	Hexagon	Lissajous
Type	1D, continuous	2D, discrete	2D, quasi-continuous
Speed	10.5 kHz/s	0.56 s hold time	≈2 Hz resp. 100 Hz
Loop Duration	8.5 hr	11.7 min	≈ 0.5 sec

Table 4.3.: Scan patterns during Initial Acquisition. The outermost loop is the frequency ramp (1-D) while the two other loops scan over the angles (2×2D).

the frequency offset is 320 MHz, which is over swept with 10.5 kHz/s, resulting in about 8.5 h for a full scan (Abich et al., 2019).

The spatial scans are realized using the FSM. On the transponder S/C, the fastest loop is performed, which is a Lissajous shaped scan pattern at 100 Hz and almost 2 Hz in the two axes, while the master's FSM scans a hexagonal pattern with increasing radius which consists of 1200 points and a hold time of 0.56 s per setpoint (Dubovitsky, 2016b). A guideline, how these scan patterns are realized onboard the S/C can be found in appendix A. The angles of the scan patterns are added to the reference directions during the scan, which are provided by the AOCS and describe the pointing error of the satellite w.r.t. the estimated LoS.

During these scans, the FFT within the LRP continuously computes spectra of the QPD samples such that every 100 µs a amplitude spectrum with a bin width of roughly 10 kHz is obtained. The LRP then applies a peak finding algorithm on these spectra. If a peak is exceeding a predetermined threshold, a heterodyne beatnote frequency was recorded, which means that all pointing and frequency requirements were fulfilled. The corresponding peak amplitude, laser frequencies and FSM excursion are stored and later down-linked to be analyzed on ground to determine the optimal parameters (Dubovitsky, 2016b; Abich et al., 2019). The analyzed initial acquisition scan, in terms of the angular offsets, of June 13, 2018 can be seen in fig. 4.10. Frequency offset results are not shown. The pattern agrees well with simulation results obtained by Mahrdt (2014): The '+'-shaped distribution of detected flashes originates from the slits in the QPDs. The transponders result shows two maxima, which arise from the delay between the FSM position, that was commanded as setpoint and the actual position, measured by the PSS, in the faster of the two Lissajous axes. This delay can be computed and corrected easily. The scans were performed twice, such that both S/C are in master and transponder role once. The magnitude of the pointing offsets derived from the two scans were all in the range of 0.5...1 mrad, the exact values are shown in table 4.4.

After uploading these offsets to both S/C, the LRI was booted into reacquisition mode with GF-2 as master and GF-1 as transponder. The reacquisition is a scan comparable to the initial acquisition but

Spacecraft	Pitch	Yaw
GF-1	-913.2	-691.1
GF-2	-446.6	-638.2

Table 4.4.: Angular pointing offsets as derived from the initial acquisition scans. All angles in µrad.

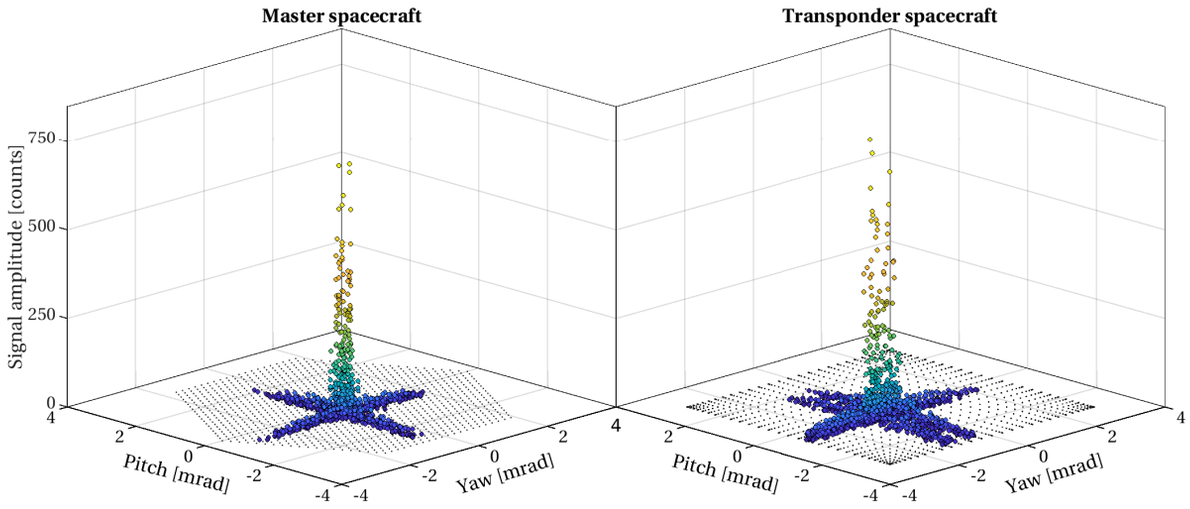

Figure 4.10.: Results of the first Initial Acquisition scan in terms of angular offsets. The z-axis and color represent the beatnote amplitude while the two angular offsets, pitch and yaw, between the FSM zero position and the LoS are on the x-y-plane. The black dots in the plane represent the angular setpoints of the scan patterns. **Left:** GF-1, which is in master role, scanning the hexagon pattern. **Right:** GF-2 being in transponder role, scanning the fast Lissajous pattern.

with reduced ranges for the parameter space. If a peak is detected in the FFT spectrum during this scan, the current FSM position is held and the LRP automatically switches to science mode, if the lock was successful.

On 14th of June 2018 at 13:23:35 UTC, the LRI went into science mode for the very first time after a short reacquisition scan. During the following days, a role swap was tried. Due to an operational mistake, it was not successful and it was decided to stay with the initial roles with GF-2 as master and GF-1 as transponder S/C. The longest contiguous segment in the first year of operation are shown in table C.1. The longest segment without interruption was longer than 55 days.

IPU Failure on GF-2

On 19th of July 2018, the IPU on GF-2 autonomously shut down due to an unexpected low current draw (NASA/JPL, 2018; Webb et al., 2018). The IPU is the primary processor and responsible for the MWI ranging data as well as for a precise timing and GPS navigation. Due to the anomaly, the AOCS on GF-2 left the normal fine pointing mode, which causes the LRI laser link to break down. Each S/C is equipped with two IPUs, of which one is redundant. It was decided to switch to the redundant unit, which was powered on in mid October 2018 (GFZ-Potsdam, 2018). Its behavior is nominal and the LRI was commanded back to science mode in mid December.

OBC Failure on GF-2

On 6th of February 2019, the OBC on GF-2 encountered an internal error, which is related to a bus communication failure (Webb et al., 2019). As a consequence, the science instruments were shut down. The MWI was turned back on in late February, while the LRI resumed the data collection on 18th of May 2019.

4.7.3. Science Phase

On 28th of January 2019, the IOC phase ended and the mission transitioned into science phase (GFZ-Potsdam, 2018). The first data was released publicly in late May 23, 2019 and started with data from May 22, 2018 (PO.DAAC JPL), including all data products except LRI. Those will follow in late July 2019.

5. Data Processing

5.1. SDS Data Products

The official data processing for GRACE and GRACE-FO is performed by the Science Data System (SDS), which is a distributed consortium at JPL, Center for Space Research at the University of Texas (CSR) and Geoforschungszentrum Potsdam (GFZ). The aim of the SDS is to receive, process and archive the science and housekeeping telemetry. Beginning from Level-0 telemetry, there are three more major levels of processing, shown in fig. 5.1.

Level-0 is the raw telemetry as downloaded from each spacecraft at ground station passes. Whenever the S/C fly over the virtual cone of a ground station antenna, used for up- and downlink by German Space Operations Center (GSOC), it is called a pass. There are mainly four ground stations used for the GRACE-FO mission, located in Weilheim and Neustritz (both in Germany, operated by Deutsche Luft und Raumfahrtgesellschaft (DLR)), McMurdo (Antarctica, as part of the NASA Near Earth Network (NEN)) and in Ny-Ålesund (Spitzbergen, operated by GFZ). The two DLR stations are used the most for regular downlink, while the others get involved by higher commanding duties. For each downlink pass, there are three new files per spacecraft: Science (Virtual Channel VC-4) and Housekeeping (HK) data (VC-2), which both contain data streams of the S/C payload, and OFFRED data, which contains telemetry from the S/C themselves. The two payload packets are called Level-0 data, which are the packages, the author of this thesis dealt the most with.

Furthermore, the Level-0 processing stage contains data of diagnostic scans of the LRI instrument. These scans are taken irregularly to observe specific data streams at higher sampling rates. Some of them will be utilized throughout this thesis. Those are briefly explained in appendix B.

The next data product is split into two parts, Level-1A and Level-1B. To compute Level-1A from Level-0 data, only non-destructive conversions are used, such as sensor calibration factors and conversions to engineering units. Some status flags about the data products correctness and integrity are added and the whole data gets reformatted from binary to ascii format to be processed further. For

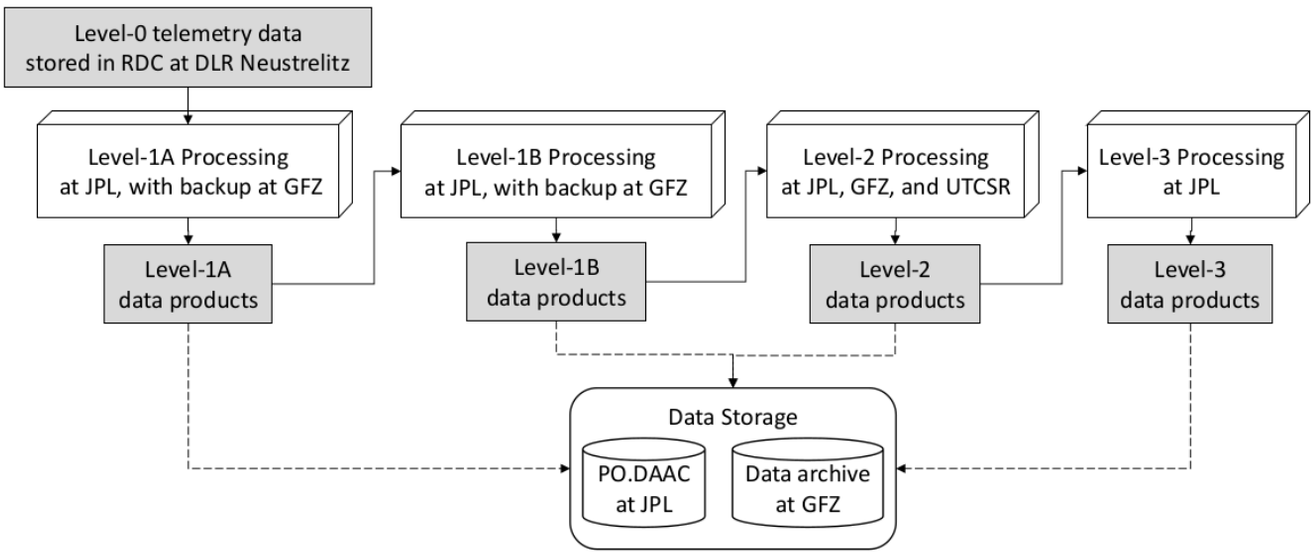

Figure 5.1.: Flowchart of subsequent SDS processing levels (Wen et al., 2019)

most data products, Level-1A has a higher data rate than the later processing levels. Level-1A was not publicly released for GRACE, but it will be for GRACE-FO.

In Level-1B data, the data streams are converted to the observables suitable to perform gravity field recovery. For example, ranging data is derived by converting the phase measurements of KBR and LRI into an inter-S/C range. This processing stage comprises resampling of measurements to GPS time with regular sampling, which accounts for USO drifts, for instance (cf. section 3.3). Moreover, the data is filtered and downsampled to handy rates for gravity field recovery. Thus, Level-1B is obtained through irreversible or destructive processing from Level-1A.

The Level-1 data was initially released on May 23, 2019 and thenceforward not later than 30 days after recording. Level-1 in general is a preparation stage for the higher data product levels.

The Level-1 data is delivered nominally on a daily basis, with approximately 50 Level-1 data files or products. A complete list of all data product types can be found in the Level-1 User Handbook (Wen et al., 2019). The data products contain data reaching from scientific instrument measurements (ACC, GPS, LRI, FSM, SCA, ...) over Timing Offsets (TIM, CLK, LLK), onboard mass variations (MAS) and thruster activations (THR) to tank temperatures and pressure (TNK). All products are reported for both S/C independently, except from KBR1B, LRI1B, PLT1A and LLT1A, which are derived from data of both S/C.

Level-2 and Level-3 are higher level data products such as Earth gravity potential (in terms of spherical harmonics), precise orbit solutions and mapping of this data to a geographical grid to produce gravity maps. These data products are planned to be released at least 60 days after recording (Wen et al., 2019). The gravity field recovery itself is beyond the scope of this thesis and thus these data products are not of further relevance.

5.2. Level-0 Data Processing

As shown in fig. 5.1, the raw telemetry called Level-0 telemetry, is stored at the Raw Data Center (RDC) at DLR, after it is downloaded from the S/C by the GSOC. The LRI team has access to both, Level-0 and Level-1 data. Besides using the Level-1 data products (see below), the LRI team is processing the Level-0 data by themselves, because firstly, there is much more information in it that is needed to characterize the instrument and understand its behavior in detail, especially diagnostic data. Secondly, the Level-0 telemetry is provided directly by DLR via an FTP server and therefore the time delay between the satellite downlink and the data availability is very short. One more major benefit of the raw data over the processed data is the pureness, because it is telemetry without ground processing. On the other hand, the time frame conversion of LRI data can be very challenging (cf. section 3.3).

For each ground station pass of a S/C, two new LRI related files are downloaded. They are split by their usage as science data or instrument housekeeping data. A third data type is the so called OFFRED data. The processing of Level-0 data within the LRI team at Albert Einstein Institute (AEI) is described in the next section.

5.2.1. gislparser Toolbox

During his thesis time, the author developed a MATLAB based toolbox in close collaboration with V. Müller. This toolbox is designated to do the ground-processing of Level-0 telemetry at AEI including some conversions and analysis aspects, as well as some monitoring capability. In the following, the main functionalities of the toolbox are listed and explained briefly, while the structure itself is described in the following section.

- **Autonomous Processing:** The toolbox automatically detects new downlinked files on the RDC FTP server, which are then downloaded and processed. This includes the LRI telemetry and OFFRED files.

- **Gap Detection**: During processing, all new files are analyzed for gaps in the telemetry. This is done individually for VC-2 and VC-4. Gaps may arise from reboots, missing telemetry packets, e.g. one line containing 30 samples of QPD phase measurements, or missing downlink files. In all cases, the current processing state is limited to the time of the gap. In case of a delay at the RDC, i.e. if a downlink file is missing and shared later, the packet gets processed later on. Other gaps need manual inspection and can be put on a whitelist to be ignored for further processing.

- **Accumulation:** The Level-0 telemetry is locally stored within daily accumulators. The downlink files in general have overlapping content and so have the locally stored daily files. Thus, simply stacking subsequent days of data is not feasible. Therefore, subroutines for accumulation of data are provided. These include Level-0 telemetry, OFFRED data as well as deglitched phase data (see below) and the official SDS data products, which are used frequently alongside the Level-0 data for analysis purposes and comparison, cf. section 5.3.

- **Eternal Data:** A few data streams, that are reported only sparsely, are accumulated and stored in an individual data file for the whole mission duration. These include datation reports, AGC gain changes, master and transponder role switches as well as information about LRP reboots. This grants an easy correction of e.g. AGC gains and datation reports.

- **Deglitching:** All QPD phase measurements get deglitched to remove phase jumps. Those phase jumps are explained in detail in section 6.2. The deglitched data is not only stored on a daily basis but also in chunks of ten subsequent days, providing a fast way for accumulation, without the need of merging to many files. Furthermore, within the creation of the long-term deglitched files, contiguous phase segments are identified. All segments since LRI commissioning are shown in appendix C.

- **Watchdog:** An independently running bash and MATLAB script is checking the data integrity. If specific data streams cross predefined boundaries, the processing did not produce new data for more than six hours or the LRI state switches out of the science mode, an e-Mail notification is sent.

- **Data Plotting:** The Level-0 telemetry is plotted directly after being processed. Therefore, we provide near-realtime plots of the LRI data streams. This includes all raw telemetry data streams which are referred as Level-0A. Also calibrated and converted plots, e.g. to derive engineering units are shown, referred as Level-0B. Furthermore, models of the absolute laser frequency estimates (cf. section 6.1) and the CNR (cf. section 6.3) are included alongside plots of diagnostic data, if those are present. All in all, the Level-0 plots comprise almost 140 plots, and another 60 plots for the OFFRED data, which are concatenated within two pdf files.

- **Status Page:** To keep track of the enormous amount of data, the first page of the concatenated Level-0 pdf file is a status page. It quickly informs about the current status of the processing, i.e. the time stamp of the last processed files for each S/C as well as the time stamps of the latest reboot. Also the current LRI mode is given. If this mode says “science”, the duration and corresponding number of orbital revolutions since entering science mode is given.

- **Remote Supervision:** To be able to monitor the LRI remotely, the concatenated plot files are uploaded to an AEI cloud service, known as wolke7, which is based on Nextcloud. The upload includes the latest three and eight days of Level-0 plots, latest five days of OFFRED plots and diagnostic scan binaries and their plots, if present.

- **Date Time Conversion:** We provide a comprehensive set of helper functions to convert between several time frames. This includes GPS time, GRACE GPS time, UTC time as six-element vector (year, month, day, hour, min, sec), Doy-Year as five-element vector (year, doy, hour, min, sec) as well as Julian date and modified Julian date. Also the correction of datation reports for each spacecraft can be done easily by using the eternal data file (see above).

- **Long Term Plots:** Beside the regular processing chain and it's Level-0A and Level-0B plotting engine, an extensive framework for long term analysis of arbitrary data streams is given. This include the so called arglat-plots, in which data can be plotted against the orbital position of the S/C and time. Accordingly, the considered data can be plotted along the ground track of the S/C. These two representations are helpful to identify repeating patterns in both, spatial and time domain, and will be used throughout the following investigations.

- **LTPDA:** We use the LTPDA toolbox (Hewitson et al., 2009) for spectral estimation, filtering and more.

All data investigations and plots of LRI data shown throughout this thesis are created using subroutines of this `gislparser` toolbox.

5.2.2. Structure of the gislparser Toolbox

Figure 5.2 shows a flowchart of the `gislparser` toolbox. The data from the satellites is downloaded and stored by the RDC of the DLR and is accessible by the LRI team at AEI. It is provided in a binary format, using the Packet Utilization Standard (PUS). It is a standard introduced by the European Space Agency (ESA) introduced to unify the telecommand and telemetry packets for applications in a wide range of space missions (Donati, 2001). Within this standard, a unique process identifier is connected to each application process. For example, the IDs for the LRI reach from 50 to 59, where 50 is used for Command and Control packets while the IDs 51 to 59 contain Science packets (Airbus Defence & Space, 2015). In order to further process the binary files, the PUS headers that belong to the LRI need

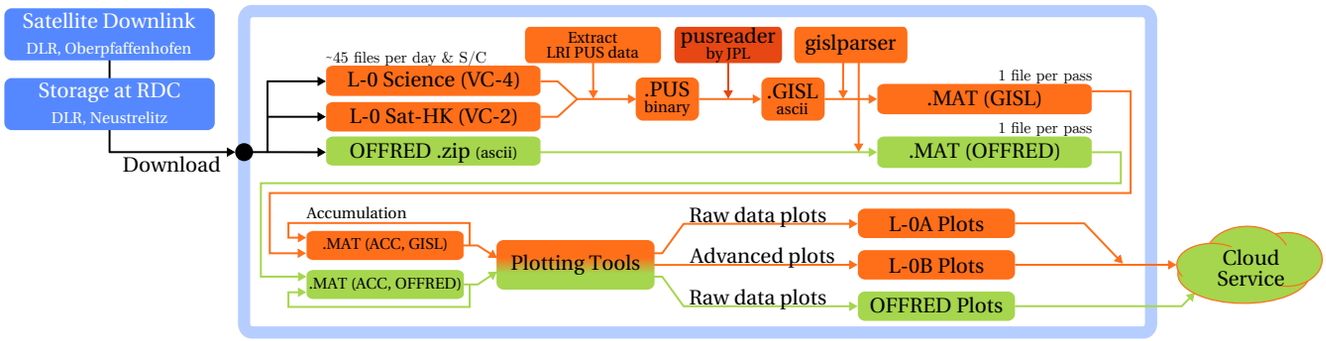

Figure 5.2.: Flowchart of the `gislparser` toolbox, the inside of the light blue box. Science and Housekeeping (HK) data processing steps are shown in orange, OFFRED data in green. The `pusreader` (red) is an external tool used.

to be extracted. This is necessary because the binary-to-text converter, provided by JPL to the LRI team at AEI, only processes LRI data. The so called `pusreader` is used, together with the LRI header information, to create so called `gisl` files. The `gisl` files contain science and housekeeping data in ascii format. It can then easily be parsed by using the so called `gislparser`, a MATLAB subroutine, that converts the text data to binary `.mat` files, which is the native format for MATLAB.

Another type of files provided by the RDC is the so called OFFRED data. It again contains housekeeping data. However, this data is not from a specific onboard instrument but from the S/C itself, like temperatures, voltages and currents. The processing of these files is much easier, because they are text-formatted tables.

For both types, `gisl` and OFFRED, one file is written per downlink pass. They are furthermore accumulated on a daily basis. Since the data of each pass spans about three hours, the daily assignment is based on the UTC downlink time and is not splitted at midnight. These daily files build the base archive at the AEI. They can easily be accumulated to larger time spans, e.g. three, five or eight days.

These accumulated files are then sent to the plotting engine. Here, all the data gets plotted for a quick overview of the data. A distinction is made between Level-0A and Level-0B plots. The former plots contain only raw data, including diagnostic data types if present, whereas the data for the latter ones has undergone some processing like merging different data streams, unit conversions, filtering or Phase Jump removal (see section 6.2.4).

In the end, the plots of diagnostic data (as it occurs), `gisl` data (for the last three and eight days) and offred data (for the last five days) gets upload to an AEI cloud service. In this way, a user-friendly monitoring of the LRI data streams and it's behavior is easily possible.

5.2.3. LRI Housekeeping Data

Non-science and auxiliary data gets stored within the Housekeeping packets. The main packets are listed below.

- **Event Report:** The event report packets are the LRP internal logbook and comprise various information, that are downlinked as they occur. These messages may be purely informational, warnings or even errors. Some of the reported values are listed below.
  - Mode state: science, acquisition, idle, diagnostic
  - Role: master or transponder
  - AGC gains for each QPD channel
  - Reacquisition data: FSM position alongside amplitude and frequency of a peak in the FFT spectrum during acquisition (cf. sections 4.6 and 4.7.2). Note, that data for the *initial* acquisition is downlinked as a separate data file.
  - File operations: Information about file writing, copying and deletion as well as loading of software images, update of parameters and more.
  - Boot messages
- **Health Monitor:** Data streams to calculate the CNR (cf. section 6.3), phase tracking information, i.e. i- and q-values, as well as for PDH loop monitoring. They are reported at a rate of 0.1 Hz.
- **Housekeeping Telemetry:** LRI mode, laser and FPGA state as in the event reports, but sampled regularly every 60 s.
- **Heartbeat:** Every 30 s, a single byte is sent to verify that the LRP is still online.

5.2.4. Science Data

The science data contains periodic reports of the main observables of the LRI. This includes the two main scientific signals, i.e. phase measurements of the QPD segments and the FSM angles, alongside others. The packets are listed below.

- **QPD telemetry:** 10 Hz data of unsigned 64-bit integer phase measurements. Tuples of 30 samples are reported every three seconds.
- **FSM telemetry:** 10 Hz data of FSM angles. Reported are the commanded position as well as the measured position by the PSS as unsigned 12-bit integer. A sign can be retrieved via the two's-complement. As for the QPD telemetry, tuples of 30 samples are reported every three seconds.
- **Laser Telemetry:** 1 Hz data of the laser state, i.e. the voltages and temperatures alongside the DC power of each QPD channel. These are reported as unsigned 12-bit integer. Furthermore, the control loop status of the thermal and PZT actuators (cf. section 4.2) are reported as unsigned 32-bit integer and can be given a sign using the two's complement. Tuples of 12 samples are downlinked at once.
- **ADC Samples:** The three packages above are only reported, if the LRI is in science mode. Therefore, the data for the laser and FSM are reported again with a lower data rate, i.e. once per 120 s. This ensures a monitoring without being in science mode. Alongside the already mentioned data streams, some voltages, temperatures and currents are monitored as well. They are downlinked as unsigned 12-bit integer, except the thermal and PZT loop data streams, which are unsigned 16-bit integers. The data is reported once per 20 s.
- **File Downlink:** The data recorded by diagnostic scans is downlinked as a file. These files are split in several parts, where each part contains up to 2 kB. A checksum is reported alongside to verify the file integrity on ground.
- **Directory Listing:** After every file write, uncompressing or deletion process, a directory listing should be requested to verify the successful completion of the process.

5.2.5. OFFRED Data

As mentioned above, the OFFRED data contains the satellite's housekeeping telemetry. Hence, this includes temperatures of the LRI subsystems, measured with sensors that are attached at the housings and controlled by the OBC. These sensors are basically on every part of the LRI, like the cavity, laser unit, OBS and the TMA. Voltages and currents of the LRI units can be monitored as well. Furthermore, GPS solutions, i.e. position and velocity of the S/C are given in various reference frames, as well as reference directions, which give the expected pointing direction, in which the distant S/C is anticipated to be. These data streams are not for scientific investigations but only for monitoring purposes.

5.3. RL00-Quicklook Conversion

During the commissioning and early science phase of the GRACE-FO mission, the SDS computed and distributed the mission data as a pre-release called Quicklook or RL00 (Release 00). The purpose of the data is two-fold. First ly, it serves as preparation and testing stage of the Level-1A and Level-1B data products at SDS. The gathered experience directly improves the first public data release. Secondly, it is distributed to the payload instrument developers to assess the functionalities and performance of

their payload instruments. Hence, this Quicklook data is used by the LRI team at AEI, including the author of this thesis, to characterize the LRI.

On 23rd of May, 2019, the first Level-1 data products for the GRACE-FO mission got publicly available as RL04. The published data begins on 22nd of May, 2018, i.e. directly after the launch of GRACE-FO. However, this does not include LRI related products, which will be released by end of July, 2019 (GFZ-Potsdam, 2018).

Each data product is an ascii file, with a YAML-formatted header and a tabular body. YAML is a human-readable data serialization language, designed to be used with a large variety of programming languages (Ben-Kiki et al., 2009). The file body contains the variables described in the header, one data set per line. The data products and their format is well described in the Level-1 data product user handbook by Wen et al. (2019). On nominal days of scientific measurements, the Level-1 data has a size of approximately 1 GB per day.

In order to use this data for analyzing the LRI behavior, another tool has been programmed by the author of this thesis using a combination of Perl and MATLAB. Perl is an open-source script language and is used because of it's high capabilities of string manipulations (Wall et al., 2000). In a first stage, a Perl script is interpreting the header and storing the ascii body in an intermediate csv file. In some cases there is a product flag at the beginning of each line, specifying the variables following in the line. This is especially used, if the data is repeating very often. In order to save memory, the repeating parts of each line are not stored every time, but only when they change. The Perl tool automatically interprets this product flag and fills the right table entries with data, leaving others empty. In that way, a complete array is written in the csv file, which can easily be interpreted by MATLAB. In the end, the data is stored on a local workstation in the binary `.mat` format. These data products are used by the LRI team at AEI.

5.4. LRI Related Level-1 Data Products

In this section, the SDS data products that contain the LRI data are briefly introduced. It should be noted, that these data streams are comparable to Level-0 data, which was introduced in sections 5.2.3 and 5.2.4. The following sections are based on the *GRACE-FO Level-1 Data Product User Handbook* in the version of May 21, 2019 (Wen et al., 2019) and the header information from the RL00 data.

In general, the Level-1A data products have the IPU receiver time as reference, while Level-1B is resampled to GPS time, see section 3.3.

LLG1A

The LLG1A package contains the log messages, i.e. event reports (cf. section 5.2.3). It is only available as Level-1A product. The log packets contain information about the top level state of the LRP, i.e. if the instrument is in science state. Parameter file writes, recordings of diagnostic data and instrument reboots are also logged here. This data product is event driven and has no fixed data rate.

LLT1A

To calculate the lighttime correction within the LRI1B product, the LLT1A package is used. It is done to compensate for the finite speed of light. In the above sections, especially in section 4.1.1, it is assumed that the S/C do not move during the flight time of a photon and it therefore accumulates twice the same Doppler shift. The computation of the lighttime correction now corrects for the relative velocity

of the two S/C during the photon flight time. Therefore, this data products provides the signal travel time for both directions, from the master to the transponder S/C and back, together with the inertial coordinates and velocities of both S/C at a rate of 1 Hz. The computation itself is beyond the scope of this thesis, hence the reader is referred to Müller (2017, chapter 2.5).

LHK1A/B

The LHK1A product contains housekeeping telemetry of the LRI. If the LRI is in science mode, the LHK package reports the data from the laser telemetry (see above). Otherwise, the ADC samples are reported. In the first case, the data rate is 1 Hz, otherwise it is once per 20 s. The difference between Level-1A and Level-1B is only the time-tag conversion to GPS time.

LRI1A/B

The main scientific data is packed in the LRI product. In Level-1A, this product contains the 64-bit phase measurements of all four QPD segments, splitted in upper and lower 32-bit numbers with a resolution of $1/(10\cdot 2^{24})$ cycles for the Least Significant Bit (LSB). One cycle can be given an equivalent account of the wavelength, e.g. 1064 nm. The 64-bit phase counts can easily be converted to cycles. Given the upper and lower 32 bits from the telemetry for each QPD channel, $\phi_{i,\mathrm{up}}$ and $\phi_{i,\mathrm{low}}$, where the i marks the four channels, the phase in cycles is computed as

$$\phi_i\,[\mathrm{cycles}] = \frac{2^{32}\cdot\phi_{i,\mathrm{up}} + \phi_{i,\mathrm{low}}}{10\cdot 2^{24}}\,. \tag{5.1}$$

Additionally, an averaged phase over the four segments is provided in double precision as well as the `fftSNR`, `noise8_9` and `noise11_12`. The latter three quantities originate from the health monitor (see section 5.2.3) and are used to compute the CNR, which is intensely studied in section 6.3. The phase is reported at

$$f_{\mathrm{USO}}/40\,000 \approx 9.664\,\mathrm{Hz} \tag{5.2}$$

with $f_{\mathrm{USO}} \approx 39\,\mathrm{MHz}$ as given in section 3.2.5. Therefore the `fftSNR` and noise levels, originating from ADC Samples at a rate of 0.1 Hz, are up-sampled by previous-neighbor interpolation to this rate.

For the LRI1B data product, the range and its first two derivatives are computed. They are given at a rate of 0.2 Hz in a combined data product for both S/C. Furthermore, a parameter for the light time correction is given (see the LLT1A data product above).

To verify the data, the conversion from phase cycles to range can be performed by subtracting the transponder's phase measurements, which approximately is a constant offset phase ramp corresponding to $f_{\mathrm{off}} = 10\,\mathrm{MHz}$ and then using a scale factor to derive the range (cf. eq. (4.9)). Additionally, the phase is averaged over the four QPD channels and the light time correction needs to be applied:

$$\rho_{\mathrm{LRI}}\,[\mathrm{m}] = \frac{1}{2}\sum_{i=0}^{3}\frac{\phi_i - 2\pi f_{\mathrm{off}}\,t}{4}\cdot\frac{c}{\nu} + \rho_{\mathrm{LTC}}\,. \tag{5.3}$$

Here, c denotes the speed of light and ν the frequency of the electromagnetic wave, i.e. of the light emitted by the master laser. The additional division by two arises from the conversion of a full-roundtrip range to the half-roundtrip range. It is advised to subtract the offset phase ramp in the 64-bit regime and then convert to floating point numbers, e.g. double, in order to not loose numerical precision.

The estimation of the correct scale factor, which is equivalent to the question of the absolute laser frequency, can be done in different ways. First, one can use a calibrated model for the frequency of the flight lasers. One could secondly cross-correlate the LRI range with the KBR range and estimate the scale factor. This is done by the SDS. A third method, which will be done during gravity field recovery, is to estimate the LRI scale factor by minimizing the post-fit residuals of the ranging signal. The first two methods are compared in section 6.1 while gravity field recovery using ranging data of the LRI is currently being performed.

LSM1A/B

The steering mirror data is provided in the LSM packages. The LSM1A data is sampled at 10 Hz and contains the state of the FSM (see section 4.4). There are four data streams, two per angle, which contain the commanded and the measured position. The sensing is done using the Position Sensing System (PSS) included in the FSM. The data streams have a resolution of approximately 4 µrad for the LSB.

The corresponding LSM1B data product contains the pointing angles, pitch and yaw, in the LOF in units of µrad. Again, the time tags are converted to GPS time for Level-1B.

LLK1B

The LLK1B product contains the offsets between the GPS and LRI time frames. In general, they have a bias and a drift. The drift is usually constant while the bias is reset whenever the IPU or the LRP reboot. To derive GPS time from LRI time, one needs to add the values contained in this package to the LRI time tags. In essence, LLK1B should be a combination of the CLK1B package, which gives the offset of the IPU receiver time w.r.t. GPS time and the datation reports of the LRP, which give the constant offset of the LRI time to the IPU receiver time. However, in RL00 and RL04, the timing offset is estimated by correlating KBR and LRI range measurements, since the KBR timing (IPU receiver time) is known. For more information, see section 3.3 on time frames.

6. Investigations

6.1. Determination of the Absolute Laser Frequency

The knowledge of the absolute laser frequencies of the two lasers is important for the ranging measurement, since it is needed for the conversion from the phase change $\Delta\phi$ and physical displacements $\Delta\rho$ cf. eq. (2.1). The motivation of a precisely known laser frequency, or wavelength, is given by fig. 4.3, where a frequency uncertainty of only 1 ppm results in equivalent ranging errors, that are reaching the LRI noise requirement, not only for the orbital periods but for large parts of the gravity signal's frequency band.

6.1.1. Calibrated Frequency Model

As introduced in section 4.2.2, the absolute laser frequencies for both S/C $\nu_{\text{GF-1}}$ and $\nu_{\text{GF-2}}$ can be modeled linearly (cf. eq. (4.14)) using the laser setpoints (thermal and PZT) and temperature information. These estimates of the absolute laser frequency for both S/C have been investigated for almost one year in orbit, of which in approximately five month the LRI was in science mode. By this analysis, the reliability of the frequency model should be confirmed, i.e. if the model's coupling factor in table 4.1 are valid and give physical results. The absolute frequencies for both S/C are shown in fig. 6.1. Four major periods are marked. In the first two periods, GF-2 acts as master S/C. Both segments show a lower absolute laser frequency than the last two segments, where GF-1 is in master role. This can be related to slightly different lengths of the cavities on the two S/C. Moreover, the SDS estimate of the laser frequency, which can be calculated using the LRI1B data product (see section 5.4) and the β-angle are shown, however, they are discussed later.

In general it is evident, that the frequency models for the two flight lasers are in good agreement among each other. The traces shapes follow each other closely. Only in the last period (4), the frequency of GF-2 is increasing significantly faster than the frequency of GF-1. However, the two frequencies only differ by a few MHz, which is well below the model's accuracy of ±60 MHz.

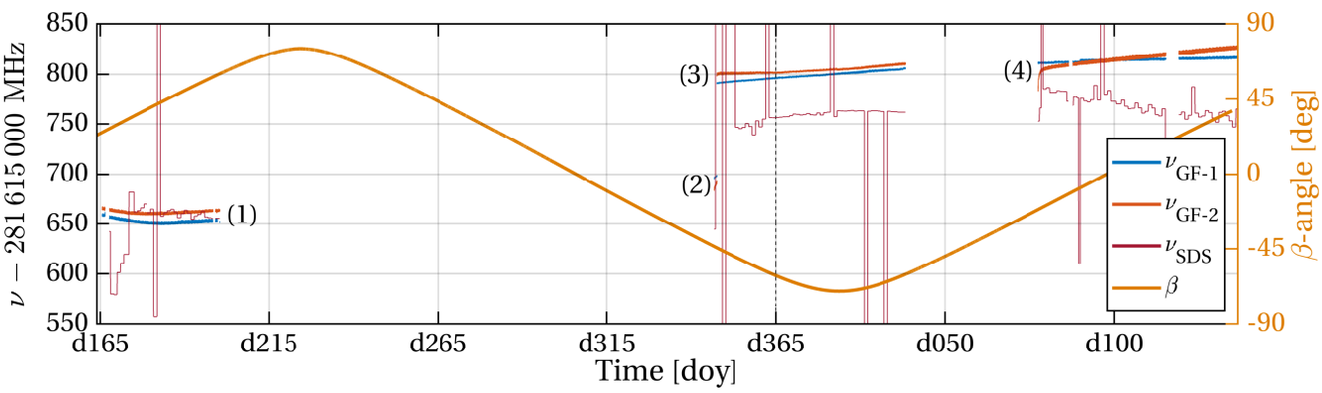

Figure 6.1.: Absolute laser frequency of both S/C using the calibrated model alongside the SDS estimate. Four periods are distinguished. (1): June/July 2018, GF-1 is master. (2): One day in December 2018, GF-2 is master. (3): December 2018/January 2019, GF-1 is master. (4) March to May 2019, GF-1 is master.

A dedicated visualization of the master laser's frequency, plotted against the argument of latitude and time, is shown in fig. 6.2a. Note the different color bars to account for the different frequencies between the three larger periods. For the later two periods of the data, GF-1 was in master role. Within each period, orbital variations of a few MHz are clearly visible. They are caused by temperature variations at the TRP, that couple into the frequency model. Within a ranging ASD, they will manifest as higher amplitudes at the orbital frequency and it's higher harmonics. However, as introduced in section 4.2.2, the coupling factor for the TRP has the largest uncertainty.

Not only the master laser's frequency but also the transponder laser's frequency and thus the frequency difference can be determined by the model. This difference $\nu_T - \nu_M$ is shown in fig. 6.2b. If the model was perfect, this difference is expected to be the offset frequency of 10 MHz plus one-way Doppler shift. However, because of the wavemeter uncertainty and the model's inaccuracy, the frequency difference does not perfectly represent the beatnote frequency as derived from phase measurements. Nevertheless, it gives a rough estimate about the relative stability and accuracy of the coupling factors. The orbital variations, which are caused by temperature variations in the difference time series, are reduced since they are common mode on both S/C.

In general, the obtained values are close to the expected value of approximately 10 MHz, and do not differ more than 25 MHz, which is below 0.1 ppm ≈ 30 MHz. Furthermore, all of these variations can be deduced to the ±60 MHz uncertainty of the wavemeter, that was used for calibration (Müller et al., 2017b).

The first period shows about −10 MHz and is rather constant. The second period is too short to be investigated, however, in the third period, the difference frequency is decreasing from 10 MHz to roughly 5 MHz. The fourth period spans a range from −5 to 12 MHz. During this period, the frequency of the master unit, GF-1, was quite stable but the transponder, GF-2, shows a larger drift, which is connected to a drift in the Therm_{IL} values in the telemetry, which increases by about 0.01, corresponding to a frequency shift of $0.01 \cdot c_{\text{Therm,IL,GF-2}} \approx 11$ MHz. All other quantities stay fairly constant. A preliminary explanation for the overall drift of the laser frequency estimates is aging of the NPRO crystal, whose output frequency is assumed to change over time (priv. comm. R. Spero, NASA/JPL, 2019).

Especially notable is the trend of the frequency difference in the periods (3) and (4), which closely follow the evolution of the β-angle, shown in figs. 6.1 and 6.2c. The β-angle describes the orientation of the orbital plane w.r.t. the sun position. If this β-angle is zero, the vector, pointing from the earth to the sun, lies within the orbital plane. In this case, the satellites spend the largest amount of time in shadow, approximately 36 min. If the magnitude of the β-angle is larger than 68 degree, the satellites do not transit into the shadow of the earth at all. Though, an orbital periodicity of the thermal conditions is still present due to the differing satellite surface's orientations w.r.t. the sun. The β-angle has impact on the whole thermal environment of the S/C and therefore on several onboard systems (Fulcher, 2016). Further conclusions on this correlation can be done when more data is recorded, hence it will be done in the future.

The frequency stability is achieved by locking the laser frequency to a resonance frequency of the reference cavity using the PDH technique (cf. section 2.4). Variations in the cavity length, for instance through thermal expansion, can alter the frequency. Some preliminary analysis showed no enhancement, by means of reduced orbital variations, when introducing a coupling factor for the cavity temperature in the frequency model (cf. eq. (4.14)).

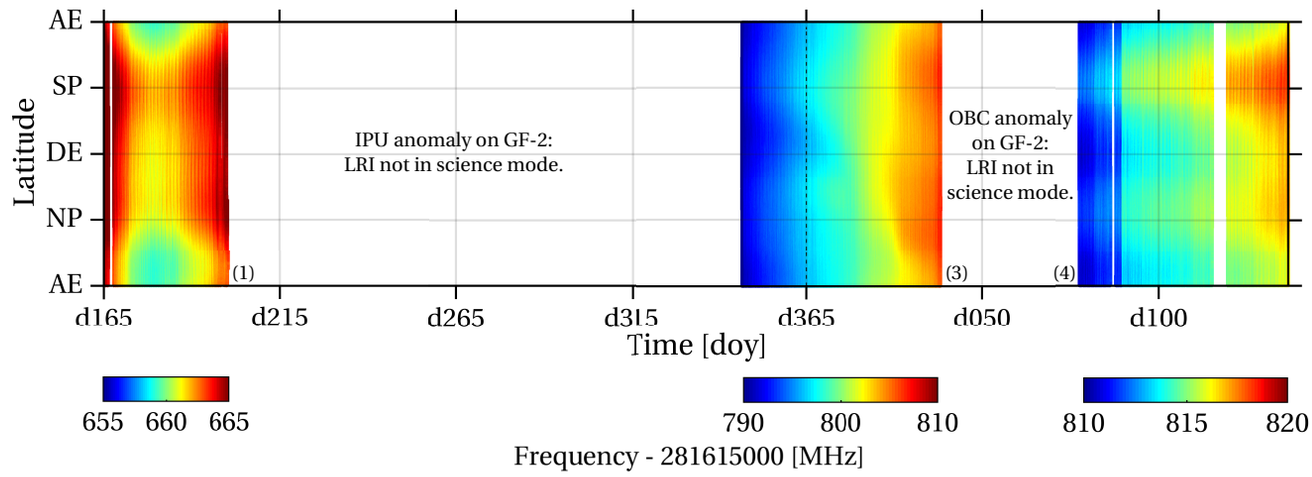

(a) Estimated laser frequency of the master S/C, i.e. GF-2 for period (1), GF-1 for the two periods (3) and (4). Different colorbars for each of the longer periods are used to maintain the visibility of the orbital variations, once to twice per orbital revolution and of the overall drift.

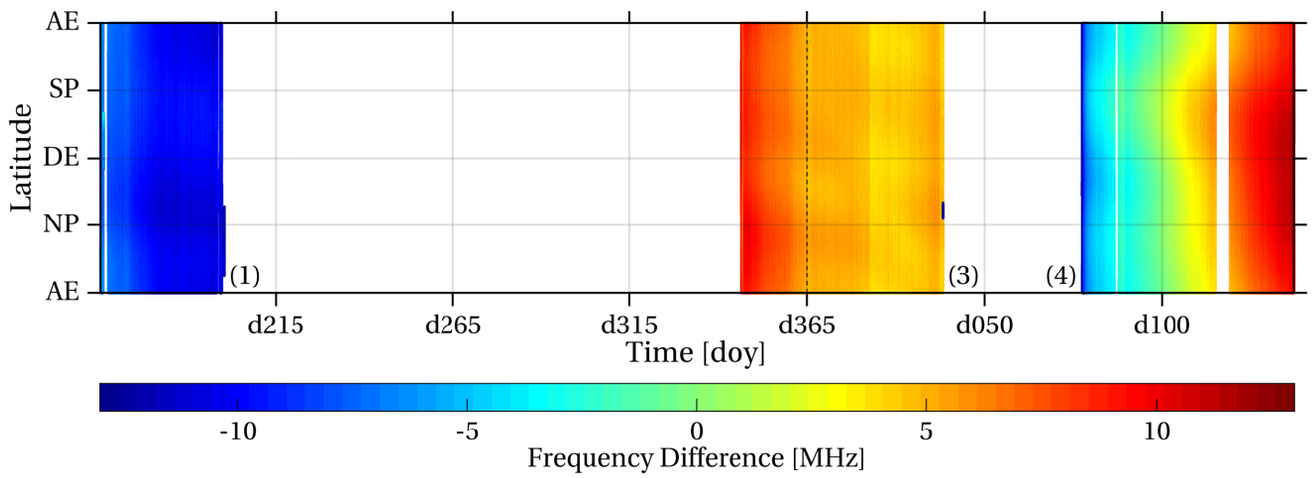

(b) Laser frequency difference $\nu_T - \nu_M$. T and M stand for transponder and master role, respectively.

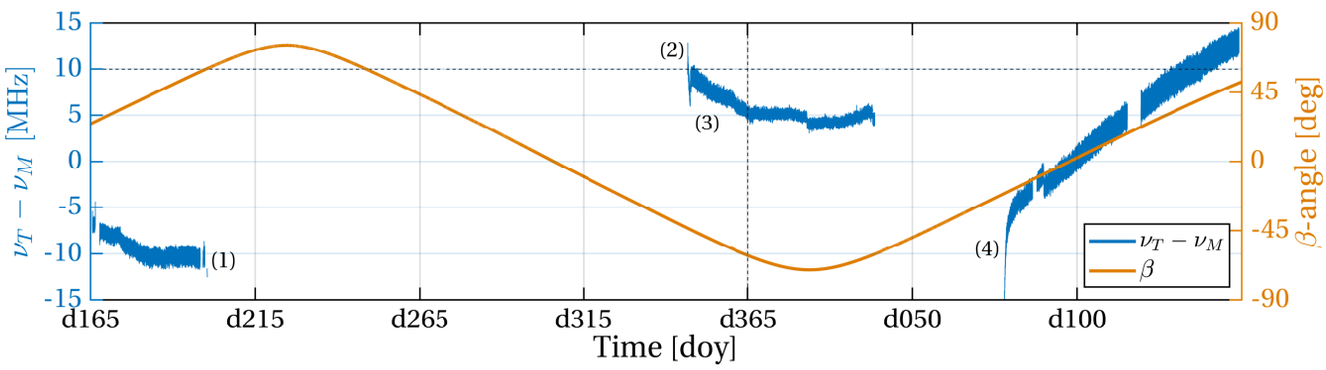

(c) Laser frequency difference $\nu_T - \nu_M$ plotted alongside the β-angle. The orbital plane is derived using the centroid of the two S/C, the solar coordinates are computed by using a simple estimation formula, see e.g. Montenbruck et al. (2000) and Van Flandern et al. (1979). The horizontal dashed line indicates the expectated offset frequency of 10 MHz

Figure 6.2.: Upper: Absolute laser frequency variations of the master S/C. **Center:** Difference of absolute transponder and master frequencies $\nu_T - \nu_M$. **Lower:** Another representation of the difference frequency alongside the β-angle between the orbital plane and the sun position for almost one year of operation.

6.1.2. SDS Method: Cross Correlation

The SDS does not use the LRI telemetry to estimate the frequency, but computes a cross-correlation between the LRI and KBR ranging measurements once per day to estimate the scale factor s. The absolute frequency is computed as

$$\nu_{\mathrm{SDS}} = \nu_{0,\mathrm{SDS}} \cdot (1 - s) \tag{6.1}$$

$$\text{with} \quad \nu_{0,\mathrm{SDS}} = 281\,614\,800\,\mathrm{MHz}\,. \tag{6.2}$$

The scale factor s is reported in the LRI1B data product (cf. section 5.4) for the S/C in master role, which is sufficient. By doing the cross-correlation other error sources, such as tone errors in LRI or KBR can falsify the scale factor. The accuracy of the KBR ranging depends on the KBR scale factor, which is derived from the KBR frequencies and the underlying USO frequency. The drifts of the USO are determined w.r.t. GPS.

Since this cross-correlation method does not rely on the laser telemetry, knowledge about time variability of the calibrated frequency model's coupling factors is not needed. They might change in space due to the different environmental conditions. Even if the wavemeter, that was used for the model calibration, directly removes atmospheric effects of the local temperature and air pressure, it does not hold perfectly, since GRACE-FO is orbiting in a LEO which still has a non-negligible atmosphere. The laser frequency may also be dependent on the actual atmospheric density. Therefore, the temporal stability of the model can not be granted and should be kept under surveillance. Therefore, the SDS cross-correlation method can be regarded as an independent estimate for the laser frequencies, which can be used in comparison to the calibrated model. However, the estimation rate of the the scale factor is only once per day, which does not allow for measurements of orbital variations. These may originate from thermal conditions due to sunlight and shadow transitions.

The SDS laser frequency ν_{SDS} and the calibrated models $\nu_{\mathrm{GF\text{-}1}}$ and $\nu_{\mathrm{GF\text{-}2}}$ are shown in fig. 6.1 and in general, they seem to fit well. For period (1), they almost show the same trace, while for the periods (3) and (4), they differ by about 50 to 70 MHz at maximum, which still can be deduced to the wavemeter uncertainty of 60 MHz. However, the SDS frequency estimate shows outliers on some days, which are connected to IPU reboots and a corresponding error in the cross-correlation (priv. comm. R. Spero, NASA/JPL, 2019). Furthermore, it shows some oscillatory patterns, especially in period (4). During

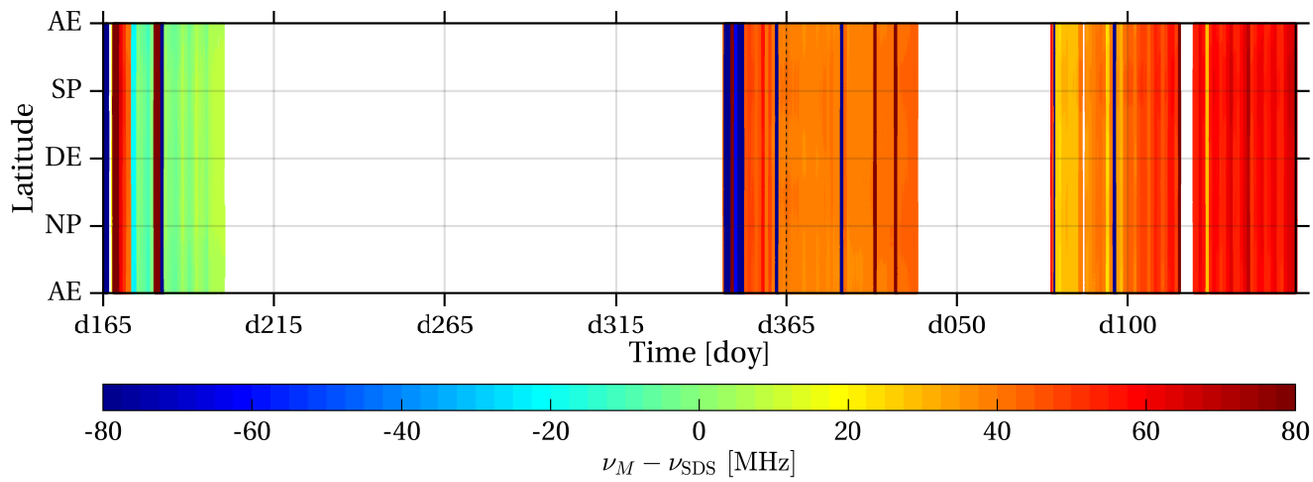

Figure 6.3.: Difference of the calibrated laser frequency model and the SDS estimate $\nu_M - \nu_{\mathrm{SDS}}$. Individual traces shown in fig. 6.1.

period (3), the offset between the two estimates is almost constant, while in the fourth period they show contrary trends. The difference of the master S/C frequency using the calibrated model and the SDS estimate is shown in fig. 6.3. For most of the time, they agree up to ±60 MHz, which again can be associated with the wavemeter uncertainty. However, the agreement was best in the first period of LRI data in June and July 2018 while for later periods, the frequency estimate using the calibrated model is about 50 to 70 MHz above the SDS result.

6.2. Phase Jumps

The ranging signal provided by the LRI is in good agreement to the KBR ranging (Abich et al., 2019, Fig. 4). However, when looking in detail, there are jumps in the biased LRI range, that can not be caused by gravitational or non-gravitational accelerations. These Phase Jumps (PJs), or glitches, occur in both, master and transponder phase measurement. Their shape can be modeled as a step function in the ranging phase, filtered by the decimation filter used within the LRP to derive the 10 Hz phase data for down link (cf. fig. 4.8). They have the same amplitude within both phase measurements. PJs can easily be identified by analyzing the transponder's phase, which nominally is a phase ramp corresponding to the 10 MHz offset frequency. The PJs stand out as steps after the removal of the phase ramp. Most of these steps have a magnitude lower than 30 cycles, which corresponds to a longitudinal pathlength signal of about 15 µm for the half roundtrip. An exemplary PJ is shown in fig. 6.4. It is extracted from the transponder phase and has a magnitude of roughly 6 cycles.

The following two sections concern the physical origin of these PJs and the removal in post-processing using data solely from LRI.

6.2.1. Physical Origin of Phase Jumps

A hint, where the PJ might come from, was given by the satellite's geographical position at the occurrence of a PJ. Most of them were observed near the geomagnetic equator. Shown in fig. 6.5 is the satellites ground track for about ten days in June and July 2018 in red, while white crosses indicate a step in the transponder phase, as shown in fig. 6.4. The background coloring shows the inclination angle of the magnetic field lines. The inclination is the angle between the field vector and a local horizontal plane, which is defined via the WGS84 ellipsoid (Chulliat et al., 2015). Near the geomagnetic equator, the satellites magneto-torque rods for controlling the roll angle have no effect, since the magnetic field lines are parallel to the roll torque (Herman et al., 2004). Thus, the AOCS needs to activate

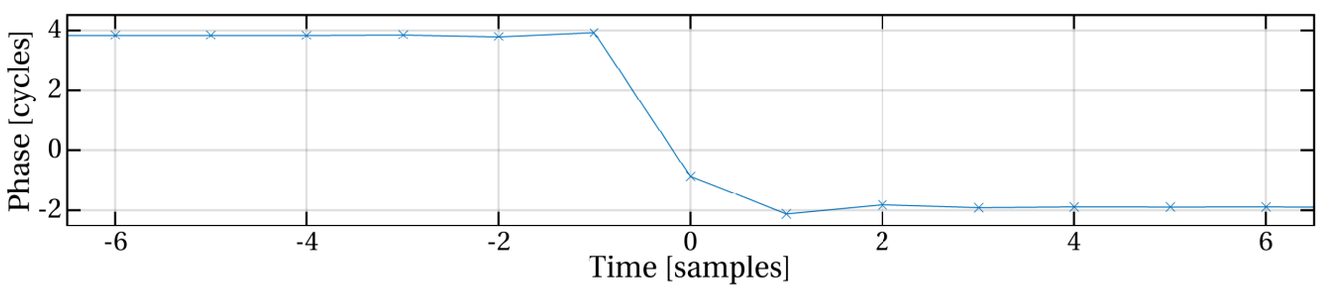

Figure 6.4.: Exemplary PJ in the transponder phase with a magnitude of approximately 6 cycles. Since they stand out clearly, they can easily be identified. The direction of the PJs, if up- or downwards, is random.

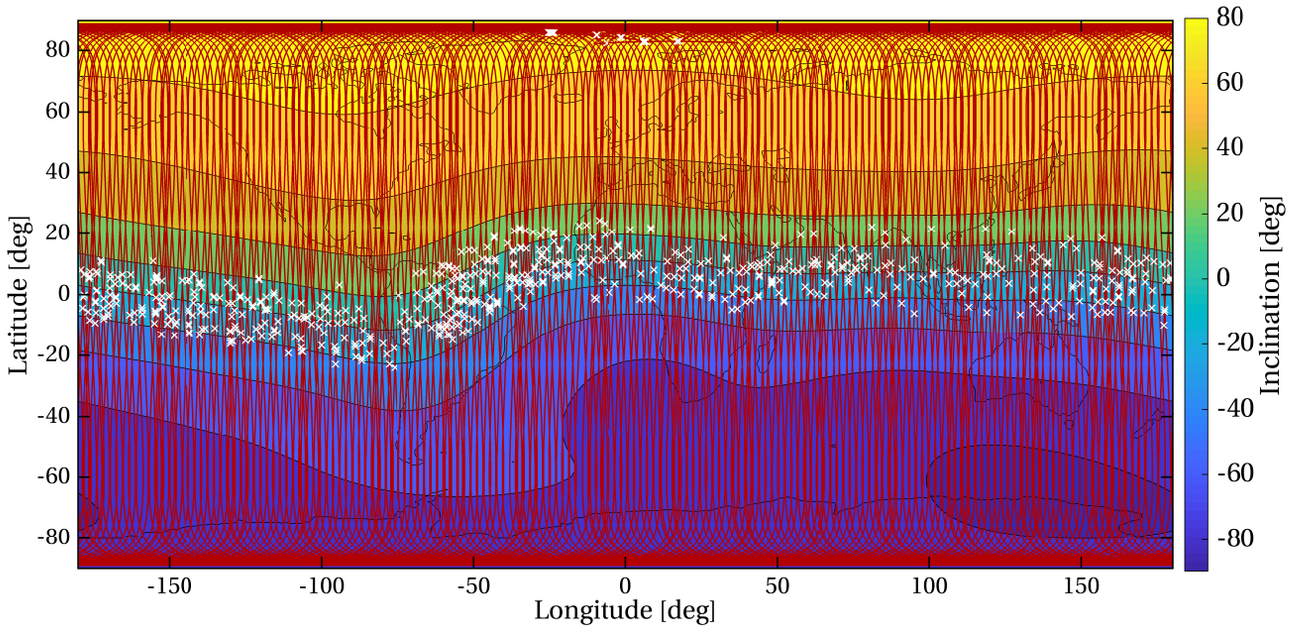

Figure 6.5.: Distribution of Phase Jumps on a map. The red line is the groundtrack of GF-1 between 2018-06-23 and 2018-07-05 while the white crosses indicate a step in the transponders phase ramp (also GF-1), that is larger than a predefined threshold. The background coloring shows the main magnetic field inclination angle and is taken from the World Magnetic Model of 2015 (WMM, Chulliat et al. (2015)) at an Altitude of 450 km.

a roll thruster. Therefore, most of the roll thruster events are located near the geomagnetic equator. Additionally, it can be concluded that the roll thruster activations produce the largest PJ, since the PJ near the geomagnetic equator appear most frequently for the chosen threshold. Only a few white crosses are located at the north pole, where the magneto-torque rod in yaw direction has no effect (Herman et al., 2004).

The physical reason for these jumps is likely a mechanical coupling between the laser crystal and the satellite platform, which vibrates upon thruster usage. A closer investigation of the coupling of thruster firings into the ranging phase is presented in this section.

Since most of the PJs occur at a geographical location along the orbit, the LRI team was able to schedule diagnostic scans when the S/C pass this region. A diagnostic scan is a recording of data with a higher sampling rate than in nominal operation. There are several different types of scans, that provide different data sets. For the analysis of the phase jumps, two types of scans are especially relevant: Diagnostic scan type 1 and type 7.

6.2.2. Diagnostic Scan Type 1: Cavity Data

Scan type 1 records cavity data at a rate of

$$f_s = f_{\mathrm{USO}}/4000 \approx 10\,\mathrm{kHz}\,. \tag{6.3}$$

The exact scan length can be computed via the total memory limit for the scan, which is 4 MB, and the size of an `uint32` number, which is 4 B. Thus, the scan duration is $4\,\mathrm{MB}/(2 \cdot f_s \cdot 4\,\mathrm{B}) = 51.74\,\mathrm{s}$. The division by two arises from the number of recorded quantities, which are the PDH error signal and the DC power reflected by the cavity. The PDH error signal is a measurement for the mismatch

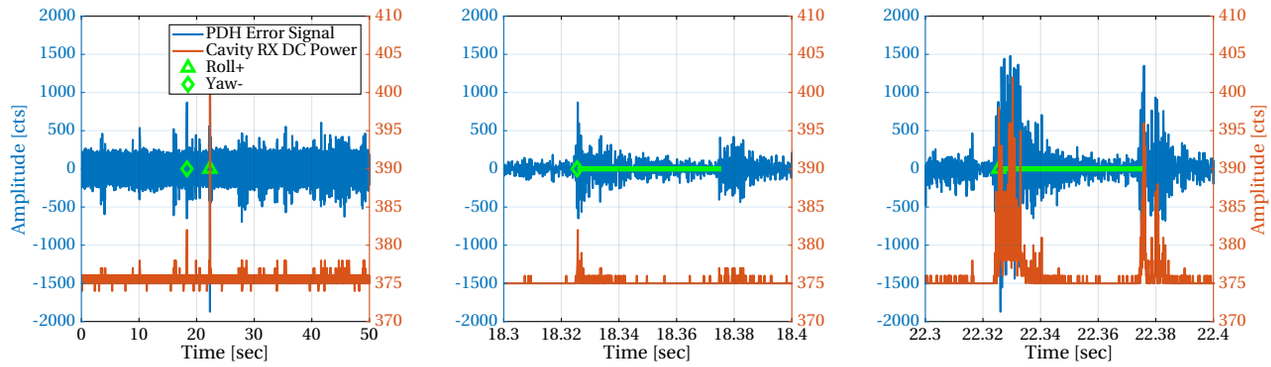

(a) Full scan time series **(b)** Zoom to yaw(-) thruster **(c)** Zoom to roll(+) thruster

Figure 6.6.: Plot of an exemplary diagnostic scan type 1, which is cavity data at a rate of 10 kHz, from the file `GF1_NEN_20180834T144226_diagDataType1_2.bin`. Shown are the PDH error signal (blue), the cavity RX DC power (orange) and the thruster firings (green). In this particular scan, there were two thruster events, roll(+) and yaw(-) on GF-1 and the scan was performed on GF-1 as well. The green bars represent the thruster-on-time. The amplitudes are in uncalibrated units ([cts]). **Left:** Full scan time series. **Center:** Zoom to the yaw(-) thruster firing. **Right:** Zoom to the roll(+) thruster firing.

between the actual laser frequency and the cavity resonance, which is used as feedback signal for the PDH control loop. The reflected DC power is minimal at the cavity resonance and increases, if laser frequency is not locked to the cavity resonance properly, see section 2.4. Changes in these quantities can be related to changes either in the laser frequency or the length of the cavity, that are not tracked by the PDH lock. The latter effect should be negligible by design of the cavity.

30 scans of this type were executed on GF-1 between 2018-08-23 and 2018-08-24, 61 scans on GF-2 between 2018-08-27 and 2018-08-28 and another 22 scans on GF-1 between 2018-09-07 and 2018-09-08. All of them were scheduled such that the data gets recorded when flying over the geomagnetic equator. The amount of scans is inevitable since thruster activations can not be commanded explicitly and thus, in some of the scans, there were no thruster firings. Therefore, several records could not be used for further investigations.

In approximately half of the scans taken on GF-2, the laser was turned off. Hence, no light was entering the cavity and the cavity signals were expected to show no response on thruster firings, which was confirmed. Arising from this observation, an electromagnetic coupling into the phase readout and digitization system, i.e. the QPD currents, during the thruster firings could be excluded as explanation for the PJs. When the laser was on, it could be revealed that each thruster firing on the master side, that occurred during one of the scans, lead to a response in the cavity signals. Beforehand, it was assumed that only roll thrusters cause a PJ.

The response in the cavity data indicates that the laser's frequency changes faster than the PDH lock can track and adjust the frequency, since the bandwidth, i.e. the unity gain frequency of the control loop, is too low.

Within the high-rate cavity data it is even possible to see that the cavity signals show two spikes during the time of an active thruster, when turning it on and off. This can be seen in fig. 6.6. These plots show the cavity responses for two thruster firings on GF-1, one of which is a roll thrust and the other is a yaw thrust. The response on the roll thruster has a higher magnitude in both, PDH error signal and RX DC power compared to the yaw thruster firing. This is not only the case for the specific scan showed above, but was observed within all scans and on both S/C.

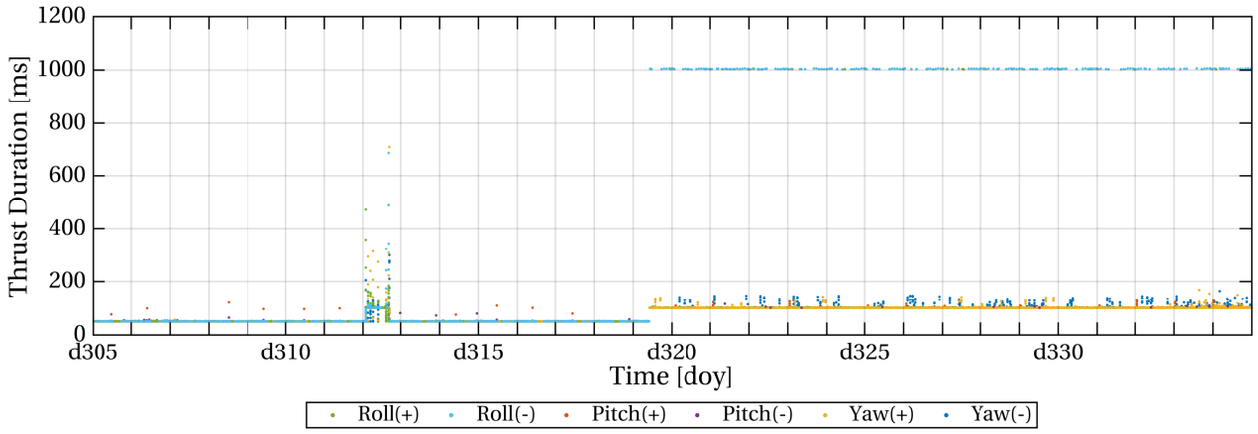

Figure 6.7.: Thruster events on GF-1 during November 2018. On day of year (doy) 319 the AOCS behavior was changed from 50 ms thrust duration for all thrusters to 100 ms (pitch and yaw) and 1000 ms (roll), respectively. The amount of thruster activations could be reduced. On doy 312, a CoM-calibration maneuver was performed, explaining the higher amount of thrusts in order to restore the attitude after the maneuver. The total number of thruster activations in this plot 2901 for roll before the AOCS re-configuration and 204 afterwards, even if the latter time span is longer.

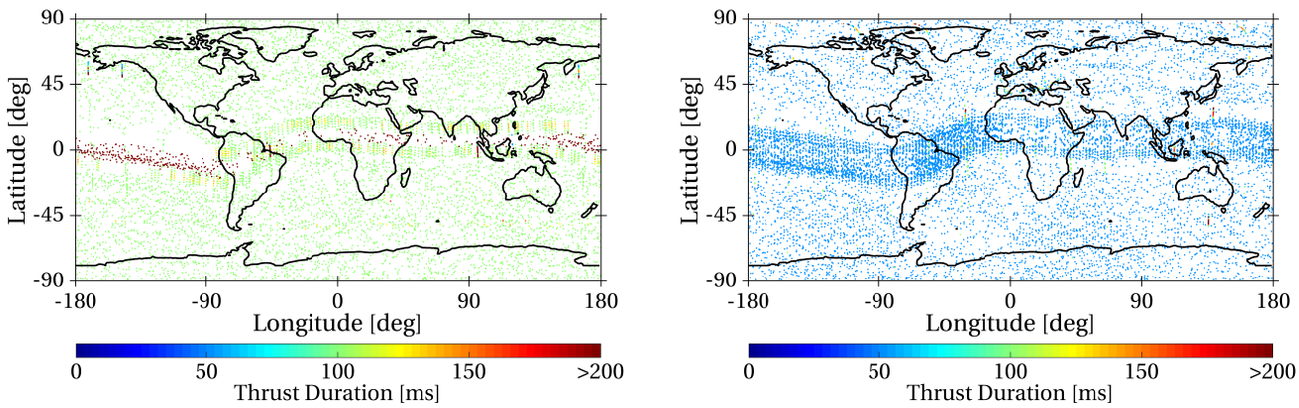

(a) Thrust duration and location on a map for January 2019

(b) Thrust duration and location on a map for April 2019

Figure 6.8.: Duration and location of all thruster firings on GF-1 plotted on a map with the S/C position for January and April 2019. While in January (left) the AOCS mode allowed for long thrusts of up to one second, this was reversed in February. Thus, in April (right) there are more brief thrusts. In both cases, the color axis is clipped at 200 ms, while in January the red coloring is dominated by 1 s thrust events.

It is concluded that the cavity scans of type 1 shows a response for all thrusters, but they have the highest magnitude for roll thrusters. Furthermore, not the acceleration caused by the thrust but the opening and closing of the valve cause mechanic vibrations, that influence the NPRO laser crystal and therefore the laser's frequency. This observation was confirmed by the LRI team in collaboration with Airbus, the constructors of the satellites.

During the mission lifetime, the behavior of the AOCS was changed several times. At launch, the duration of roll thruster firings was usually approximately 50 ms. There have been about 200 roll thruster firings per day in a representative segment of 10 days length in June 2018 per S/C, of which most of the thrusts on master side resulted in a PJ. The roll thrust duration was extended to 1 s in mid November 2018 (see fig. 6.7), which reduced the roll thruster firings to less than 10 per day. The duration of the other thruster firings for yaw and pitch direction have also been increased from 50 ms to 100 ms in November 2018. Thus, the total amount of thruster firings could be reduced from approximately 500 to 300 per day and S/C and accordingly, the number of PJs was reduced. A timeline of thruster events during November 2018 on GF-1 can be seen in fig. 6.7. It shows the thrust duration increasing from 50 ms for all thrusters to 100 ms for pitch and yaw and 1 s for the roll thrusts, respectively. Additionally, fig. 6.8 shows the thrust duration for two month with different AOCS modes on a world map. The higher roll thrust duration causes a reduced amount of thruster activations along the geomagnetic equator. Since the AOCS mode was switched back to the shorter thrusts in February 2019 on both S/C, the two panels of fig. 6.8 show both AOCS modes. Both panels show data of of GF-1.

6.2.3. Diagnostic Scan Type 7: Phasemeter Data

The other diagnostic scans of type 7 is a record of high-rate phasemeter data. In total, 16 data streams of `uint32` numbers are recorded. They contain the four QPD phase measurements, which have 64-bit depth, packed into two 32-bit numbers, and the i- and q-values. For a description of the phasemeter output see section 4.6 about the LRP. The scan has a duration of $4\,\mathrm{MB}/(16 \cdot f_s \cdot 4\,\mathrm{B}) \approx 6.47\,\mathrm{s}$ with the sampling rate $f_s = f_{\mathrm{USO}}/4000 \approx 10\,\mathrm{kHz}$.

In fig. 6.9, one of these scans is shown, where the LRI was turned on and both S/C fired one thruster during the scan. The shown plot uses data taken on GF-1 on 2018-07-17, where the duration of a thruster firing was still 50 ms. This plot clearly shows a response in the high-rate phase measurement whenever a thruster on any S/C fires. Since GF-1 was transponder during this period, it is clear that PJs do not emerge within the cavity, because the transponder does not use the cavity at all but only the frequency-offset DPLL. However, the magnitude of the phase response is lower for the transponder's thruster firing. The diagnostic scan of type 7 again shows two responses per thruster firing, when opening and closing the valve. The actual PJ can be made visible by low-pass filtering the high-rate data which is shown in fig. 6.9a with a cut-off frequency of 10 Hz. This low-pass filter effectively simulates decimation within the LRP (cf. section 4.6). The filtered mean phase is shown in fig. 6.10. Apparently, the roll thrust on the master S/C, which is GF-2, results in a PJ of approximately 50 nm magnitude in the full roundtrip, while the roll thrust on the transponder side does not show a PJ at all. The step arises since the integral over an enveloped oscillation in general is non-zero. The high-frequency vibration of the NPRO, caused by the thruster activations, and the corresponding frequency fluctuations can be regarded as this oscillation, which is enveloped by the control loop's damping capabilities.

Further investigations showed that the major part of PJs, more than 99 %, arise from thruster firings on the master side, since the PDH lock has a narrower bandwidth compared to the frequency-offset DPLL, which is able to track most of the thruster induced frequency variations properly. Even those PJs, that are caused by master thrusters, travel the full roundtrip and are tracked by the frequency-

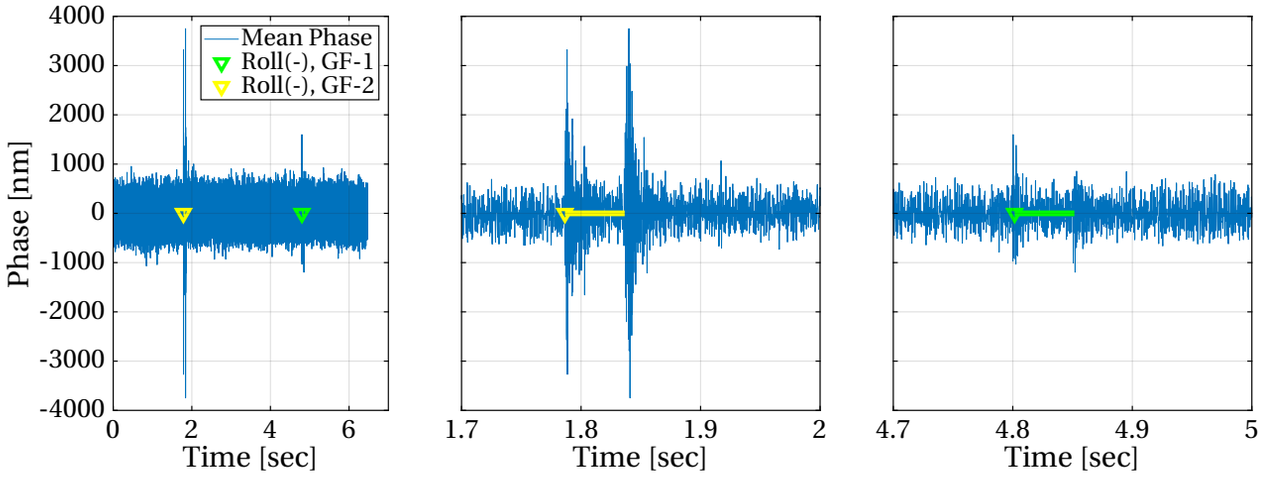

(a) Full scan time series **(b)** Zoom to roll(-) Thruster on GF-2 **(c)** Zoom to roll(-) Thruster on GF-1

Figure 6.9.: Plot of an exemplary diagnostic scan type 7, which is phasemeter data at a rate of 10 kHz based on the file `GF1_NYA_20180717T165455_diagDataType7_5.bin`. Shown is the debiased mean phase over the four QPD channels (blue), and the thruster firings on GF-1 (green) and GF-2 (yellow). In this particular scan, there were two thruster events, a roll(-) firing on each S/C. The bars represent the thruster-on time. Note, that this scan is taken on GF-1, which was the transponder, but shows a large response corresponding to a roll thruster firing on GF-2. Also here, like in scan type 1, two signal responses per thruster firing are observable, caused by the valve opening and closure. **Left:** Full scan time series. **Center:** Zoom to the roll(-) thruster firing with a duration of 50 ms on GF-2. **Right:** Zoom to the roll(-) thruster firing with a duration of 50 ms on GF-1. Even if the magnitude is smaller than in the center image, the phase response clearly stands out in the high-rate data.

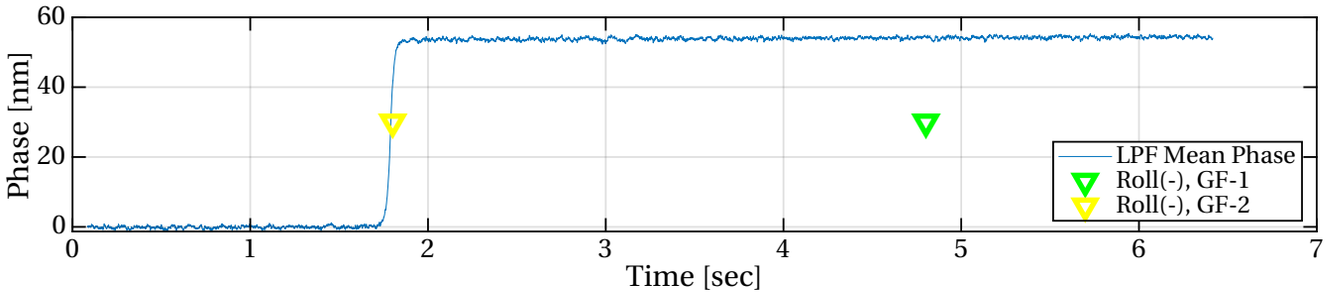

Figure 6.10.: Low-pass filtered mean phase of a diagnostic scan type 7. The step, that arises from the roll thruster activation on the master S/C (GF-2) is clearly visible. In contradiction, the phase at the GF-1 roll thruster firing does not show a step after low-pass filtering.

offset DPLL until they are measured on the master side. Moreover, the majority of the PJs are caused by roll thrusts, which is in good agreement to the observations made from diagnostic scan type 1, which shows larger magnitude for these thrusts compared to the other directions. It is presumed, that the pitch and yaw thrusts cause a PJ as well, but with a magnitude that is not exceeding the noise level in the phase measurements such that they can not be recognized as a PJ, which is in agreement to fig. 6.10, where the transponder's roll thrust does not show up after filtering.

6.2.4. Removal of Phase Jumps

The removal of PJs can be made with three different methods, which do all have their own advantages and disadvantages:

1. **Interpolation approach:** Use the master phase only and interpolate whenever a PJ is detected.
   Advantages:
   - Interpolation is easy to implement
   - No inter-S/C clock correction is needed
   - Uses the master phase only
   - Adjustable threshold for PJ detection

   Disadvantages:
   - Needs a PJ detection algorithm, which may be hard to implement on the master phase, since it contains large gravitational variations. Aggressive high-pass filtering is needed
   - Does not maintain the master's phase near PJs, due to interpolation
2. **Subtraction approach:** Subtract the transponder phase from the master phase. Since PJs occur on both, one removes the PJs alongside the frequency-offset phase ramp to clean the master's phase.
   Advantages:
   - Easy to implement
   - No PJ detection algorithm necessary

   Disadvantages:
   - PJ are sampled differently on master and transponder, which may yield PJ residuals (see text below and fig. 6.12)
   - Needs a precise inter-S/C clock correction
   - Does not account for cycle slips
3. **Template-based approach:** Identify PJs and use a template to model and subtract each PJ from transponder and master phase.
   Advantages:
   - PJ detection algorithm easy to implement on the transponder phase
   - Adjustable threshold for PJ detection
   - Can account for cycle slips
   - Does only need a rough timing and allows to perform a precise clock correction
   - Shows least residuals of all three methods
   - Is the least destructive of the three methods

   Disadvantages:
   - Removal algorithm hard to implement
   - Knowledge of the shape of a PJ, i.e. a template, is needed

Since the interpolation approach is very easy to implement and has only few free parameters, it is currently done by the SDS. However, the author of this thesis and V. Müller implemented the template based approach into the `gislparser` toolbox to achieve high purity of the science data. Hence, this approach is discussed in detail here.

First of all, the template has to be created. Therefor, the exact timing of several PJs in the transponder phase is determined and they are centered around zero. Furthermore, the step height is normalized to one cycle, see fig. 6.11a. Shown are 30 phase segments $\phi(t)$ that contain a PJ. They are scaled by the amplitude of the step h_T which is furthermore depicted as the coloring. Apparently, the shape of a PJ does not depend on the step height. From this finding, the first approach of a PJ or glitch-template was created using a sum-of-sines fit. It was then refined by the step-response of the decimation filter, that is used within the LRP. However, the differences are marginal. The coefficients of the glitch template are shown in appendix D and the template itself is shown in fig. 6.11a as the green trace. The template is bound by ±6.5 samples and is constant beyond.

The "deglitching"-algorithm, which then uses the template, works as follows:

1. Identify steps in the transponder phase ramps, that are larger than a predefined threshold. For these PJ, the corresponding GPS time is estimated with an accuracy of a second, i.e. within a few samples around the PJ center. The PJ spans multiple samples of the 10 Hz science data, due to the decimation filter, see fig. 6.11a.
2. Perform a fit of the template to the transponder phase for each identified PJ to get the transponder PJ model,
$$m_{\mathrm{PJ},T}(t) = h_T \cdot \texttt{glitch\_template}(t + \Delta t_T)\,. \tag{6.4}$$
The fit parameters are the step height h_T in cycles and the exact timing Δt_T in samples. The template is shown and described in fig. 6.11 and appendix D, respectively. This model is a function of the time t, which is given in units of samples.
3. Identify the approximate timing offsets between transponder and master phase time series using datation reports. Afterwards, subtract a polynomial of uneven order from the master phase

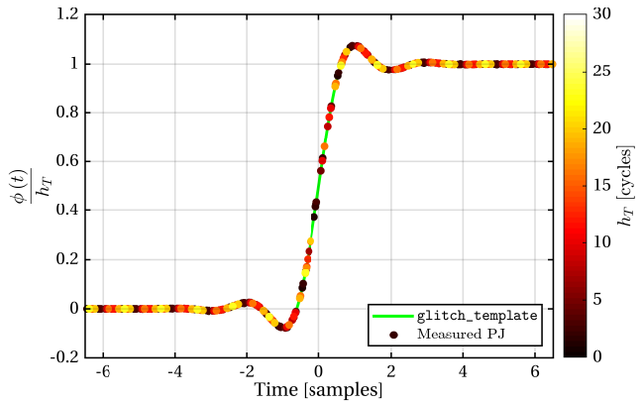

(a) Measured PJs and the glitch template

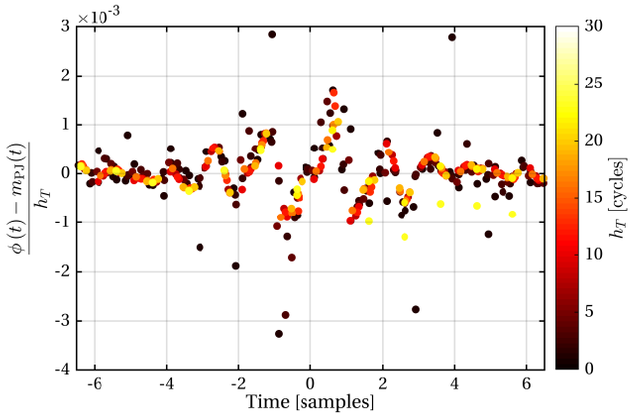

(b) Residuals after model subtraction, scaled with the fitted PJ height, h_T.

Figure 6.11.: Left: Template for removal of PJs (green) and 30 exemplary phase segments of 13 samples length, containing a PJ. Each PJ is scaled to a uniform step of one cycle and centered. The shape of a PJ is not dependent on the actual PJ amplitude, which is indicated by the coloring. **Right:** Phase samples after removal of the model, scaled by the fitted PJ amplitude.

and fit the template, using the same amplitude h_T as for the transponder (step 2). The exact PJ time Δt_M w.r.t. the master time series is the free parameter, which needs to be fitted due to the inaccuracies of the datation reports. This results in the master's model

$$m_{\mathrm{PJ},M}(t) = h_T \cdot \texttt{glitch\_template}(t + \Delta t_M)\,. \tag{6.5}$$

4. Remove the fitted models for each PJ from both, master and transponder phase measurements.
5. (Optional) Subtract the transponder from the master phase time series to remove the 10 MHz phase ramp (if not done yet) and residuals of the PJs. Therefor, the transponder phase needs to be interpolated to match the master time stamps.

It should be noted, that this template-based approach is accounting for the different sampling of PJs. Since the jump's occurrences in general are not fixed to the sampling rate, their shape in the phase time series differs. This is shown in fig. 6.12. Here, the glitch template m_{PJ} is shown alongside four different realizations of the same PJ, which all have the same height $h = 1$ cycle and are sampled equally but shifted by Δt samples w.r.t. the template center. This shows the necessity of a template, since the PJs differently spans across several samples adjacent to the center. These effects will not get removed by using the subtraction approach, since the master and transponder time series' are in general sampled differently.

However, it was found earlier that thruster activations evoke two responses in the phase (see figs. 6.6 and 6.9), whose timing offset depends on the thrust duration. Hence, multiple PJs may be detected close by. For those cases, multiple templates, based on the one described above, were created. Their usage depends on the AOCS mode, since the duration of thrusts can be configured differently, cf. figs. 6.7 and 6.8. Until now, thrust durations of 50 ms, 100 ms and 1 s are mainly used, however, other thrust-on times are possible as well. The models, that are currently being used, are:

- Single PJ: the default template
- Double PJ, 50 ms: Template with two PJ separated by 50 ms with different amplitudes
- Double PJ, 100 ms: Template with two PJ separated by 100 ms with different amplitudes
- Double PJ, 1 s: Template with two PJ separated by 1 s with different amplitudes
- Double PJ, variable width: Template with two PJ, whose separation is fitted as a new parameter.

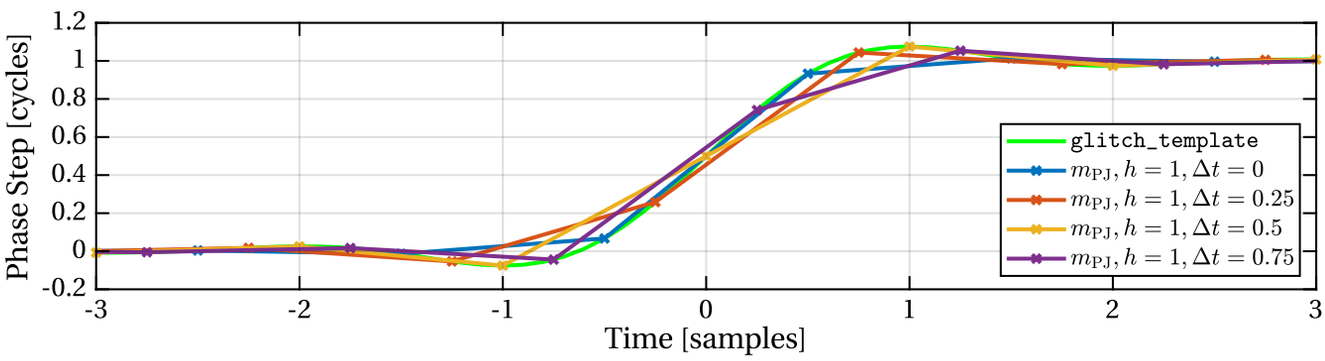

Figure 6.12.: Shape variations of PJs with varying sampling. They are different models, m_{PJ}, describing the same PJ, but their exact timing, Δt varies w.r.t. the PJ center. Δt is in units of samples

The presented algorithm always tries the single PJ template and the double PJ templates with predefined length first in step 3. The PJ models m_{PJ} get subtracted from the phase segment $\phi(t)$ and divided by the PJ height h_T in step 4. These residuals are shown in fig. 6.11b. A rms value over these residuals,

$$\mathrm{rms/h} = \mathrm{rms}\left(\frac{\phi(t) - m_{\mathrm{PJ}}(t)}{h_T}\right), \tag{6.6}$$

is a useful observable for the removal success of a PJ on a percentage basis. It is evaluated for master and transponder individually. As shown, the PJs can be removed with systematic errors of up to 0.2 %. However, an enveloped sinusoidal shape remains (cf. fig. 6.11b), which might be a starting point for further refinements.

The model with the least rms/h value is chosen as candidate for the removal in step 4, if it does not exceed a predefined threshold of $\mathrm{rms/h}_{\mathrm{max}} = 0.2\,\%$. If the best model's rms/h value is above this threshold, i.e. if the model does not remove the PJ well enough, the computational more expensive fit of the double PJ with variable width is performed to minimize the rms/h value further. In most cases, this last model removes the PJs well, however, if it does not, the best model until then is chosen.

Using the described algorithm, the PJs can be removed almost perfectly, with residual rms/h phase disturbances being in the order of 0.002 cycles, which is the threshold value, $\mathrm{rms/h}_{\mathrm{max}}$. Disturbances in this order of magnitude do not significantly influence the ranging observations, since the nominal LRI noise has rms values around 0.001 cycles. However, fig. 6.11b indicates that a little more fine-tuning would further improve the PJ removal.

Another benefit of this template-based approach is the capability to remove Cycle Slips (CSs). These are errors of the phase tracking DPLL and manifest in steps in the phase measurement, that have an integer amplitude. They occur more frequently, the lower the CNR is (see below). Since the phase steps of a CS are decimated in the LRP as well, the same template can be used to model and remove them. The major difference between PJs and CSs is, that CSs may occur in single channels only. Hence, for a correct removal, the four channels need to be handled individually.

6.3. Carrier to Noise Ratio (CNR)

The Carrier to Noise Ratio (CNR), or more precise, the Carrier to Noise density ratio, is an important quantity to make assumptions about the quality of the phase readout of the beatnote, or carrier. The CNR depends on the interferometric contrast, i.e. the overlap of the LO and RX beams, the available light power of the RX beam and the overall noise in the measurement system, which consists of the QPR, OBE and the ADC. In general, the CNR is defined as

$$\mathrm{CNR} = \frac{V_{\mathrm{Carrier}}^2}{\tilde{V}^2}, \tag{6.7}$$

where V_{Carrier} is the signal amplitude at the beatnote frequency, which may be expressed as a voltage, and $\tilde{V}^2$ is the measurement system's noise Power Spectral Density (PSD) at the beatnote frequency. The unit of the CNR is Hz. One might use this quantity in the decibel regime, where the unit dB Hz is common. The LRI requirement for the CNR is 70 dB Hz (Abich et al., 2019). Above, the phasemeter should be able to reliably track the phase of the beatnote oscillation. If the CNR is too low, the phase detection is prone to CS (see above and Bachman et al. (2017)) or may fail to lock to the beat signal.

An accurate estimate of the CNR would support the characterization of the LRI, since changes in the CNR can point to changes in the setup. These include a degradation of the laser output power, QPD responsivity, alignment or contamination of the optical components including the TMA and changes

in the laser beam shape, which may lower the contrast. The CNR is expected to decrease over the LRI lifetime, e.g. caused by aging of the NPRO crystals and the QPDs.

6.3.1. CNR Calculation: Simple Approach

The carrier amplitude V_{Carrier} also called `fftSNR` in the telemetry of the LRI, is computed within the LRP, see section 4.6. The LRP digitizes the QPD readings, i.e. the oscillating beatnote, with a sampling rate $f_{\text{USO}} \approx 39\,\text{MHz}$. An FFT algorithm is executed on every 4096 samples, yielding a complex vector with 4096 FFT coefficients nearly every 100 µs. The `fftSNR` is the magnitude of the highest peak in this spectrum. However, the amplitudes A of the complex-valued output y of the real-to-complex FFT algorithm are not calculated as

$$A = \sqrt{\Re(y)^2 + \Im(y)^2}\,, \tag{6.8}$$

with $\Re$ and $\Im$ denoting the real and imaginary part of y, but by using an approximation method. Here, the amplitude is calculated as (Levitt et al., 1977)

$$A \approx \begin{cases} X + \frac{1}{8}Y & \text{if } X \geq 3Y \\ \frac{7}{8}X + \frac{1}{2}Y & \text{if } X < 3Y \end{cases}\,, \tag{6.9}$$

where

$$X = \max\left(\left|\Re(y)\right|, \left|\Im(y)\right|\right) \tag{6.10}$$

and

$$Y = \min\left(\left|\Re(y)\right|, \left|\Im(y)\right|\right)\,. \tag{6.11}$$

This approximation is used since it has lower demands to the processing unit, because the square and square root operations are computationally complex. Also, the square terms would need to be stored intermediately, requiring twice the bit depth compared to the numbers $\Re(y)$ and $\Im(y)$ themselves. The approximation can be performed with integer arithmetics only. The maximal error of this approximation is 2.77 %, which is equivalent to 0.25 dB, while the mean error is at 0.82 % (Levitt et al., 1977, Table 1).

Since the rms noise power $\tilde{V}^2$ at the beatnote frequency is not accessible directly, it is estimated from the FFT amplitudes in the adjacent frequency bands. These are defined as `noise8_9` and `noise11_12` and are located between 8...9 MHz and 11...12 MHz, respectively. Given the FFT amplitudes $A(f_i)$ for the discrete Fourier frequencies f_i the noise estimates are calculated as:

$$\texttt{noise8\_9} = \sqrt{\frac{1}{N}\sum_{f_i} A(f_i)^2} \quad \text{with} \quad f_i \in [8, 9]\,\text{MHz} \tag{6.12}$$

and

$$\texttt{noise11\_12} = \sqrt{\frac{1}{N}\sum_{f_i} A(f_i)^2} \quad \text{with} \quad f_i \in [11, 12]\,\text{MHz}. \tag{6.13}$$

Furthermore, they get average over 1 s (priv. comm. C. Woodruff, NASA/JPL, 2019). The values of `noise8_9` and `noise11_12` are by means of the square root of the average noise power within that frequency band. Here,

$$N \approx \frac{1\,\text{MHz}}{10\,\text{kHz}} = 100 \tag{6.14}$$

denotes the number of discrete frequency bins within each measurement band.

In the Level-0 telemetry, the `fftSNR` and noise estimates have a data rate of roughly 0.1 Hz and are reported in the LRI Health Monitor packet, see section 5.2.3. The downsampling is, to the knowledge of the author, performed by simply selecting the last available value, cf. fig. 4.8.

The CNR of the LRI phase tracking can be calculated as (Dubovitsky et al., 2018)

$$\mathrm{CNR}_{\mathrm{simple}} = 20\log_{10}\left(\frac{\sqrt{10^4}\cdot \texttt{fftSNR}}{\min(\texttt{noise8\_9}, \texttt{noise11\_12})}\right). \tag{6.15}$$

The additional factor of $\sqrt{10^4}$ arises from the conversion of the noise amplitudes to a noise density, accounting for the FFT bin width of approximately 10 kHz, while the square root accounts for the conversion from power to amplitude spectra.

This approach (eq. (6.15)) is fine, as long as the noise $\tilde{V}^2$ is constant, i.e. white, between eight and twelve MHz. However, shown in fig. 6.13 are ASDs of the measured noise of the ADC channels in the LRP, when the lasers where turned off. Therefore, these ASDs represent the intrinsic noise of the measurement system, which comprises of the QPR, OBE and ADC. Both LRI units show a linear decreasing trend from lower to higher Fourier frequencies. However, taking the average instead of the minimum in the denominator of eq. (6.15) is only feasible on the transponder side. On the master S/C, the beatnote sometimes reaches Fourier frequencies below 9 MHz or above 11 MHz due to Doppler shifts caused by the relative motion of the two S/C. This causes the noise estimate in the frequency band to increase, since a part of the carrier amplitude is measured there. Thus, the result is falsified, since the noise floor at the beatnote frequency in absence of a beat signal can not be estimated correctly.

An exemplary time series of the noise measurements while the beatnote frequency sweeps through

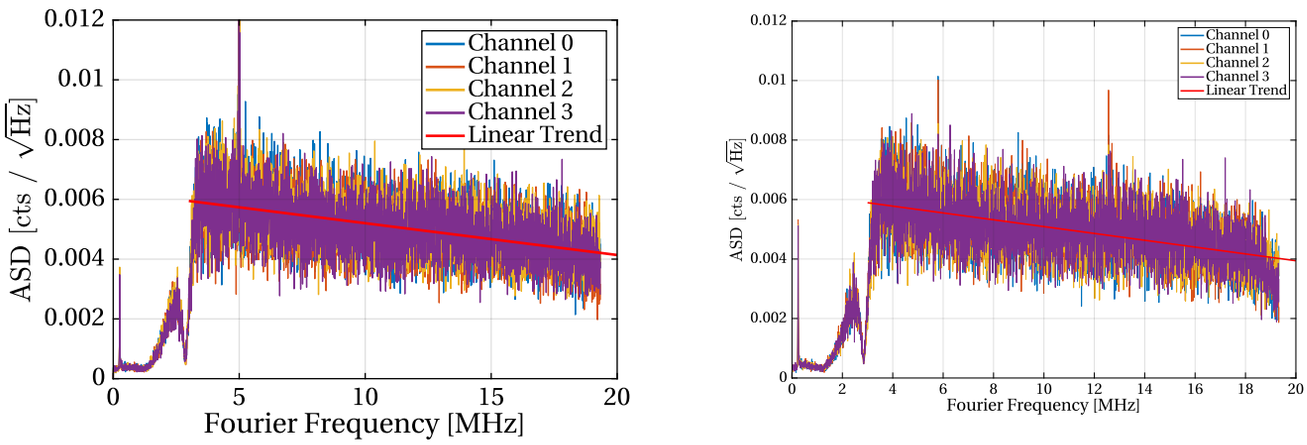

(a) ASD of diagnostic scan type 19 on GF-1

(b) ASD of diagnostic scan type 19 on GF-2

Figure 6.13.: Amplitude Spectral Density (ASD) of the measured noise of the measurement system (QPR, OBE and ADC) on each S/C. These diagnostic scans of type 19 were taken on 2018-06-11 on GF-1 (left) and on the next day on GF-2 (right), when both lasers were still turned off. Thus the QPDs only measure intrinsic electronic noise. The scan contains the phase of all four channels after the ADC at the full rate of $f_{\mathrm{USO}} \approx 39$ MHz for about 1.7 ms. The ASD is computed using a rectangular window. Note the almost linear decreasing trend within both scans for Fourier frequencies higher than 4 MHz. Images based on the files `GF1_NYA_20180611T171126_diagDataType19_2.bin` and `GF2_NYA_20180612T165047_diagDataType19_2.bin`, respectively.

one of the frequency bands is shown in the mid panel of fig. 6.14. The green curve of `noise11_12` reaches values of more than 100 cts at maximum, though the actual noise floor is 12 cts and the `fftSNR` only shows high-frequency noise.

Another fact, arising from using the minimum in eq. (6.15) is that the LRP does not always rely on the same measurement, e.g. always `noise11_12`, but jumps between the two estimates, whenever the beatnote frequency sweeps into the nominally lower noise frequency band. The computation then immediately takes the other noise level. As a consequence, the CNR shows jumps of about 2.5 dB Hz, corresponding to the difference of 12 cts and 16 cts noise level of `noise8_9` and `noise11_12`, respectively, This can be verified easily with an exemplary value for the `fftSNR` of 4000 cts. i.e.

$$20\log_{10}\left(\frac{100\cdot 4000}{12}\right) - 20\log_{10}\left(\frac{100\cdot 4000}{16}\right) \approx 2.5\,\mathrm{dB} \tag{6.16}$$

This effect is also shown in fig. 6.14: Whenever the green `noise11_12` measurement increases due to the beatnote frequency (upper panel) moving into this frequency band, the values for $\mathrm{CNR}_{\mathrm{simple}}$ (lower panel, blue trace) drop. This is caused by the choice of the noise estimate, that is jumping between `noise8_9` and `noise11_12`. The drops of $\mathrm{CNR}_{\mathrm{simple}}$ are non-physical and only related to a wrongly estimated noise at the beatnote frequency. Besides these jumps of 2.5 dB Hz, the blue trace in fig. 6.14 shows a high-frequency noise with a magnitude of approximately 1 dB Hz, which originates

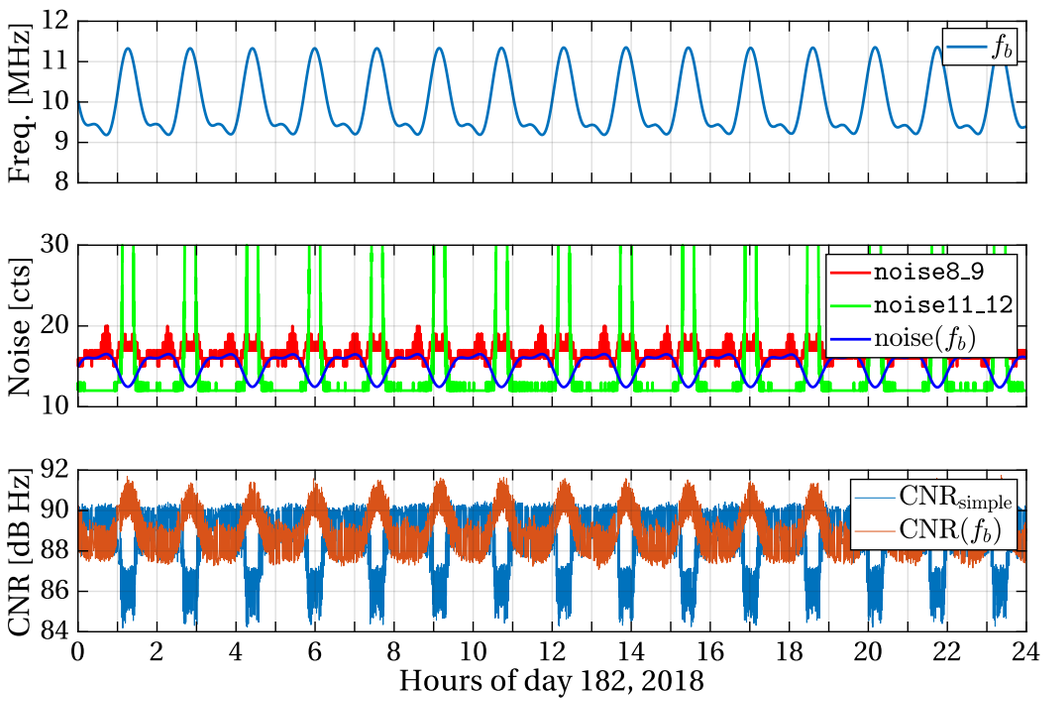

Figure 6.14.: Upper: Beatnote frequency, f_b, measured on the LRI master unit (GF-2). Due to relative velocities and the orbital constellation of the two S/C, it varies between 9.2 and 11.3 MHz. **Mid:** Square root of the rms noise power as determined by the LRP. Apparently, the noise for lower Fourier frequencies is higher (minimum of red curve lies above minimum of the green curve). The peaks in the `noise11_12` values occur once per orbit, whenever the Doppler shift is high enough such that f_b is above 11 MHz. The beatnote frequency dependent noise density estimation, noise(f_b), is shown as blue trace. **Lower:** $\mathrm{CNR}_{\mathrm{simple}}$ calculated using eq. (6.15) (blue) and CNR(f_b) (orange), using the enhanced formula, eq. (6.16).

from the fftSNR measurement and is investigated below.

The noise floor of the ADC channels, i.e. of the opto-electronic chain consisting of the QPR, OBE and ADC, may change over the mission lifetime. Hence, it is not desirable to replace the noise estimate by a constant value.

6.3.2. Enhanced Noise Estimation

As part of this thesis, an improved method for the noise estimation at the beatnote frequency was derived. It accounts for the limitations, that are present for the simple approach introduced above. A good estimation of the mean noise in the measurement bands, i.e. noise8_9 and noise11_12, can be achieved by excluding all high peaks where the beatnote might affect the estimation and then calculate the mean noise. For the example given in fig. 6.14, the levels are around 16 cts for the lower and 12 cts for the higher frequency band, hence these values get assigned to frequencies of 8.5 MHz and 11.5 MHz, respectively. A linear fit, noise(f), is derived and the enhanced calculation of the CNR, formerly done with eq. (6.15), now reads

$$\mathrm{CNR}(f_b) = 20\log_{10}\left(\frac{\sqrt{10^4}\cdot \mathtt{fftSNR}}{\mathrm{noise}(f_b)}\right) \tag{6.17}$$

where f_b denotes the beatnote frequency, derived from phase measurements. This new formula efficiently prevents a wrong CNR calculation caused by incorrect estimation of the background noise.

An example of this new computation is also shown in fig. 6.14. The noise level, noise(f_b), in the mid panel is derived depending on the beatnote frequency in the uppermost panel, preventing the drops as shown for simple approach. Now, the CNR even increases as the beatnote frequency gets higher, since the measurement system's noise is lower in those frequency regions (cf. fig. 6.13) and thus, the beatnote stands out more clearly. All in all, using the interpolated noise model gives a more physical and reliable estimate of the CNR.

6.3.3. Correction of the Inter-S/C Distance

The fftSNR, being the maximum value of an Amplitude Spectrum (AS), is proportional to the root of the power of the RX beam P_{RX} which in turn is inverse proportional to the total distance L (cf. eq. (2.12)). Therefore, the fftSNR is inverse proportional to the total distance:

$$\mathtt{fftSNR} \propto \sqrt{P_{\mathrm{RX}}} \propto L^{-1}\,. \tag{6.18}$$

Thus, the numerical values of the fftSNR decrease, if the inter-S/C distance increases and vice versa. However, this decreasing fftSNR must not be wrongly interpreted as e.g. degradation of the QPD. Therefore, it is advised to correct for the inter-S/C distance, when comparing CNR values for different times throughout the mission.

Therefore, the numerical values of the fftSNR are normalized to a nominal distance of 220 km to be comparable in terms of long-term degradation. This correction has no large impact by looking at daily variations, but over the mission lifetime, the range will reach the outer boundaries of 170 km to 270 km. The CNR would then yield different values. Hence, the normalized value reads

$$\mathtt{fftSNR}_{\mathrm{norm}} = \frac{L}{220\,\mathrm{km}}\cdot \mathtt{fftSNR}\,. \tag{6.19}$$

The normalized CNR in fig. 6.15 shows less distance-dependent behavior, especially regions where the range has an extreme point (i.e. days 170, 2018 and 78, 2019), where the $\mathrm{CNR}_{\mathrm{norm}}$ is much more linearized compared to the CNR estimates without this normalization.

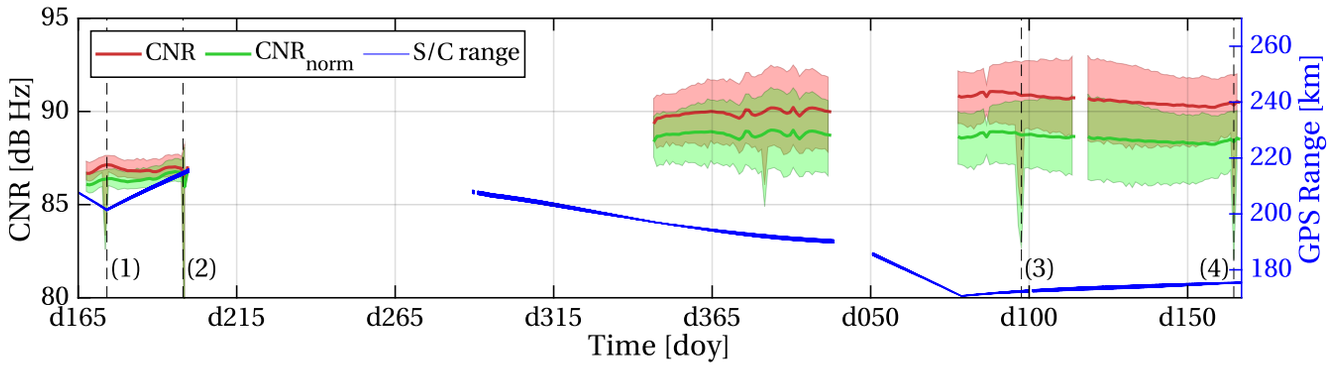

(a) CNR for GF-1

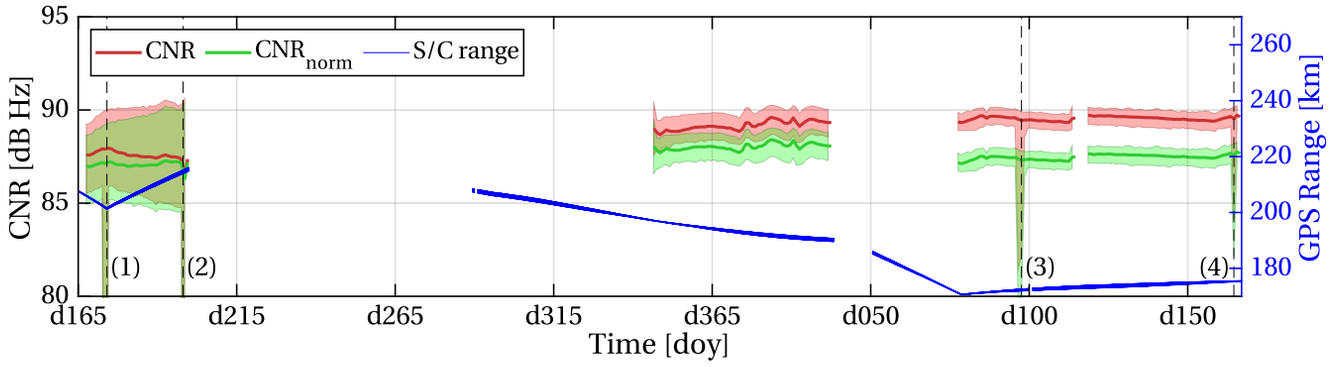

(b) CNR for GF-1

Figure 6.15.: CNR and its normalization to 220 km for GF-1 (upper panel) and GF-2 (lower panel). The solid lines for CNR represent the average value over one full day while the area shows the minimum and maximum values for each day. The GPS range (blue, right y-axis) is derived from GNV1B data. When there are gaps, no GNV1B products are available for one of the S/C. **Annotations:** As a consequence of some maneuvers, the CNR decreases, e.g. due to lower interferometric contrast. (1): Collision avoidance maneuver, (2) and (4): DWS Scan, (3): Sun blindings.

6.4. Scalloping Loss Investigations

As introduced in section 2.6.2, spectral estimates by means of FFTs are susceptible to scalloping loss, and so are the `fftSNR` values, which are used to derive the CNR. Scalloping loss describes the phenomenon that the amplitude of signals with a frequency, that does not perfectly match the center of one discrete FFT frequency bins, is not represented correctly. However, since the phase telemetry provides an independent measure for the actual beatnote frequency, it is possible to calculate the magnitude of the loss and correct it.

In order to get an accurate CNR estimate, the magnitude of the scalloping loss has to be determined for each `fftSNR` sample and added before calculating the CNR. According to eq. (2.40), the scalloping loss for the rectangular window used in the LRP has a maximum value of about −3.92 dB at the edges of each frequency bin.

6.4.1. Estimation of the Scalloping Loss from Flight Data

The `fftSNR` recordings can be concatenated to a continuous time series. It is assumed, that the `fftSNR` values are mainly determined by two degrees of freedom, which are the inter-S/C distance

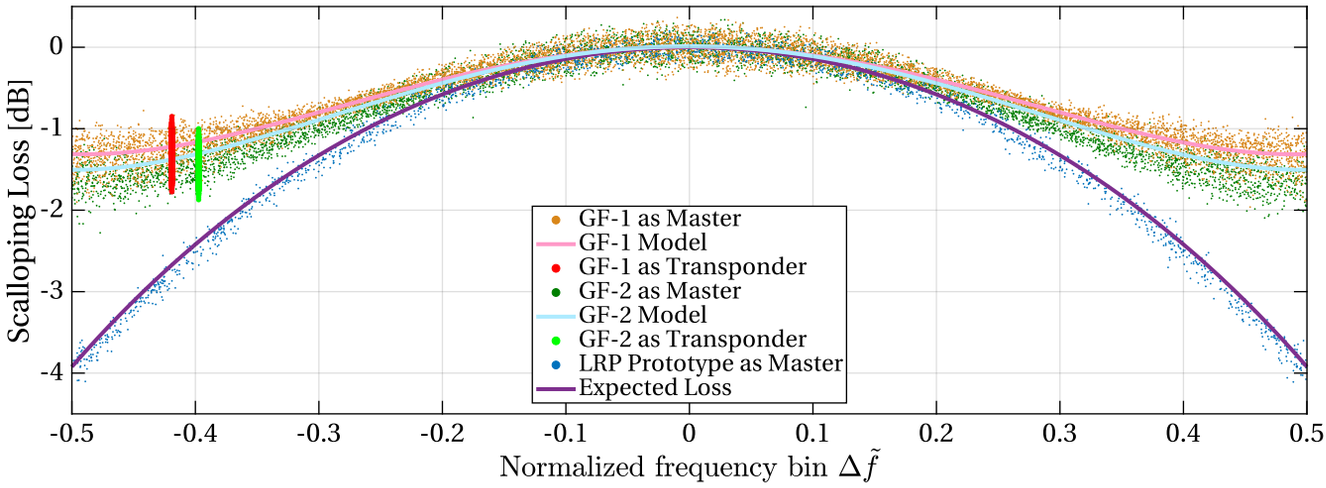

Figure 6.16.: Scalloping Loss for both flight units and the LRP prototype. The prototype data is based on the file `Tlm-2019-0226-110010.gisl`. For the LRI being in transponder role, whose frequency is locked to 10 MHz, it is only possible to derive the scattering for a fixed frequency. Thus, the bias of approx. −1 dB is estimated by comparing to the master values. The scattering with a magnitude of roughly 1 dB in transponder role matches for both flight units in comparison to the master role. The apparent frequency offset between the two flight units in transponder role originates from the different clock rate f_{USO} and the corresponding differences of the normalized frequency bin. Models for GF-1 and GF-2 derived using the coefficients in table 6.1.

(cf. section 6.3.3) and the scalloping loss. However, long-term drifts of the `fftSNR` due to distance variations can be considered as negligibly small for a time interval of up to a few days. Hence, the distance correction is not needed for the following analysis, since time spans of only up to 24 h are considered, but may be important on longer time spans.

Since scalloping loss is dependent on the actual beatnote frequency, the frequency corresponding to each `fftSNR` sample is calculated by differentiation of the phase measurements. The frequency estimate is accurate enough, since the phase telemetry has a rate of 10 Hz, compared to the `fftSNR` data rate of 0.1 Hz, and the beatnote frequency does not change fast within this time scale. Subsequently, the frequency gets normalized by the bin width f_{bin}. This normalized frequency is denoted as $\tilde{f}$. In a last step, all frequency values are wrapped into the interval $[-0.5, 0.5)$, which represents a normalized frequency bin (cf. eq. (2.37)).

The scalloping loss can then be estimated by converting the `fftSNR` into dB regime and map them to the previously computed frequency bin estimates $\Delta\tilde{f}$. One may subtract the mean value of a small interval around the bin center to remove the actual FFT amplitude in order to normalize the values to 0 dB at the bin center. A plot of the scalloping loss is shown in fig. 6.16.

The expected maximal loss arising from eq. (2.40) is approximately 4 dB, regardless of the role as master or transponder. A detailed investigation of the scalloping loss is performed in the following sections.

6.4.2. Scalloping Loss in Master Role

The orange and dark green dots in fig. 6.16 show the calculated scalloping loss against the normalized frequency bin. GF-1 shows a average loss of 1.5 dB, GF-2 of 2 dB at the frequency bin edges. This does

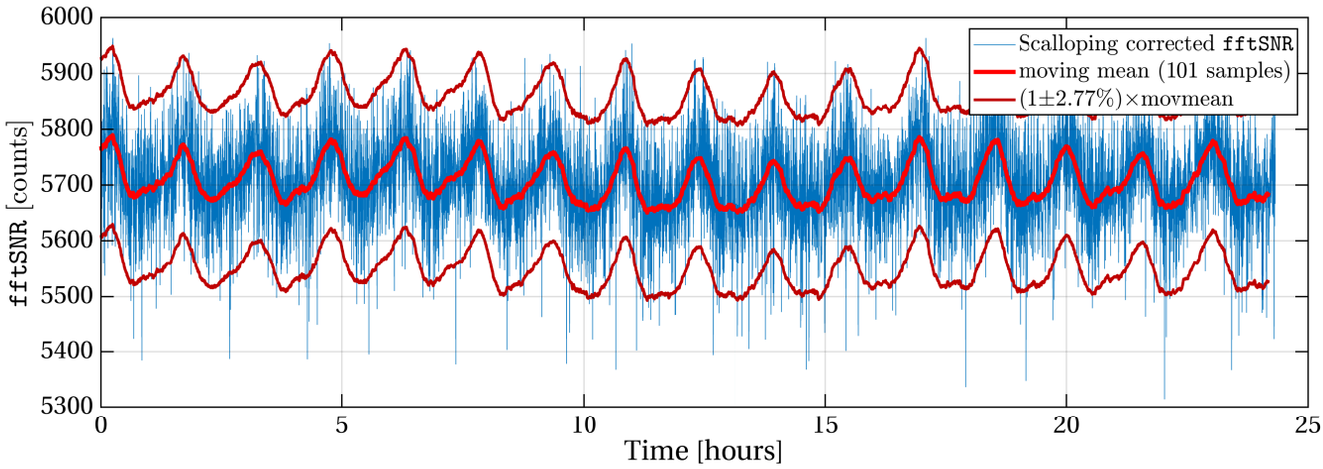

Figure 6.17.: High frequency variations of scalloping corrected `fftSNR`. This particular data was taken on GF-1 in January 2019. Shown is the `fftSNR` (blue) after scalloping correction, using the polynomial model (cf. table 6.1), a low-pass filtered `fftSNR` using a moving mean over 101 samples (red) and the 2.77 % error interval, corresponding to the amplitude approximation error (wine red).

not match the expectations. Hence, in order to correct the loss, a polynomial of fourth degree, i.e.

$$L\left(\Delta\tilde{f}\right) = a_4\Delta\tilde{f}^4 + a_3\Delta\tilde{f}^3 + a_2\Delta\tilde{f}^2 + a_1\Delta\tilde{f} + a_0\,, \tag{6.20}$$

is fitted to the data to derive a model for the loss. This is done individually for the two S/C. The model coefficients are reported in table 6.1, the model's traces shown in fig. 6.16. These coefficients seem to be stationary over time, however this may become evident in the future. After subtracting this model from the `fftSNR`, the residual high-frequency noise, shown in fig. 6.17, can almost entirely be explained by the used approximation for the magnitude (cf. section 6.3.1), which has an error of 2.77 %. Remaining are variations at orbital period. These are caused by the range variations of several hundred meters and the corresponding varying optical power of the received light.

6.4.3. Scalloping Loss of the LRP Prototype

A prototype model of the LRP, located at JPL, has been used to measure the scalloping loss by generating a signal and feed this into the LRP as simulated QPD readings. The input signal has a carrier frequency of $\omega_0 = 2\pi \cdot 10\,\text{MHz}$ with a sinusoidal frequency modulation with a modulation index $\omega_m = 2\pi \cdot 0.5\,\text{MHz}$ and a modulation frequency of $\delta\omega = 2\pi \cdot 200\,\mu\text{Hz}$, i.e.

$$y_{\text{in}} = \sin\left(\omega_0\, t - \frac{\delta\omega}{\omega_m} \cdot \cos(\omega_m\, t)\right)\,. \tag{6.21}$$

S/C	a_4	a_3	a_2	a_1	a_0
GF-1	23.1121	0.0060	−11.0585	−0.0022	0.0090
GF-2	24.9661	0.0431	−12.3081	−0.0110	0.0122

Table 6.1.: Coefficients of the polynomial models for the scalloping loss, eq. (6.20). All coefficients in units of dB.

This parameter set is quite close to a real orbital configuration, where the orbital frequency is about 170 µHz. Thus, this test should reproduce the on-orbit behavior well. The result of the investigation using this prototype data showed the expected number of 3.92 dB loss with added noise of 0.25 dB caused by the amplitude approximation. The result is shown as green dots in fig. 6.16. Thus, the scalloping loss is in very good agreement to the expectation.

These results were confirmed independently by simulating the frequency modulated signal at a rate of f_{USO} and recreating the FFT and amplitude estimation, like it is done within the LRP. Thus, it is concluded, that the LRP prototype at JPL behaves as expected, however it should be noted that the generated electric signal has very low noise compared to the in-flight QPD readings, which e.g. shows laser frequency noise.

6.4.4. Scalloping Loss in Transponder Role

On the transponder side, the beatnote frequency is fixed at 10 MHz, using the frequency-offset DPLL. Therefore the FFT amplitude of this constant frequency should not vary on short time scales. Thus, it is not possible to derive the exact value of the scalloping loss, but only biased variations. Shown in fig. 6.16 are the variations of the loss, which are about 1 dB in magnitude for both units. It matches the scattering when being in master role at the corresponding positions in the normalized bin. The bias of approximately −0.9 dB is estimated using values of the same S/C in master role.

6.4.5. Scalloping Loss in High-Rate Data

A diagnostic scan of type 19, which was previously used in section 6.3.1 to determine the photoreceiver noise before the laser link was established, has been taken one more time after the link acquisition on each S/C. They have not been taken simultaneously. Figure 6.18a shows the beatnote frequency on both S/C. On the transponder (GF-1), the beatnote frequency is at 10 MHz while on the master (GF-2), the beatnote frequency is at roughly 9.92 MHz. The Doppler shift of 80 kHz in the full round trip matches the relative velocity of about 4 cm/s by the time of that scan, which could be confirmed using the GNV1B data product.

It is recalled, that diagnostic type 19 contains approximately 1.7 ms of digitized QPD current values before the DPLL (cf. fig. 4.8). The total number of samples is 65536, sampled with $f_{\mathrm{USO}} \approx 39\,\mathrm{MHz}$. The time series is divided into 16 segments, each with 4096 samples ($4096 \cdot 16 = 65536$). Each 4096 samples correspond to the actual segment length of the FFT within the LRP (cf. section 4.6). For each of these 16 parts, an FFT is calculated and the amplitude is estimated using the approximation method (cf. section 6.4.1). The results are visualized in figs. 6.18b and 6.18c in two ways: As individual spectra and also as spectrogram, which features a time resolution. Within these spectral representations, the scalloping loss can be deduced from the amplitude difference of the respective highest peak out of the 16 spectra.

On the master side (GF-2, fig. 6.18c) a maximal loss of 1.65 dB is visible. However, this value has little meaning, since the beatnote frequency does not pass over to another FFT bin and therefore does not reach the edge of a bin. Since the phase telemetry stopped roughly 10 s before the diagnostic scan, due to the non-science mode of the LRI, the actual beatnote frequency at the scan time needs to be assessed by linear interpolation. This is much more precise than using GPS observations, since an error of 1 mm/s of the inter-S/C velocity corresponds to a beatnote frequency error of roughly 1 kHz (cf. eq. (4.3)). The beatnote frequency reads $f_{\mathrm{b}} \approx 9.919\,262\,\mathrm{MHz}$. The frequency slope is roughly 1208.5 Hz/s. Within the scan of 1.7 ms length, the beatnote frequency changes by 2 Hz. The corresponding position within the normalized frequency bin is $\Delta\tilde{f}_{\mathrm{b}} \approx 0.026$, which is close to the center.

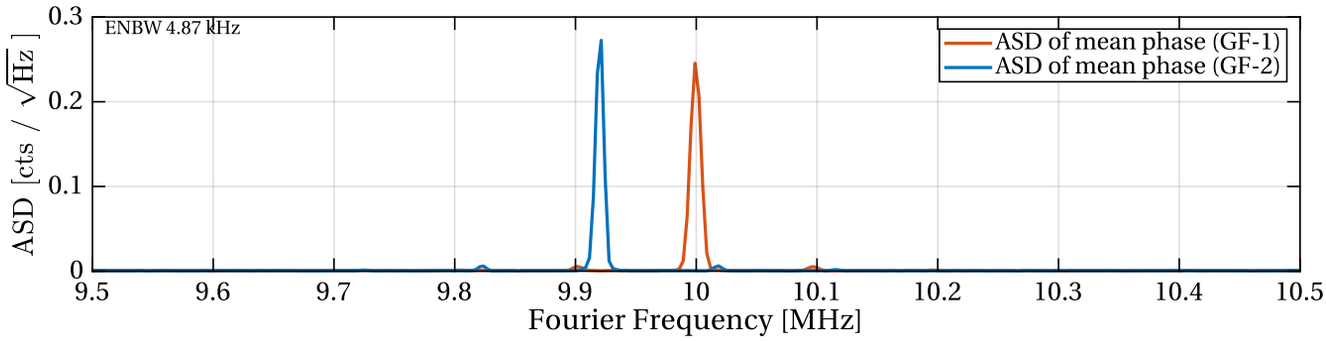

(a) ASD for the entire duration of Diagnostic Type 19 for both S/C. GF-1 is in transponder role and thus shows the offset frequency of 10 MHz. GF-2 is in master role, showing 10 MHz plus a Doppler shift of roughly 80 kHz in full round trip, caused by a relative velocity of 4 cm/s. The small sidebands, roughly 100 kHz besides the carrier frequency, originate from a PZT resonance (priv. comm. K. McKenzie, NASA/JPL, 2019).

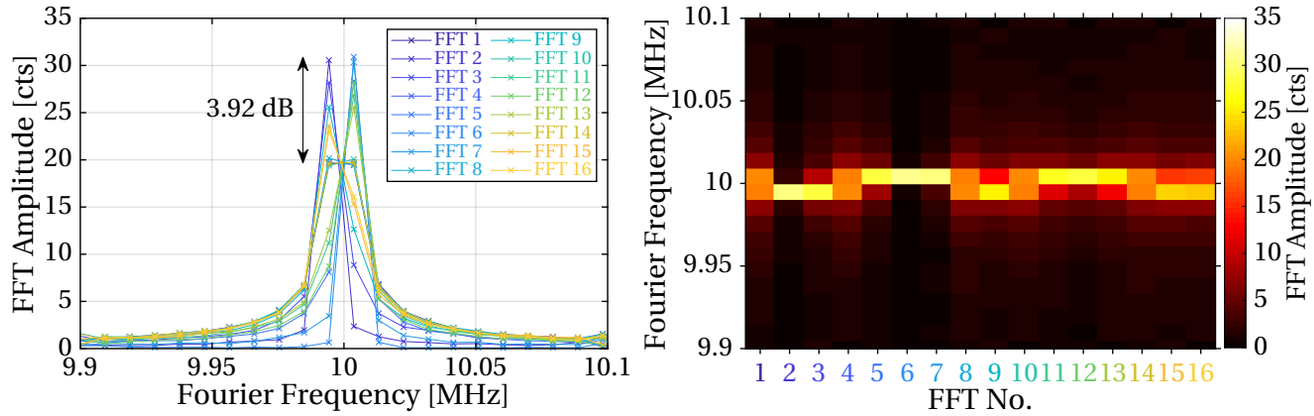

(b) GF-1: FFT amplitudes and spectrogram for segments of 4096 samples of Diagnostic Type 19. The actual beatnote frequency is at 10 MHz and thus in between of two FFT bins (see the markers, which denote the bin centers). Also, the beatnote frequency fluctuates with 1.5 kHz rms remaining laser frequency noise, which has not been removed by the DPLL due to the finite loop gain. Thus, amplitude fluctuations due to scalloping loss of up to 3.92 dB are visible.

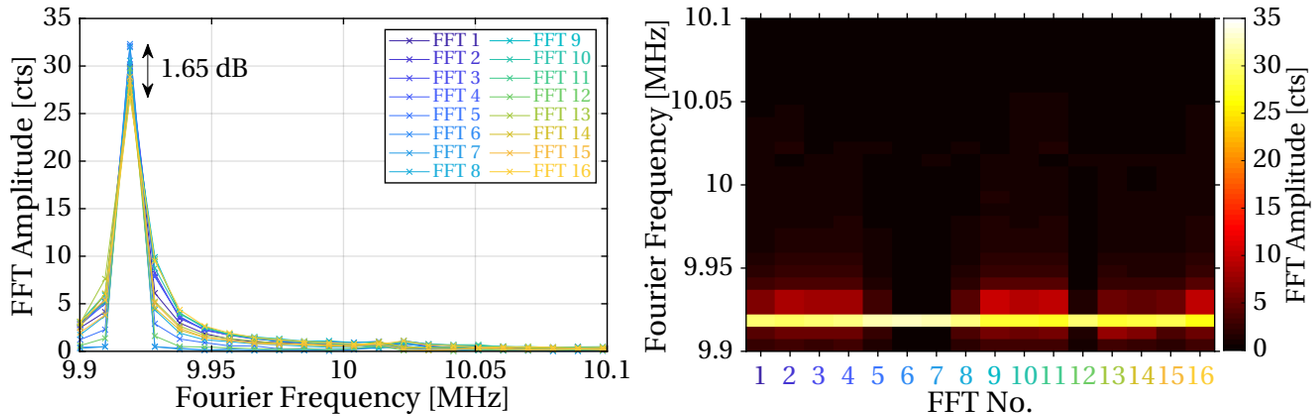

(c) GF-2: FFT amplitudes and spectrogram for segments of 4096 samples of Diagnostic Type 19. The beatnote frequency is estimated to be 9.919 262 MHz (see text). This corresponds to the relative velocity in the order of 4 cm/s. The beatnote frequency is fixed within one bin, hence a loss of 3.92 dB is not expected.

Figure 6.18.: Spectral analysis of Diagnostic Type 19 for both S/C, taken on 2018-06-15. See the individual captions for details. For the lower two panels, each FFT has a length of 4096 samples at a rate of f_{USO}, giving a length of approximately 100 µs per FFT. Images are based on `GF1_NYA_20180615T093014_diagDataType19_1.bin` and `GF2_NEN_20180615T110425_diagDataType19_1.bin`, respectively.

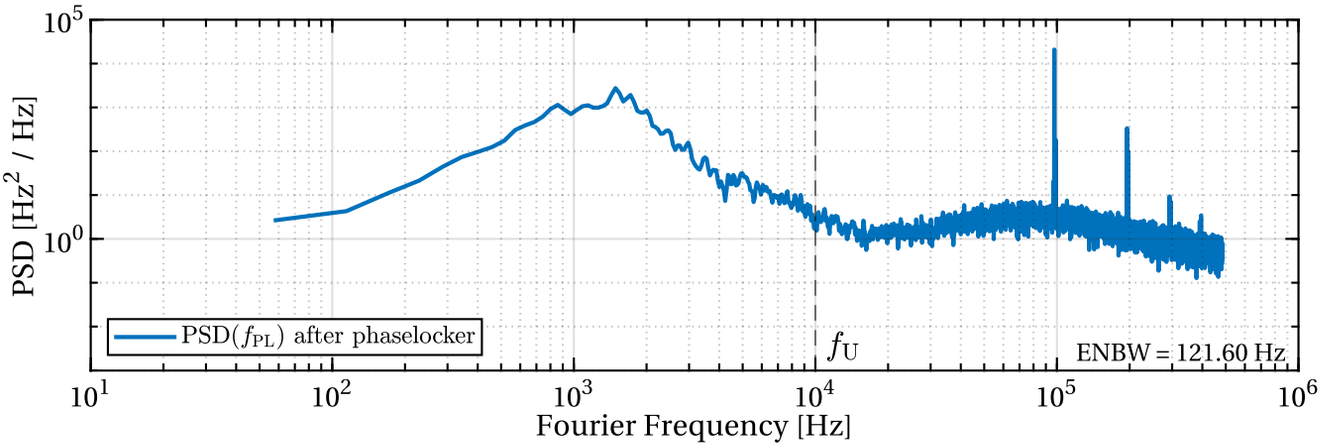

Figure 6.19.: PSD of the diagnostic scan of type 10, which yields an estimate of the free running phaselocker noise. This particular scan has been taken on 2018-06-15 on GF-1. By integrating over the frequency axis, one obtains the free running frequency noise. Here, $\tilde{f} \approx 1.428\,\text{kHz}$. At 100 kHz, the PZT resonance is visible, as well as it's higher harmonics (cf. fig. 6.18a). Image based on the file `GF1_NYA_20180615T093014_diagDataType10_3.bin`, PSD created using Nuttall4a window and a decent averaging.

Since the analytical model and the polynomial assessment of the scalloping loss do not differ much in the center region of $-0.2 \leq \Delta\tilde{f}_\text{b} \leq 0.2$ (cf. fig. 6.16), a conclusion of which model applies here can not be drawn.

In contrast, for GF-1 (fig. 6.18b), the magnitude of the FFT coefficients is fluctuating between two adjacent frequency bins. The magnitude of this fluctuation can be derived by comparing the FFT samples, where the energy is split equally between two subsequent bins, e.g. for FFT number 1, 4, 8, and the ones where the amplitude is maximal in one of the two bins. The loss arising from this observation is

$$L_\text{GF-1} = 20 \cdot \log_{10}\left(\frac{30.9\,\text{cts}}{19.7\,\text{cts}}\right) \approx 3.9\,\text{dB}\,. \tag{6.22}$$

This is in good agreement to the analytical expression for the scalloping loss, cf. eq. (2.40).

These frequency fluctuations on the transponder side are caused by residual laser frequency noise, which is not entirely suppressed by the frequency-offset DPLL. This frequency-offset DPLL is sometimes also called phaselocker, which offset-frequency locks the transponder's laser frequency to the incoming beam (cf. fig. 4.8). It actively suppresses phase variations at low Fourier frequencies, which are mainly dominated by laser frequency noise. The residual frequency variations are accessible from a diagnostic scan of type 10, which contains phase rate measurements f_PL directly after the phaselocker. The phase rate is recorded at a rate of $f_\text{USO}/40 \approx 1\,\text{MHz}$ (Dubovitsky et al., 2018). By computing a PSD of the phase rate, and integrating this spectrum up to an upper frequency bound $f_\text{U} = 10\,\text{kHz}$, it is possible to derive the rms residual frequency noise,

$$\tilde{f} = \pm\sqrt{\int_0^{f_\text{U}} \text{PSD}(f)\,\text{d}f}\,, \tag{6.23}$$

that is not getting suppressed. The upper frequency f_U is chosen such that it compares to the rate, at which the FFTs are computed within the LRP. Therefore, the integral $\tilde{f}$ is an estimate of the variations of different evaluations of the FFT.

The only diagnostic scan of type 10 ever recorded was scheduled on 2018-06-15. It's PSD is shown in fig. 6.19. The integral up to $f_U = 10\,\text{kHz}$ yields a phaselocker noise of approximately $\tilde{f} \approx \pm 1.428\,\text{kHz}$. For comparison, the phaselocker noise up to Fourier frequencies of nearly 5 kHz can also be estimated from a diagnostic scan of type 11, providing phase measurements ϕ_{PL} at a rate of roughly 10 kHz (Dubovitsky et al., 2018). The phase can be transferred to equivalent phase rates by derivation, i.e. $f_{PL} = \mathrm{d}\phi_{PL}/\mathrm{d}t$. Afterwards, the integral can be calculated as before. These scans of type 11 have been taken several times in order to investigate PJs. Averaging over 40 of these diagnostic scans gave an rms free running frequency noise of $\tilde{f} \approx \pm(1.685 \pm 0.191)\,\text{kHz}$ below Fourier frequencies of 5 kHz, which is in agreement to the number derived from diagnostic data type 10 above.

It is recalled, that the FFT frequency bins have a width of roughly 9.5 kHz. The transponder's beatnote frequency of 10 MHz is located closer than 1 kHz to the edge of it's frequency bin, see fig. 6.16. Therefore, the free running phaselocker noise of $\tilde{f} \approx 1.5\,\text{kHz}$ can indeed cause the FFT peak to move to the adjacent Fourier frequency bin. A simulation, in which frequency variations of 1.5 kHz at low Fourier frequencies are added on to a 10 MHz carrier frequency, showed results that are in good agreement to fig. 6.18b. Differences are only barely visible, therefore the results are not shown. However, these beatnote frequency variations are only observable in the high rate data since it is filtered out during the low-pass filtering, i.e. decimation, to the science sampling rate of 10 Hz.

For the CNR calculations, these residual beatnote frequency variations would not matter that much, if the offset frequency of 10 MHz was in the center of a bin of width 9.5 kHz. However, since the offset frequency is almost at the edge of a bin, the FFT estimates fluctuate between two adjacent frequency bins.

6.4.6. Summary of Scalloping Loss Investigations

The investigations presented above, help a lot for the enhancement of the CNR estimation. The effect of the amplitude approximation method for the FFT amplitudes was investigated and was shown to cause high-frequency variations, which add to the values of the `fftSNR`, see section 6.4.2 and fig. 6.17. Furthermore, the expected scalloping loss for each single FFT computation within the LRP was proven using the high-rate data of diagnostic scan types 10 and 11, see section 6.4.5. Consequently, variations due to residual laser frequency noise, which is not getting suppressed by the phaselocker was investigated and given an approximate value of ±1.428 kHz.

However, the scalloping loss in the low-rate `fftSNR` time series can not be explained. It is either related to the FFT implementation within the LRP or of the decimation from the high-rate FFT amplitude arising from QPD currents to the low rate values for the `fftSNR` looks like. It is clear, that the FFT algorithm computes a spectrum at a rate of nearly 10 kHz, of which the maximal value is estimated using the amplitude approximation. To the knowledge of the author, no dedicated decimation filter is applied on these maxima, but the last computed value is reported at a rate of 0.1 Hz. However, a picking of the last computed sample would yield values in the range of [-4,0] dB, but as shown in fig. 6.16, this does not hold. Therefore, further simulations including an averaging over several FFT maxima, e.g. over 1 s, are performed, but did not coincide with the observations. A simulated phase time series at a rate of f_{USO} was created for this analysis, i.e. the same as used in section 6.4.3. For each 4096 samples, an FFT is calculated and the peak amplitude is computed using the approximation method and the exact value. The resulting time series of FFT peak amplitudes is down sampled by averaging over different intervals. The maximal loss out of these averaged time series is depicted as the scalloping loss in fig. 6.20. However, even if the averaging time is up to 10 s, which is the data rate of the `fftSNR` in the LRI telemetry, the scalloping loss for averaged FFT peak amplitudes does not reach values up to −2 dB but stays close to the expected value of −3.92 dB.

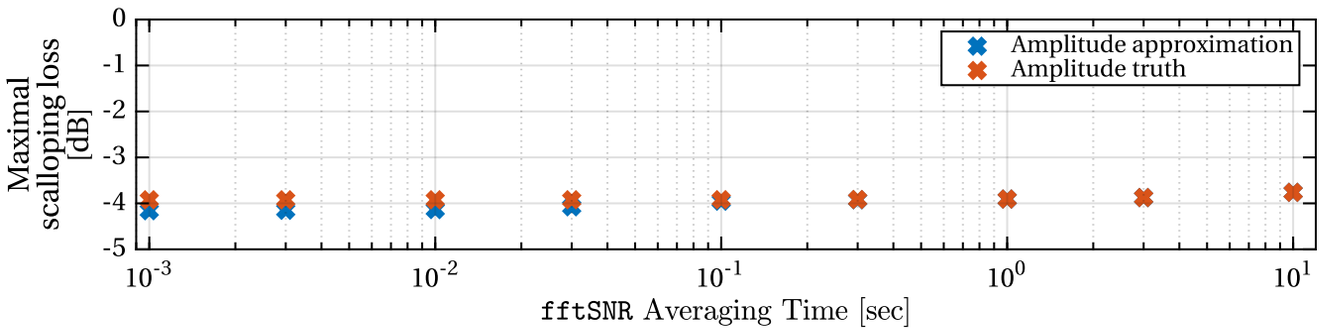

Figure 6.20.: Simulations of the scalloping loss using different lengths of averaging time. For amplitude estimation of the highest FFT peak, the exact value as well as the approximation method are used. Neither of them shows the in-flight behavior of only about 2 dB scalloping loss. See text for a description of the simulation.

6.5. Spatial Beam Properties in the Far-Field

The beam properties have been measured on-ground and projected to the far-field, i.e. 220 ± 50 km, but the actual flight data allows to verify the predictions and to assess the accuracy of the used ground measurement system, for example, with regard to future missions. Furthermore, knowledge about the laser beam properties can help to analyze and understand the LRI data. Especially of interest is the TMA co-alignment error, which manifests in a non-parallelism of the incoming and outgoing beam.

During the commissioning phase in July 2018, a DWS scan was taken on each S/C. During this scan, the DWS setpoints for both axes, pitch and yaw (corresponding to rotations around y and z in the SRF), are modulated with a hexagon-shaped spiral pattern with a maximal amplitude of 100 µrad, as shown in fig. 6.21. By applying non-zero DWS setpoints, $\mathrm{DWS}_{\mathrm{h},0}$ and $\mathrm{DWS}_{\mathrm{v},0}$, to the DWS-FSM control loop on one of the two S/C, the transmitting beam is intentionally misaligned w.r.t. the nominal beam

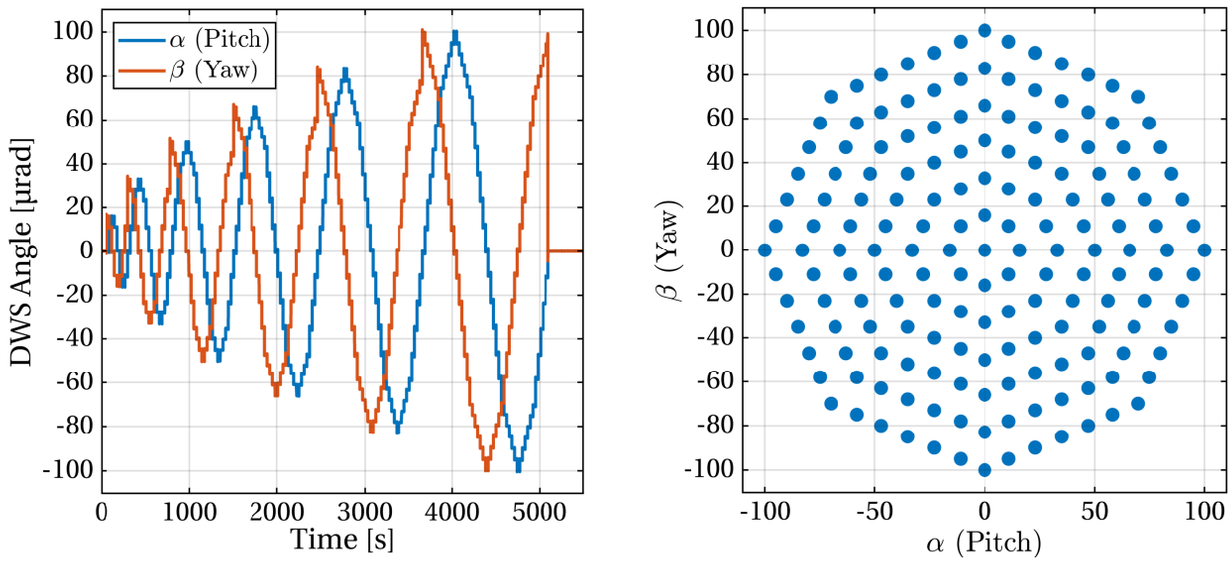

Figure 6.21.: DWS Scan pattern in time and spatial domain. This plot is not made from measured DWS angles but from the parameter files, that got uploaded to the S/C. It consists of 168 setpoints with a hold-time of 30 s

axis. For a TMA without co-alignment errors, the nominal beam axis would be co-aligned to the LoS.

However, even if the pointing is changed, the DWS-FSM control loop on the receiver side is not affected, since the phasefronts in the far-field are spherical and locally flat. Hence, plane waves will be sensed, perpendicular to the LoS. However, due to the Gaussian shaped intensity profile, the received power at the distant S/C decreases, since the beam spot's maximum does not hit the distant aperture. This lowers the CNR on the receiving S/C. Furthermore, the wavefronts of the LO and RX beams on the transmitting S/C are intentionally tilted against each other. Therefore, the interferometric contrast on the QPD and the CNR locally decrease as well.

By rasterizing the pitch-yaw plane for one of the S/C, it is possible to derive spatial characteristics of the beam. These characteristics are usually split into the intensity profile and the phasefront. These two are investigated further in the following.

6.5.1. Intensity Profile

The intensity profile in the far-field is expected to be elliptic and the laser beam can be modeled as a Simple Astigmatic Gaussian Beam (SAGB), see section 2.1. An SAGB features different waist sizes and locations for the two principal beam axes and thus an elliptical beam spot.

The position, at which the maximal intensity of the profile is sensed, mainly shows the direction of the beam pointing. However, other than introduced in eq. (2.16), the intensity profile in the scope of a DWS scan is not parameterized using Cartesian coordinates but by means of DWS setpoint angles, α and β. The intensity profile of a SAGB has only few free parameters. These are the TMA co-alignment errors in pitch and yaw direction, α_0 and β_0, and the beam's divergence angles, Θ_1 and Θ_2. Furthermore, a rotational degree of freedom around the LoS, ϑ, is introduced, since the beam's principal axes are in general not co-aligned with the DWS directions in the LRI optical frame (LOF). The divergence angles, Θ_1 and Θ_2, are given along the beam's principal axes. The maximal intensity is denoted as $A_{\max}$. Hence, the intensity profile reads

$$I = A_{\max} \cdot \exp\left[-\left(\frac{(\alpha-\alpha_0)\cos(\vartheta) + (\beta-\beta_0)\sin(\vartheta)}{\Theta_1} \right)^2 - \left(\frac{-(\alpha-\alpha_0)\sin(\vartheta) + (\beta-\beta_0)\cos(\vartheta)}{\Theta_2} \right)^2 \right] . \tag{6.24}$$

This model is applied to the amplitude measurements of the beatnote, i.e. the recordings of the i- and q-values of the DPLL on the receiving S/C, as introduced in eq. (2.33) and section 2.5. However, the amplitude of the profile is normalized by $A_{\max}$ in the following, since the interest lies on the beam shape, i.e. on the divergence angles Θ_1 and Θ_2 and the TMA co-alignment errors α_0 and β_0.

The fit results of all parameters are shown in table 6.2, while a graphical representation of the measured intensities as well as the intensity models are shown in fig. 6.22. The optical power link budget (OPLB, v. 19.0, (priv. comm. V. Müller, AEI, 2019)) yields upper limits for the ellipticity of the beams. They are given in table 6.3 by means of divergence angles. These estimates have been derived from on-ground measurements of the beam spot properties. It should be noted, that the OPLB angles are not given in the principal beam axis but are fixed to the measurement instruments reference frame. In general, the values obtained by the DWS scan are reasonable. However, the far-field beam shape shows a higher ellipticity compared to the on-ground estimates. The ellipticity m is the ratio of the divergence angles. Since the beam's properties depend on environmental conditions like the atmospheric density, the deviations from the on-ground and in-flight measurements are acceptable.

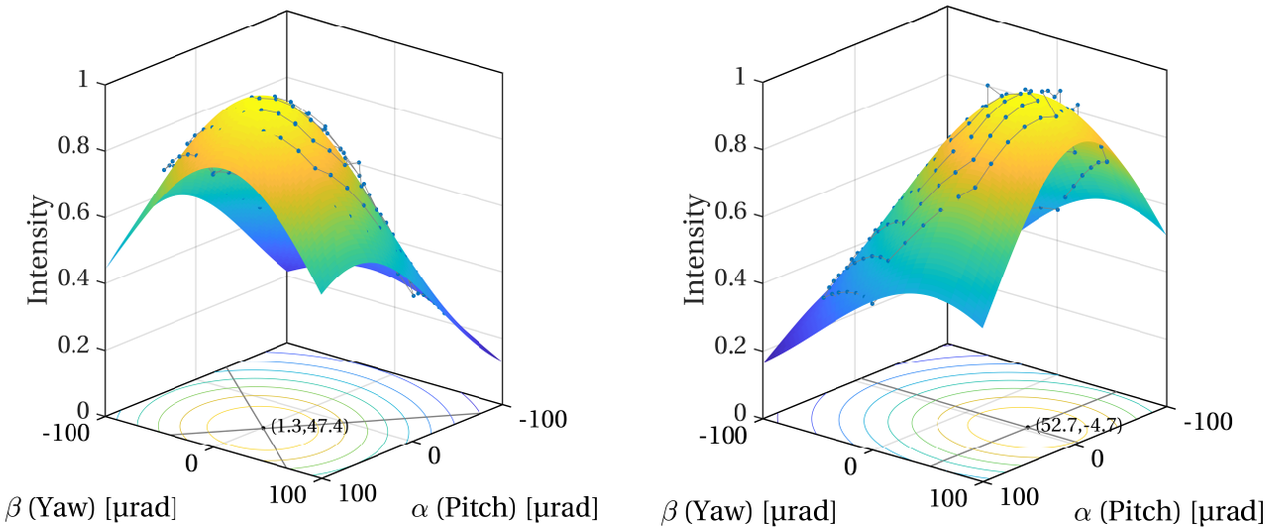

(a) Intensity profile of GF-1 as seen by GF-2

(b) Intensity profile of GF-2 as seen by GF-1

Figure 6.22.: Normalized far-field intensities for both S/C as derived from the DWS scans. The intensity axis is normalized to their respective maximum value. Blue dots mark the measured data points, while the colored surface, as well as the contour in the Pitch-Yaw plane, are derived using eq. (6.24). The black dot marks the maximum of the intensity profile, the gray lines indicate the beam's principal axes.

Parameter	Description	GF-1	GF-2
$A_{\max}$	Amplitude [a.u.]	10.545	10.996
α_0	TMA error (Pitch) [µrad]	47.36	−4.69
β_0	TMA error (Yaw) [µrad]	1.33	52.68
Θ_1	Divergence angle 1 [µrad]	146.45	144.75
Θ_2	Divergence angle 2 [µrad]	124.13	127.78
ϑ	Rotation [rad]	0.672	0.011

Table 6.2.: Fitted parameters of the far-field beam shape using an elliptical Gaussian beam (cf. eq. (6.24)). The divergence angle axes are given by means of yaw and pitch, rotated by the angle ϑ. They denote the radius in which $(1-1/e^2) \approx 86\,\%$ of the beam's optical power is transported.

Divergence	$\Theta_{1',\mathrm{OPLB}}$	$\Theta_{2',\mathrm{OPLB}}$	m_{OPLB}	Θ_1	Θ_2	$m_{\mathrm{meas.}}$
Unit	µrad	µrad	-	µrad	µrad	-
GF-1	117	131	1.12	146.45	124.13	1.18
GF-2	128	138	1.08	144.75	127.78	1.13

Table 6.3.: Beam divergence angles and ellipticity from the optical power link budget (priv. comm. V. Müller, AEI, 2019, OPLB, v. 19.0) and the corresponding quantities from the DWS measurements. The ellipticity m is the ratio of the larger over the smaller divergence angle. The OPLB divergence angles are not given within the beam's principal axes.

Furthermore, the principal axes of the beam emitted by GF-1 (gray lines in fig. 6.22a) are rotated by 0.672 rad w.r.t. the pitch and yaw axis in the LOF, while the principal beam axes of GF-2 are basically co-aligned to the pitch and yaw directions. The TMA co-alignment errors have reasonable magnitudes.

6.5.2. Phasefront Center of Curvature

Surfaces of equiphase of the electromagnetic field of a laser beam are called a phase- or wavefront. For a fundamental Gaussian Beam (GB), the phasefront in the far-field is spherical, with a radius of curvature R, cf. eq. (2.9). However, this spherical shape can change due to various reasons. Effects like ellipticity due to astigmatism can be well described. However, others, like reflections on non-planar mirror surfaces, may change the phasefront in an unexpected manner. If the shape of the phasefront is non-spherical, effects of TTL coupling may become observable, cf. section 4.3.2. Remember, TTL describes apparent phase (or length) changes under rotations. Therefore, knowledge about the phasefront's curvature may be helpful to describe peculiar behavior of the LRI.

Throughout this investigations, the laser beams are assumed to be Simple Astigmatic Gaussian Beam (SAGB), which have an elliptical beam intensity profile and phasefronts, and can therefore be characterized by two sets of waist offsets from an arbitrary reference point and the waist radii, cf. section 2.1.2. Within this model, the curvature in the far-field is constant in the two beam's principal axes, lateral to the propagation axis.

Different phasefronts in the far-field are sketched in fig. 6.23. They are shown on the right hand side as curved, solid lines in green and red. Their curvature and thus their radius of curvature yields a virtual point, that defines the Center of Curvature (CoC) $\vec{P}_{CoC}$ and $\vec{P}_{CoC,2}$. In essence, the CoC is the center point of the equiphase spheres. In the far-field and for free-beam propagation, it holds that the CoC position asymptotically approaches the position of the Gaussian beam's waist. This simplifying assumption, that the CoC coincides with the waist position is used within the following analysis.

The common beam path $y_1 + y_2 + y_3$ which starts at the actual rotational pivot point $\vec{P}_p$ is folded by the optical components and can be unfolded as shown. Since the phasefront in the far-field asymptotically converges to a spherical shape (cf. eq. (2.9) for $z - z_0 \gg z_R$), a steering of the FSM, seem to rotate the phasefronts around the virtual FSM pivot point $\vec{P'}_p$.

In the upper panel of fig. 6.23, the nominal case is shown. No DWS offset is applied and therefore, the central axis of the two depicted beams directly points at the aperture Ap of the distant S/C, regardless of their actual CoC location. However, if the FSM is rotated, the central axis intentionally points beside the distant aperture. While the red beam, whose CoC is co-located with the rotational pivot point $\vec{P'}_p$ yields the same phase as in the nominal case, a different phase is measured for the green beam. It should be noted, that such a CoC offset can only be determined by measuring the phasefront and not by the intensity profile, since the beam's central axis remains the same for both beams in the lower panel of fig. 6.23 and thus, they yield the very same intensity at the aperture. Figure 6.23 only shows one of the two lateral beam axes, however, the CoC may be located differently for the two axes, yielding a SAGB.

The amplitude of a phase change upon an angular change can be measured during a DWS scan. No phase response is expected for the case, where the CoC, or waist, is co-located with the FSM, which is the pivot point of rotation. However, phase variations at the aperture are expected for the beam depicted in green in fig. 6.23. The measured phase change in terms of the biased full roundtrip range is examplarily shown for a DWS setpoint change of approximately 100 µrad in fig. 6.24 for the last step of the DWS scan (see fig. 6.21). The phase response on is a step of about 14 nm. Steps of this magnitude can be extracted quite well, while smaller ones become critical due to the noise in the ranging phase.

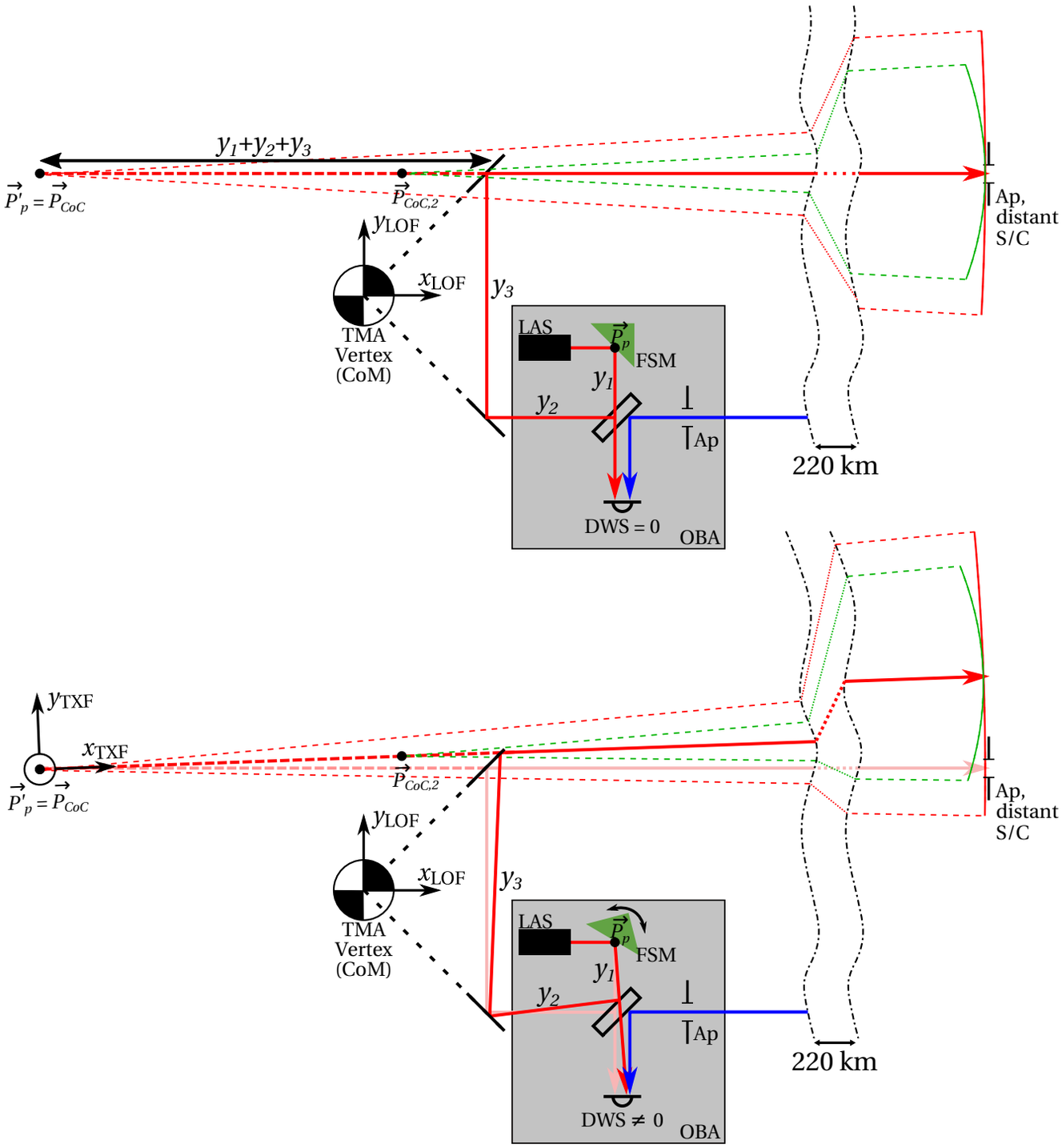

Figure 6.23.: Principle of phase changes caused by longitudinal beam waist offsets in one plane. The red dashed cone shows the beam divergence for the nominal case. Here, the CoC position $\vec{P}_{CoC}$ and FSM pivot point $\vec{P}'_p$ along the unwrapped beam path are co-located. The green phasefront has a CoC at $\vec{P}_{CoC,2}$. The solid lines on the right hand side, before the aperture Ap are lines of equiphase. Drawing not to scale. **Upper:** Nominal case without DWS offset. Both beams, with and without CoC offset, point exactly at the distant aperture, Ap, with their central axis. **Lower:** The DWS setpoint is non-zero and the control loop rotates the FSM. The red beam yields the same phase at the aperture as in the upper panel, while the green beam shows a different phase. This phase change is measurable with the LRI.

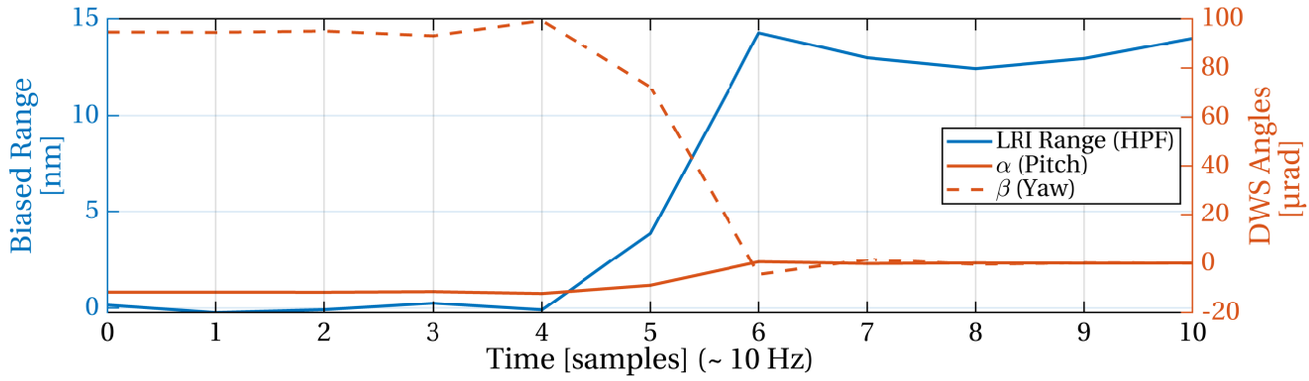

Figure 6.24.: DWS signals and ranging phase for the last step of the DWS scan. The full roundtrip range is high-pass filtered to assess the steps. The actual rotation of the FSM is much faster than shown by the DWS measurement, because the phase (and thus DWS) signals are filtered for decimation with a long filter (cf. fig. 4.8).

It is notable that this 14 nm step is observed during a DWS scan on GF-2. The magnitudes for GF-1 are smaller.

Other beam path related effects that might invoke phase changes, such as polarization and thus phase changes due to non-homogeneous mirror coatings, are in the order of nm/mrad (Müller, 2013, Appendix D) and thus negligible, since the DWS scan only approaches magnitudes of up to 100 µrad.

6.5.3. Analytical Model for the Far-Field Phasefront

To pursue an approach of the CoC induced phase changes, the laser beams are modeled as SAGB, i.e. utilizing eq. (2.17), which gives the phase of a SAGB at a specific point in space. It is recalled that the phase reads

$$\phi(x,\mathfrak{r}) = -k(x-x_0) + \eta(x) - \sum_{i=1}^{2} \frac{k\mathfrak{r}_i^2}{2R_i(x)} \tag{6.25}$$

with x and $\mathfrak{r} = (y,z)^\intercal$ given in the LOF. A Cartesian coordinate system, the TX Beam Frame (TXF), is assumed. Its center is co-located with the unwrapped FSM location $\vec{P}'_p$ (cf. fig. 6.23). The x-direction is defined as the beam propagation axis, y and z are the two lateral axes, whose concrete orientation will be introduced later. In what follows, the equations are given by means of this reference frame, if nothing else is indicated.

In the nominal setup of zero DWS setpoint and no TMA co-alignment error, the distant S/C's aperture is located at $\vec{r}_0 = (L,0,0)^\intercal$, i.e. the x-direction is co-aligned with the LoS. L is the absolute inter-satellite distance. The DWS angles α and β denote rotations around the y and z axis of the LOF, respectively. Therefore, the TXF is rotated by these angles w.r.t. the LOF.

The coordinates of the distant S/C's aperture, expressed in the TXF, are thus given by rotating the nominal position $\vec{r}_0$ by the DWS angles, $(\alpha,\ \beta)$, i.e.

$$\vec{r}_{(\alpha,\beta)} = \hat{R}(\alpha,\beta)\cdot\vec{r}_0\ . \tag{6.26}$$

The matrix $\hat{R}$ denotes the product of fundamental rotation matrices around the y- and z-axes, i.e.

$$\hat{R}(\alpha,\beta) = \begin{pmatrix} \cos(\beta) & -\sin(\beta) & 0 \\ \sin(\beta) & \cos(\beta) & 0 \\ 0 & 0 & 1 \end{pmatrix} \cdot \begin{pmatrix} \cos(\alpha) & 0 & \sin(\alpha) \\ 0 & 1 & 0 \\ -\sin(\alpha) & 0 & \cos(\alpha) \end{pmatrix} . \tag{6.27}$$

The optical pathlength of the laser beam in free space can easily be calculated by converting eq. (6.25) to units of meters, i.e. via dividing by the wavenumber k. If the CoC, in one or both lateral directions, is shifted along the beam path, this manifests in non-zero waist positions, $x_{0,\alpha}$ for pitch and $x_{0,\beta}$ for yaw. Thus, an optical pathlength difference between the nominal beam without CoC offsets and a beam with these parameters can be measured. Equation (6.25) is extended by two additional arguments to account for the CoC offset and thus, the ranging step ℓ can be expressed as

$$\ell = \frac{1}{k}\left(\phi\left(\vec{r}_0, 0, 0\right) - \phi\left(\vec{r}_{(\alpha,\beta)}, x_{0,\alpha}, x_{0,\beta}\right)\right) \tag{6.28}$$

$$= L - \eta(x_0) - \left[x_{(\alpha,\beta)} - \eta(x_{(\alpha,\beta)}) + \frac{\left(y_{(\alpha,\beta)}\right)^2}{2R\left(x_{(\alpha,\beta)} - x_{0,\alpha}\right)} + \frac{\left(z_{(\alpha,\beta)}\right)^2}{2R\left(x_{(\alpha,\beta)} - x_{0,\beta}\right)} \right] \tag{6.29}$$

$$= L - \left[x_{(\alpha,\beta)} + \frac{\left(y_{(\alpha,\beta)}\right)^2}{2R\left(x_{(\alpha,\beta)} - x_{0,\alpha}\right)} + \frac{\left(z_{(\alpha,\beta)}\right)^2}{2R\left(x_{(\alpha,\beta)} - x_{0,\beta}\right)} \right] , \tag{6.30}$$

where, in the last step, it is assumed that the Gouy phase terms cancel out, because they approach

$$\eta\left(x_0^{\mathrm{TX}}\right) \approx \eta\left(x_{(\alpha,\beta)}^{\mathrm{TX}}\right) \approx \pi/2 \tag{6.31}$$

in the far-field. The variables $x_{(\alpha,\beta)}$, $y_{(\alpha,\beta)}$ and $z_{(\alpha,\beta)}$ are the components of $\vec{r}_{(\alpha,\beta)}$. Note, that $x_{(\alpha,\beta)}$ has a value in the order of L and thus, the equivalent range change ℓ can be considered small, i.e. in the order of nm to µm.

A two dimensional Taylor expansion in the DWS angles α and β to the second order around zero yields

$$\begin{aligned} \mathcal{T}_{(\alpha,\beta)}\,\ell = &-\frac{1}{2}\left[\alpha^2 \cdot x_{0,\alpha} + \beta^2 \cdot x_{0,\beta}\right] \\ &-\frac{1}{2L}\left[\alpha^2 \cdot {x_{0,\alpha}}^2 + \beta^2 \cdot {x_{0,\beta}}^2\right] \\ &-\frac{1}{2L^2}\left[\alpha^2 \cdot {x_{0,\alpha}}^3 + \beta^2 \cdot {x_{0,\beta}}^3 - 3x_R^2\left(\alpha^2 \cdot x_{0,\alpha} + \beta^2 \cdot x_{0,\beta}\right)\right] \\ &+\mathcal{O}\left(\alpha^3, \beta^3\right) , \end{aligned} \tag{6.32}$$

where the first line defines the quadratic order of an elliptic phasefront, as expected for an SAGB. The latter two lines are negligible, because the numerically small values for the CoC offsets and DWS angles get divided by the large inter-S/C distance L or even L^2.

To assess the properties of the beam, i.e. the CoC offsets $x_{0,\alpha}$ and $x_{0,\beta}$, it turned out to be beneficial to operate on the phasefront gradients, i.e. the derivative with respect to the DWS angles α and β,

which are derived as

$$\frac{\mathrm{d}\ell}{\mathrm{d}\alpha} = -\alpha \cdot x_{0,\alpha} \tag{6.33}$$

$$\frac{\mathrm{d}\ell}{\mathrm{d}\beta} = -\beta \cdot x_{0,\beta}\,. \tag{6.34}$$

However, this analytical model is not complete, yet. As introduced at the beginning of this section, the rotation of the beam's principal axes w.r.t. the LOF are unknown. Hence, the last parameter that needs to be estimated is the rotation angle ϑ. This rotation is compensating the angular misalignment between the axis of the LOF and the actual lateral beam axes w.r.t. the ellipse semi-axes. This can easily be implemented using a 2-D rotation as follows and in a later step, utilizing a minimization algorithm to get the actual angle ϑ. The rotated DWS angles in the TXF, arising from the measured angles in the LOF, are simply computed as

$$\begin{pmatrix}\alpha\\ \beta\end{pmatrix} = \begin{pmatrix}\cos(\vartheta) & -\sin(\vartheta)\\ \sin(\vartheta) & \cos(\vartheta)\end{pmatrix} \cdot \begin{pmatrix}\alpha^{\mathrm{LOF}}\\ \beta^{\mathrm{LOF}}\end{pmatrix}. \tag{6.35}$$

6.5.4. Application to DWS Scan Data

To be applicable to the LRI telemetry, eqs. (6.33) and (6.34) need to be discretized. The derivative on the left hand side becomes a difference quotient, hence the differential DWS angles are defined as

$$\mathrm{d}\alpha_i = \alpha_{i+1} - \alpha_i \tag{6.36}$$

$$\mathrm{d}\beta_i = \beta_{i+1} - \beta_i\,. \tag{6.37}$$

with $i = 1, 2, \ldots$ counting the discrete samples of DWS angles, at approximately 10 Hz. The steps in the ranging measurement read

$$\mathrm{d}\ell_i = \rho_{i+1} - \rho_i \tag{6.38}$$

Since the difference quotient is evaluated in between of two discrete samples, the DWS angles need to be evaluated accordingly. Therefore, the averaged angles $\overline{\alpha}$ and $\overline{\beta}$ which are calculated as the arithmetic mean of two subsequent DWS angle samples α and β are introduced as

$$\overline{\alpha}_i = \frac{1}{2}\left(\alpha_{i+1} + \alpha_i\right) \tag{6.39}$$

$$\overline{\beta}_i = \frac{1}{2}\left(\beta_{i+1} + \beta_i\right)\,. \tag{6.40}$$

Furthermore, α and β are rewritten by means of the averaged DWS angles and initially unknown static offsets α_0 and β_0. These offsets account for the TMA co-alignment error, which introduces an angular mismatch of the RX and TX beams after the alignment via the DWS-FSM control loop (cf. section 4.3). In the case of an error-free TMA, the x-axes of the TXF and the LOF would be perfectly parallel, but in fact they differ by these offset angles due to imperfect alignment either of the TMA vertex w.r.t. the CoM or the orthogonality of the three mirrors. Hence, the following substitution is used:

$$\alpha \to \overline{\alpha} - \alpha_0 \tag{6.41}$$

$$\text{and} \quad \beta \to \overline{\beta} - \beta_0\,. \tag{6.42}$$

Equations (6.33) and (6.34), with substituted expressions for the DWS angles on the right hand side and in a discretized form, yield the phasefront gradients

$$\frac{\mathrm{d}\ell_i}{\mathrm{d}\alpha_i} \approx -(\bar{\alpha}_i - \alpha_0) \cdot x_{0,\alpha} \tag{6.43}$$

$$\frac{\mathrm{d}\ell_i}{\mathrm{d}\beta_i} \approx -(\bar{\beta}_i - \beta_0) \cdot x_{0,\beta}\,. \tag{6.44}$$

These expressions model the coupling between a given step in the DWS angles and the corresponding step in the ranging phase. The phase change $\mathrm{d}\ell$ is linear upon a DWS setpoint change $\bar{\alpha}$ or $\bar{\beta}$ with slope $x_{0,\alpha}$ or $x_{0,\beta}$ and with an offset α_0 or β_0. Since the two directions α and β are independent, the superposition principle holds and an expression for the step in the ranging phase is derived:

$$\mathrm{d}\ell_i = -(\bar{\alpha}_i - \alpha_0) \cdot x_{0,\alpha} \cdot \mathrm{d}\alpha_i - (\bar{\beta}_i - \beta_0) \cdot x_{0,\beta} \cdot \mathrm{d}\beta_i\,. \tag{6.45}$$

For retrieving the four unknown numbers, i.e. the two CoC offsets $x_{0,\alpha}$ and $x_{0,\beta}$ as well as the TMA co-alignment errors α_0 and β_0 a Least Squares (LSQ) minimization is performed.

The linear LSQ method is an algorithm to solve for the j coefficients κ_j of the linear problem (Wooldridge, 2015)

$$y_i = \kappa_j X_{ij} + r_i \tag{6.46}$$

by minimizing the sum S over the squared residuals r_i

$$r_i = y_i - \kappa_j X_{ij} \tag{6.47}$$

$$S = \sum_{i=1}^{N} r_i^2\,. \tag{6.48}$$

Here, y_i are the observations made, i.e. steps in the range $\mathrm{d}\ell$, X_{ij} the design matrix of the problem and κ_j the coefficients, that need to be determined. The design matrix

$$X_{ij} = v_j(x_i) \tag{6.49}$$

itself is a function v_j of the variables x_i of the problem. This function v may be non-linear with respect to the x_i, however the problem itself remains linear in κ_j (Fahrmeir et al., 2013). The parameters itself are derived by calculating

$$\kappa_j = (X_{ij}^\mathsf{T} X_{ij})^{-1} X_{ij}^\mathsf{T} y_i\,. \tag{6.50}$$

The covariance matrix C_{ij} is symmetric and contains the non-zero variances of κ_j on the diagonal elements and co-variances of the parameters κ_j on the off-diagonal elements. It can be used to compute the correlation matrix R_{ij}, which gives, as the name is hinting, the correlation between each two elements of κ. It is symmetric and computed as (Fahrmeir et al., 2013)

$$R_{ij} = \frac{C_{ij}}{\sqrt{C_{ii} \cdot C_{jj}}}\,. \tag{6.51}$$

The correlation matrix R_{ij} will be used in later sections to assess the independence of the modeled parameters and to improve the DWS scan, however it is introduced here for completeness. A more extensive introduction to the LSQ method is given in appendix E, including the error estimation and propagation.

For the purpose of this analysis, the observation data

$$y_i = \mathrm{d}\ell_i = \rho_{i+1} - \rho_i \tag{6.52}$$

are the steps in the ranging phase at about 10 Hz, represented as difference of subsequent phase samples. The functional model $\kappa_j X_{ij}$ can be obtained from eq. (6.45) as

$$\kappa_j X_{ij} = -(\bar{\alpha}_i - \alpha_0) \cdot x_{0,\alpha} \cdot \mathrm{d}\alpha_i - (\bar{\beta}_i - \beta_0) \cdot x_{0,\beta} \cdot \mathrm{d}\beta_i \tag{6.53}$$

$$= -\bar{\alpha}_i \mathrm{d}\alpha_i \cdot x_{0,\alpha} + \mathrm{d}\alpha_i \cdot x_{0,\alpha}\alpha_0 - \bar{\beta}_i \mathrm{d}\beta_i \cdot x_{0,\beta} + \mathrm{d}\beta_i \cdot x_{0,\beta}\beta_0 \,, \tag{6.54}$$

with the parameters κ_j being

$$\kappa_j = \begin{pmatrix} \kappa_1 & \kappa_2 & \kappa_3 & \kappa_4 \end{pmatrix}^\mathsf{T} = \begin{pmatrix} x_{0,\alpha} & x_{0,\alpha} \cdot \alpha_0 & x_{0,\beta} & x_{0,\beta} \cdot \beta_0 \end{pmatrix}^\mathsf{T} . \tag{6.55}$$

This representation yields the design matrix

$$X_{ij} = \begin{pmatrix} -\bar{\alpha}^{\mathrm{TX}} \cdot \mathrm{d}\alpha & \mathrm{d}\alpha & -\bar{\beta}^{\mathrm{TX}} \cdot \mathrm{d}\beta & \mathrm{d}\beta \end{pmatrix} . \tag{6.56}$$

Finally, to derive the actual TMA co-alignment errors, α_0 and β_0, the coefficients of κ are rewritten such that

$$\kappa'_j = \begin{pmatrix} \kappa_1 & \dfrac{\kappa_2}{\kappa_1} & \kappa_3 & \dfrac{\kappa_4}{\kappa_3} \end{pmatrix}^\mathsf{T} = \begin{pmatrix} x_{0,\alpha} & \alpha_0 & x_{0,\beta} & \beta_0 \end{pmatrix}^\mathsf{T} . \tag{6.57}$$

The standard error for the two newly derived coefficients in eq. (6.57) propagate as shown in appendix E.2.

To derive the fifth and last parameter of the phasefront, which is the rotation angle ϑ of the TXF w.r.t. the LOF, the rms of the residuals, i.e.

$$\mathrm{rms}(r_i) = \sqrt{\frac{1}{N}\sum_{i=1}^{N} r_i^2} \tag{6.58}$$

is used as figure of merit for a non-linear minimization. This is performed as an outer loop over the LSQ algorithm by first deriving the rotated DWS angles (cf. eq. (6.35)), calculating the ranging steps, difference and average angles (eqs. (6.36) to (6.40)) and then performing the LSQ minimization for the other four beam parameters κ and thus κ'_j.

However, to measure the ranging phase steps $\mathrm{d}\ell$, that appear at every setpoint change of the DWS scan, the full roundtrip range differences $\mathrm{d}\ell$ need to be high-pass filtered. To ensure the accuracy of the LSQ method and its error analysis later on, a data set with a white distribution, i.e. with a constant probability density function, is needed (Wooldridge, 2015, Appendix E). Thus, the cut-off frequency for the high-pass filter needs to be chosen such that the low-frequency variations due to the gravity signal and orbital configuration are well suppressed, but a sufficient "whiteness" of the spectrum is preserved. Some configurations of the high-pass filter have been tested and are shown as a PSD in fig. 6.25. A cut-off frequency of $f_c = 0.125\,\mathrm{Hz}$ was found to be well suited to assess the steps in the high frequency regime of the ranging phase ρ, while the power in lower frequencies does not exceed the high frequency regime. Furthermore, the rows of the design matrix are high-pass filtered as well using the very same parameters.

Using these definitions, the presented algorithm can be used to derive the best estimate κ'_j, such that the sum S over the square residuals (eq. (6.48)) is minimized. In other words, the model (eq. (6.54))

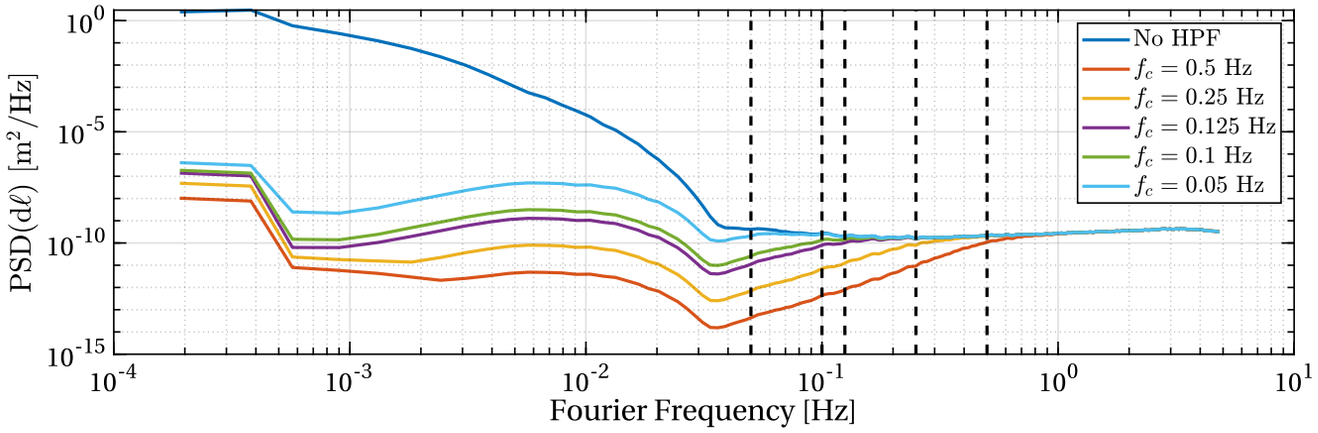

Figure 6.25.: PSD of the ranging steps $d\ell$ during DWS scan for different high-pass filters. Black vertical lines indicate the different cut-off frequencies of the filter. The purple curve, where $f_c = 0.125\,\text{Hz}$ shows the best compromise between a suppression of the low-frequency regime and the preserved whiteness of the PSD and thus is chosen for further analysis.

with the parameters κ'_j fits best to the measured data $d\ell$. It should be noted, that for eq. (6.57), it is assumed, that the two static spatial offsets, $x_{0,\alpha}$ and $x_{0,\beta}$, do not equal zero, because one needs to divide by these quantities to derive the static angular offsets α_0 and β_0. They should also not be too small to ensure a trustworthy numerical precision at the division. For an ideal LSQ result, the residuals r_i after minimization do only contain the noise of the ranging, but no more phasefront related phase variations.

6.5.5. Phasefront Derivation using DWS Scans

The DWS scans, that have been taken on 2018-07-18 were intensely analyzed in the manner described in the above sections. This led to the results shown in table 6.4.

The results obtained are in good agreement to the expectations. The LRI beams have a Rayleigh Range of $x_R \approx 18.5\,\text{m}$ and it is expected, that the waist is located within this range, which is confirmed. The difference of the two waist position offsets is in the order 1 m for both S/C, hence the beams of both LRI units is slightly elliptic. The two TMA co-alignment errors α_0 and β_0 are within an expected range. However, the results have large uncertainties, especially the results for GF-1. This has two reasons: First, the DWS angles α and β are measured on S/C, on which the scan is executed, while the ranging phase and thus the phase changes $d\ell$ are always measured on the master S/C. Therefore, for the GF-1 scan, the DWS angles are measured on GF-1, the ranging phase on GF-2. Hence, the steps in DWS and range are sampled differently. The effect of this different sampling is comparable to the PJ removal, cf. section 6.2 and fig. 6.12. The LSQ method does not account for the sampling of the steps. Furthermore, the time series are not the same and the DWS time series is interpolated to match the timing of ranging phase samples. An improved approach is to simulate the DWS steps using the PJ template, as if it was recorded on the master S/C. This would reduce the uncertainties arising from the different sampling. Besides that, the CoC offsets for GF-1 have small numerical values. As mentioned before, this may yield problems for the numerical precision of the TMA co-alignment errors α_0 and β_0 due to the division (cf. eq. (6.57)). Additionally, during the DWS scan on GF-1, there have been a few thruster activations, whose PJ residuals in the phase data might also affect the LSQ algorithm.

The results for the TMA co-alignment assessment from the phasefront investigations are, at least for

	Parameter	$x_{0,\alpha}$	α_0	$x_{0,\beta}$	β_0	ϑ	
	Unit	m	µrad	m	µrad	rad	deg
GF-1	Value	−0.287	174.578	0.304	−70.355	0.008	0.5
	95% Interval	±131.90	±81226.69	±99.36	±30925.35	-	
GF-2	Value	−4.169	13.872	−2.835	101.916	−0.293	−16.8
	95% Interval	±90.00	±702.38	±69.04	±2172.65	-	

Table 6.4.: Beam waist offsets and TMA co-alignment errors as derived from DWS scans. The negative sign for the spatial offsets $x_{0,\alpha}$ and $x_{0,\beta}$ means that the CoC is shifted from the FSM pivot point in the beam propagation direction, i.e. towards the TMA. The minimization w.r.t. ϑ is not a LSQ regression and thus, no confidence is calculated. During this period, GF-2 was in master role.

GF-2, in the order of magnitude as observed from the far-field intensity profile. It is expected, that the two observation types are not the same, since intensity profile and phasefront shape are not equal, but that they agree up to a certain degree, which is confirmed.

The correlation matrix, cf. eq. (6.51), calculated using the covariance matrix from the above LSQ minimization for GF-2, reads

$$R_{ij} = \begin{array}{c} \begin{matrix} \kappa_1 & \kappa_2 & \kappa_3 & \kappa_4 \end{matrix} \\ \begin{bmatrix} 1 & 0.0790 & 0.5583 & 0.3220 \\ 0.0790 & 1 & 0.1230 & -0.0352 \\ 0.5883 & 0.1230 & 1 & 0.5267 \\ 0.3220 & -0.0352 & 0.5267 & 1 \end{bmatrix} \end{array} \begin{matrix} \kappa_1 \\ \kappa_3 \\ \kappa_3 \\ \kappa_4 \end{matrix} . \tag{6.59}$$

It is expected, that the correlation between the pitch-coefficients κ_1 and κ_2 as well as the yaw-coefficients κ_3 and κ_4 is high, since they are linear combinations. However, this is only observed for yaw, but not for pitch. Simulations, using a simulated SAGB with the LRI parameters and arbitrary chosen angular offsets, showed, that this might be due to the very small value of the static offset angle α_0. The effect did not occur for larger angular offsets.

Arising from the current DWS pattern, i.e. the hexagonal shape, there is also a high correlation between the DWS axes. This is visible within the R_{13} coefficient, which is at roughly 0.6. Thus, for a less correlated pattern w.r.t. the DWS setpoints, the accuracy of the LSQ would profit. The values for the correlations could quantitatively be confirmed by simulation and lead to the idea of a random pattern, which will be introduced in the following section.

6.5.6. Proposal for an Enhanced DWS Scan

The current DWS scan, which intentionally was designed to assess the far-field intensity profile (cf. section 6.5.1) has some disadvantages for the presented algorithm to retrieve the phasefront parameters. These are:

- The DWS axes are highly correlated, because of the 90° phase shift of the hexagonal pattern.

- Each setpoint is held for 30 s and thus, the whole scan lasts for roughly one orbital period. Therefore, orbital variations may couple into the measurement.
- The scan only offers 168 measurement points.
- The pattern of the scan only yields DWS step magnitudes of up to 25 µrad. The phase change upon such a small step is only barely accessible within the phase measurements.

Therefore, a new proposal for a DWS scan is presented here.

To increase the statistics reliability, the number of setpoints, N, should be sufficiently large, for example $N = 1000$. These setpoints are uniformly distributed within a specific area, that will be defined later. The high number of data points will improve the statistics, while the random distribution will ensure a low correlation between the two axes.

The hold time per setpoint can be drastically reduced, because the phase readings, that are solely needed for the phasefront derivation, are sampled with roughly 10 Hz, other than the LRP i-values, that are needed for the far-field intensity profile, cf. section 6.5.1. The proposed hold time per setpoint is 1 s. Faster scanning is not advised, due to the decimation filter, whose step response affects approximately five samples around the actual step, which corresponds to approximately 0.5 s.

The boundaries of the parameter space for the two angles can either be chosen to be a circle or a square, where for both the maximal angular excursion is ±100 µrad in each axis. A higher excursion is not advised, since the CNR might drop too low due to the local tip and tilt, that decreases the interferometric contrast. A second reason is the retrieval of angular information using DWS, which only works within the interval $[-\pi, \pi)$ and shows phase wrapping otherwise. The diameter of the scanned area is given by $d_{\text{square}} = \sqrt{2} \cdot 200\,\mu\text{rad}$ or $d_{\text{disk}} = 200\,\mu\text{rad}$, respectively. With uniformly distributed setpoints within these areas, one obtains the expectation value for the step size, i.e. the euclidean distance between two subsequent setpoints, according to Dunbar (1997), as

$$A_{\text{square}} = \frac{2 + 5\sqrt{2}\ln\left(\sqrt{2}+1\right) + 2\sqrt{2}}{30} d_{\text{square}} \approx 104\,\mu\text{rad} \tag{6.60}$$

$$A_{\text{disk}} = \frac{64}{45\pi} d_{\text{disk}} \approx 90\,\mu\text{rad}\,. \tag{6.61}$$

Given in fig. 6.26 is a comparison between four different patterns, where the upper left panel shows the current hexagonal scan, that is non-randomly distributed. The average step size is very low, at about 13 µrad. In the upper right, a realization of random setpoints within a square is shown, which has the highest average step size of about 105 µrad. The lower two panels show the realization of a disk area. It is important to note, that the uniform distribution for the disk can not be created by using polar coordinates (r, θ), but must be generated in Cartesian space. Otherwise, area scaling functions need to be applied to ensure that the density in Cartesian space is constant and not contracted by the coordinate transformation. As a visualization of this effect, note the distribution and step size differences between figs. 6.26c and 6.26d. For a data generation in Cartesian space, the average step size reaches 90 µrad while in the right panel, random variables in polar coordinates are used. This shows a lower average step size of 72 µrad.

Since a higher DWS step has larger corresponding response in the ranging signal, it stands out more clearly in the noise and thus, the LSQ retrieval would benefit. For example, the 100 µrad step shown in fig. 6.24 has a response of about 14 nm in the ranging phase, which is easily visible even by eye. Even though all considered patterns show an increased average step size compared to the previously executed pattern (fig. 6.26a), the best choice in terms of the average step size is the square shaped pattern, fig. 6.26b.

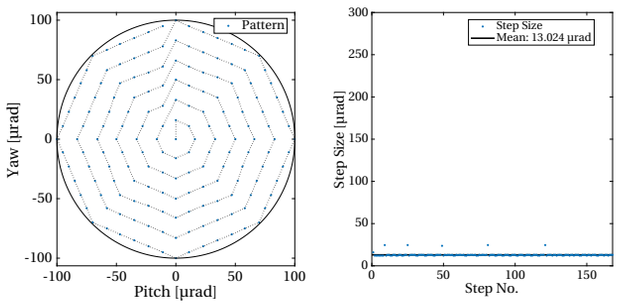

(a) DWS pattern, as executed on both S/C and analyzed within this thesis. The gray line which connects the setpoints shows the order of the setpoints, starting from the center.

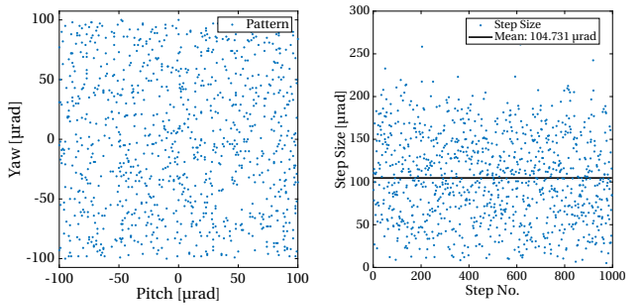

(b) Random setpoints within a square.

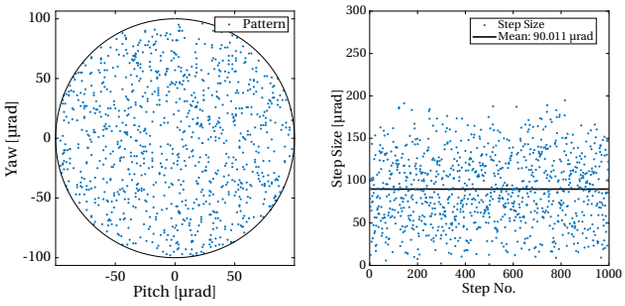

(c) Random setpoints within a disk with uniform distribution in Cartesian space.

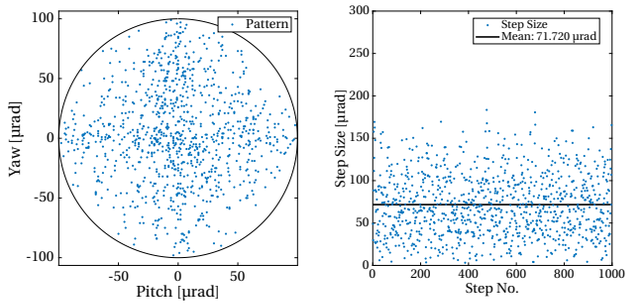

(d) Random setpoints within a disk with uniform distribution of the radius and angle in polar space.

Figure 6.26.: Comparison of the current DWS scan and different proposals. On the left sides, the pattern is shown in spatial domain, while on the right sides the step size by means of the euclidean distance of two subsequent setpoints is shown, as well as the average over all steps.

However, it should be noted, that by deflecting the beam, the intensity of the beam at the distant S/C decreases, due to the beam's Gaussian shaped intensity profile. As shown in table 6.2, the $1/e^2$ beam radius is at a DWS excursion between 120 and 145 µrad. Thus, the square pattern, shown in fig. 6.26b, should be considered critical, because the maximal excursion reaches up to 140 µrad. Therefore, the random distribution within a disk shaped field with $N = 1000$ setpoints wass proposed for execution on the S/C.

6.5.7. Phasefront Derivation using Enhanced DWS Scans

On 2019-06-14, the proposed, new DWS scan was executed on both S/C using the pattern shown in fig. 6.26c. The data is analyzed in the manner described previously. The results are shown in table 6.5. In comparison to the former scans, the new results show reduced uncertainty ranges for all parameters. The estimated CoC offset are reasonably small, well below the Rayleigh range of $x_R \approx 18.5\,\text{m}$ and even the uncertainties are in the order of a few meter. However, the values for the TMA co-alignment errors α_0 and β_0 as well as the principal beam axes rotation angle ϑ changed significantly compared to the first assessments. It is again apparent, that the results for the master S/C, which is GF-1 here, have lower uncertainties.

Furthermore, the correlation between the two DWS axes is well reduced. The correlation matrix of GF-2 is shown examplarily:

$$R_{ij} = \begin{array}{c} \begin{matrix} \kappa_1 & \kappa_2 & \kappa_3 & \kappa_4 \end{matrix} \\ \begin{bmatrix} 1 & 0.0193 & 0.0331 & 0.0223 \\ 0.0193 & 1 & -0.0189 & 0.0065 \\ 0.0331 & 0.0189 & 1 & 0.0036 \\ 0.0223 & 0.0065 & 0.0ß36 & 1 \end{bmatrix} \end{array} \begin{matrix} \kappa_1 \\ \kappa_3 \\ \kappa_3 \\ \kappa_4 \end{matrix} . \tag{6.62}$$

Here, the cross-correlation between κ_1 and κ_3 is well reduced and even the correlations between κ_1 and κ_2 or κ_3 and κ_4 are small.

6.5.8. Conclusion on the Far-Field Beam Properties

The parameters of the LRI laser beams in the far-field are well accessible using the DWS scan. The intensity profile can be derived by using the amplitude measurements from the DPLL and an elliptic Gaussian beam model. The TMA co-alignment error is derived, which is lower than 50 µrad in both lateral directions on the two S/C.

Furthermore, the offsets of the Gaussian beam waist or the CoC from the rotational pivot point can be determined using the phase measurements during the DWS scan. A comprehensive framework to derive these properties is given by introducing the TXF and deriving an analytical expression for the coupling of such an offset into the ranging measurements. However, the assessments using a LSQ minimization are tainted with large uncertainties. Therefore, a new scan pattern was proposed, which has more setpoints are a random distribution. This proposal was executed on both S/C on 2019-06-14 and yields improved results over the first generation of DWS scans. However, the data analysis techniques can still be improved, since problems are arising from different sampling rates on master and transponder S/C. This occurs, if the transponder executes the scan pattern and therefore records the DWS angle information, but the master is recording the ranging phase. An approach, do simulate the DWS readings on the master S/C was suggested, which will be implemented in the future.

	Parameter	$x_{0,\alpha}$	α_0	$x_{0,\beta}$	β_0	ϑ	
	Unit	m	µrad	m	µrad	rad	deg
GF-1	Value	−0.623	45.331	0.405	47.783	−0.194	−11.1
	95% Interval	±3.20	±289.16	±2.97	±427.74	-	
GF-2	Value	−1.182	66.716	−0.939	58.799	−0.727	−41.7
	95% Interval	±6.80	±427.81	±6.33	±463.89	-	

Table 6.5.: Beam waist offsets and TMA co-alignment errors as derived from enhanced DWS scans, taken on 2019-06-14. The negative sign for the CoC offsets, $x_{0,\alpha}$ and $x_{0,\beta}$, means that the CoC is shifted from the FSM pivot point in the beam propagation direction, i.e. towards the TMA. The minimization w.r.t. ϑ is not a LSQ regression and thus, no confidence is calculated. During this period, GF-1 was in master role.

6.6. Spectral Analysis of Ranging Variations

A spectral investigation of the ranging time series is inevitable for the understanding of the LRI and which noise sources are dominant. The ranging variations of the LRI at low Fourier frequencies ($f \ll 37\,\mathrm{mHz}$) are dominated by the gravity signal. However, at high Fourier frequencies, without the dominating gravity signal, a detailed investigation can be performed.

Shown in fig. 6.27 are two ASD of the ranging signal, computed using ten contiguous days of LRI data in July 2018 and January 2019. PJ have been removed, as described in section 6.2.4. The cyan line indicates the LRI ranging noise requirement, i.e. Heinzel et al. (2012)

$$\tilde{x}(f) < \frac{80\,\mathrm{nm}}{\sqrt{\mathrm{Hz}}} \cdot \mathrm{NSF}(f) \quad \text{for} \quad 2\,\mathrm{mHz} < f < 100\,\mathrm{mHz} \tag{6.63}$$

with the noise-shape function

$$\mathrm{NSF}(f) = \sqrt{1 + \left(\frac{f}{3\,\mathrm{mHz}}\right)^{-2}} \cdot \sqrt{1 + \left(\frac{f}{10\,\mathrm{mHz}}\right)^{-2}} \,. \tag{6.64}$$

The green line is an estimated noise level for the KBR, see e.g. Darbeheshti et al. (2017); Müller (2017). The ASDs traces clearly show the expected gravity signal and related peaks at the orbital frequency of about 170 µHz, as well as higher harmonics. The two traces are qualitatively identical for Fourier frequencies below 37 mHz. Above this limit, the LRI noise, which is mainly driven by laser frequency noise and pointing induced noise (cf. sections 4.2.1 and 4.3.2), is surpassing the gravity signal amplitudes. At 1 Hz, both curves approach the estimated equivalent laser frequency noise (yellow trace).

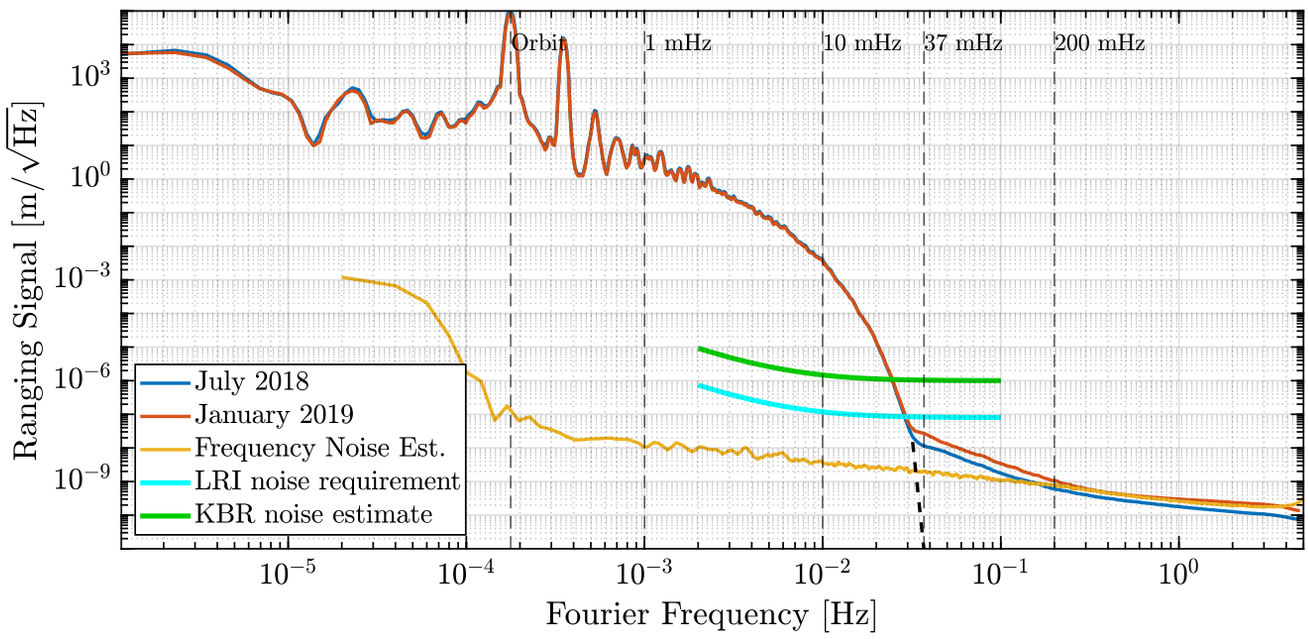

Figure 6.27.: ASD of the ranging signal for ten days in July 2018 and January 2019 with logarithmic scaled frequency axis. Nuttall4a is used as window function for spectral estimation. The cyan line shows the noise requirement, proving that the performance of the LRI lies well below and it outperforms the KBR, whose estimated noise level is indicated by the green line. An equivalent ranging noise of a laser frequency noise measurement on ground is shown in yellow, projected on a absolute distance of 200 km (cf. eq. (4.13)).

This estimate is based on a ground measurement and projected on a baseline of 200 km (cf. eq. (4.13)). The high frequency noise has an equivalent ranging signal of one to two hundred pm/$\sqrt{\text{Hz}}$. The differences for the noise levels of the two depicted traces may have several reasons. First, the laser frequency noise scales with the inter-S/C distance. Second, the two traces show measurements, that have been taken half a year apart, in which the LRI was not in science mode. Therefore, the outer conditions like temperatures due to sun intrusions might be different. Third, the master role has changed in between. While GF-2 was in master role for the data in July, GF-1 was in master role in January. There may be differences in the laser frequency noise between the two S/C, since only the master's cavity is used and the PDH lock might behave differently on the two S/C.

In the following, the spectrum of the LRI range is investigated with a special focus on the high-frequency noise.

6.6.1. Ranging Variations on Short Time Scales

Figure 6.27 shows the spectral distribution of ranging variations for a time series of ten days. However, it is possible to derive spectral estimates on short time scales to see it evolving over the orbit. For this analysis, the ranging signal, ρ, is split into several segments, called arcs, ρ_i. The length of one arc for spectral estimation is chosen as a tenth of the orbit length, roughly 9.5 min, while subsequent arcs are 90 % overlapping. Hence, every orbit is covered by roughly 100 arcs. For each of these arcs, ρ_i, a PSD is computed using a Kaiser window with a PSLL of −200 dB (cf. section 2.6.1), to effectively suppress spectral leakage from frequencies that show high amplitudes, i.e. at the orbital frequency. Afterwards, the PSD is integrated over a specific frequency region to derive rms ranging variations

$$\tilde{\rho}_i = \sqrt{\int_{f_1}^{f_2} \text{PSD}(\rho_i)\, \mathrm{d}f}\,, \tag{6.65}$$

for the frequency region $[f_1, f_2]$ and the considered arc ρ_i.

By analyzing different frequency regions independently, it is possible to draw conclusions about very specific parts in the full spectrum, such as the quality of the gravity signal and the evolution of the LRI noise. The four frequency regions chosen for analysis within this thesis are shown in table 6.6 and fig. 6.27, and are chosen such, that they show individual features throughout the spectrum. They will be called low-frequency signal (LS), gravity signal (GS), low-frequency noise (LN) and high-frequency noise (HN) regions. While the uppermost frequency bound is determined by the sampling rate of the phase measurements, the lower one is determined by the arc length.

Name	Abbreviation	f_1	f_2
Low-frequency signal	LS	1.8 mHz	10 mHz
Gravity signal	GS	10 mHz	37 mHz
Low-frequency noise	LN	37 mHz	200 mHz
High-frequency noise	HN	200 mHz	4.8 Hz

Table 6.6.: Frequency regions as chosen for spectral analysis on short time scales. Note that the lower LS frequency is, more precisely, $1/(9.5 \cdot 60)$Hz $\approx$ 1.75 mHz and the upper HN frequency is $f_{\text{USO}}/4000000/2 \approx 4.83$ Hz.

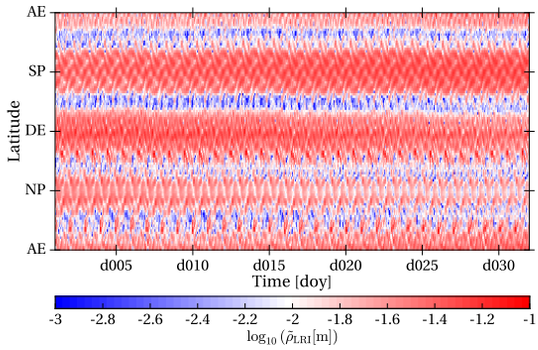

(a) Orbital ranging variations for LS

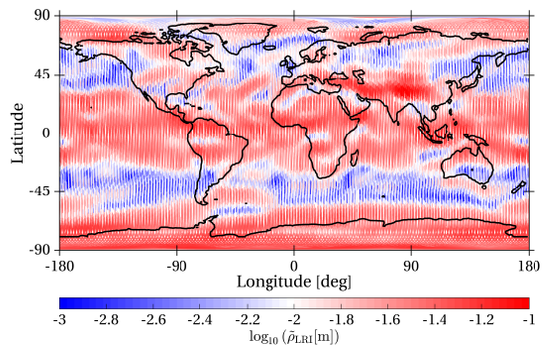

(b) LS ranging variations on a map

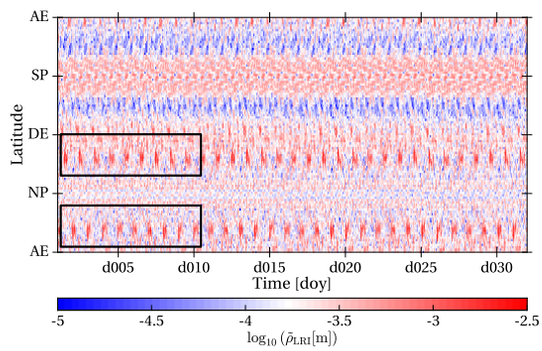

(c) Orbital ranging variations for GS

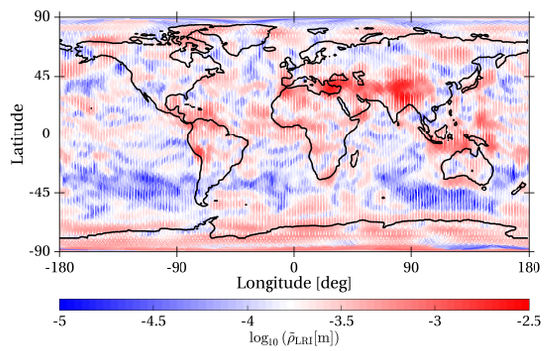

(d) GS ranging variations on a map

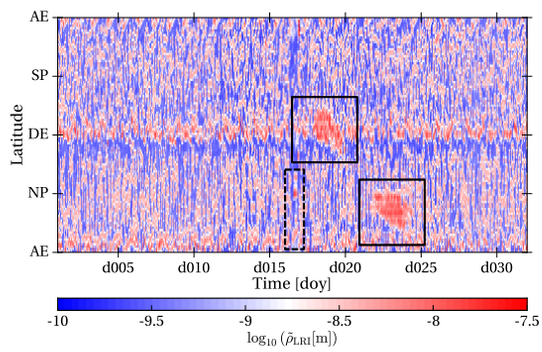

(e) Orbital ranging variations for LN

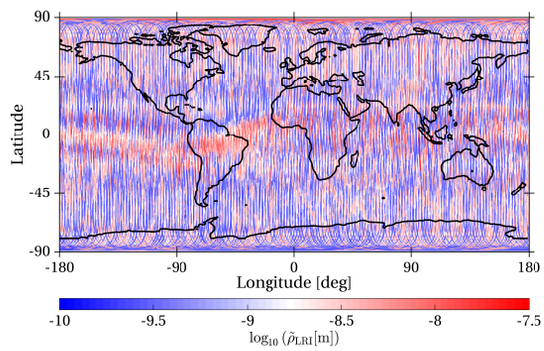

(f) LN ranging variations on a map

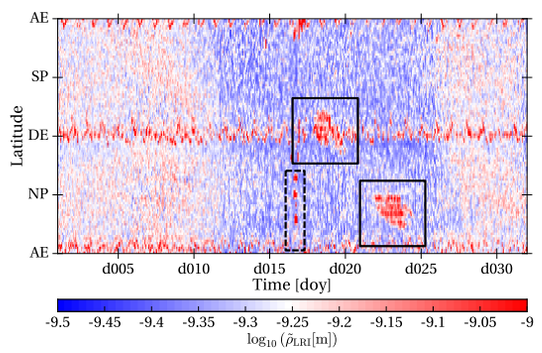

(g) Orbital ranging variations for HN

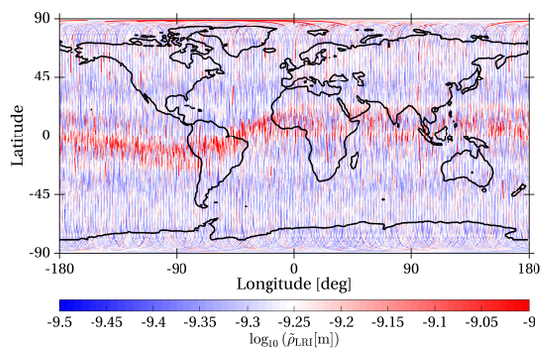

(h) HN ranging variations on a map

Figure 6.28.: LRI ranging variations $\tilde{\rho}_{\mathrm{LRI}}$ for the four frequency regimes defined in table 6.6. **Left column:** Coloring as function of time and position in orbit. NP/SP: North-/South-Pole; AE/DE: Ascending/Descending Equator. **Right column:** Ranging variations mapped on the satellites ground track.

In the following, the rms ranging variations $\tilde{\rho}_i$ are represented in two different ways: first, by plotting $\tilde{\rho}_i$ over the argument of latitude and time or second, by plotting the ground track of the centroid's geographical location of the two satellites on a map. The rms frequency variations $\tilde{\rho}_i$ are represented by color codes in both cases. The first approach easily shows time-dependent variations, while the other representation can show spatial localized effects, like for example increased gravity induced ranging variations near the Himalayas and Antarctica.

For this analysis, the month of January 2019 is chosen, since it is the very first complete month of LRI ranging measurements without any interruptions. Furthermore, it shows some interesting features like a CoM calibration maneuver and SCA blindings.

Signal Regions: LS and GS

The LS region is determined by the orbital period and it's higher harmonics. Thus, without proper modeling and removing of orbit dynamics, it is expected to show an oscillatory progression connected to those higher harmonics, as apparent in fig. 6.28b. The LS part, as well as the GS frequency regime shown in fig. 6.28d, even shows similarities compared to gravity field maps. They clearly show higher ranging variations in Oceania and near the Andes Mountains and the Himalayas, where higher signal amplitudes are presumed. Some of these features are also visible in fig. 6.28c, e.g. the daily repeating red stripes, marked with the black rectangles, belong to the Himalayas region. Summarizing, figs. 6.28a to 6.28d represent the gravity signal of interest and are in good agreement to the expectations.

Noise Regions: LN and HN

The lower four plots of fig. 6.28 show the noise dominated part of the spectrum, which is divided here into a low-frequency and high-frequency region. They show similar patterns in both, time and spatial domain. In spatial domain, they are clearly dominated by a structure, spanning along the geomagnetic equator, that is related to the more frequent thruster activation (cf. section 6.2 and fig. 6.5). It will be investigated in more detail below.

In the time domain, there are two more noticeable features. The first one is marked with black squares, showing small regions of high ranging variations, that occur once per orbit on two to three subsequent days. These regions are in coincidence with the CHU availability on GF-2. Figure 6.29 shows the number of available Camera Head Units (CHUs) for both S/C. For GF-1, most of the time there are all three cameras available, other than on GF-2, which more often has only two or even one head available. In particular, for GF-2 there are two major and one minor spot of blinding, while for GF-1 there is only one minor spot. The major spots of GF-2 can be assigned to the regions of high ranging variations in the LN and HN region. During these periods, the attitude is not determined as precise as usually. This causes the AOCS to activate thrusters more frequently.

The second region, marked with the dashed rectangle in figs. 6.28e and 6.28g, shows the time of a CoM calibration maneuver. For this maneuver, the AOCS attitude mode is switched from NOM-FP (Fine-Pointing) to NOM-AH (Attitude Hold), which deactivates the thrusters and has more relaxed requirements in terms of the relative S/C pointing. After the maneuver, the AOCS recovers the attitude requirements of the NOM-FP mode, using several thrust events.

Thruster firings can cause ranging variations in three different ways: Linear accelerations, attitude variations, that cause TTL or residuals of the PJ removal. The first two effects will be discussed in the following, while the latter quantity is not well accessible.

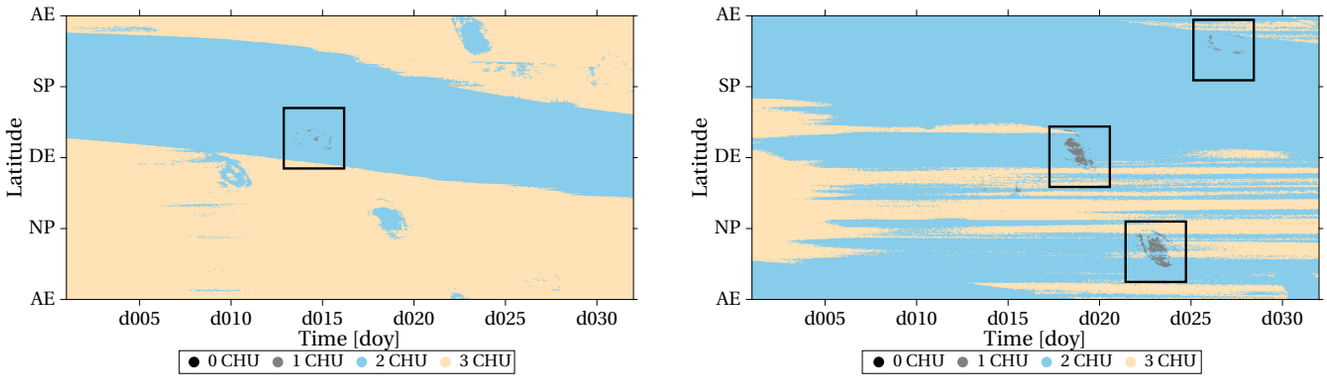

(a) Number of available CHU for GF-1

(b) Number of available CHU for GF-2

Figure 6.29.: Number of available Camera Head Units (CHUs) in January 2019. GF-1 in general shows a better performance in terms of available CHU. For some periods, only one CHU available, marked with squares. These regions match the ones of higher ranging variations (cf. figs. 6.28e and 6.28g).

6.6.2. Non-Gravitational LoS Accelerations

The ACC measurements include linear accelerations in all three degrees of freedom (cf. section 3.2.1). An exemplary time series of all linear accelerations for three hours of d001, 2019 is shown in fig. 6.30. Here, every thruster activation clearly stands out as linear acceleration. For each thruster, the linear accelerations show different amplitudes in the different axes. The thruster activations couple, because the actual applied force by the thrusters is not symmetric w.r.t. the CoM (cf. section 3.2.1) and therefore do not cause only rotational accelerations. Hence, these accelerations have an impact on the ranging measurement. This is not visible within the KBR data, but since the LRI has lower noise, the linear acceleration in x-direction in the SRF, which is approximately co-aligned with the LoS, is measurable. It should be noted, that the ACC units in GRACE-FO have problems to dissolve the accelerations caused by thrusters and show some unexpected noise, e.g. at transitioning into Earth's shadow. Therefore, the ACC1A and ACC1B data products are obsolete and replaced by a transplanted ACT product, which is to be used (McCullough et al., 2018). Furthermore, for this analysis, it is advised to use ACT1A, because of the higher data rate of 10 Hz, compared to ACT1B, which is additionally low-pass filtered with a cut-off at roughly 35 mHz (cf. green traces in fig. 6.31).

By integrating the linear accelerations in x-direction twice for both S/C, the equivalent ranging signal is derived:

$$x_{\mathrm{ACT,GF}\text{-}i} = \iint a_{\mathrm{ACT,GF}\text{-}i}\, \mathrm{d}^2 t\,. \tag{6.66}$$

The integration constants can be ignored, since these ranging estimates are evaluated by means of an ASD, which does not account for constant terms. The sum over the signals of both S/C gives the range variations caused by non-gravitational accelerations,

$$\rho_{\mathrm{ACT}} = x_{\mathrm{ACT,GF\text{-}1}} + x_{\mathrm{ACT,GF\text{-}2}}\,. \tag{6.67}$$

The sum is used instead of the difference, because the SRF, i.e. the x-direction, of the leading S/C is already inverted. Using this estimated non-gravitational ranging signal, ρ_{ACT}, a spectrum can be calculated for both, the raw LRI ranging, ρ_{LRI}, and the LRI ranging with subtracted ACT range estimate, $\rho_{\mathrm{LRI}} - \rho_{\mathrm{ACT}}$. These are shown in fig. 6.31 for the first of January 2019 (d001) and first of May 2019 (d121). For the ACT correction, both processing levels, 1A and 1B, are shown for comparison. A fourth trace

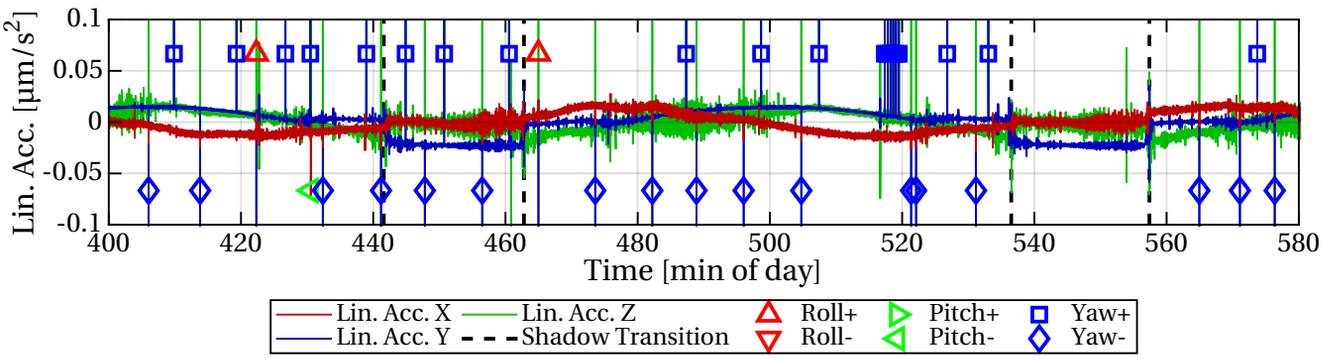

Figure 6.30.: Linear accelerations, measured by ACC on GF-1 for three hours on January 1, 2019, represented in the SRF. For every thruster activation, marked above or below the center to indicate the rotational direction, a huge spike in the linear accelerations is visible. The y-axis is cutted at $\pm 0.1\,\mu m/s^2$, but in fact, thruster activation causes linear accelerations up to $3\,\mu m/s^2$. The black dashed lines indicate transitions from sunlight into Earth's shadow and vice versa. Effects like solar radiation pressure are observable. The data is from the ACT1A-RL04 product.

shows the equivalent ranging noise arising from laser frequency noise, cf. eq. (4.13). Apparently, for both considered days, the blue trace, which represents the ACT corrected range using Level 1A, gets closer to the expected ranging noise, $\widetilde{\delta x}$ (cf. eq. (4.13) and fig. 6.27). The green trace, arising from the ACT1B product, is not very useful in this frequency band due to the filtering.

However, the raw LRI range, ρ_{LRI}, on d121 has half an order of magnitude lower noise between 30 and 50 mHz, compared to the same frequency band on d001 and it falls off more rapidly. This is indicated by the wine red lines in fig. 6.31. A preliminary explanation, based on the different AOCS thruster modes, could be discarded and the reason for the differences in the assessed ranging signal after ACT removal is still unclear. Nevertheless, the following investigation is continued using the data of January, but it is kept in mind that the actual ranging variations in the LN frequency band may be lower.

The laser frequency noise equivalent, $\widetilde{\delta x}$, is linearly projected from ground based measurements and may not be true for the in-flight performance. Therefore, the fact that the ACT1A corrected ranging signal (blue trace in fig. 6.31) is lower than the expected laser frequency noise should not be given too much attention here.

It should be noted, that the linear accelerations in LoS cause physical displacements. Therefore, this effect must not be attributed as an error, but as non-gravitational ranging signal. To conclude with this impact of non-gravitational ranging signal, the very same spectral investigation as for fig. 6.28 is done using the ACT1A corrected range, $\rho_{\mathrm{LRI}} - \rho_{\mathrm{ACT1A}}$. Since the linear acceleration's impact is only visible for the frequency domains, that are not dominated by the gravity signal, only the third and fourth frequency regions (cf. table 6.6) are shown. It is clearly visible, that the two noise frequency regions show much lower ranging variations. The overall noise level is well reduced for the normal conditions, e.g. d001 to d015, especially for regions apart from the magnetic equator. During the periods of SCA blindings as well as for parts of the CoM calibration maneuver, the rms ranging variations can be reduced by one order of magnitude from 10^{-8} m to 10^{-9} m. The reduction might actually be even better, if the ACT product's quality improves in future data releases. However, the reduction of ranging variations is not that good for the equator region, which still shows ranging variations in the order of 10^{-8} m in figs. 6.32c and 6.32d.

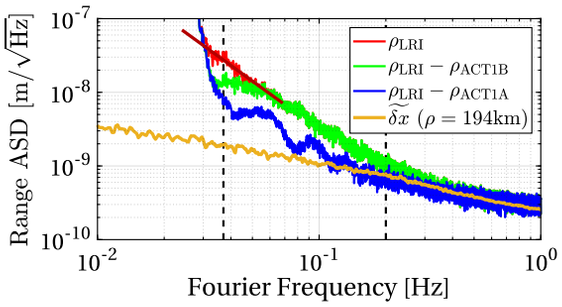

(a) LRI Range and ACT correction for d001, 2019

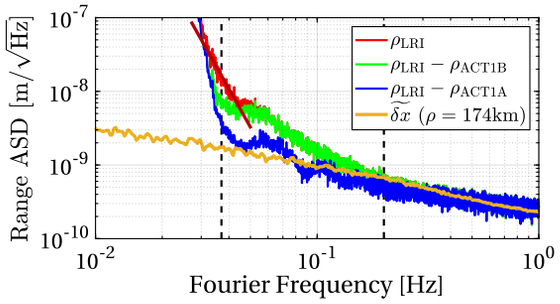

(b) LRI Range and ACT correction for d121, 2019

Figure 6.31.: ASD of the LRI range and ACT corrected range for d001 and d121, 2019. ACT corrected means, that ranging variations caused by linear accelerations have been subtracted to remove the non-gravitational impact on the range. Shown in yellow is the estimated ranging error, $\widetilde{\delta x}$, due to laser frequency noise (cf. eq. (4.13)). It is obvious, that the low-pass filter for the ACT1B data product removes a lot of signal above 35 mHz. The differences between January (d001, left) and May (d121, right) can not be explained, yet. The dashed lines indicate the frequency band boundaries (cf. table 6.6).

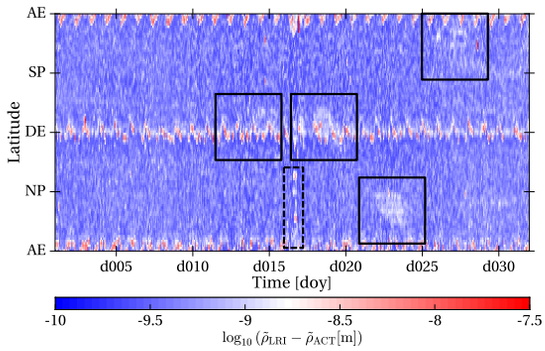

(a) ACT1A corrected ranging variations for LN

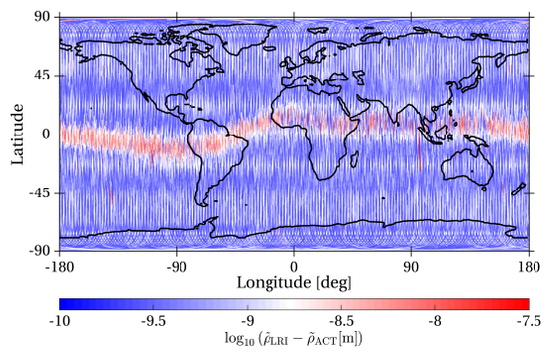

(b) ACT1A corrected LN ranging variations on a map

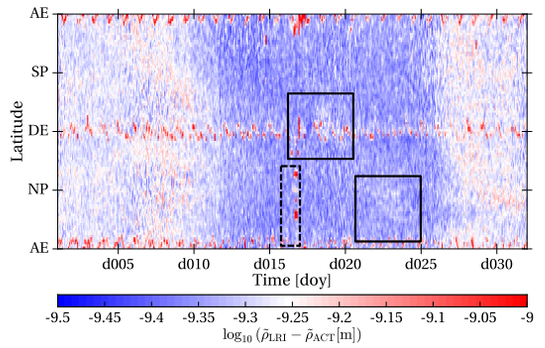

(c) ACT1A corrected ranging variations for HN

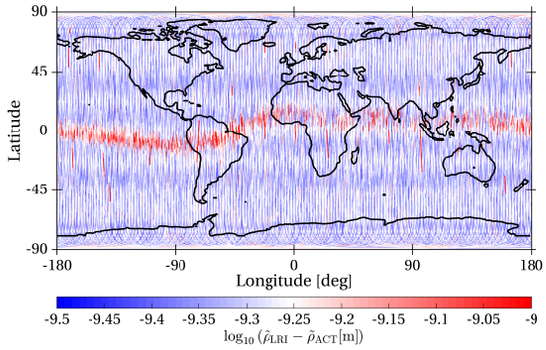

(d) ACT1A corrected HN ranging variations on a map

Figure 6.32.: ACT1A corrected LRI ranging variations, $\tilde{\rho}_{\mathrm{LRI}} - \tilde{\rho}_{\mathrm{ACT1A}}$, for the two noise dominated frequency regimes defined in table 6.6. Notations and colorbar limits as in fig. 6.28. The actual suppression of the marked regions (squares or dashed rectangle) might be even higher, due to the imperfections in the ACT1A product in January (cf. fig. 6.31).

6.6.3. Tilt-to-Length Coupling Induced Ranging Variations

One of the contributor to ranging errors, beside the laser frequency noise, is satellite pointing induced noise, i.e. TTL (cf. section 4.3.2). It can originate from the TMA (cf. section 4.3). If the TMA vertex point is not co-located with the rotational pivot point, i.e. the CoM, the pathlength through the TMA is not constant for different orientations of the incident beam. The TTL error occurs independently on both S/C and is to first order linearly dependent on the attitude angles θ_i (Wegener et al., 2018).

Even though the estimation of the actual TTL coupling factors itself is not part of this thesis, an assessment of the magnitude of this effect is performed. The estimation of the ranging error due to TTL is computed according to eq. (4.19), i.e.

$$\delta\rho_{\mathrm{TTL}} = \sum_{i=\{y,z\}} \left(\zeta_{i,\text{GF-1}} \cdot \delta\theta_{i,\text{GF-1}} + \zeta_{i,\text{GF-2}} \cdot \delta\theta_{i,\text{GF-2}}\right) . \tag{6.68}$$

In the following, the coupling factors are all assumed to be $\zeta_{y,z} = 100\,\mu\mathrm{m/rad}$ in the two angular degrees of freedom that are lateral to the beam propagation axis, i.e. the pitch and yaw angles, for both S/C. The attitude information, given in the Science Reference Frame (SRF), is gained from the FSM angles, which are reported in the LSM1B data product. This estimated TTL ranging error time series $\delta\rho_{\mathrm{TTL}}$ is visualized based on the processing introduced in section 6.6. The results are shown in fig. 6.33.

It is noticeable, that in the highest frequency region, HN, no TTL induced variations can be observed. It is presumed, that within that frequency band, only quantization noise of the Position Sensing System (PSS) is observable, which approximately is of the order of magnitude, that is apparent in fig. 6.33g, i.e.

$$\log_{10}\left(\sqrt{4} \cdot 2\,\mu\mathrm{rad} \cdot 100\,\mu\mathrm{m/rad}\right) \approx -9.4 . \tag{6.69}$$

The factor of $\sqrt{4}$ arises from the four observations, i.e. two FSM angles per S/C and the FSM noise of $2\,\mu\mathrm{rad}$ is assessed from an ASD of the angles from the LSM1B data product.

Hence, the previously described spots arising from increasing amounts of thrust events can be observed throughout all other frequencies. The plots clearly show effects caused by the SCA blindings, thrusters at the geomagnetic equator as well as the CoM calibration maneuver. The magnitude of ranging errors at these spots varies from 10^{-7} m in the LS frequencies to 10^{-9} m in the LN frequencies. However, they are small compared to the variations of the ACT corrected LRI range, cf. fig. 6.32. Only during the CoM calibration maneuver within the LN frequencies, the estimated TTL induced ranging variations $\delta\rho_{\mathrm{TTL}}$ are in the order of the LRI measurements.

It is concluded, that the TTL induced ranging error can not entirely explain the ranging variations that are remaining after ACT subtraction.

6.6.4. Conclusion on Ranging Variations

The ranging variations $\tilde{\rho}$ in the frequency regimes LN (37...200 mHz) and HN (>200 mHz) are noise dominated, because the gravity signal rolls off very quickly, cf. fig. 6.27. The variations in these frequency regions are correlated to thruster activity. The high amount of thrust events along the geomagnetic equator is caused by the missing torque of the magneto-torque rods in roll direction, while the two highlighted spots (black squares in figs. 6.28e and 6.28g) are due to CHU blindings, cf. fig. 6.29.

Each thrust event causes linear accelerations. Therefore, the LRI range can be purified by subtracting the displacements caused by linear accelerations, ρ_{ACT}, using the ACT1A data product. The remaining ranging variations are, especially within the LN frequency band, well reduced (cf. fig. 6.32).

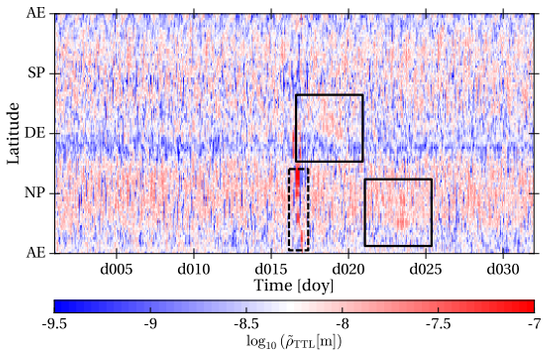

(a) Orbital TTL error variations for LS

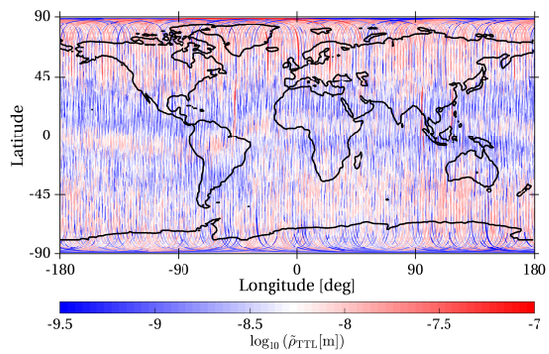

(b) LS TTL error variations on a map

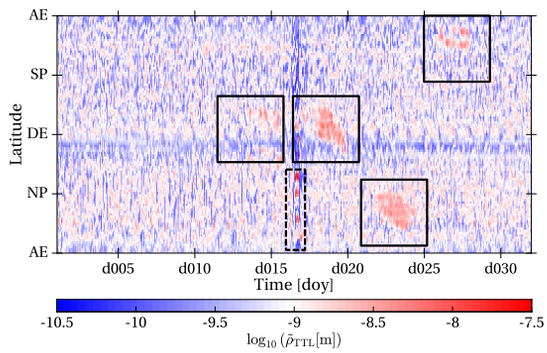

(c) Orbital TTL error variations for GS

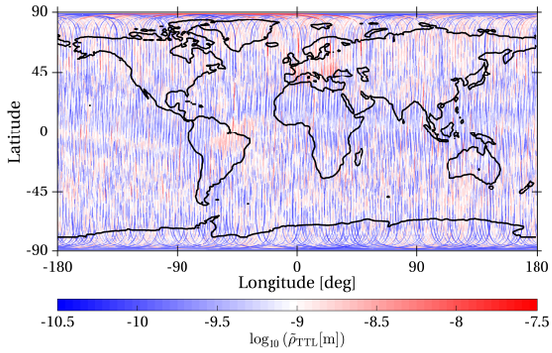

(d) GS TTL error variations on a map

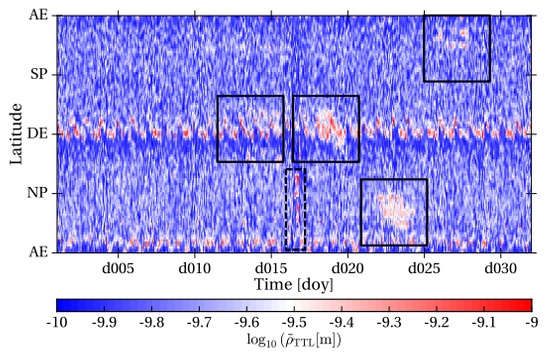

(e) Orbital TTL error variations for LN

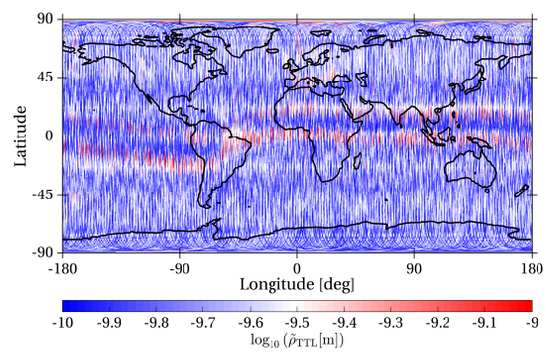

(f) LN TTL error variations on a map

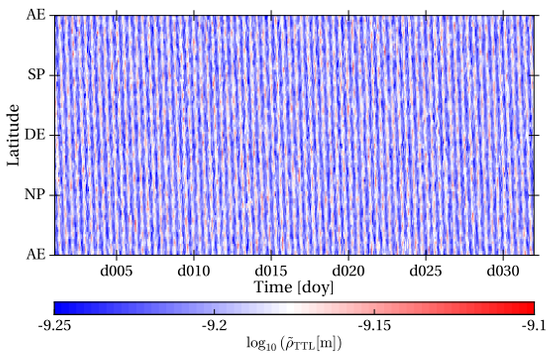

(g) Orbital TTL error variations for HN

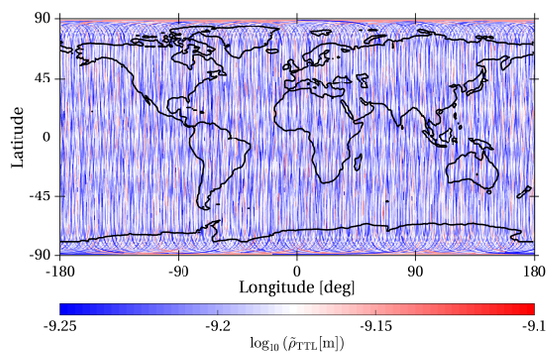

(h) HN TTL error variations on a map

Figure 6.33.: Estimated TTL error variations, $\tilde{\rho}_{\mathrm{TTL}}$, for the four frequency regimes defined in table 6.6. **Left column:** Coloring as function of Time and position in Orbit. NP/SP: North-/South-Pole; AE/DE: Ascending/Descending Equator. **Right column:** TTL error variations variations mapped on the satellites ground track.

However, the ACT product uses a thruster response model, that replaces the actual measured accelerations when a thruster fires. Hence, the removal of linear accelerations from the LRI ranging signal could be refined further by improvements of the thruster models.

In order to assess, if the variations during CHU blindings could be caused by TTL, a simulation using moderate TTL coupling factors has been done. It could be shown by using measured attitude information, that TTL coupling induces ranging error in some of the chosen frequency bands, but not in the HN regime (cf. fig. 6.33g). Thus, it is concluded that for the HN regime, TTL can not cause the variations seen in fig. 6.28g.

Another contributor to ranging variations in high frequency regimes are residuals from PJ removal. As shown in section 6.2.4, even after the removal, there are residuals of the PJs present. Therefore, a refinement of the PJ template could further decrease the ranging variations.

7. Conclusion and Outlook

The LRI is capable of tracking the inter-S/C distance without interruptions over many weeks. The obtained phase measurements have in general a good quality and are presumed to enhance the quality of the recovered gravity field. Even though the GRACE-FO mission encountered some problems during the first year in orbit (IPU on GF-2, ACC on GF-2), none of these were related to the LRI. Therefore, the feasibility of laser interferometry for inter-S/C ranging measurements was successfully demonstrated, which will find its usage in future space-based geodesy missions as well as in the Laser Interferometer Space Antenna (LISA).

This thesis started with a brief introduction of the functional concepts of modern laser interferometry in chapter 2. Afterwards, the architecture of the GRACE-FO satellites and of the LRI were presented in the chapters 3 and 4.

Processing strategies of the telemetry were shown in chapter 5, which include the SDS data products as well as the local processing at the AEI. The software framework used for the AEI processing, called the `gislparser`, was described. The development, maintenance and improvement of the `gislparser` toolbox was a part of the author's tasks during his thesis time. It grew to a powerful set of subroutines to effectively process all data streams included in the LRI telemetry. Most of the data investigations and the creation of many figures shown within this thesis have been performed by using subroutines of this toolbox. Furthermore, the `gislparser` is connected to a cloud server, which lets the LRI team easily monitor the instrument status.

In chapter 6, various kinds of data investigations were presented. It started with the investigation of the absolute laser frequency in section 6.1. Here, the applicability of a calibrated pre-flight model for the frequencies of the two lasers was tested with in-flight data. It could be shown, that the model, which uses data solely from the LRI, i.e. the laser telemetry and thermal information, is stable and within the range of the expected precision. As an interesting observation, a probable correlation was observed between the traces of the laser frequency and the so called β-angle of the orbital configuration. More data for longer time spans will reveal if the correlation remains.

The next topic, section 6.2, covered the Phase Jumps (PJs), that are related to activations of the cold-gas thrusters for attitude control of the S/C. First, the origin of those apparent frequency excursions was investigated. The LRI team found, that mechanical vibrations, caused by the opening and closing of the thruster's valve, perturb the frequency emitted by the laser. An explanation, why most of the observed PJs occur on the master side, was given. Furthermore, three algorithms that can be used for the removal of those PJs were presented, with a special attention to the one used within the `gislparser` framework. The algorithm is able to reduce those steps in the range measurement to a level, which is expected to not infer with the gravity field recovery. However, fig. 6.11b showed a deterministic pattern in the phase residuals after PJ removal, which is a starting point for further investigation.

The signal strength of the LRI phase measurement is described by the Carrier to Noise Ratio (CNR), which is defined as the ratio between the amplitude of the heterodyne beatnote and the background noise of the measurement system. The requirement of 70 dB Hz was met with ample of margin, with the average CNR being larger than 85 dB Hz, cf. fig. 6.15. However, the CNR calculation as proposed by JPL is not ideal for multiple reasons. Therefore, a new way to derive an accurate estimate of the CNR was developed, which improves the quality and validity of this measure. One of the contributors to variations of the CNR, regardless of the calculation method, is the scalloping loss, which was studied intensely in section 6.4. It is an apparent loss in the amplitude obtained by FFT methods, if the actual

frequency of the beatnote does not exactly match the center of a discrete FFT frequency bin. The scalloping loss has a magnitude of 3.9 dB for a rectangular window function. Since the derivative of phase measurements is an independent measure for the frequency, it is possible to determine and correct this loss. However, it was found that the scalloping loss for the LRI units only shows approximately 2 dB of scalloping loss. Several investigations on this topic, including simulations and on-ground measurements on a LRP prototype, did not yield an explanation yet. Nevertheless, a model to correct for the apparent scalloping loss was developed, which is able to remove the loss well, such that only high-frequency noise arising from the amplitude approximation remains. Further investigations may deepen the understanding, why the scalloping loss does not behave as expected.

From DWS scans, taken in July 2018, the laser beam's far-field properties were deduced in section 6.5. During these scans, the DWS setpoints are modulated, such that the transmit beam of one satellite is steered in space. In that way, the plane transversal to the propagation axis can be rasterized on the transmitting S/C and will be sensed by the distant S/C. The information gained from these scans include the intensity profile, which can be measured using the DPLL i- and q-values. The measured intensity shape of both S/C is in good agreement to ground-based assessments. Furthermore, the TMA co-alignment error was deduced. It matches the expectations and is within a few µrad for the pitch- and yaw-axes on both S/C.

Furthermore, the phasefront was assessed from the DWS scans. For this, a formalism including the TX Beam Frame (TXF) was developed to estimate the phasefront's Center of Curvature (CoC) using a least squares algorithm. The CoC can be regarded as the mismatch between the Gaussian beam's waist position and the FSM position, which is the pivot point of FSM rotations. Again, the investigations showed that the quantities are within the expected ranges. However, it was found that the DWS scan pattern is not ideal for the retrieval of these information. Therefore, a proposal for a new scan pattern was developed, which has been executed on the S/C. The telemetry from this new DWS scan yielded more accurate results for the CoC offsets and the TMA co-alignment errors, as proposed.

The last investigations in section 6.6 covered the distribution of the spectral ranging variations along the orbital location and along the geographical position. Beneath examining variations in the spectral density of the LRI range for a large time segment, it is performed on very short arcs, which last a fraction of the orbital period. This method is comparable to a spectrogram. In this way, it is possible to discover effects, that are narrowly geographically or temporally bounded. These effects, where higher ranging signal variations can be observed, include variations across the geomagnetic equator in the spatial domain, as well as blindings of the Star Camera Assembly (SCA) or effects due to a CoM calibration maneuver in the time domain. A connection between SCA blindings, more frequent thruster activation and a corresponding higher ranging noise was detected. The coupling of thruster activations into the ranging phase, can occur through three channels: Tilt-To-Length coupling (TTL), linear accelerations of the S/C or residuals of PJ removal. The first two of those are studied intensely. It was found, that the frequency variations in the so-called "bump" region ($37\,\mathrm{mHz} < f < 200\,\mathrm{mHz}$) indeed originate from linear accelerations. However, the effect of TTL is too small to dominate in any frequency regime.

In the future, the remaining open questions may become solved, too. This includes the scalloping loss, which is lower than expected. The problem could be traced back to either the FFT algorithm or the decimation in this thesis, which can be further investigated. Furthermore, there are indications that the PJ removal could be further improved. Possibly, the presented algorithm may get implemented into the SDS data products as well. Since the enhanced DWS scans have been taken recently, the analysis of the measurements is not finished, yet. As stated, the sampling between transponder and master phase measurements is not solved optimally, which will be faced. Last but not least, the

spectral variations in the “bump” frequency regime can still be improved by analyzing the ACT data sets. However, these are not perfect yet and therefore, the LRI ranging measurement may help to improve the generation of this transplanted ACC product.

All in all, this thesis gave an insight about the processing of the LRI telemetry at the AEI. Operational aspects of the first year in orbit are covered, including the commissioning phase. The LRI team at the AEI learned a lot about the instrument. Some of the investigations that have been performed are presented within this thesis. Within this year, none of the individual LRI subsystems showed degradation and therefore, the LRI is expected to deliver ranging data for a long time.

A. Creation of Initial Acquisition Scan Patterns

This chapter gives a small introduction in the creation of the scan patterns used within the Initial Acquisition like it is described in section 4.7.2. A realization of those pattern can be seen in the Pitch-Yaw-plane of fig. 4.10. The full procedure of creating these patterns and interpreting the Initial Acquisition data is described in detail in Dubovitsky (2016b). Both patterns can be found in fig. A.1.

A.1. Hexagonal Master scan pattern

The hexagonal pattern for Initial Acquisition contains of 20 rings with a maximal offset, or amplitude, of 3700 µrad from the center. Each ring consists of $N = n \cdot 6 + 1$ points, where $n = 0...20 \in \mathbb{N}$. These N points within each ring are spaced equally between the vertex points of the hexagon where the starting point is the same as the end point. The rings are then shifted around by one index, such that the first point of the current ring is in-line with the last point from the previous ring. The hold time at each point is 0.56 s, which is equivalent to the slower transponder Lissajous frequency.

In the case of Re-Acquisition, the pattern has a lower amplitude and is scanned once more, but in reversed order. So the scan slowly moves outwards and then back to the center again.

A.2. Lissajous Transponder scan pattern

The realization of the fast Lissajous pattern on the Transponder S/C needs some tricks. The problem is, that the PSS readings do not only include the instantaneous pattern angle but consist of four parts:

1. Reference directions, i.e. the S/C reporting about it's local attitude deviations w.r.t the estimated LoS
2. Static LRI offsets like TMA co-alignment errors
3. Pattern pointing, which is the desired observable
4. FSM overshoots, delays, ...

Thus, using the PSS readings would ask for a lot of error correction in post-processing.

An index-based approach of scan pattern creation was found to yield better knowledge about the actual position. In this case, the FSM does not really scan a Lissajous figure, but something close to. For both axes, a Look-Up Table (LUT) is created in FPGA consisting of $N = 31$ points with sinusoidal pattern. The implementation used for the scans in June 2018 have the same LUT but the axes are sampled differently ($f_x = 100\,\text{Hz},\ f_y = f_x/56 \approx 1.786\,\text{Hz}$). The pattern can be created by using

$$\text{LUT}_i = \text{trunc}\left(A \cdot \sin\left(2\pi \cdot \frac{i+1}{31}\right)\right), \tag{A.1}$$

where i is the index running from $0...N-1 = 30$, the amplitude is $A = 743$[cts] and `trunc` means truncation, i.e. the cut-off of non-integer parts. The calibration factor for converting these values into angles is 4.044 µrad/count. To get the pattern out of theses LUT, the calculation is given below as implemented in `Matlab`.

```
A = 743; % maximum Amplitude in Counts. 1 cts = 4.044 urad
Fx = 100; % Hz
Fy = Fx/56; % Hz
Pattern_Len = 31;
N_Transponder = Pattern_Len * Fx/Fy; % Here: N_Transponder = 1736

trunc = @(a) fix(a); % Matlab-implementation of truncation
LUT = trunc(A*sin(2*pi*[1:Pattern_Len]/Pattern_Len)); % create the LUT

xidx = 0:N_Transponder-1;
yidx = trunc(xidx*(Fy/Fx));
Pattern_x = LUT(mod(xidx, Pattern_Len)+1);
Pattern_y = LUT(mod(yidx, Pattern_Len)+1);
```

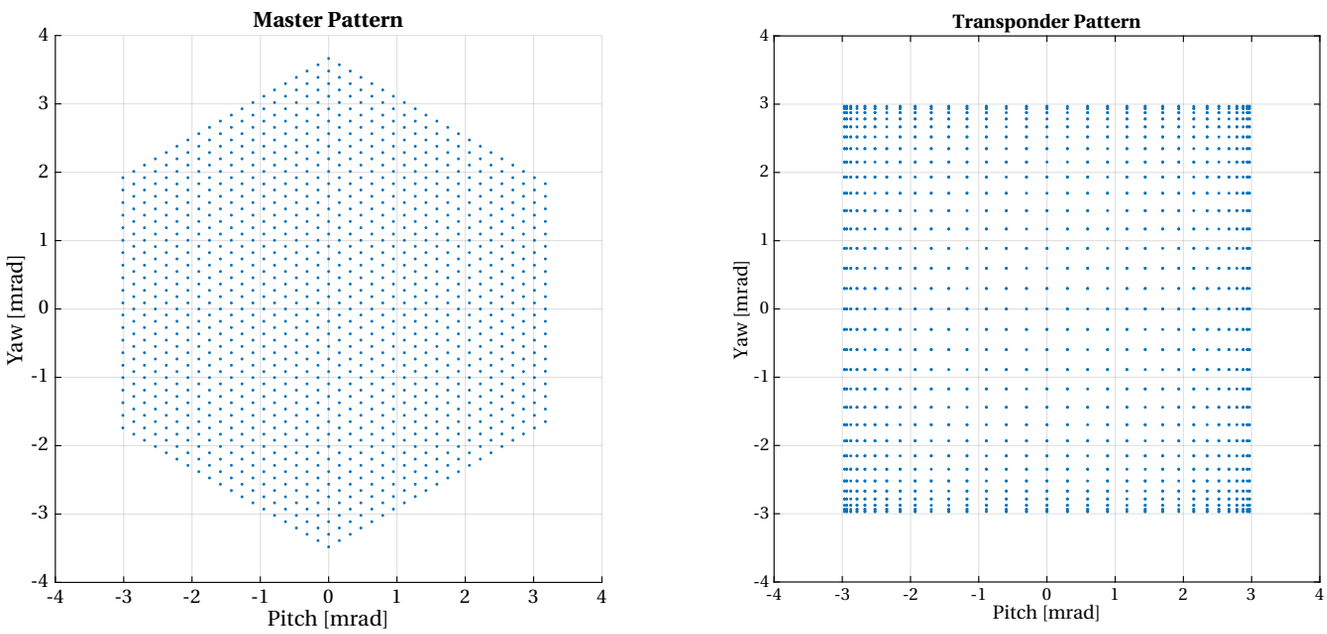

Figure A.1.: Initial Acquisition patterns for Master and Transponder role.

B. Description of Diagnostic Data Types

Throughout this thesis, varies kinds of diagnostic scans are mentioned. These scans can be scheduled from ground to take specific data streams, that are not reported within the nominal telemetry, or to record present data streams at a higher rate. Some of the scans can be performed with an active laser link, while others can not. In the following table B.1, the types used in this thesis are introduced briefly. More details and the other types of diagnostic data can be found in the LRI User Manual (Dubovitsky et al., 2018).

Table B.1.: Description of Diagnostic Scan Types. Annotations are explained below.

Type No.	Description	Sampling rate	Duration	Data Streams
1	Cavity Scan	10 kHz [1.]	51.74 s	• PHD Error Signal (12-bit)
				• Reflected Cavity DC Power (12-bit)
7	Phasemeter	10 kHz [1.]	6.47 s	• In-Phase and Quadrature values for the QPD channels 0...3 (32-bit)
10	Phaselocker	1 MHz [1.]	67.8 ms	• Phaserate of channel 3 (64-bit)
				• Phaserate of channel 4 (64-bit) [2.]
11	Phaselocker	10 kHz [1.]	25.86 s	• Phase of channel 3 (64-bit)
				• Phase of channel 4 (64-bit) [2.]
19	ADC 0-3	f_{USO}	1.74 ms	• Phase of all four QPD channels (64-bit)

Notes

1. The actual sampling rate is $f_{USO}/4000 \approx 10\,\text{kHz}$.
2. Channel 4 is used for the frequency-offset DPLL on transponder side. Refer to fig. 4.8 for the nomenclature.

C. List of Contiguous LRI Ranging Phase Segments

Table C.1.: List of all contiguous LRI ranging phase segments until 2019-06-27. Boldface lines mark segments longer than ten days, while the blue lines indicate huge gaps. Short gaps of 0.01 days indicate reboots, either spontaneous or for transition into diagnostic mode. Segments shorter than 10 seconds are not considered. The numbering coincides with the AEI internal counting.

No	Date started [UTC]	Date ended [UTC]	Length [days / orbits]	Gap before [days]
1	2018-06-14 13:23:35	2018-06-15 06:40:01	0.72 / 11.03	–
2	2018-06-15 10:11:11	2018-06-15 09:50:44	0.01 / 0.22	0.13
3	2018-06-16 17:00:16	2018-06-22 19:22:14	6.10 / 93.43	1.28
4	2018-06-22 20:36:23	2018-06-22 21:35:17	0.04 / 0.63	0.05
5	**2018-06-22 21:44:08**	**2018-07-17 09:28:02**	**24.49 / 375.15**	**0.01**
6	2018-07-18 05:09:10	2018-07-18 08:46:24	0.15 / 2.31	0.82
7	2018-07-18 08:51:59	2018-07-18 10:20:52	0.06 / 0.95	0.01
8	2018-07-18 10:25:09	2018-07-18 12:59:01	0.11 / 1.63	0.01
9	2018-07-18 13:19:29	2018-07-18 18:00:30	0.20 / 2.99	0.01
10	2018-07-18 18:05:16	2018-07-18 18:29:02	0.02 / 0.25	0.01
11	2018-07-19 11:16:28	2018-07-19 11:41:12	0.02 / 0.26	0.70
12	2018-12-12 14:35:50	2018-12-13 09:31:30	0.79 / 12.08	146.12
13	**2018-12-13 09:33:36**	**2019-02-06 15:00:01**	**55.23 / 846.03**	**0.01**
14	2019-02-06 17:30:50	2019-02-07 08:26:24	0.62 / 9.53	0.10
15	2019-03-18 13:23:48	2019-03-19 13:28:01	1.00 / 15.36	39.21
16	2019-03-19 13:37:00	2019-03-27 13:37:00	7.99 / 122.46	0.01
17	2019-03-28 19:45:49	2019-03-30 21:38:38	2.08 / 31.84	1.26
18	**2019-03-30 21:40:12**	**2019-04-25 03:31:29**	**25.24 / 386.72**	**0.01**
19	**2019-04-29 06:03:12**	**2019-06-27 00:33:49**	**58.77 / 900.33**	**4.11**

D. Phase Jump Template

The listing below shows the Matlab implementation of the creation of the phase jump, or glitch, template for the deglitching algorithm, as explained in section 6.2.4. The shape of it can be seen in fig. 6.11.

```
function g = glitch_template(t)
%% Function to create the glitch template at given times t
% t in units of samples
% fitted parameters are given to a precision of four digits
  tt = t / 8.0050;      % stretch factor of sine waves
  y = t ...             % linear part plus sine waves
      - 9.3174 * sin(1 * tt) ...
      + 1.8525 * sin(3 * tt) ...
      - 0.3089 * sin(5 * tt) ...
      + 0.4426 * sin(7 * tt) ...
      + 0.2227 * sin(11 * tt) ...
      + 0.1707 * sin(15 * tt) ...
      + 0.1228 * sin(19 * tt) ...
      + 0.0779 * sin(23 * tt) ...
      + 0.0327 * sin(27 * tt) ...
      + 0.0076 * sin(31 * tt);
  g = 0.5 * (y + 1.0);  % set to interval [0,1]
  g(t > 6.5) = 1;       % re-set to constant
  g(t < -6.5) = 0;      % re-set to constant
end
```

E. Least Squares Estimation and Error Propagation

Within this appendix, matrices and vectors are written in boldface font, lower indices denote components. For a comprehensive introduction, refer to Fahrmeir et al. (2013) or Wooldridge (2015).

E.1. General Introduction

The linear Least Squares (LSQ) method is an algorithm to find the best fit of a functional model u to some observed data stream $\boldsymbol{y}$, i.e. (Fahrmeir et al., 2013)

$$\boldsymbol{y} = u(\boldsymbol{x}, \boldsymbol{\kappa}) + \boldsymbol{r} \,. \tag{E.1}$$

During the algorithm, the sum S of squared residuals r_i with

$$r_i = y_i - u(\boldsymbol{x}_i, \boldsymbol{\kappa}) \tag{E.2}$$

$$S = \sum_{i=1}^{N} r_i^2 \tag{E.3}$$

is minimized. The model function u is a function of the M-dimensional input vector, $\boldsymbol{x}$, and the function parameters, $\boldsymbol{\kappa}$, that are to be estimated such that S gets minimal. N is the number of measured data points, i.e. $\boldsymbol{y}$ is a column vector of size N. The function u can be a linear combination of the parameters $\boldsymbol{\kappa}$,

$$u(x_i, \boldsymbol{\kappa}) = \sum_{j=1}^{M} \boldsymbol{\kappa}_j \boldsymbol{v}_j(\boldsymbol{x}_i) \,, \tag{E.4}$$

where $\boldsymbol{v}_j$ is a function of the input data $\boldsymbol{x}_i$ and M is the number of parameters used in the model. $\boldsymbol{v}_j$ may be a non-linear function of $\boldsymbol{x}_i$. It can be rewritten in a matrix form as (Wooldridge, 2015, Appendix E)

$$X_{ij} = \boldsymbol{v}_j(\boldsymbol{x}_i) \,, \tag{E.5}$$

leading to the normal equation

$$\boldsymbol{\kappa} = (\boldsymbol{X}^\mathsf{T}\boldsymbol{X})^{-1}\boldsymbol{X}^\mathsf{T}\boldsymbol{y} \,. \tag{E.6}$$

$\boldsymbol{X}$ is also called the design matrix and has the size $(N \times M)$.

Error analysis is also possible in the scope of LSQ methods. First, if the variance, σ_y^2, of the measurement, $\boldsymbol{y}$, is not known, it needs to be estimated using the unbiased estimator $\hat{\sigma}_y^2$ (Wooldridge, 2015, chapter 2.5),

$$\hat{\sigma}_y^2 = \frac{1}{N-2} \cdot S \,. \tag{E.7}$$

The hat denotes the unbiased estimator in comparison to the actual variance without a hat. However, this estimate is only valid if the input data, $\boldsymbol{y}$, has a random, or white, sampling, i.e. has a constant

probability density function (Wooldridge, 2015, Appendix E). Hence, the covariance matrix can be calculated as

$$\boldsymbol{C} = \hat{\sigma}_y^2 \cdot \left(\boldsymbol{X}^\mathsf{T}\boldsymbol{X}\right)^{-1} . \tag{E.8}$$

The diagonal elements of $\boldsymbol{C}$ are the non-negative estimators $\hat{\sigma}^2_{\boldsymbol{\kappa}}$ of the variances $\boldsymbol{\kappa}$, while the off-diagonal elements of the symmetric matrix $\boldsymbol{C}$ are referred as the covariance $\hat{\sigma}_{\kappa_i\kappa_j}$ between each two elements of $\boldsymbol{\kappa}$. Note that the quantities $\hat{\sigma}_{\boldsymbol{\kappa}}$ are not referred as the standard deviation but as their natural estimator, which is called the standard error of $\boldsymbol{\kappa}$ (Wooldridge, 2015, chapter 2.5).

The correlation matrix $\boldsymbol{R}_{ij}$ denotes, as the name is hinting, the correlation between each two elements of $\boldsymbol{\kappa}$. It is computed as (Fahrmeir et al., 2013, chapter B.2)

$$\boldsymbol{R}_{ij} = \frac{\boldsymbol{C}_{ij}}{\sqrt{\boldsymbol{C}_{ii} \cdot \boldsymbol{C}_{jj}}} . \tag{E.9}$$

Obviously, the diagonal elements $\boldsymbol{R}_{ii}$ are equal to one, while the other elements are in the range of [-1,1].

E.2. Application to TMA Co-Alignment Error Estimation

Within the scope of section 6.5.4, the desired coefficients α_0 and β_0, i.e. the TMA co-alignment errors, are linear combinations of elements of

$$\boldsymbol{\kappa} = \begin{pmatrix} x_{0,\alpha} & x_{0,\alpha}\alpha_0 & x_{0,\beta} & x_{0,\beta}\beta_0 \end{pmatrix}^\mathsf{T} . \tag{E.10}$$

Thus, to finally retrieve the quantities α_0 and β_0, $\boldsymbol{\kappa}$ is redefined as

$$\boldsymbol{\kappa}' = \begin{pmatrix} \kappa_1 & \frac{\kappa_2}{\kappa_1} & \kappa_3 & \frac{\kappa_4}{\kappa_3} \end{pmatrix}^\mathsf{T} = \begin{pmatrix} x_{0,\alpha} & \alpha_0 & x_{0,\beta} & \beta_0 \end{pmatrix}^\mathsf{T} . \tag{E.11}$$

In general, the newly derived quantities in $\boldsymbol{\kappa}'$ can be expressed as a ratio $r = A/B$ of the two known variables A and B with variance $\hat{\sigma}^2_A$ and $\hat{\sigma}^2_B$ and covariance $\hat{\sigma}_{AB}$. Thus, the error propagates as (Lee et al., 2005, eq. 4.12f)

$$\hat{\sigma}_r^2 \approx r^2 \left[\left(\frac{\hat{\sigma}_A}{A}\right)^2 + \left(\frac{\hat{\sigma}_B}{B}\right)^2 - 2\frac{\hat{\sigma}_{AB}}{AB} \right] , \tag{E.12}$$

which applies for the second and fourth element of $\boldsymbol{\kappa}'$.

For the variance estimator $\hat{\sigma}^2_{\boldsymbol{\kappa}'}$, a 95 % confidence interval I can be computed as

$$I_{95\%} = \boldsymbol{\kappa}' \pm 1.96 \cdot \sqrt{\hat{\sigma}^2_{\boldsymbol{\kappa}'}} . \tag{E.13}$$

The usage of 1.96 for the interval estimate is fine, because of the high number of data points N, which is in the order of several thousand (Wooldridge, 2015, chapter 6.4). This redefinition of $\boldsymbol{\kappa}$ to $\boldsymbol{\kappa}'$ yields the wanted quantities, i.e.

$$\boldsymbol{\kappa}' = \begin{pmatrix} x_{0,\alpha} & \alpha_0 & x_{0,\beta} & \beta_0 \end{pmatrix}^\mathsf{T} \tag{E.14}$$

and the corresponding standard errors

$$\hat{\sigma}_{\boldsymbol{\kappa}'} = \begin{pmatrix} \hat{\sigma}_{x_{0,\alpha}} & \hat{\sigma}_{\alpha_0} & \hat{\sigma}_{x_{0,\beta}} & \hat{\sigma}_{\beta_0} \end{pmatrix}^\mathsf{T} . \tag{E.15}$$

Acknowledgments

First of all, I owe deep gratitude to Dr. Vitali Müller, whose expertise, curiosity, patience and relentless will to share his knowledge is exemplary.

Secondly, my thanks go to Prof. Dr. Karsten Danzmann, whose inspiring motivation, to push the borders of what's possible even further, flows over to all institute members.

I'd also like to thank the Space Interferometry group, headed by Prof. Dr. Gerhard Heinzel, for the open-minded and friendly atmosphere, which stimulated and pushed me further on every day in office. Especially mentioned is the GRACE-FO Data Analysis group for the fruitful discussions.

I would not have mastered the physics studies without my Grøbe. Thank you guys, for learning sessions, gossip, party and serious conversations in "our" kitchen for barbecue, beer and pizza.

A special shout-out to my girlfriend, Mara, for your open heart and open mind, discussions, motivation speeches, your support and your love.

Last but not least, I thank my friends and family, that keep loving and supporting me, even if I shine with absence from time to time, whenever physics grabs my full attention.

Bibliography

Abich, Klaus et al. (2019). "On orbit performance of the GRACE Follow-On Laser Ranging Interferometer." In: *Physical Review Letters*. Paper accepted, to be published soon.

Airbus Defence & Space (June 2015). *GFO Packet Utilization Standard (G-PUS)*. GFO.IF.ASTR.SY.00001. Airbus Defence & Space.

Ales, Filippo et al. (Jan. 2014). "Modeling and Simulation of a Laser Ranging Interferometer Acquisition and Guidance Algorithm." In: *Journal of Spacecraft and Rockets* 51, pp. 226–238.

Astrium GmbH (Nov. 2013). *GRACE-FO Satellite Design Description, Section 5.10: Attitude & Orbit Control*. GFO.DD.ASTR.SY.00001. Astrium GmbH.

Bachman, B. et al. (May 2017). "Flight phasemeter on the Laser Ranging Interferometer on the GRACE Follow-On mission." In: *Journal of Physics: Conference Series* 840, p. 012011. ISSN: 1742-6596.

Ben-Kiki, Oren et al. (2009). *YAML Ain't Markup Language (YAML™) Version 1.2*. 3rd ed.

Beucher, Ottmar (2019). *Signale und Systeme: Theorie, Simulation, Anwendung*. Springer Berlin Heidelberg.

Black, Eric D. (Jan. 2001). "An introduction to Pound–Drever–Hall laser frequency stabilization." In: *American Journal of Physics* 69.1, pp. 79–87.

Breitenbach, Arvid (1999). "Against spectral leakage." In: *Measurement* 25.2, pp. 135–142.

Chen, J. L. et al. (2006). "Antarctic mass rates from GRACE." in: *Geophysical Research Letters* 33.11.

Christophe, B. et al. (2015). "A new generation of ultra-sensitive electrostatic accelerometers for GRACE Follow-on and towards the next generation gravity missions." In: *Acta Astronautica* 117, pp. 1–7. ISSN: 0094-5765.

Chulliat, A et al. (2015). "The US/UK World Magnetic Model for 2015-2020." In: *NOAA National Geophysical Data Center*.

Danzmann, K. (Oct. 2003). "LISA — An ESA cornerstone mission for the detection and observation of gravitational waves." In: *Advances in Space Research* 32.7, pp. 1233–1242.

Darbeheshti, Neda et al. (Nov. 2017). "Instrument data simulations for GRACE Follow-on: observation and noise models." In: *Earth System Science Data* 9.2, pp. 833–848.

Donati, Alessandro (2001). "Benefits from the Packet Utilization Standard in Telematics Application for Space Mission Control." In: *IFAC Proceedings Volumes* 34.9. IFAC Conference on Telematics Applications in Automation and Robotics, Weingarten, Germany, 24-26 July 2001, pp. 123–127.

Dubovitsky, Serge (2016a). *Definition of Time Specification Relevant to LRI Operations*. Tech. rep. ver. 7. NASA Jet Propulsion Laboratory / California Institute of Technology.

Dubovitsky, Serge (2016b). *Initial Acquisition Processing*. Tech. rep. ver. 12. NASA Jet Propulsion Laboratory / California Institute of Technology.

Dubovitsky, Serge et al. (Nov. 2018). *Laser Ranging Interferometer User Manual*. Rev. D. NASA/JPL.

Dunbar, Steven R. (1997). "The Average Distance between Points in Geometric Figures." In: *The College Mathematics Journal* 28.3, pp. 187–197. ISSN: 07468342, 19311346.

ESA eoPortal (n.d.). *GRACE Follow On*. [Online; accessed 20-May-2019]. URL: https://www.gfz-potsdam.de/en/section/global-geomonitoring-and-gravity-field/projects/gravity-recovery-and-climate-experiment-follow-on-grace-fo-mission/news/.

Fahrmeir, Ludwig et al. (2013). *Regression*. Springer Berlin Heidelberg.

Feng, Wei et al. (July 2015). "Global sea level variations from altimetry, GRACE and Argo data over 2005–2014." In: *Geodesy and Geodynamics* 6.4, pp. 274–279.
Flechtner, Frank et al. (Sept. 2015). "What Can be Expected from the GRACE-FO Laser Ranging Interferometer for Earth Science Applications?" In: *Surveys in Geophysics* 37.2, pp. 453–470.
Folkner, W. M. et al. (2010). *Laser frequency stabilization for GRACE-II*. tech. rep. NASA/JPL.
Franzen, Alexander (2016). *Component Library*. Version Three. Licensed under Creative Commons Attribution-NonCommercial 3.0 Unported License.
Fulcher, Ryan (2016). "Temperature fluctuation analysis for GRACE twin satellites." MA thesis. The University of Texas at Austin.

GFZ-Potsdam (2018). *Gravity Recovery and Climate Experiment-Follow-On (GRACE-FO) Mission - News*. [Online; accessed 30-January-2019]. URL: https://www.gfz-potsdam.de/en/section/global-geomonitoring-and-gravity-field/projects/gravity-recovery-and-climate-experiment-follow-on-grace-fo-mission/news/.
Girerd, André et al. (2014). *GRACE Follow-On Systems Timing Description*. Tech. rep. Technical Report JPL D-81406. NASA Jet Propulsion Laboratory / California Institute of Technology.
Goswami, S. et al. (June 2018). "Analysis of Attitude Errors in GRACE Range-Rate Residuals—A Comparison Between SCA1B and the Fused Attitude Product (SCA1B + ACC1B)." in: *IEEE Sensors Letters* 2.2, pp. 1–4. ISSN: 2475-1472.

Halliday, David et al. (2010). *Fundamentals of Physics, Extended 9th Edition*. Ed. by Stuart Johnson. John Wiley & Sons.
Heinzel, G. et al. (2002). "Spectrum and spectral density estimation by the Discrete Fourier transform (DFT), including a comprehensive list of window functions and some new flat-top windows." In: *Max Planck Society eDoc Server* 395068.0.
Heinzel, Gerhard et al. (Nov. 2012). "Laser Ranging Interferometer for GRACE Follow-On." In: *International Conference on Space Optics — ICSO 2012*. Ed. by Errico Armandillo et al. SPIE.
Herman, J et al. (2004). "Attitude control for GRACE." in: *18th International Symposium on Space Flight Dynamics*. Vol. 548, p. 27.
Hewitson, Martin et al. (2009). "Data analysis for the LISA Technology Package." In: *Classical and Quantum Gravity* 26.9, p. 094003.

Kim, Jeongrae (2000). "Simulation Study of a Low-low Satellite-to-satellite Tracking Mission." PhD thesis. The University of Texas at Austin. ISBN: 0-599-89859-3.
Koch, Alexander et al. (Oct. 2018). "Line of sight calibration for the laser ranging interferometer on-board the GRACE Follow-On mission: on-ground experimental validation." In: *Opt. Express* 26.20, pp. 25892–25908.
Kochkina, Evgenia (2013). "Stigmatic and Astigmatic Gaussian Beams in Fundamental Mode: Impact of Beam Model Choice on Interferometric Pathlength Signal Estimates." PhD thesis. Leibniz Universität Hannover.
Kornfeld, Richard P. et al. (2019). "GRACE-FO: The Gravity Recovery and Climate Experiment Follow-On Mission." In: *Journal of Spacecraft and Rockets* 56.3, pp. 931–951.

Langenbach, Harald et al. (June 2005). "Fast steering mirror for laser communication." In: *Esa Special Publications* 591, pp. 27–33.
Lee, Eun Sul et al. (2005). *Analyzing complex survey data*. Vol. 71. Sage Publications.
Lefèvre, Hervé C. (Jan. 1997). "Fundamentals of the interferometric fiber-optic gyroscope." In: *Optical Review* 4.1.

Levitt, B. K. et al. (1977). “An improved digital algorithm for fast amplitude approximations of quadrature pairs.” In: *NASA DSN Progress Report* 42, p. 40.

Luthcke, Scott B et al. (2008). “Recent glacier mass changes in the Gulf of Alaska region from GRACE mascon solutions.” In: *Journal of Glaciology* 54.188, pp. 767–777.

Mahrdt, Christoph (2014). “Laser link acquisition for the GRACE follow-on laser ranging interferometer.” PhD thesis. Leibniz Universität Hannover.

Mathworks, Inc (2018). *Matlab Documentation*. R2018b.

McCullough, Christopher M. et al. (Dec. 2018). *Description of Calibrated GRACE-FO Accelerometer DataProducts (ACT)*. JPL D-103863 of May 20, 2019. Jet Propulsion Laboratory.

Michelson, Albert Abraham et al. (1887). “On the Relative Motion of the Earth and the Luminiferous Ether.” In: *American Journal of Science* 34, pp. 333–345.

Montenbruck, Oliver et al. (2000). *Satellite Orbits*. Springer Berlin Heidelberg.

Morrison, Euan et al. (Aug. 1994). “Automatic alignment of optical interferometers.” In: *Applied Optics* 33.22, pp. 5041–5049.

Müller, Vitali (2013). “Simulations for LISA & GRACE-Follow-On.” MA thesis. Leibniz Universität Hannover.

Müller, Vitali (July 2017). “Design Considerations for Future Geodesy Missions and for Space Laser Interferometry.” PhD thesis. Leibniz Universität Hannover.

Müller, Vitali et al. (June 2017a). *Absolute Laser Frequency Model of the GRACE Follow-On LRI*. tech. rep. AEI Hannover, NASA/JPL.

Müller, Vitali et al. (June 2017b). *Calibration of WS6 Wavelength Meter with an Iodine Standard*. Tech. rep. AEI Hannover.

NASA (2017). *GRACE-FO Mission Brochure*. NP-2017-4-002-GSFC. [Online; accessed 25-February-2019].

NASA/CalTech (2019). *Illustration of GRACE-FO (View 4)*. [Online; accessed 27-June-2019]. URL: https://gracefo.jpl.nasa.gov/resources/44/illustration-of-grace-fo-view-4/.

NASA/JPL (Sept. 2018). *GRACE-FO Satellite Switching to Backup Instrument Processing Unit*. [Online; accessed 21-May-2019]. URL: https://gracefo.jpl.nasa.gov/news/139/grace-fo-satellite-switching-to-backup-instrument-processing-unit/.

NASA/JPL (May 2019). *JPL GRACE-FO Level 1A/1B ASCII RL04 Datasets Release*. [Online; accessed 02-June-2019]. URL: https://podaac.jpl.nasa.gov/announcements/2019-05-23_JPL_GRACE-FO_Level1A_1B_ASCII_RL04_Datasets_Release.

Reider, Georg A. (2016). *Photonics*. Springer International Publishing. ISBN: 9783319260761.

Saleh, B.E.A. et al. (2007). *Fundamentals of Photonics*. Wiley Series in Pure and Applied Optics. Wiley. ISBN: 9780471358329.

Schmidt, R. et al. (Apr. 2008). “Hydrological Signals Observed by the GRACE Satellites.” In: *Surveys in Geophysics* 29.4-5, pp. 319–334.

Schütze, Daniel (2015). “Intersatellite Laser Interferometry: Test Environments for GRACE Follow-on.” PhD thesis. Leibniz Universität Hannover.

Schütze, Daniel et al. (Oct. 2014a). “Laser beam steering for GRACE Follow-On intersatellite interferometry.” In: *Opt. Express* 22.20, pp. 24117–24132.

Schütze, Daniel et al. (Apr. 2014b). “Retroreflector for GRACE follow-on: Vertex vs. point of minimal coupling.” In: *Opt. Express* 22.8, pp. 9324–9333.

Shaddock, Daniel (May 2008). “Space-based gravitational wave detection with LISA.” in: *Classical and Quantum Gravity* 25.11, p. 114012.

Sheard, B. S. et al. (Dec. 2012). "Intersatellite laser ranging instrument for the GRACE follow-on mission." In: *Journal of Geodesy* 86.12, pp. 1083–1095. ISSN: 1432-1394.

SpaceX (2018). *Iridium-6/GRACE-FO Mission*. [Online; accessed 09-August-2018]. URL: https://www.spacex.com/news/2018/05/22/iridium-6grace-fo-mission.

Tapley, B. D. et al. (2003). "Large scale ocean circulation from the GRACE GGM01 Geoid." In: *Geophysical Research Letters* 30.22.

Tapley, B. D. et al. (2004). "The gravity recovery and climate experiment: Mission overview and early results." In: *Geophysical Research Letters* 31.9.

Thompson, R. et al. (May 2011). "A flight-like optical reference cavity for GRACE follow-on laser frequency stabilization." In: *Joint Conference of the IEEE International Frequency Control and the European Frequency and Time Forum (FCS) Proceedings*. IEEE.

Van Flandern, TC et al. (1979). "Low-precision formulae for planetary positions." In: *The Astrophysical Journal Supplement Series* 41, pp. 391–411.

Wahr, John et al. (1998). "Time variability of the Earth's gravity field: Hydrological and oceanic effects and their possible detection using GRACE." in: *Journal of Geophysical Research: Solid Earth* 103.B12, pp. 30205–30229.

Wahr, John et al. (June 2004). "Time-variable gravity from GRACE: First results." In: *Geophysical Research Letters* 31.11, n/a–n/a.

Wall, Larry et al. (2000). *Programming perl*. O'Reilly Media, Inc.

Wang, Furun (2003). "Study on center of mass calibration and K -band ranging system calibration of the GRACE mission." Copyright - Database copyright ProQuest LLC; ProQuest does not claim copyright in the individual underlying works; Last updated - 2016-05-19. PhD thesis. The University of Texas at Austin, p. 258.

Wang, Hansheng et al. (July 2015). "Water storage changes in North America retrieved from GRACE gravity and GPS data." In: *Geodesy and Geodynamics* 6.4, pp. 267–273.

Ward, R L et al. (Apr. 2014). "The design and construction of a prototype lateral-transfer retro-reflector for inter-satellite laser ranging." In: *Classical and Quantum Gravity* 31.9, p. 095015.

Ware, B. et al. (2006). "Phase Measurement System for Inter-Spacecraft Laser Metrology." In: *Earth Science Technology Conference ESTC*.

Weaver, Gregory et al. (2010). *The performance of ultra-stable oscillators for the Gravity Recovery And Interior Laboratory (GRAIL)*. tech. rep. Johns Hopkins University: Applied Physics Laboratory.

Webb, Frank et al. (2018). *GRACE FO SDS Newsletter. Report: Oct-Nov 2018 (No. 1)*. [Online; accessed 22-June-2019]. URL: https://media.gfz-potsdam.de/gfz/sec12/pdf/GRACE_FO_SDS_NL_11_2018.pdf.

Webb, Frank et al. (2019). *GRACE FO SDS Newsletter. Report: Jan-Mar 2019 (No. 2)*. [Online; accessed 22-June-2019]. URL: https://media.gfz-potsdam.de/gfz/sec12/pdf/GRACE_FO_SDS_newsletter_No2.pdf.

Wegener, Henry et al. (Apr. 2018). "Reducing Pointing Induced Errors in the GRACE Follow-On Laser Ranging Measurement Using Dedicated Calibration Maneuvers." In: *EGU Vienna 2018*.

Wen, Hui Ying et al. (May 2019). *GRACE-FO Level-1 Data Product User Handbook*. JPL D-56935, Version of May 21, 2019. Jet Propulsion Laboratory.

Wooldridge, Jeffrey M (2015). *Introductory econometrics: A modern approach*. Nelson Education.

Eigenständigkeitserklärung

Hiermit versichere ich, dass ich die vorliegende Arbeit selbständig verfasst und keine anderen als die angegebenen Quellen und Hilfsmittel benutzt habe. Alle Stellen der Arbeit, die wörtlich oder sinngemäß aus anderen Quellen übernommen wurden sind als solche kenntlich gemacht und die Arbeit hat noch keiner Prüfungsbehörde in dieser oder ähnlicher Form vorgelegen.

Ort, Datum

Unterschrift